The Added Value of Advanced Multi-Modal Magnetic Resonance Imaging in the Diagnosis and Management of Childhood Cancer

By

Karen Angela Manias

A thesis submitted to the University of Birmingham for the degree of DOCTOR OF PHILOSOPHY

Institute of Cancer and Genomic Sciences
College of Medical and Dental Sciences
University of Birmingham

March 2019

UNIVERSITY OF BIRMINGHAM

Abstract

Background: Magnetic Resonance Imaging (MRI) provides images with excellent structural detail, but imparts limited information about the characteristics of paediatric tumours. MRI based functional imaging probes tissue properties to provide clinically important information about metabolites, structure and cellularity.

Aim: To determine the added value of advanced MRI, particularly diffusion-weighted imaging (DWI) and magnetic resonance spectroscopy (MRS), in non-invasive diagnosis and management of paediatric tumours, and facilitate integration into clinical practice.

Methods: Children with newly diagnosed body and brain tumours were imaged using multi b-value DWI and MRS respectively. Imaging data was used to develop a clinical decision support system for presentation to clinicians. Added diagnostic and clinical value of additional information was ascertained through retrospective and prospective evaluation.

Results: Quantitative DWI confers added diagnostic accuracy beyond conventional MRI, allowing discrimination of benign from malignant body tumours through morphological and quantifiably significant differences in Apparent Diffusion Coefficient (ADC) histograms. Chemotherapeutic response is reflected through visually apparent and quantifiably significant histogram changes. Review of MRS improves diagnostic accuracy of paediatric brain tumours, adding therapeutic value through avoiding biopsy of indolent lesions, aiding tumour characterisation, and allowing earlier treatment planning and clinical decision-making.

Conclusion: Advanced MRI adds value to non-invasive diagnosis and management of paediatric tumours in a real-time clinical setting. Presentation of complex information through a decision support system makes it accessible and comprehensible for clinicians, overcoming barriers precluding clinical use. Multicentre assessment is needed to promote integration of these techniques into the clinical workflow to improve care of children with cancer.

Dedication

For Babi,

for being with me, every step of the way. Always and forever.

Declaration

I declare that work presented in this thesis is entirely my own. The following aspects of this study were performed in collaboration:

1) The diffusion weighted imaging protocol for paediatric body tumours was developed by Professor Andrew Peet and Dr. Jan Novak.

2) The magnetic resonance spectroscopy protocol for paediatric brain tumours was developed by Professor Andrew Peet, Dr Nigel Davies and Dr Martin Wilson in close discussion with Children's Cancer and Leukaemia Function Imaging Group (CCLG FIG) members.

3) DWI, MRI and MRS investigations were acquired by radiographers in the Radiology Department at Birmingham Children's Hospital and made available for research by Shaheen Latif. MRS data transfer and processing aided by the radiographers was performed with the Children's Brain Tumour Research Group, in particular Heather Rose.

5) MIROR software development for analysis of quantitative diffusion weighted imaging and the Clinical Decision Support System was undertaken initially by Dr Niloufar Zarinabad, with support from Emma Meeus in calculation of IVIM parameters. Later software development of MIROR was undertaken by Dr Heather Rose and Dr Arfan Ahmed.

4) Dr. Martin Wilson developed TARQUIN and devised programming scripts that generated TARQUIN analysis of in vivo MRS.

5) Mean MR spectra for inclusion in the booklet designed to guide radiologists' interpretation of MRS data were produced with help from by Dr Simrandip Gill and Dr Ben Barbourina-Brookes.

6) Reporting of DWI, MRI and MRS data at the Birmingham Children's Hospital was performed by Consultant Radiology staff, in particular Dr Lesley Macpherson, Dr Katharine Foster, Dr Adam Oates, Dr Benjamin Pinkey and Dr Sana Ali.

Acknowledgments

I would like to thank my supervisors Professor Andrew Peet, Professor Bruce Morland and Dr Niloufar Zarinabad for their encouragement, support and guidance. This work would not have been possible without them. Thank you to the members of the Children's Brain Tumour Research Group in particular Dr. Heather Rose, Chris Bennet, Emma Metcalff-Smith and Dr Paul Davis for their advice throughout specifically computing and statistics guidance. Also thank you to other members of the group, Dr Sarah Kohe, Emma Meeus, Jane Crouch, Dr Ben Babourina-Brooks, Dr Simrandip Gill, Dr Dominic Carlin and Dr Lara Worthington for making me feel so welcome when I first joined.

A huge thank you the radiology department staff at the Birmingham Children's Hospital particularly the radiographers for acquiring the MRS and DWI data and booking clerks for facilitating scanning of body tumour patients on scanners suitable for data analysis. I would like to thank Shaheen Latif for her contribution in facilitating diagnostic MRS. Thank you to consultant radiologists with special mention for Dr Lesley Macpherson, Dr Adam Oates, Dr Ben Pinkey, Dr Katherine Foster and Dr Sana Ali for providing time and expertise for research studies. Thank you to Dr Niloufar Zarinabad for working so hard on MIROR, and to Dr Simrandip Gill for providing example mean MR spectra for incorporation in a guide for radiologists' interpretation.

I would also like to thank staff at the tumour registry and clinical research nurses at Birmingham Children's Hospital. And thanks to Dr Nigel Davies, Dr Emma Meeus, Dadi Zao and Dr Simrandip Gill for providing figures for use in this thesis.

An additional thank you to the charities involved in the funding for my work in particular the National Institute for Health Research (NIHR) for their invaluable funding for the 3 T MR research centre, and Help Harry Help Others.

Above all, thank you to my wonderful family, Andreas, Alex, Tom, Nick and Emma, for (and I quote) "donating [your] wife and mother to cancer research" for the last three years!

Funding: The PhD was funded by the National Institute for Health Research (NIHR) grant code 13-0053 and Help Harry Help Others Cure The research benefitted from collaborative work funded by various other funding bodies.

Role of the Funding Source: The sponsor had no role in the writing of this report.

Journal publications

In Press

Manias, KA, Gill SK, MacPherson LM, Oates A, Pinkey B, Davies P, Zarinabad N, Davies NP, Babourina-Brooks B, Wilson M, Peet AC. Diagnostic accuracy and added value of qualitative radiological review of ^{1}H-Magnetic Resonance Spectroscopy in evaluation of childhood brain tumors. Neuro-Oncology Practice. Accepted December 2018.

First Author Publications

1. **Manias KA**, Peet AC. Arch Dis Child Educ Pract Ed. What is MR Spectroscopy? 2017 Aug 26. pii: edpract-2017-312839. doi: 10.1136/archdischild-2017-312839

2. **Manias KA**, Gill SK, Zarinabad N, Davies P, English M, Ford D, Peet AC. Evaluation of the added value of 1H-magnetic resonance spectroscopy for the diagnosis of pediatric brain lesions in clinical practice. Neuro-Oncology Practice. 2017. doi:10.1093/nop/npx005

3. **Manias KA**, Gill SK, MacPherson LP, Peet AC. MRI based functional imaging in paediatric oncology. European Journal Of Cancer. 2017 Feb;72:251-265. doi: 10.1016/j.ejca.2016.10.037.

Named Author Publications

1. Zarinabad N, Meeus EM, **Manias KA**, Foster K, Peet A. Automated Modular Magnetic Resonance Imaging Clinical Decision Support System (MIROR): An Application in Pediatric Cancer Diagnosis. JMIR Med Inform. 2018 May 2;6(2):e30. doi: 10.2196/medinform.9171

2. Meeus EM, Zarinabad N, **Manias KA**, Novak J, Rose HEL, Dehghani H, Foster K, Morland B, Peet AC. Diffusion-weighted MRI and intravoxel incoherent motion model for diagnosis of pediatric solid abdominal tumors. J Magn Reson Imaging. 2017 Nov 21. doi: 10.1002/jmri.25901.

3. Zarinabad N, Wilson MP, Gill SK, **Manias KA**, Davies NP, Peet AC. Multiclass imbalance learning: Improving classification of paediatric brain tumours from magnetic resonance spectroscopy: Imbalanced learning for MRS tumour classification. Magn Reson Med. 2016 Jul 12. doi: 10.1002/mrm.26318.

Conference papers resulting from this work

Awards and Prizes

1. Magna Cum Laude Award (Best Conference Abstract), International Society of Magnetic Resonance Imaging (ISMRM), Hawaii 2017

2. Childhood Cancer and Leukaemia Group Prize (Best Presentation), Childhood Cancer and Leukaemia Group (CCLG) Annual Summer Meeting, Newcastle 2016

3. Sankey Research Runner Up Prize, Sankey Research Regional Meeting, Birmingham 2016

First Author Oral Presentations

1. **Manias K**, Rose HEL, Withey S, Peet AC. Functional Imaging in CNS Germ Cell Tumors. SIOPe, Prague, September 2017

2. **Manias K**, English M, Ford D, Gill SK, MacPherson L, Nicklaus-Wollenteit I, Rodrigues D, Peet AC. Added value of ^{1}H-MRS for the diagnosis of paediatric brain tumors. SIOPe, Prague, September 2017

3. **Manias KA,** Foster K, Zarinbad N, Peet AC. Differentiating between benign and malignant solid paediatric tumours and identifying tumour type using diffusion-weighted MRI and quantitative Apparent Diffusion Coefficient (ADC)). Childhood Cancer and Leukaemia Group (CCLG) Annual Summer Meeting, London, July 2017

4. **Manias K**, Zarinabad N, Foster K, Peet AC. Evaluating chemotherapeutic response of paediatric solid tumours using diffusion-weighted MRI and quantitative apparent diffusion coefficient (ADC). Childhood Cancer and Leukaemia Group (CCLG) Annual Summer Meeting, Newcastle, July 2016

5. **Manias K**., English, M., Ford, D., Gill, S.K., MacPherson, L., Nicklaus-Wollenteit, I., Rodrigues, D., Peet, A. Added value of 1-H Magnetic Resonance Spectroscopy for the non-invasive diagnosis of paediatric brain lesions in clinical practice. Sankey Research Regional Meeting, Queen Elizabeth Hospital, Birmingham, July 2016

6. **Manias K**, English M, Ford D, Gill SK, MacPherson L, Nicklaus-Wollenteit I, Rodrigues D, Peet AC. Added value of 1-H Magnetic Resonance Spectroscopy for the non-invasive diagnosis of paediatric brain lesions in clinical practice. International Society of Paediatric Neuro-Oncology (ISPNO) Meeting, Liverpool, June 2016; Neuro-Oncology 18 (suppl:iii167.1-iii167 • June 2016 DOI: 10.1093/neuonc/now083.10

First Author Poster Presentations

1. **Manias KA,** Gill SK, Macpherson L, Oates A, Pinkey B, Peet AC. Diagnostic accuracy and added value of qualitative radiological review of ^{1}H-MRS in evaluation of childhood brain tumors. International Society of Paediatric Neuro-Oncology (ISPNO) Meeting, Denver, June 2018

2. **Manias KA**, Zarinabad N, Foster K, Peet AC. The role of ADC histogram analysis in differentiating benign from malignant childhood tumours. International Society of Magnetic Resonance Imaging (ISMRM) Annual Scientific Meeting, Honolulu, Hawaii, April 2017.

3. **Manias KA**, Zarinabad N, Foster K, Peet AC. Evaluating chemotherapeutic response of paediatric solid tumours using diffusion-weighted MRI and quantitative apparent diffusion coefficient (ADC). Childhood Cancer and Leukaemia Group (CCLG) Annual Summer Meeting, Newcastle, July 2016

CONTENTS

LIST OF FIGURES

LIST OF TABLES

ABBREVIATIONS

ADC – Apparent Diffusion Coefficient
ASL – Arterial spin-labelling
ATRT - Atypical Teratoid Rhabdoid Tumour
AUC – Area under the curve
BS – Brain stem
CCLG – Childhood Cancer and Leukaemia Group
CDSS – Clinical decision support system
Cho – Choline
Cit - Citrate
CNS - Central nervous system
Cr - Creatine
CSF – Cerebrospinal fluid
CSI – Chemical shift imaging
DCE – Dynamic contrast enhanced
DIPG - Diffuse pontine glioma
DSC – Dynamic susceptibility contrast
DSS – Decision support system
DTI – Diffusion tensor imaging
DWI – Diffusion weighted imaging
EPI – Echo-planar imaging
FID - Free induction decay
FT – Fourier transform
FWHM - Full width half maximum
Gln - Glutamine
Glu - Glutamate
Glx - Glutamate + Glutamine
Gly - Glycine
GPC - Glycerophosphocholine
GUI – Graphical user interface
IVIM – Intravoxel incoherent motion
LDA - Linear discriminant analysis
LGG – low grade glioma
LMM – Lipids and macromolecules
MDT – Multidisciplinary team
MIROR – Modular medical image region of interest analysis tool and repository
mM - Millimolar
mIns - Myo-inositol
MR - Magnetic resonance
MRI - Magnetic resonance imaging
MRSI - Magnetic resonance spectroscopic imaging
MRS - Magnetic resonance spectroscopy
ms - milliseconds
NAA - N-acetyl aspartate
NF - Neurofibromatosis
NGGCT – Non-germinomatous germ cell tumour
NMR – Nuclear magnetic resonance
PCH- Phosphocholine

PF – Posterior fossa
PGSE – Pulsed gradient spin echo
PNET - Primitive neuro-ectodermal tumour
Ppm - Parts per million
PRESS - Point resolved spectroscopy
PWI – Perfusion weighted imaging
QC - Quality control
RF – Radiofrequency
ROC – Receiver operator curve
ROI - Region of interest
SIOPE – International Society of Pediatric Oncology Europe
SNR - Signal-to-noise
SS – Single slice
ST - Supratentorial
STARD –Standards for reporting of diagnostic accuracy
STEAM – Simulated echo acquisition mode
SVS - Single voxel spectroscopy
Tau - Taurine
tCho - Total choline
TE - echo time
TR – Repetition time
T - Tesla
WHO - World Health Organisation
WT – Whole tumour

Chapter 1: Introduction

1.1. Imaging in the diagnosis and management of paediatric tumours

Imaging is central to the diagnosis and management of solid tumours in children. Although conventional Magnetic Resonance Imaging (MRI) can accurately define the size and location of tumours and provide images with excellent structural detail, it often cannot answer other important questions influencing clinical management decisions. Tumour type, aggressiveness, metastatic potential or early treatment response cannot be determined accurately using conventional imaging techniques (Peet et al., 2012).

Functional imaging examines specific tissue properties relevant to the underlying biology of tumours. Techniques include diffusion and perfusion weighted imaging (DWI and PWI), assessing tissue structure and blood flow, and ^{1}H-magnetic resonance spectroscopy (MRS), measuring metabolite profiles. These complimentary modalities provide important information about tumour characteristics, allowing derivation of a more complete biological picture (Panigrahy and Bluml, 2009; Panigrahy et al., 2010). As conventional imaging cannot reliably discriminate between different types of tumours, biopsy and histopathology is usually necessary to determine a definitive diagnosis and treatment plan (Louis et al., 2007). Novel imaging methods can give improved information on tumour type and prognosis and allow treatment response to be monitored through providing data about the composition of imaged tissue (Peet et al., 2012).

Significant advances have been made in developing advanced imaging techniques and considering their implementation. This thesis evaluates the added value of novel functional imaging methods in paediatric oncology and investigates the optimum way of integrating these techniques into clinical practice to guide clinical decision-making and improve patient care.

1.2. Functional imaging techniques investigated

1.2.1. Diffusion Weighted Imaging

Diffusion weighted imaging (DWI) provides qualitative and quantitative information that may be used to improve tumour detection, characterization and monitoring of treatment response (Koh et al., 2007). DWI is based on microscopic water diffusion in tissue. Images acquired with high- and low-diffusion weighting (b-values) are used to develop Apparent Diffusion Coefficient (ADC) maps (Poretti et al., 2012). ADC values are a quantitative measure of diffusion with an inverse relationship with cellularity (Humphries et al., 2007) that may be useful for tumour characterisation.

Solid malignant tumours have high tissue cellularity, a high nuclear-to-cytoplasm ratio and a large number of cell membranes per unit volume. Densely packed and randomly organized cells inhibit motion of extracellular water protons and restrict diffusion, reflected quantitatively by a reduction in ADC. Highly cellular malignant tumours have low ADC (Humphries et al., 2007), as do abscesses and inflammation which restrict diffusion due to their cellular inflammatory exudate and high protein levels (Gawande et al., 2013). Benign solid tumours, cystic lesions and necrosis display less restricted diffusion and have a higher ADC due to their high water content, low tissue cellularity and low number of cell membranes.

1.2.2. Magnetic Resonance Spectroscopy

MRS is a non-invasive technique that is most commonly used to aid discrimination between different types and grades of brain tumour. ^{1}H-MRS uses the property that each hydrogen containing molecule resonates at a slightly different frequency in the MRI scanner to measure

the chemical composition of tissue. Information is provided about intermediary metabolites such as choline (involved in membrane synthesis) N-acetyl aspartate (neuronal marker) and mobile lipids (apoptosis and necrosis) (Orphanidou-Vlachou et al., 2018) The frequencies and intensities of resonances are presented graphically in a magnetic resonance spectrum (Figure 1.1).

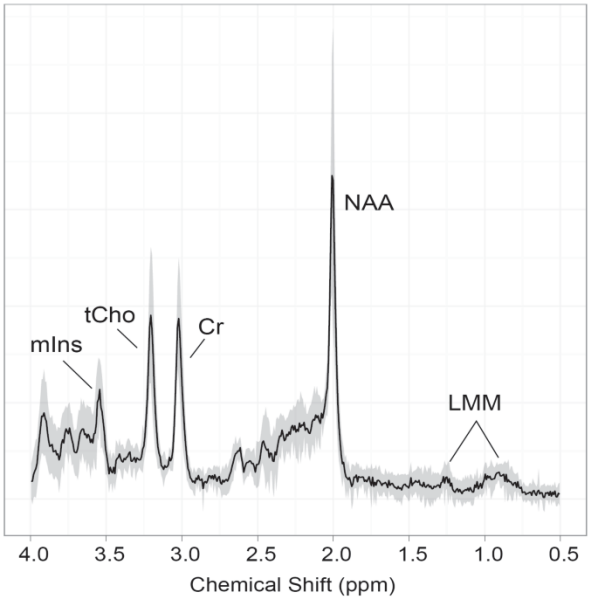

Figure 1.1. Mean magnetic resonance spectrum (MRS) of normal brain (white matter). mIns – myo-Inositol; tCho – total choline; Cr – creatine; NAA – N-acetyl aspartate ; LMM – lipids and macromolecules

Single voxel spectroscopy (SVS) acquires MRS data from a single region of interest (ROI) and has been used successfully in multicentre paediatric studies (Davies et al., 2010a). Mulitvoxel spectroscopy (also called chemical shift imaging, CSI, or magnetic resonance spectroscopic imaging, MRSI) provides information on tissue heterogeneity but is more complex to acquire and analyse.

MRS is widely available clinically and could be incorporated into a standard MRI protocol during diagnostic imaging and at follow-up. Although magnetic resonance spectra may be

used for clinical decision-making, routine implementation and interpretation has presented challenges in clinical practice.

1.2.3. Perfusion Imaging

Perfusion MRI evaluates blood flow and volume to impart information about microvasculature and angiogenesis. Techniques include dynamic contrast enhanced (DCE) and dynamic susceptibility contrast (DSC) MRI, arterial spin-labelling (ASL) and intavoxel incoherent motion (IVIM). Increased perfusion may reflect increased vascular growth associated with higher grade tumours (Laigle-Donadey et al., 2008).

DCE and DSC-MRI are performed using rapid sequence MRI following contrast injection via a mechanical pump that is often incompatible with central venous lines. Arterial spin-labelling (ASL) is a promising alternative in children (Hirai et al., 2011; White et al., 2014; Knutsson et al., 2010), allowing non-invasive quantitative measurement of cerebral perfusion without contrast injection and the associated requirement for IV access (Proisy et al., 2015). IVIM is a relatively new and largely experimental technique that uses an adaptation of DWI to detect the bulk motion of water molecules in the capillaries as a measure of perfusion (Le Bihan et al., 1988).

1.3. Clinical uses of functional imaging techniques in paediatric oncology

Functional imaging provides information to facilitate clinical decision-making in paediatric oncology that is not available with conventional imaging techniques. Additional information could be used for diagnosis, to provide prognostic biomarkers, to guide biopsy and to monitor

treatment response. Although there is considerable evidence in the adult oncology literature for the role of functional imaging, this cannot be extrapolated directly to the paediatric population in view of age and tumour specific differences (Peet et al., 2012). Evaluation of paediatric tumours is complex due to their diverse histological presentation and biological behaviours, confounded by technical challenges in performing complex imaging in young children.

This thesis focuses on the clinical use of DWI in solid paediatric body tumours and MRS in brain tumours. In view of this, this introductory chapter will focus primarily on these imaging techniques and applications.

1.3.1. Diagnosis before treatment

Pre-operative diagnosis can be difficult using conventional MRI alone (Orphanidou-Vlachou et al., 2013; Panigrahy et al., 2006). Radiologists use information about tumour site and size in combination with other imaging features such as enhancement, diffusion characteristics and clinical factors to form a differential diagnosis. Intraoperative histopathology is often inaccurate and does not permit pre-operative planning, and definitive histopathology is generally unavailable until several days after surgery (Ng et al., 2008). Functional imaging has potential to improve patient care through early diagnosis. Improved diagnostic information could guide surgical decision-making and provide information at an early stage to enable treatment planning to optimise outcome and minimise morbidity.

1.3.1.1. Non-invasive diagnosis of body tumours using DWI

Although there is evidence in the literature that quantitative DWI and ADC provide useful information for diagnosis of body tumours in adult oncology, there is a paucity of prospective data from paediatric patients. Studies in adults have shown DWI to be sensitive and specific for detecting colorectal tumours (Ichikawa et al., 2006), pancreatico-biliary tumours (Ichikawa et al., 2007), liver metastases (Koh et al., 2008), and differentiating malignant liver tumours from abscesses (Chan et al., 2001). The limited number of studies in children suggest DWI has potential value in paediatric oncology (Kocaoglu et al., 2010; Humphries et al., 2007; Alibek et al., 2009; Abdel Razek et al., 2009; Battal et al., 2012; Gawande et al., 2013; McDonald et al., 2011).

Paediatric studies have demonstrated ADC of malignant body lesions to be lower than benign lesions (Kocaoglu et al., 2010; Humphries et al., 2007; Alibek et al., 2009; Abdel Razek et al., 2009; Battal et al., 2012; Gawande et al., 2013; McDonald et al., 2011). Although an early small prospective study reported lower mean ADC in malignant than benign abdominal masses without reaching significance (Humphries et al., 2007), more recent studies suggest ADC can reliably characterise tumours (Kocaoglu et al., 2010; Abdel Razek et al., 2009; Lope et al., 2010; Neubauer et al., 2012). Evaluation of head and neck masses found mean ADC values of malignant, benign solid and benign cystic lesions of 0.93, 1.57 and 2.01 x 10^{-3} respectively, with significant difference between malignant and benign masses (Abdel Razek et al., 2009). Average ADC values of benign and malignant abdominal (2.28 and 0.84 x 10^{-3} respectively) (Kocaoglu et al., 2010), musculoskeletal (1.71 and 0.78 x 10^{-3} respectively) (Neubauer et al., 2012) and orbital tumours (Lope et al., 2010) were also significantly different. Most studies compare solid malignant with cystic benign lesions, possibly leading to an artificially elevated comparator mean ADC in benign masses. A retrospective analysis

did, however, demonstrate a significant difference between mean ADC in benign and malignant solid abdominal tumours (1.6 and 1.07 x 10^{-3} respectively) (Gawande et al., 2013).

Cut-off ADC values have been proposed for diagnosing malignant body tumours and are similar across studies. Evaluation of abdominal masses suggested ADC cut-offs of 1.1 (Kocaoglu et al., 2010) or 1.29 x 10^{-3} (sensitivity 77%, specificity 82%) (Gawande et al., 2013). A value of 1.25 x 10^{-3} differentiated malignant from benign head and neck masses (sensitivity 94.4%, specificity 91.2%) (Abdel Razek et al., 2009) and $\leq$ 1.03 x 10^{-3} was proposed for musculoskeletal tumours (sensitivity 90%, specificity 91%) (Neubauer et al., 2012). Sensitivity may be higher for solid, homogeneous tumours compared to necrotic tumours (Gawande et al., 2013).

Further research is needed into quantitative DWI in paediatric oncology. Direct comparison of results is difficult as evidence consists of small heterogeneous retrospective case series with variations in study design, ADC parameters, region of interest (ROI) measurement (Rumboldt et al., 2006; Gauvain et al., 2001; Yamashita et al., 2009; Yeom et al., 2013), b-values (Neubauer et al., 2012) and inclusion criteria (Yamasaki et al., 2005; Gauvain et al., 2001).

1.3.1.2. Non-invasive diagnosis of brain tumours using MRS

MRS may be used in combination with conventional imaging to support non-invasive diagnosis of childhood brain tumours (Panigrahy et al., 2006; Davies et al., 2008; 2010b). Brain tumours in children are histologically diverse entities with overlapping and heterogeneous imaging features. Chemical profiles are a useful diagnostic aid, with different tumour types displaying characteristic patterns of metabolite levels (Panigrahy et al., 2006;

Davies et al., 2008; 2010b). Studies in adults have found MRS in conjunction with MRI improves accuracy of non-invasive diagnosis of brain tumours (Julia-Sape et al., 2012) and combining MRS with pattern recognition gives diagnostic precision comparable to histopathology in a multi-centre setting (Garcia-Gomez et al., 2009). Pattern recognition of MRS profiles has been a useful aid to diagnosis in children (Panigrahy et al., 2006; Davies et al., 2008).

Quantitative interpretation of metabolites measured by MRS can facilitate non-invasive tumour categorisation. Brain tumours in general have high levels of choline and lactate and reduced N-acetyl aspartate (Arle et al., 1997; Davies et al., 2008), and individual metabolites may be used quantitatively to determine tumour type. High grade tumours have high levels of choline, lipids (Astrakas et al., 2004) and glycine (Davies et al., 2010b), while taurine has a strong association with primitive neuroectodermal tumours (Kovanlikaya et al., 2005) and medulloblastomas (Panigrahy et al., 2006; Davies et al., 2008). Creatine is significantly lower in pilocytic astrocytomas than in other paediatric brain tumours ($p<0.000001$) (Panigrahy et al., 2006). The differences between the mean spectra of the three most common paediatric posterior fossa tumours is illustrated in Figure 1.2.

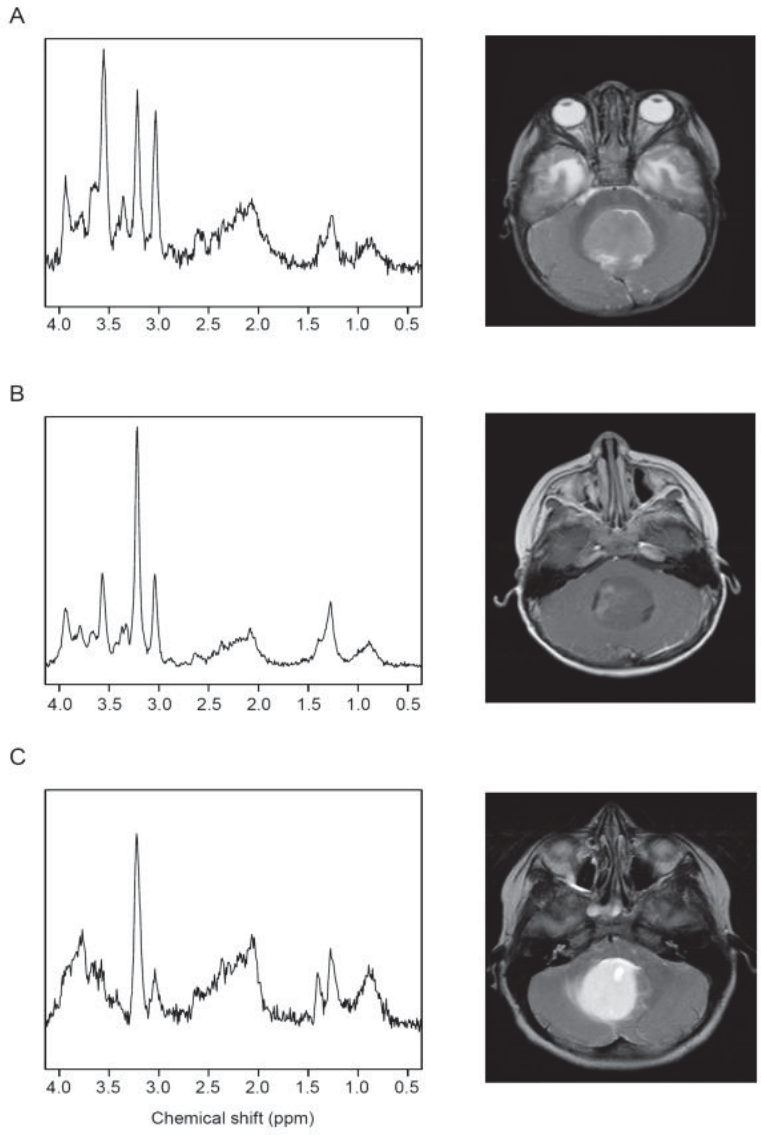

Figure 1.2. Comparison of MRS profiles and MR images of posterior fossa tumours, demonstrating (A) ependymoma, (B) medulloblastoma and (C) pilocytic astrocytoma.

Paediatric pilocytic astrocytomas, medulloblastomas and ependymomas have been accurately classified using MRS (Wang et al., 1995; Arle et al., 1997; Davies et al., 2008; Vicente et al., 2013). Metabolite ratios of NAA:Cho and Cr:Cho differentiated these tumours with accuracy of 0.85 (Wang et al., 1995), as did a neural network, using ratios of N-acetyl aspartate, choline and creatine (accuracy 0.88) (Arle et al., 1997) and Linear Discriminant Analysis (LDA) (accuracy 0.93) (Davies et al., 2008). Diagnostic classifiers, as illustrated in Figure 1.3., have been assessed in a multinational setting (accuracy 0.98) (Vicente et al., 2013).

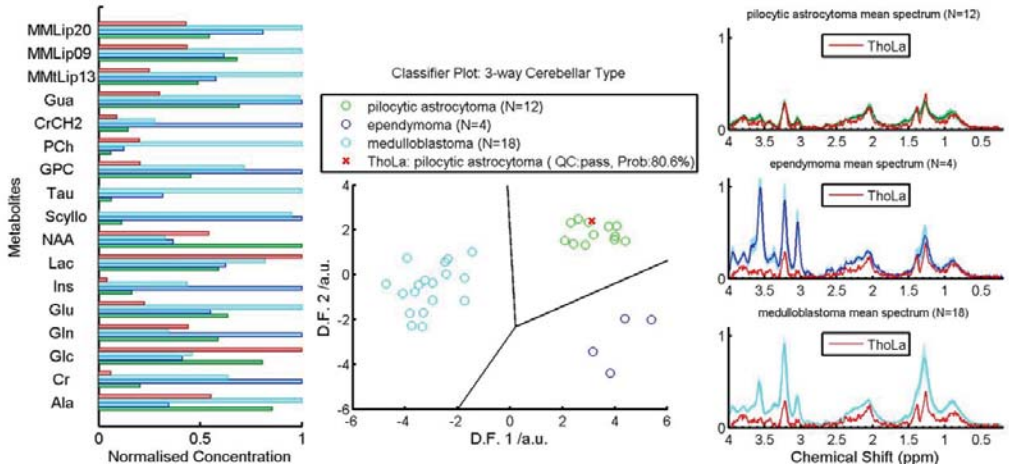

Figure 1.3. Decision Support System (DSS) output showing normalised metabolite profiles (left), linear discriminant function (D.F.) scores (centre) and MR spectra (right) for a case (red) compared with mean values for pilocytic astrocytoma (green), ependymoma (blue) and medulloblastoma (cyan). (Davies et al., 2016)

MRS can facilitate diagnosis of paediatric low-grade glioma subgroups. Significantly different choline and myo-inositol concentrations have been found in glioneuronal and glial tumours compared to other histological subtypes (Orphanidou-Vlachou et al., 2013). Metabolite profiles of pilocytic astrocytomas and unbiopsied optic pathway gliomas differ significantly depending on neurofibromatosis type I status and location (Orphanidou-Vlachou et al., 2013). As these tumours are often unbiopsied and treatment response differs between subtypes, accurate non-invasive diagnosis could improve outcome.

Although MRS can add value in diagnosing adult brain tumours in clinical practice (Murphy et al., 2002; Moller-Hartmann et al., 2002; Galanaud et al., 2006; Panigrahy et al., 2006; Julia-Sape et al., 2012), there is a paucity of evidence in children. A retrospective study found MRS significantly improved accuracy of radiological diagnosis of paediatric brain tumours over MRI alone (Shiroishi et al., 2015), with 63% correctly diagnosed using MRI compared with 87% with MRI and MRS (Shiroishi et al., 2015). Added value for MRS compared with conventional radiology was found in a further retrospective study of paediatric brain tumour

patients (Davies et al). Prospective studies are needed to validate these promising results in a clinical setting.

1.3.2. Guiding biopsy

Biopsy plays an important role in establishing histological diagnosis in paediatric malignancy, often with considerable morbidity and risk of sampling error. While conventional MRI cannot always determine optimal biopsy site of heterogeneous tumours (Martin et al., 2001), functional imaging can help target biopsy in tumours containing cystic or necrotic elements. DWI can identify densely packed tumour cells (Humphries et al., 2007), potentially guiding biopsy to areas likely to give a diagnostic yield. MRS with MRSI may guide biopsy in diffuse or large complex brain tumours in which heterogeneity poses a risk of sampling unrepresentative tissue.

1.3.3. Prognostic markers for childhood cancer

Prognosis of histopathologically similar paediatric tumours varies considerably, with differences in clinical behaviour related to underlying biology. There is little evidence that volume of a primary tumour at diagnosis is a useful prognostic factor for most malignancies (Olsen, 2015). Functional imaging provides novel non-invasive biomarkers to facilitate tumour characterization (Peet et al., 2007) and on-going risk stratification. This additional information has potential to be clinically useful through allowing individualization of treatment, with intensification in high-risk patients and reduction in those found to be low-risk.

1.3.3.1. Prognostic markers in body tumours derived from DWI

DWI could aid risk stratification in paediatric oncology through identification of high-grade tumours. Water diffusion is restricted by molecular and macromolecular barriers within the matrix of high-grade tumours due to the dense structure of tumour tissue. It has been hypothesized that restriction in diffusion increases with tumour grade, corresponding to reduction in ADC values in higher grade tumours in adult studies (Wang et al., 2011). Further research is needed to determine if this is applicable to tumours in children.

1.3.3.2. Prognostic markers in paediatric brain tumours derived from MRS

MRS has identified several non-invasive prognostic biomarkers in CNS tumours. Lipids and scyllo-inositol are predictive of poor survival, whereas glutamine and N-acetyl aspartate suggest improved survival (Wilson et al., 2013). Mobile lipids correlate negatively with intracellular glutamine (essential to lipogenesis in hypoxic tumour cells), implying a functional link (Wilson et al., 2013).

High intracellular macromolecules and lipids are associated with aggressive brain tumours (Vicente et al., 2013) with correlation between grade and mobile lipids (Astrakas et al., 2004). Medulloblastoma and ependymoma have greater lipid concentrations than pilocytic astrocytoma (Vicente et al., 2013). Choline is higher in medulloblastoma (grade IV) and ependymoma (grade II) than pilocytic astrocytoma (grade I) (Vicente et al., 2013), predicting poor survival in other non-metastatic CNS tumours (Marcus et al., 2007). An increased pre-treatment ratio of choline to N-acetyl aspartate predicts shorter survival in DIPG (Hipp et al., 2011). High citrate suggests poor survival in grade II astrocytoma (Bluml et al., 2011) and glutamate signifies poor prognosis in medulloblastoma (Wilson et al., 2014).

Low choline to N-acetyl aspartate ratio is predictive of good prognosis (Warren et al., 2000) and high myo-inositol levels are a biomarker of long progression-free survival in supratentorial pilocytic astrocytoma (Harris et al., 2008). Low creatine, common in grade I pilocytic astrocytoma (Harris et al., 2008), indicates good prognosis in grade II and III glioma (Hattingen et al., 2010). A multivariate model of survival across all CNS tumours based on 3 MRS biomarkers at diagnosis (lipids, glutamine and scyllo-inositol) had similar accuracy to histopathological grade in predicting survival (Wilson et al., 2013).

Metabolite profiles of metastatic and localised brain tumours differ, reflecting disparities in underlying biology and suggesting the possibility of identifying tumours at risk of metastatic relapse. Metastatic medulloblastomas have lower mobile lipids and higher total choline than localised tumours, suggesting decreased cell death and increased cell growth (Peet et al., 2007).

1.3.4. Early indicators of response

Clinicians rely on changes in tumour size to assess treatment response. This can take weeks or months to become apparent and does not always reflect the degree of histological response, particularly in lesions undergoing significant necrosis. A tumour may undergo tissue differentiation despite increasing in volume or conversely decrease in size but remain predominantly composed of malignant cells. Non-invasive biomarkers of response would be particularly helpful in monitoring tumours that are un- or incompletely resected, slow to respond to chemotherapy, or those that appear to progress through treatment.

1.3.4.1. Early indicators of response in paediatric body tumours derived from DWI

ADC is a potential biomarker of response in body tumours not treated by upfront resection (Humphries et al., 2007). DWI could detect early therapeutic success at a cellular level as cell death, loss of membrane integrity and reduced cellular density are reflected by increased ADC (Oka et al., 2010). Serial ADC measurements may allow quantitative response monitoring and continuous risk stratification. Measurable changes in ADC distribution have been reported, with tumours with histopathologically good response demonstrating greater increase in median ADC (McDonald et al., 2011). Minimum ADC has reflected response in osteosarcoma, with higher values post-chemotherapy correlating significantly with improved histological response (Oka et al., 2010). A small retrospective study of abdomino-pelvic neuroblastoma revealed significantly higher post-chemotherapy ADC (Demir et al., 2015).

1.3.4.2. Early indicators of response in paediatric brain tumours derived from MRS

Monitoring treatment response of brain tumours enables continuing risk stratification and treatment planning. The conventional method of measuring change in size on structural MRI is confounded by difficulties differentiating tumour from post-treatment changes. MRS provides information about characteristic changes in metabolites such as mobile lipids, myo-inositol and total choline that are potential early markers of response (Harris et al., 2008). Myo-inositol is a potential biomarker for monitoring supratentorial pilocytic astrocytomas, with future progression predicted by decreasing levels of this metabolite (Harris et al., 2008). Developing "real time" non-invasive biomarkers would be of clinical benefit through allowing adaptation of treatment as disease evolves (Peet et al., 2007).

1.3.5. Identifying active tumour after treatment, characterising pseudoprogression and diagnosing relapse in brain tumours using MRS

Differentiating tumour progression from pseudoprogression and diagnosing relapse and metastatic disease can be difficult using conventional MR imaging alone. Emerging evidence suggests functional imaging may add value in this area. Comparing MRS profiles of paediatric brain tumours at diagnosis and relapse may distinguish relapse from pseudoprogression and radiation necrosis, as no significant difference has been observed in any metabolite, lipid or macromolecule measured at diagnosis and first local or distant relapse (Gill et al., 2013).

1.4. Advances in analysis of functional imaging parameters

1.4.1. DWI Histograms

Tumours are heterogeneous masses consisting of a mixture of histological cell types, interspersed with necrosis and chemotherapy-induced changes. Mean or median ADC may be unrepresentative as high ADC in non-viable regions counteracts low values in cellular regions. Calculating ADC histograms using a multi-Gaussian model (Hales et al., 2015) provides information about distinct cellular subpopulations. Histogram peaks correspond to different tissue types and reflect chemotherapy-induced changes as differentiation occurs. Histograms could guide biopsy to target malignant regions avoiding cysts and necrosis.

Constructing a whole-tumour ROI allows histogram analysis of an entire tumour (Woo et al., 2014a), allowing reflection of heterogeneity. This technique has shown promise in differentiation and grading of paediatric CNS lesions (Bull et al., 2012) and differentiating tumour type and grade in adults (Pereira et al., 2015; Mimura et al., 2016; Hao et al., 2016).

ADC parameters decrease as grade increases (Pereira et al., 2015), with higher grade histograms having left shift, more positive skew and higher kurtosis (Pereira et al., 2015).

ADC histograms have been used in Wilms tumours to determine predominant histological cell type and predict subtype after chemotherapy (Hales et al., 2015). Comparing pre- and post- treatment histograms show an increase in mean ADC, with a shift to the right reflecting transformation to less cellular stromal tissue (Hales et al., 2015) (Figure 1.4.).

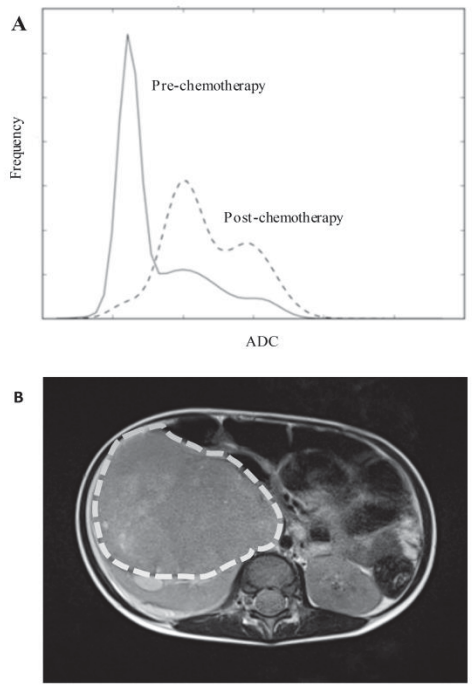

Figure 1.4. Diffusion Weighted Imaging (DWI) used to assess chemotherapeutic response in a Wilms tumour. A) ADC Histogram demonstrating shift to the right following response to neo-adjuvant chemotherapy. B) Region of Interest (ROI) drawn around the tumour. (Hales et al., 2015)

1.4.2. Intravoxel Incoherent Motion (IVIM)

More sophisticated methods of DWI analysis are emerging as understanding of ADC parameters improves. DWI is influenced by both structural components and perfusion in biological tissues, leading to variation in ADC depending on choice of b-values (Mazaheri et al., 2012). This variability can limit identification of threshold ADC values to differentiate benign from malignant lesions and makes study comparison difficult.

The intravoxel incoherent motion (IVIM) model allows extraction of additional information about perfusion from multi b-value DW-MRI to further characterise tumour tissue (Le Bihan et al., 1988). IVIM separates pure diffusion (D) from the pseudodiffusion component (D*) arising from microcirculatory perfusion and allows calculation of a perfusion fraction (f) corresponding to signal from the vasculature (Le Bihan et al., 1988). IVIM-D has performed better than ADC in discriminating low- from high-grade hepatocellular carcinoma (Woo et al., 2014b). Although IVIM is a very new technique and not in routine clinical use at present, it has successfully differentiated benign from malignant lesions in adults (Kang et al., 2014; Klauss et al., 2016). IVIM-f has differentiated high- from low-grade brain gliomas (Federau et al., 2012).

1.5. Multimodal advanced imaging

The techniques described in this thesis are largely complimentary and there is an increasing recognition that a multi-modal approach to data acquisition should be followed (Peet et al., 2012). The International Society of Pediatric Oncology Europe (SIOPE) Brain Imaging Group has agreed a protocol for brain tumours which includes single voxel MRS, Diffusion Tensor Imaging (DTI) and DSC-MRI. In the UK, the Children's Cancer and Leukaemia Group's Functional Imaging Group have advocated a protocol for abdominal tumours including multi b-value DWI. The main parameter sets for these protocols are given in the supplementary material (Appendix 1 and 2). Specific clinical situations may make other protocols optimal but adaptations require significant local experience in using the technique.

1.6. Implementing functional Imaging and integration into routine clinical practice

A number of issues must be addressed when considering clinical use of functional imaging in paediatric oncology. There are several challenges to routine implementation of these techniques into clinical practice, including developing standardised acquisition protocols with appropriate quality control measures, processing and presenting information, and handling complex quantitative data that requires presentation in a format comprehensible to clinicians.

1.6.1. Integration of diffusion weighted imaging into clinical practice

DWI is suitable for paediatric use as it requires no IV access, contrast injection or compliance with breath-hold techniques. Routine clinical integration is feasible as multi b-value DWI can be performed on all modern MR scanners as part of a standardised protocol. Acquisition times are short, with additional scanning time of 2-7 minutes for body protocols. ADC values are independent of magnetic field strength (Gawande et al., 2013) which aids translation across different scanners.

Although qualitative DWI is used routinely in brain tumours and to some extent in non-CNS tumours, there is a need for further research into quantitative applications prior to incorporation into routine clinical practice. Most evidence consists of small retrospective case series confounded by lack of standardization of DWI techniques. There is no standard method for determination of Region of Interest (ROI): some studies have drawn several small ROIs in the solid component of a tumour (Gawande et al., 2013; Oka et al., 2010), whereas others have included the entire tumour volume with and without cystic (Kocaoglu et al., 2010; Abdel Razek et al., 2009; Humphries et al., 2007) and necrotic (Littooij et al., 2015; McDonald et al., 2011) areas. Choice of b-values also varies between studies leading to inconsistencies in ADC values and making direct comparison of results difficult. Technical

difficulties could lead to misinterpretation of ADC, with small tumour size, necrosis, bleeding and calcification influencing measurements.

Although quantitative ADC measurements may be clinically useful, analysis of quantified data represents a departure from traditional working for radiologists, necessitating further training and attitudinal shift. Further challenges include ensuring reproducibility of DWI, both within and between centres. Inter-observer reliability should be addressed, although good inter-observer correlations between ADC measurements have been reported (Gawande et al., 2013; Littooij et al., 2015). Standardized protocols and diffusion phantoms are required to ensure ADC values before and after treatment accurately reflect changes in diffusion, and centres should adhere to set protocols and implement robust quality assurance.

1.6.2. Implementation of MRS

MRS is not widely used in clinical practice and a number of challenges must be overcome to allow its implementation as a routine tool in clinical decision-making. Implementation has been hampered by lack of agreed quality control measures, acquisition protocols and analysis techniques for specific clinical scenarios. Further challenges include processing and presenting information, assessing quality of spectra and accurately interpreting data.

MRS can be performed during routine MRI scanning without need for additional IV access or general anaesthesia. An MRS protocol consisting of acquisition of a single voxel spectrum should add no more than 5 minutes to total examination time. Better data can be acquired in a shorter time period using MRI scanners with higher field strength (e.g. 3T systems). Single voxel MRS could be used in centres without additional spectroscopy support as data is relatively easy to acquire, assess and interpret. More complicated techniques such as multi-

voxel MRS are more difficult to integrate into mainstream practice due to delays in reporting and the requirement for MR spectroscopist help with interpretation.

There is a paucity of research into how to implement diagnostic information from MRS into the clinical diagnostic pathway in routine clinical practice. Biomarkers need to be evaluated in well-defined diagnostic groups treated in a standardized manner as part of a clinical trial. Prospective studies are needed to evaluate the diagnostic impact of MRS over MRI alone in brain tumours in children. The STARD (Standards for Reporting of Diagnostic Accuracy) Guidelines for reporting diagnostic accuracy (Bossuyt et al., 2003) should be adhered to ensuring studies of sufficient quality are conducted to provide high quality evidence for the added value of this technique.

1.7. Clinical Decision Support Systems (CDSSs)

Advancements in MRI techniques have highlighted the need for analysis tools to extract and analyse relevant information to aid clinical decision-making. A major hurdle to incorporating multimodal functional imaging into real time radiological diagnosis is the difficulty in timely analysis of quantitative data, especially in busy radiology departments and the emergency setting. As radiologists are not trained to quantitatively evaluate functional imaging data it is important to present comprehensible information and minimise need for complex analysis.

Clinical Decision Support Systems (CDSSs) have potential to make complex advanced MRI data available to aid clinical decision-making. CDSSs aim to facilitate optimum human performance through harnessing advanced imaging and analysis techniques and allowing them to be used in conjunction with the clinical user's decision-making skills and abilities. Availability of a user-friendly and flexible CDSS that encompasses a variety of medical

image analysis techniques and post-processing methods could facilitate uptake of advanced MRI techniques such as DWI and MRS in a real-time clinical setting.

There are, at the time of writing, no CDSSs available to facilitate clinical use of multi b-value DWI for the diagnosis, characterisation or treatment monitoring of solid body tumours. Although MRS classifiers are being developed for adults brain tumour diagnosis (Tate et al., 2006), data cannot be extrapolated for paediatric use as childhood tumours are very different entities. One challenge in paediatrics is developing robust classifiers from small patient numbers given the numerous different types of childhood brain tumours, extensive subcategorisation, and need to restrict cases by patient age and tumour location. It is difficult to obtain sufficient cases to formulate robust classifiers and impossible to develop and implement classifiers to distinguish all types of paediatric brain tumours.

Providing CDSSs that are acceptable to clinicians is challenging. A CDSS should be user-friendly with an intuitive graphical user interface, adaptable as data sets and diagnostic classification schemes are regularly updated, and appropriate for use in a clinical setting. As clinicians are reluctant to use systems that do not fit into routine clinical practice, integration with other diagnostic tools is essential. A Participatory Design approach may be used in developing a CDSS, actively involving clinicians in the design process to ensure the final product meets the needs of those intended to use it (Dredger et al., 2007). Once established, user acceptance studies should be conducted in the clinical environment to determine the value of the CDSS.

1.8. Summary

Functional imaging provides information on tumour properties unavailable from conventional MR imaging. Clinically, functional imaging can improve non-invasive diagnosis and early treatment monitoring, as well as providing biomarkers of prognosis. Further research is needed to define the optimum use of functional imaging in a clinical setting and integrate these promising new techniques into routine practice to improve care of children with cancer.

1.9. Aims and Objectives

Overall Aims

The aims of this work were to determine the added value of functional imaging and its derived biomarkers for diagnosis and treatment monitoring in paediatric oncology when compared with reporting of conventional imaging used in routine practice. A secondary aim was to facilitate the integration of advanced MR imaging techniques into clinical practice.

Objectives

1. To establish the role of quantitative DWI and ADC histogram analysis in the diagnosis of paediatric solid body tumours.
2. To prospectively evaluate the added value of DWI and ADC histogram analysis in non-invasive differentiation of benign from malignant childhood tumours.
3. To evaluate DWI and quantitative ADC and IVIM histogram analysis as potential biomarkers for evaluating the chemotherapeutic response of paediatric solid tumours.
4. To determine the reproducibility of ADC histogram-derived parameters and formulate recommendations for methodology of ROI selection.
5. To determine the added value of qualitative radiological review of single voxel MRS in the non-invasive diagnosis of paediatric brain tumours.

6. To review clinical use of MRS over a defined time period, explore its added therapeutic value over conventional imaging and its role in non-invasive diagnosis and clinical decision-making, and investigate its potential impact on patient care.
7. To contribute to the design, development, and evaluation a clinical decision support system for automatic processing, evaluation and representation of advanced magnetic resonance imaging data to provide real-time diagnostic support for clinicians.

1.10. Thesis organisation and contributions

The theory of advanced MR imaging, including DWI and MR spectroscopy, is summarised in chapter 2. Study methodology and a summary of statistical analysis techniques used in this work are described in chapter 3.

Chapter 4 focuses on establishing the added value of quantitative DWI and ADC histogram analysis in the diagnosis of paediatric solid body tumours to meet objective 1. Development of a CDSS through creating a repository of benign and malignant tumours with which new cases can be compared, to meet objective 7, is also described. This work has been presented orally at the Childhood Cancer and Leukaemia Group (CCLG) Summer Meeting, London, 2017, and as a poster at the International Society of Magnetic Resonance Imaging Meeting (ISMRM), Hawaii, 2017.

To fulfil objectives 2 and 7, chapter 5 is a prospective evaluation of the added value of DWI and ADC histogram analysis and the CDSS under development in the differentiation of benign from malignant childhood tumours. As ADC histogram analysis has never before been evaluated prospectively in paediatric oncology, it is important to do so to validate and explore the clinical utility of techniques found to show promise retrospectively.

Chapter 6 explores the role of DWI and quantitative ADC and IVIM histogram analysis as potential biomarkers in evaluating the chemotherapeutic response of paediatric solid tumours, in accordance with objective 3. This work was presented orally and as a poster at the Childhood Cancer and Leukaemia Group (CCLG) Annual Summer Meeting, Newcastle, July 2016.

To satisfy objective 4, chapter 7 determines the inter-rater reproducibility of ADC histogram-derived parameters and aims to formulate recommendations for methodology of ROI selection. There is as yet no established recommended method for ROI construction, and it is important to ensure that any technique proposed for incorporation into clinical practice is reproducible, clinically applicable and provides clinically relevant and robust information.

Chapter 8 aims to determine the added value of qualitative radiological review of single voxel MRS in the non-invasive diagnosis of paediatric brain tumours, in accordance with objective 5. This work was presented orally at the International Society of Paediatric Oncology (SIOPe), Prague, 2017 and the Sankey Research Regional Meeting, Birmingham, 2016, as a poster at the International Society of Paediatric Neuro-Oncology (ISPNO) Meeting, Denver, 2018, and is currently In Press for publication in Neuro-Oncology Practice.

Chapter 9 is a review of clinical use of MRS and an exploration of its added therapeutic value over conventional imaging, its role in non-invasive diagnosis and clinical decision-making and its potential impact on patient care. This work was presented orally at the International Society of Paediatric Neuro-Oncology (ISPNO) Meeting, Liverpool, 2016, and is published in Neuro-Oncology Practice.

The final chapter 10 includes the conclusions drawn from this thesis and discusses future work.

Chapter 2: Theory of Advanced MRI

2.1. Introduction

It is important to have a basic understanding of the fundamental principles of Nuclear Magnetic Resonance (NMR) and Magnetic Resonance Imaging (MRI) to understand Magnetic Resonance Spectroscopy (MRS) and Diffusion Weighted Imaging (DWI) and their roles in clinical practice. MRI detects protons (^{1}H) present in tissue, of which the majority are in water, to generate two-dimensional structural images.^{1}H MRS is designed to detect proton signals from metabolites and macromolecules to determine their relative concentrations. DWI images reflect the motion of water within tissues on the scale of Brownian motion to provide information about cellularity through degrees of diffusion restriction.

MRI, MRS and DWI are based upon nuclear magnetic resonance (NMR), a phenomenon in which nuclei absorb and emit electromagnetic radiation when placed in an external magnetic field. The hydrogen nucleus is a single, positively charged proton with an intrinsic magnetic quality termed nuclear spin that produces a magnetic field. Although other atomic nuclei also possess nuclear spin, hydrogen is used in clinical MRI and MRS due to the prevalence of hydrogen atoms in human tissue with high water content.

2.2. Magnetic Resonance Imaging (MRI)

An MRI scanner comprises a primary magnet, gradient magnets, radiofrequency (RF) coils and a computer system that generates images. Nuclear spin vectors (dipole moments) are randomly oriented in the absence of an applied magnetic field. Application of a primary external magnetic field (B_o) by the primary magnet causes hydrogen atoms in tissue to align parallel (low energy) or antiparallel (high energy) to it. A greater proportion of nuclei align parallel, contributing to a net magnetic vector (Figure 2.1.).

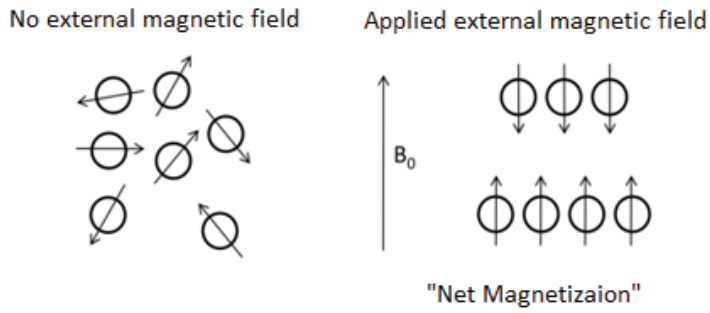

Figure 2.1. Application of a constant external magnetic field (B_o) leads to polarization of magnetic nuclear spins as the dipole moments align with the external field

Longitudinal magnetisation is when the tissue is magnetised in a direction parallel to the direction of the magnetic field. Transverse magnetization is when the direction of tissue magnetization is at a 90° angle with respect to that of the magnetic field (Figure 2.2.)

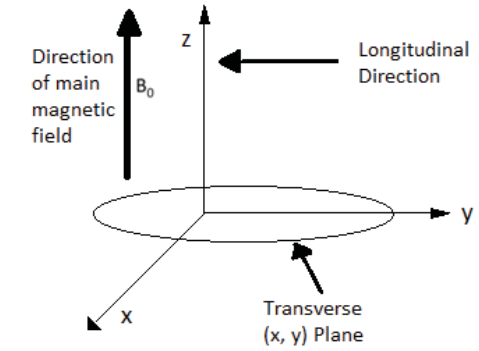

Figure 2.2. Magnetic gradient fields oriented in the Transverse (x, y) and Longitudinal (z) planes

Protons precess or spin around the long (z) axis of the primary magnetic field at a rate termed the Larmor frequency. The Larmor frequency is calculated using the Larmor equation:

$$\omega = \gamma B_o \qquad (2.1)$$

(ω = frequency, γ = gyromagnetic ratio, B = magnetic field strength)

and is thus proportional to the gyromagnetic ratio of the nucleus and the strength of the external magnetic field. Hydrogen has a relatively high gyromagnetic ratio, characterised by a large energy difference between spin states. The frequency of precession changes in proportion to the magnetic field strength measured in Tesla, with 1.5T commonly used in

clinical practice. Protons are in phase when they precess together and out of phase when they precess separately.

Magnetic gradient fields are generated from gradient coils in an MRI scanner. They are oriented in the x, y and z axes (Figure 2.2.) and allow spatial encoding or localisation for images. Radiofrequency (RF) coils allow application of a RF pulse (B_1) with the same precession frequency as the nuclei within the primary magnetic field. This causes some low-energy parallel protons to flip to a high-energy state, decreasing longitudinal magnetisation. As the protons precess in phase the net magnetization vector turns towards the transverse plane at 90° to the primary field, resulting in transverse magnetisation.

Relaxation occurs as nuclei return to the equilibrium state and is measured in two directions: longitudinal (T1) parallel to B_o (z axis), and transverse (T2) perpendicular to B_o (x-y axis). T1, "spin-lattice" or "longitudinal" relaxation time, describes the time taken for an individual nucleus to return to its equilibrium state, or recovery of the z-component of the net magnetization vector. T2, "spin-spin" or "transverse" relaxation time, is related to the effect of nuclear spins on one another and refers to time taken for precessing nuclei to fall out of alignment with one another. T2 relaxation is generally shorter than or equal to T1. Different types of tissue show different T1 and T2 relaxation, manifest as image contrast: T1 hyperintensity in tissue usually means a shorter T1, whereas T2 hyperintensity means a longer T2. Cerebrospinal fluid, for example, has a long T1 and appears dark on T1 weighted images. Pathologies can appear as either hypointense (dark) or hyperintense (bright) on T1 or T2 weighted images.

The Free Induction Decay (FID) (Figure 2.3.) is the signal detected by the receiver coil of the MR scanner, induced by the RF excitation of nuclear spins that decreases exponentially at a time constant T2*. In reality, spins dephase much faster than T2 due to inhomogeneities in the external magnetic field (B_o), which means it has different strengths at different locations. As this causes destructive interference that shortens the FID, T2* is always shorter than T2.

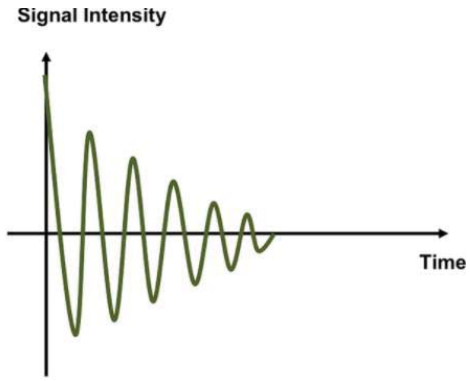

Figure 2.3. Free Induction Decay

The FID refers to the electric current changes in the receiver coil. The oscillating magnetic field generated by the precessing nuclear net magnetisation is detected by the receiver coil and used to generate images. When the MR computer detects the RF signal it undergoes analogue-to-digital conversion followed by Fourier Transform (a mathematical procedure for reconstructing images from raw data) to produce an image.

2.3. Diffusion Weighted Imaging (DWI)

2.3.1. Background to DWI

Diffusion-Weighted Imaging (DWI) is an MR technique that utilises the Brownian motion of spins to provide information about the properties of biological tissue. Diffusion represents the net displacement of a group of molecules within a pre-determined voxel between two time

points. In DWI, the thermally driven diffusion of water protons within human tissue is exploited to visualize tissue characteristics. The apparent diffusion of water reflects tissue cellularity, the composition of the extracellular space, cell membrane integrity and the viscosity of tissue fluids.

2.3.2. Acquisition of DWI

In order to generate diffusion weighting on an image, applied diffusion gradients are added to a conventional MRI sequence (Figure 2.4.). The sequence of choice for DWI is spin echo-planar imaging (EPI), which has a rapid acquisition time and encounters little motion-induced artefact, although it is prone to susceptibility artefacts (e.g. at the base of the skull). Diffusion-weighted contrast is produced by a Pulsed Gradient Spin Echo (PGSE) consisting of a 90-180° spin-echo pair of RF pulses. The first gradient applies a phase shift to the protons, which is reversed by the second gradient. Signal attenuation occurs as the second gradient is unable to undo all the changes induced by the first gradient due to the movement or diffusion of protons.

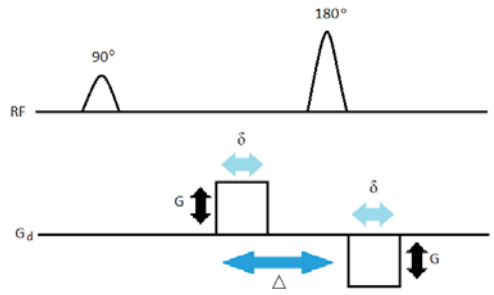

Figure 2.4. Application of diffusion gradients (G) to a conventional spin-echo MRI sequence. Two diffusion gradients of magnitude (G) and duration (δ), separated by time interval (Δ), are added symmetrical to the 180° RF pulse.

DWI exploits the different diffusion properties of water molecules in structurally different tissues, with image contrast generated as the measured signal is dependent on particle motion. Tissues with high water content have mobile molecules that lead to high signal attenuation

and deliver low signal intensity, whereas more solid and cellular tissues give less attenuation and stronger signal intensity. Signal attenuation is described by the Stejskal-Tanner equation:

$$S(b) = S_0 \cdot \exp(-b\mathrm{D}) \qquad (2.2)$$

In which *S(b)* is the signal received for a certain applied gradient or b-value (measured in units of s/mm^2), S_0 is the signal strength with no diffusion weighting, and D is the diffusion constant of the imaged tissue (measured in units of mm^2/s^{-1}).

The b-value reflects the strength and timing of gradients used to generate diffusion-weighted images. The higher the b-value, the greater the diffusion effect. Multiple DW images can be obtained with a range of b-values through altering the strength and magnitude of the applied gradient. The effect of diffusion is more prominent in images acquired with higher b-values, with values for b of up to 1000 s/mm^2 necessary to obtain good image contrast. Images obtained at b0 with no applied gradient contain no information about diffusion and are a T2 weighted structural image. The b-value is given by the equation:

$$b = \gamma^2 G^2 \delta^2 (\Delta - \delta 3) \qquad (2.3)$$

where γ is the gyromagnetic ratio (a constant, 42.58 MHz/T for protons), G the strength of the applied gradient, δ the duration of the gradient, and Δ the time between two gradients. It can thus be seen that signal loss is dependent on the strength and duration of gradients applied and the time between pulses.

2.3.3. ADC and ADC Maps

If DWI is performed with a minimum of two b-values, the Apparent Diffusion Coefficient (ADC) can be calculated as a straight line of the logarithm of the signal values. The term "apparent" is used because the parameter comprises information from tissue and capillary perfusion in addition to pure diffusion (D). ADC is expressed in units of 10^{-3} mm^2/s and is

calculated using a monoexponential fit of the b-values 0 and 1000 s/mm^2. Repeating this for each voxel within an image creates a parametric ADC map, with the ADC value in any given voxel being the slope of the line of the relationship between the logarithm of the signal intensity and the b-value (Figure 2.5.). Higher ADC values are reflected in voxels with high water diffusivity, which have a steeper slope of signal attenuation with increasing b-values. Highly cellular tissues will demonstrate a more gradual attenuation slope with lower ADC values.

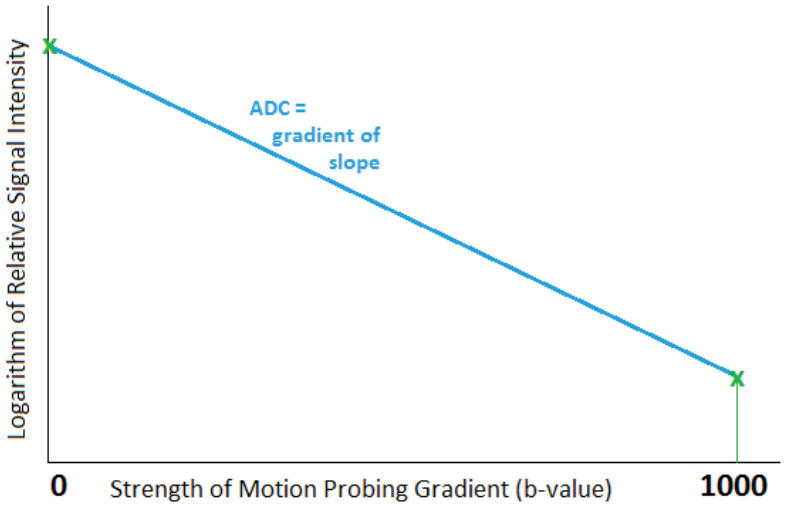

Figure 2.5. Apparent diffusion coefficient (ADC) calculation
Calculation of ADC from multi b-value DWI using a monexponential fit. The logarithm of relative signal intensity is plotted against the b-value for each image voxel acquired at same anatomic position at increasing gradients (Koh et al., 2011).

The b1000 DW image is often used to identify areas of restricted diffusion as they have high intensity. However, since the b0 image is a T2 weighted image, hyper-intense signal on the b1000 DW images may be due to inherently high T2 signal of the tissue ("T2 shine-through") rather than restricted diffusion. ADC maps are helpful as they mathematically eliminate T1 and T2 contrast effects in the images avoiding this pitfall. ADC maps facilitate visualisation of diffusion patterns as low areas of tissue diffusion appear hypo-intense, whereas high areas of diffusion are hyper-intense, the inverse of high b-value DW images. In addition to this, as

ADC is dependent on tissue properties but largely independent of other factors which vary with acquisition technique (e.g. field strength), ADC maps allow comparison of images obtained by different scanners at different centres and even at different field strengths.

2.3.4. Intravoxel Incoherent Motion (IVIM)

DWI measures the attenuation of the signal due to water motion. This has contributions from Brownian motion of water but there will also be some movement of water on a similar timescale within the capillary bed due to perfusion. Signal attenuation in DWI thus depends on the velocity of the flowing blood and the vascular architecture of the imaged tissue in addition to the diffusion of water. When DWI is conducted in well-perfused tissue within the b-value range 0–1000 s/mm^2, some of the signal attenuation at low b-values (0–100 s/mm^2) arises from microcirculation within the capillary network since this is at a faster timescale than pure diffusion (Le Bihan et al., 1988).

Multi b-value DWI has potential to non-invasively assess both diffusion and perfusion in tissue through the intravoxel incoherent motion (IVIM) model. The IVIM model uses biexponential fitting to describe DWI data given that measured signal attenuation comprises a mixture of effects of tissue perfusion and diffusion. IVIM simultaneously assesses the diffusion components corresponding to true molecular diffusion in tissue (D) and pseudo-diffusion (D*) from perfusion in the micro-capillary network. It also allows derivation of the perfusion fraction (f) from the micro-vascular network that reflects tissue vascularity (Le Bihan et al., 1988).

The biexponential relationship between b-values and the diffusion signal intensities is described by the following equation (Le Bihan et al., 1988):

$$S(b)/ S_0 = f \cdot \exp(-bD^*) + (1-f) \cdot \exp(-bD) \qquad (2.4)$$

S_0 is the signal intensity at b = 0 and $S(b)$ reflects intensities in s/mm^2. The f parameter is the perfusion fraction from flowing blood, D is the true water diffusion coefficient and D* the pseudo-diffusion coefficient in blood.

The effect of pseudodiffusion (D*) on the signal attenuation in each imaging voxel is dependent on the b-value. The relative contribution of pseudodiffusion to the DWI signal is significant at lower b-values, but only accounts for a small proportion of signal at higher b-values. D* and D can be separated as the rate of signal attenuation from pseudodiffusion is normally an order of magnitude greater than tissue diffusion. This is depicted in Figure 2.6.

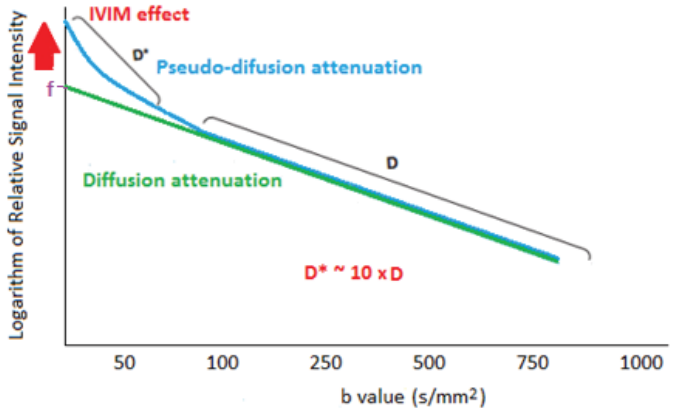

Gradient = D; Off-set of the intercept = f

Figure 2.6. Effects of diffusion (D) and pseudo-diffusion (D*) on the MRI signal

At high b-values values (>100 s/mm^2) perfusion effects are negligible with D* >> D. Linear fitting of the higher b values can be performed to calculate the D parameter from the gradient of fit. The f parameter can be deduced by extrapolating the fit to the y-axis and taking the difference to the b0 signal. At low b-values (<100 s/mm^2), perfusion effects are more pronounced resulting in a biexponential shape, with the IVIM effect appearing as a deviation of the tissue diffusion signal decay as D*>D (Koh et al., 2011).

2.3.5. Challenges and limitations of quantitative DWI

Despite advancements in DWI techniques and development of quantitative analysis to evaluate ADC values, there are inherent challenges and limitations in DWI interpretation and technical issues associated with poor spatial resolution, and lack of standardized image acquisition protocols and data analysis procedures. The main technical limitations are inherently low signal-to-noise ratio (SNR), susceptibility to artefact with echo-planar imaging (EPI) and difficulties with reproducibility. Ghosting may occur due to respiratory motion and chemical shift artefact. It is not possible to accurately calculate ADC from areas of very low signal intensity on a b0 map, particularly in areas with difficulties with susceptibility changes (e.g. haematoma), as the slope of the gradient will be insufficient to obtain a representative value. Additionally, there is no standardised recommendation for number of b-values or method of ROI construction for determining ADC values for a particular type of lesion.

"T2 shine-through" can cause difficulties with interpretation of high b-value DW images as signal intensity is influenced by T2 relaxation time. Lesions with high fluid content, such as cysts, mimic restricted diffusion as they have a long T2 relaxation time and high signal intensity even at high b-values. Referring to the ADC map is helpful as a cyst will demonstrate high signal intensity on both T2 weighted images and the ADC map, whereas true restricted diffusion will show low signal intensity on the latter. A further consideration when interpreting DWI is that slow flowing blood may demonstrate the same signal intensity characteristics as highly cellular lesions. A haemangioma with low signal intensity on an ADC map may be mistaken for a solid tumour, although interpretation should be performed in the context of other MR sequences to determine other characteristic imaging features.

Quantitative analysis can provide numerical ADC values that are robust against the effect of imaging artefact and subjective interpretation. ADC measurements can be produced for a given region by drawing regions of interest (ROIs) on the ADC map. This quantitation can reduce ambiguity, increase objectivity and allow more direct comparison of values.

2.4. Magnetic Resonance Spectroscopy (MRS)

2.4.1. Background to MRS

MRS is an advanced, non-invasive MR technique that allows biochemical characterisation of tissue *in vivo*. MRS is performed following conventional MRI by placing a voxel on an appropriately placed region of interest (ROI) and measuring the level of different metabolites in the selected tissue through producing a spectrum of resonances. The raw MR signal or Free Induction Decay (FID) is measured as a function of time. Fourier Transform (FT) converts this oscillating signal into a display of its frequency components (Jiru, 2008).

MRS detects the resonance frequency of protons subjected to a magnetic field. Metabolites in tissue are identified due to chemical shift, allowing detection of specific molecules or metabolites which are seen as peaks at different positions on a spectrum (Warren, 2004). Chemical shift occurs due to weakening of the applied magnetic field by the electron cloud surrounding the nucleus. Individual protons resonate with slightly different frequencies depending on their chemical environment, resulting in a spectrum consisting of various peaks at different radiofrequencies. The chemical shift is measured in parts per million (ppm) which, unlike frequency (Hz), is independent of magnetic field strength and is the same in all MR scanners enabling comparison of spectral profiles.

Single metabolites may give a single peak or a combination of singlets and multiplets (Figure 2.7.). When an atom is placed within a magnetic field (B_o), protons induce their own effective magnetic field. Nuclei in close proximity connected through covalent bonds influence one another's effective magnetic field. Equivalent nuclei (identical protons in the same magnetic environment) experience the same chemical shift and produce no observable peak splitting, whereas non-equivalent protons experience different chemical shifts. The effect in molecules containing more than one non-equivalent proton, known as J-coupling or spin-spin coupling, results in additional splitting of peaks in the spectrum (de Graaf, 2009) (e.g. the doublet shown by lactate). Signals at two or more resonant frequencies are then seen, rather than one signal as with equivalent nuclei (Klose, 2008).

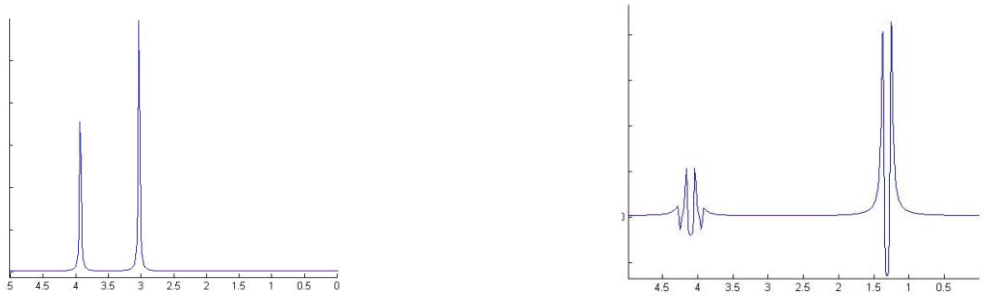

a) Creatine, two singlets with no peak splitting b) Lactate, a doublet around 1.3ppm and a quartet around 4ppm

Figure 2.7. Examples of peak splitting of different metabolites

An MR spectrum (Figure 2.8.) comprises a graphical representation in which signal intensity is displayed as a function of chemical shift, with peaks corresponding to individual metabolites. The x-axis is the chemical shift in ppm: the majority of spectra acquired *in vivo* range from 0.5 to 9.0 ppm, with metabolite information extending from 0.5 ppm to 4.5 ppm. The y-axis represents signal intensity, which increases with the concentration of the chemical within the ROI (Panigrahy et al., 2010; McRobbie et al., 2007). The area under each peak is proportional to the concentration of the corresponding metabolite.

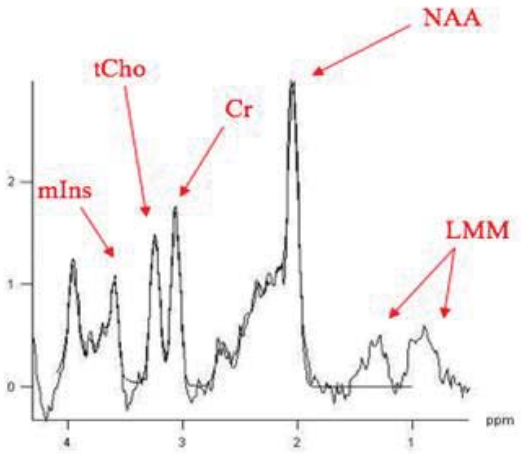

Figure 2.8. Example MR spectrum from normal brain with key metabolites labeled. Key Metabolites: Myo-inositol (mIns) - role uncertain; total choline (tCho) - cell turnover; creatine (Cr) - energy state; N-acetyl aspartate (NAA) – neuronal marker; Lipids/Macromolecule (LMM) - apoptosis and necrosis

2.4.2. Localisation Pulse Sequences: PRESS and STEAM

For In vivo MRS, complex pulse sequences are used to ensure that the signal is acquired from a specific volume of tissue. Sequences, such as point-resolved spectroscopy (PRESS) or simulated echo acquisition mode (STEAM), are applied to excite a pre-selected ROI with minimum excitation of the rest of the brain. Both techniques apply three slice-selective pulses along x, y and z in a single pulse sequence (Ross and Bluml, 2001).

Point-RESolved Spectroscopy (PRESS) (Bottomley, 1987) was used to acquire MRS data for studies described in this thesis. PRESS involves application of a 90° radiofrequency pulse (RF) followed by two 180° RF pulses, allowing the primary spin-echo to be refocused by the third pulse (Figure 2.9.) (Ross and Bluml, 2001). The echo time (TE) is the time between the 90° pulse and signal sampling, and repetition time (TR) the time interval between consecutive 90° pulses. Pulse sequences are repeated multiple times and the data added together to improve the SNR.

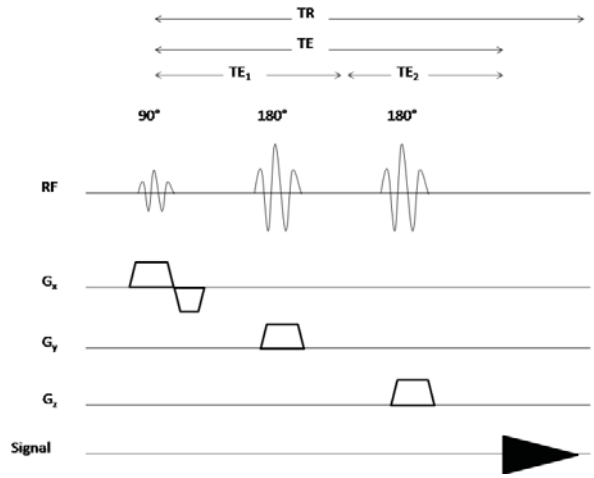

Figure 2.9. PRESS pulse sequence. Volume selection using the PRESS pulse sequence with the application of three radiofrequency pulses. The first 90°radiofrequency pulse is applied in the along the gradient Gx axis followed by a 180° pulse along Gy and another 180° pulse along Gz.

STEAM involves application of three 90° slice-selective pulses along Gx, Gy and Gz in a single pulse sequence (Ross and Bluml, 2001). It allows shorter echo times (TE) to be achieved, as TE is not influenced by time between the second and third RF pulses (Ross and Bluml, 2001). However, it produces lower SNR than PRESS.

2.4.3. Water spectrum acquisition and suppression

Tissue water is present in much higher concentrations than metabolites. As the water peak at 4.7 ppm is 10 000 fold greater than metabolite signals within a ^{1}H-MR spectrum, water suppression prevents its dominance from limiting metabolite information (Castillo et al., 1996). Once data is obtained, an additional unsuppressed water spectrum is acquired from the same volume to provide an internal reference signal to quantify metabolite signal intensities (van der Graaf, 2010).

2.4.4. Echo Time

An echo is the refocusing of spin magnetization by a pulse of resonant electromagnetic radiation. MRS may be performed at short echo time (TE) (<135ms, usually 20-40ms) or long echo time (TE) (>135ms, usually 135 or 270ms). After application of an initial 90° RF pulse, applying a second RF pulse with a precession angle of 180° after a time delay enables detection of a spin-echo. The echo time (TE) is the time between the initial application of the 90° RF pulse and the echo peak. TE determines the presence of different amounts of metabolite information in the resultant spectrum and influences the baseline, which appears flatter at long TE. The MRS signal decays at a rate dependent on T2 as the echo time increases and so the SNR is lower at longer TE.

Collecting data at different echo times allows information to be obtained from different metabolites. This is due to metabolite signals having different rates of T2 decay, and J-coupling splitting resonances into multiple components. Short TE provides more metabolite information as signals from lipids, small metabolites (e.g. myo-inositol) and metabolites with complex spectral patterns (e.g. Glu, Gln) decay at longer echo times, but overlapping peaks and signals from lipids and macromolecules can make analysis complex. Spectra obtained at longer echo times (TE >135 ms) have fewer peaks as more metabolites have decayed and are clearer to interpret. Examples of MR spectra obtained at short and long echo times are shown in Figure 2.10.

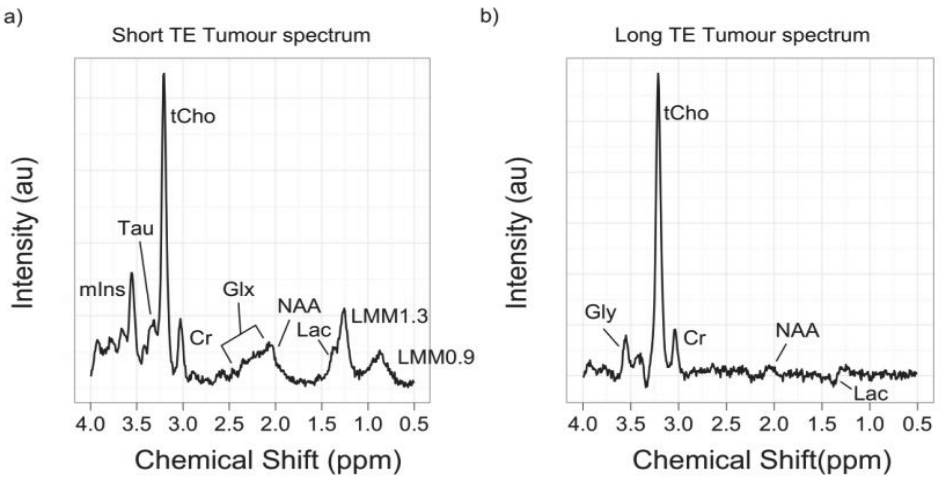

Figure 2.10. MRS acquired on the same patient with medulloblastoma at a) short TE and b) long TE. mIns: myo-inositol; Tau: taurine; tCho: total choline; Cr: creatine; Glx, Glutamate+Glutamine; NAA: N-acetyl aspartate; LMM: lipids and macromolecules

Long TE MRS has benefits of easy peak assignment and is useful for looking at metabolites such as N-acetyl aspartate, choline and creatine. Determining N-acetyl aspartate concentration in a short TE spectrum is difficult (Clementi et al., 2005) as overlapping metabolite peaks lead to overestimation, whereas Glu, Gln and LMM signals decay at long TE giving a clear N-acetyl aspartate peak. Lactate is more easily assigned as it is inverted at echo times around 135 ms. The main disadvantage with long TE MRS is loss of metabolite information, particularly as those that decay quickly (e.g. myo-inositol and LMM) are important when analysing tumours (Preul et al., 1996; Calvar et al., 2005; Kim et al., 2006; Peet et al., 2007; Wang et al., 1995; Astrakas et al., 2004; Marcus et al., 2007; Tzika et al., 2004). Short TE spectra are commonly acquired in clinical practice due to increased metabolite information and high SNR.

2.4.5. Field Strength

Magnetic field strengths of 1.5T or 3T are used in clinical practice. The appearance of ^{1}H-MRS is characterised by chemical shift and J-coupling and varies at different field strengths. Chemical shifts are dependent on the strength of the applied magnetic field: as field strength

increases, the chemical shifts of proton groups also increase. This effectively stretches the x-axis scale, improving resolution and leading to better separation of peaks. Chemical-shift is expressed in ppm because this dimensionless unit is independent of field strength and enables direct comparison with measurements at different field strength (choline, for example, will be positioned at 3.2 ppm at 1.5 or 3T). Chemical shifts expressed in Hz are spread out in proportion to the applied magnetic field. As coupling constants are independent of field strength, J-coupling is unaffected. This results in the appearance of multiplets changing with split peaks of individual metabolites appearing closer together at higher field strengths.

This can be explained by considering lactate, characterised by a doublet peak at 1.3 ppm. The prominent peak of LMM at 1.3/1.4ppm often overlaps with the lactate doublet at low field strengths, leading to miss-assignment and inaccurate quantitation. This overlap can be improved by performing MRS at higher field strengths, with separation of the lipid and lactate peaks at 3T but not 1.5T. The peaks of the lactate doublet would also appear closer together at 3T as coupling constants are independent of field strength. The effect of increasing field strength on lactate can be seen in Figure 2.11.

Lactate at 1.5 T

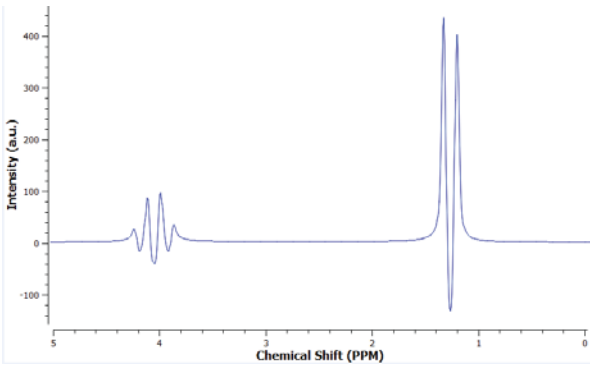

Lactate at 3 T

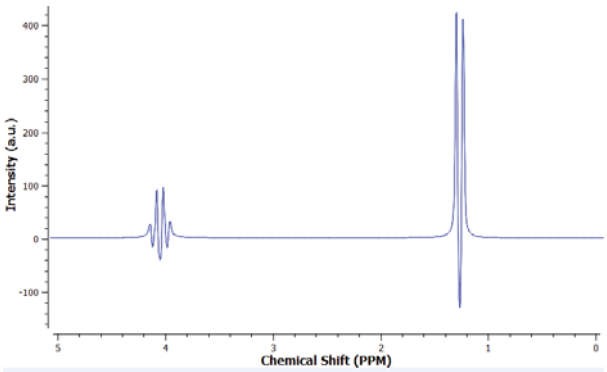

Figure 2.11. Lactate measured at 1.5T and 3T.

2.4.6. Magnetic Resonance Spectroscopy acquisition: Single Voxel Spectroscopy (SVS)

In vivo MRS is acquired following conventional MRI. ^{1}H-MRS is most commonly used *in vivo* as protons provide a stronger signal in a short time than other nuclei due to their high gyromagnetic ratio and prevalence in human tissue. MRS acquisition involves selecting an ROI or voxel based on reference images, refining the magnetic field within the voxel to make it uniform by shimming, and suppressing the protons of water within the voxel (Ross and Bluml, 2001). Processing is subsequently applied to construct a high quality MR spectrum.

MRS may be acquired as single voxel (SVS) or multivoxel spectroscopy, also termed magnetic resonance spectroscopic imaging (MRSI) or chemical shift imaging (CSI). SVS was used predominantly in this thesis, measuring an MR signal from a single ROI following placement of a single voxel in the desired region.

2.4.7. Voxel positioning

Voxel positioning is of paramount importance to obtain an MR spectrum representative of the region being assessed. The voxel should be placed fully over the ROI away from bone, scalp and air interfaces, and should not predominantly contain normal brain. Reference images from planes of all three axes are used to assess accurate voxel placement, as in Figure 2.12.

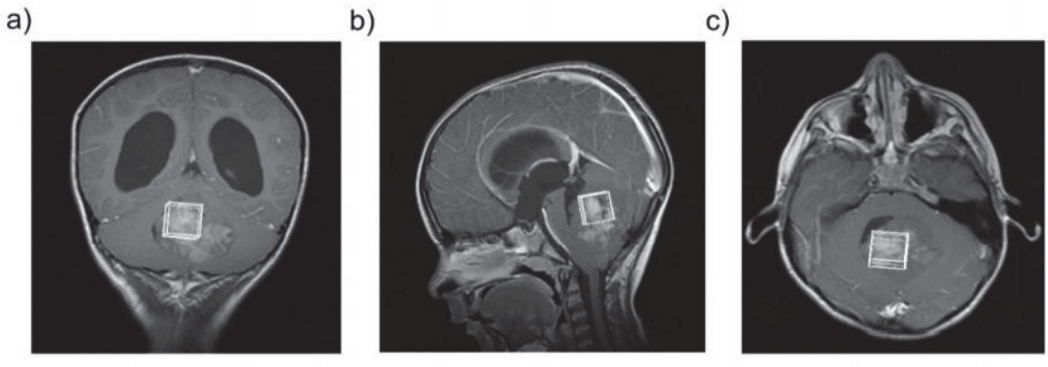

Figure 2.12. Voxel positioning. Example of voxel positioning over a tumour (medulloblastoma). Reference images from a) coronal, b) sagittal and c) axial planes

2.4.8. Shimming

Shimming produces a homogeneous magnetic field to ensure equivalent nuclei within an ROI are subjected to the same magnetic field. Good shimming leads to a high SNR and good peak resolution, whereas poorly shimmed spectra have broad metabolite peaks or line-width. Shimming is usually performed automatically. It is usually reported as the full width at half maximum height (FWHM) of the water peak or other peaks in the MRS, and is an important quality control parameter.

2.4.9. Processing: TARQUIN and LCModel

In order to produce a high quality spectrum, several processing steps are performed on the acquired FID either before (time-domain) or after (frequency-domain) the Fourier Transform. These can be applied automatically and integrated in quantification software (Jiru, 2008), such as TARQUIN (Wilson et al., 2011), LCModel (Provencher, 2001) and QUEST (Mansson et al., 2006). Processing steps include pre-processing, including removal of residual water, phase-correction and baseline correction, prior to metabolite quantification. Data in this thesis were processed using TARQUIN software (Wilson et al., 2011).

TARQUIN (Wilson et al., 2011) performs quantitation of metabolites in the time domain. As it is difficult to accurately quantitate short TE spectra due to their overlapping metabolite peaks, the entire spectrum is fitted to a set of individual metabolite spectra acquired by simulation. Fitting may be applied automatically to obtain a list of quantifiable metabolites and their relative concentrations (expressed in standard units of millimolar (mM)), with use of the water signal as a concentration reference. Fourier transformation is subsequently applied to enable visualisation of the spectrum. An example MRS with metabolite fitting using TARQUIN is shown in Figure 2.13.

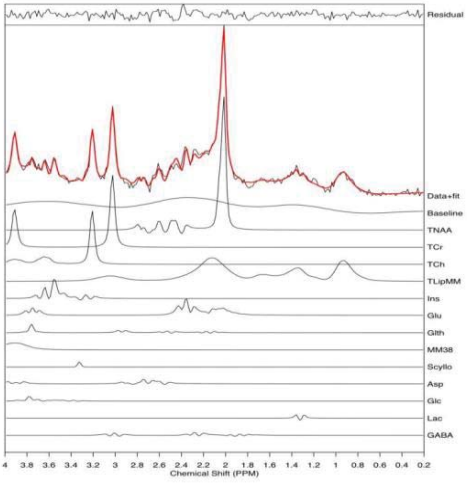

Figure 2.13. Metabolite fitting using TARQUIN

Linear Combination Model (LCModel™)(Provencher, 2001) uses fitting in the frequency-domain to generate a list of metabolite concentrations (relative to water) and their confidence estimates, using a linear combination of empirically obtained metabolite spectra to 'fit' to experimentally obtained spectra. LCModel has a choice of basis sets acquired at different echo times on a variety of scanners. The whole MR spectrum can be fitted automatically to produce a list of metabolites and their relative concentrations (Figure 2.14).

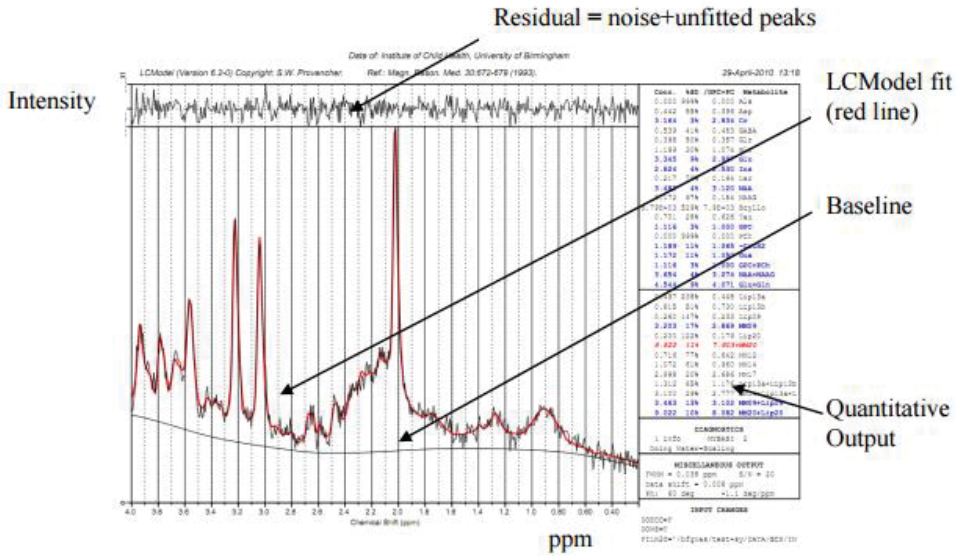

Figure 2.14. LCModel Fitted Spectrum

2.5. Interpretation of metabolites using MRS

MRS from the human brain comprises 18-20 metabolites and nine lipids and macromolecules. Metabolite profiles in normal brain differ from those in pathological brain, and pathologies differ with presence and absence of varying concentrations of different metabolites (Panigrahy et al., 2010). The following metabolites have been identified, of which the main features used in visually interpreting the spectrum will be described:

N-acetyl aspartate (NAA) (2.0 ppm)

N-acetyl aspartate (NAA), a marker of neuronal density and axonal integrity, is one of the most predominant metabolites and the largest peak seen in normal brain. Its main peak can be seen at around 2.0 ppm and is exclusively located in the central and peripheral nervous system. NAA is the most reliable marker of CNS pathology, with decreased levels in spectra of brain tumours (Wang et al., 1995; Peet et al., 2007; Harris et al., 2007; Tzika et al., 2004; Warren et al., 2000). N-acetyleaspartylglutamate (NAAG), a neurotransmitter, is closely linked to N-acetyl aspartate and may overlap as it is found at 2.04 ppm on the shoulder of the N-acetyl aspartate peak.

Total Choline (tCho) (3.2 ppm)

The total choline peak around 2ppm is comprised of free choline, phosphocholine (PCH) and glycerophosphocholine (GPC). As it is difficult to separate these three metabolites at 1.5T, the resultant complex peak at 3.2 ppm is termed total choline (tCho). These metabolites also give rise to resonances between 3 and 4ppm but these are small and difficult to visualise. Choline is involved in membrane synthesis and degradation and is a marker of membrane turnover, increasing with cell proliferation and being elevated in brain tumours (Panigrahy et al., 2006; Peet et al., 2007; Astrakas et al., 2004; Marcus et al., 2007; Davies et al., 2008;

Londono et al., 2003). Evidence suggests elevated choline is representative of CNS malignancy (Peet et al., 2007; Marcus et al., 2007; Astrakas et al., 2004).

Creatine (Cr) (3.0 ppm)

The creatine (Cr) peaks are comprised of creatine and phosphocreatine, with singlet peaks at 3.02 ppm and 3.94 ppm. Creatine is present in neuronal and glial cells and is involved in energy storage and metabolism as it provides phosphate for ATP through phosphocreatine. Although creatine levels are stable in normal brain they vary in pathology, being decreased in gliomas (Panigrahy et al., 2006; Davies et al., 2008).

Myo-inositol (mIns) (3.6 ppm)

Myo-inositol (mIns) is an osmolyte and astrocyte marker with a complex peak at 3.6 ppm at 1.5T and two peaks close to this at 3T, although its function is poorly understood (Castillo et al., 2000; Panigrahy et al., 2010). Increased mIns in glial tumours may reflect the cellular density of reactive astrocytes or membrane turnover in highly proliferative tumour cells (Hattingen et al., 2008), with varying concentrations of mIns in other brain tumours due to altered membrane metabolism (Castillo et al., 2000; Kim et al., 2006; Peet et al., 2007; Davies et al., 2008; Londono et al., 2003; Panigrahy et al., 2006; Harris et al., 2008; Panigrahy et al., 2010). mIns has been used in grading astrocytomas (Castillo et al., 2000; Kim et al., 2006) and is elevated in ependymomas (Davies et al., 2008; Harris et al., 2007) and diffuse pontine gliomas (Harris et al., 2007).

Glutamate (Glu), glutamine (Gln) and Glutamate+Glutamine (Glx) (2.0 to 2.6 ppm)

Glutamate (Glu) is the most abundant amino acid in the brain and has a role as an excitatory neurotransmitter, and glutamine (Gln) is a storage form of glutamate and an amino acid

precursor (Panigrahy et al., 2010). Both metabolites indicate abnormal brain tumour metabolism in adults (Howe and Opstad, 2003). They are present as complex overlapping multiples between 2.0 and 2.6 ppm and, as they are difficult to separate below 3T due to complex spectral overlap, Glu and Gln are often reported as a sum (Glx).

Lactate (Lac) (1.3 ppm)

Lactate is an end product of anaerobic glycolysis present as a doublet peak at 1.3 ppm. It occurs in normal brain in low concentrations and is elevated in CNS pathology (Panigrahy et al., 2010) as a marker of cell death and necrosis. Lactate levels increase with hypoxia where glycolysis is initiated in an oxygen deficient environment. Lactate levels are variable in brain tumours (Govindaraju et al., 2000; Astrakas et al., 2004; Davies et al., 2008) and the metabolite has been useful in grading gliomas (Kim et al., 2006) and identifying pilocytic astrocytomas (Wang et al., 1995). Assignment may be difficult at short TE when signals from lipids and macromolecules overlap (Marcus et al., 2007), but easier at longer echo times as lactate peaks are inverted and lipids usually less prominent. A metabolite with two visible doublet peaks is more likely to be lactate than lipid contamination.

Taurine (Tau) (3.3 ppm)

Taurine (Tau) has possible roles as an osmoregulator and modulator of neurotransmission, but its function is not fully understood. Increased levels have been found in CNS tumours (Panigrahy et al., 2006; Harris et al., 2011; Opstad et al., 2009). As taurine closely overlaps with other metabolites (e.g. tCho) at around 3.3 ppm) it may be difficult to identify at 1.5T but is split into two resonances at 3T, which can make its identification easier. Elevated levels of taurine are seen in medulloblastomas (Panigrahy et al., 2006; Davies et al., 2008) and pineal germinomas (Panigrahy et al., 2006).

Glycine (Gly) (3.55 ppm)

Glycine (Gly) is an inhibitory neurotransmitter and antioxidant (Davies et al., 2010b; Govindaraju et al., 2000). It forms a singlet peak at 3.55 ppm and is better seen at long TE as it overlaps with mIns at 1.5T. Increased Glycine has been observed in higher grade brain tumours (Davies et al., 2010b; Lehnhardt et al., 2005).

Citrate (Cit) (2.6 ppm)

Citrate (cit) is an intermediate product of the tricarboxylic acid (TCA) cycle observed at 2.6 ppm. Increased levels of citrate may occur in malignant progression (Seymour et al., 2008), with prominent peaks in a number of tumours including DIPG (Seymour et al., 2008; Costello et al., 1999).

Lipids and macromolecules (LMM) (0.9 ppm, 1.3 ppm, 2.0 ppm)

Lipids reflect membrane degradation, necrosis and apoptosis (Tzika et al., 2003), and form broad resonances at 0.9 ppm, 1.3 ppm and 2.0 ppm. Lipids occur in very low levels in normal brain but increase in brain tumours. Macromolecules occur due to cytosolic proteins or lipids (Panigrahy et al., 2010), and are difficult to assign being masked by lipid signals. Lipids may be indicators of tumour growth, with variations occurring in response to treatment (Astrakas et al., 2004; Peet et al., 2007). LMM may be due to necrosis, being high in high-grade tumours (Calvar et al., 2005; Peet et al., 2007; Astrakas et al., 2006; Marcus et al., 2007) and increasing prior to progression (Sankar et al., 2008). Caution should be exercised when interpreting lipid levels in tumours to ensure adequate voxel positioning, as high lipid levels may reflect lipid contamination from surrounding scalp tissue, inclusion of necrotic cysts or proximity to bone (Rosen and Lenkinski, 2007).

2.6. Challenges and limitations of MRS

Several challenges remain to the routine implementation of functional imaging in clinical practice. These include developing standardised acquisition protocols with appropriate quality control measures, processing and presenting information and in particular the handling of quantitative data that represents a departure from traditional radiological working.

It is essential to ensure correct voxel placement to obtain a valid spectrum, and classification rates can vary dependent on voxel placement (Ricci et al., 2000). Inclusion of normal brain within a voxel may increase N-acetyl aspartate within the MRS, causing difficulties with interpretation. Voxel placement which includes a significant component of CSF decreases the SNR but is preferable to including normal brain in the voxel which leads to contamination of the tumour signal by metabolites such as NAA.

Spectral congestion at short echo times (TE) causes lack of distinction between metabolite peaks (Clementi et al., 2005; Kim et al., 2006; Barker et al., 2001; Bartha et al., 2008) resulting in difficulties with peak assignment and quantification. Using a higher field strength may improve the SNR and resolution. Age-related variations in CNS metabolite concentrations may cause problems with paediatric MRS interpretation (Pouwels et al., 1999; Grachev and Apkarian, 2000). Concentrations of choline, myo-inositol and Glu alter in the first year of life and then remain relatively stable (Pouwels et al., 1999), and N-acetyl aspartate increases in grey matter throughout the first year (Pouwels et al., 1999). Infants have high cerebellar and grey matter concentrations of taurine, which decreases and stabilises later in life, although taurine concentration in the basal ganglia remains constant with age

(Pouwels et al., 1999). Metabolite concentrations may also vary in different regions throughout the brain (Pouwels et al., 1999; Grachev and Apkarian, 2000).

Chapter 3: Methods

3.1 Participants

Children presenting to Birmingham Children's Hospital between December 2012-July 2018 with radiological features of a brain or solid body tumour were eligible for inclusion in the studies described in this thesis. Patients were recruited prospectively following presentation during the study period into an ethically approved study entitled "Functional Imaging of Tumours". Ethical approval was granted by the East Midlands–Derby Research Ethics Committee (REC 04/MRE04/41). Informed parental consent was obtained for all participants following image acquisition, performed as part of standard care or prior to imaging if this was not considered part of standard of care.

Patients appropriate for each analysis presented in this thesis were identified retrospectively through searches of computerized records.. All children with suspected malignancy undergo standard clinical diagnostic imaging investigations including MRI and MRS for brain lesions and multi b-value DWI for body tumours. Exclusion criteria were having received treatment (chemotherapy or surgery) prior to diagnostic imaging, incomplete MRI study and solid body lesions with the largest area on a single slice <3 cm^2 in view of risk of partial volume effects. Children were aged between fetal 36 weeks gestation and 16.4 years at diagnosis.

3.2. Body Tumours

3.2.1 MRI and Diffusion-Weighted Imaging

MRI was performed on paediatric solid body tumours at diagnosis and following induction chemotherapy using a Siemens Avanto 1.5T (Siemens Healthcare, Erlangen, Germany) scanner and a 4-channel body receive coil. The imaging protocol consisted of fat-suppressed axial and coronal pre-and post-gadolinium T1-W turbo spin-echo (repetition time / echo time

[TR/TE] 760 to 817/7.7 msec), axial T2-weighted turbo spin-echo (TR/TE 3000 to 5640/67 to 87 msec) and DWI acquisition. Children were awake, sedated or under general anaesthesia depending on their ability to cooperate.

DWI was acquired using a single shot spin-echo planar imaging (EPI) sequence with up to six b-values (b = 0, 50, 100, 150, 600, 1000 s/mm^2) in an axial acquisition plane. The field of view (FOV) ranged from 221 to 350 x 172 to 317 mm, matrix size 122 to 192 x 128 to 192 depending on patient size. Slice thickness was 5.0 mm with no gap between slices. DWI was acquired in three orthogonal directions with echo time of TR/TE 3200 to 9900/92 ms and b-values including 0 and 1000 s/mm^2. For this protocol, total scan duration ranged from 1 min 37 sec to 7 min 32 sec when acquiring all six b-values. ADC maps were automatically generated from scanner software. Repeat MRI scans were performed during and following chemotherapeutic treatment as routine clinical care.

3.2.2 DWI image analysis

MRI datasets including ADC maps were transferred from the scanner to a local research and advanced applications PACS (Pukka J DICOM explorer version 6.1.1) and subsequently loaded into an in-house analysis tool (MIROR).

3.2.2.1. Modular medical Image Region Of interest analysis tool and Repository (MIROR)

A modular medical image region of interest analysis tool and repository (MIROR) was developed by our research team using MeVisLab (v. 2.7.1, MeVis Medical Solutions, Bremen, Germany) (Zarinabad et al., 2018), a rapid prototyping platform for medical image processing. MIROR allows automatic processing and classification of advanced MRI data,

including multi b-value DWI. Post-processing, quantitative and statistical analysis functionalities were developed using Python (v. 2.7, embedded within Mevislab). Research conducted during this PhD contributed to development of MIROR as a clinical decision support system (CDSS) to facilitate interpretation and analysis of advanced MRI techniques. Development of MIROR as a CDSS involved translational work aiming to integrate advanced MRI techniques into a clinical setting by presenting complex information to clinicians in an accessible and comprehensible way. This necessitated liaison between computer scientists involved in the technical design of MIROR and radiologists as end-users to collate feedback and make suggestions for on-going improvement for clinical use. Each independent component of MIROR was developed, evaluated and tested by radiologists prior to subsequent modification as an intrinsic part of the research described in this thesis.

Developing a graphical user interface (GUI) acceptable to radiologists, for example, necessitated several iterations of re-design to ensure clinical applicability. The final version of the user interface for patient view (Figure 3.1.) required import of an MR image containing sufficient structural information to allow construction of a ROI, which would subsequently be transferred to a matched ADC map for quantitative analysis. It was not appropriate to draw an ROI directly on to the ADC map due to risk of bias, with the eye being drawn to areas showing the greatest diffusion restriction. As T2-weighted and multi b-value DWI images were not registered, the tool was adapted to allow import of b0 images for ROI construction, which was acceptable to radiologists in terms of image quality. The relative size and layout of display windows for MR images (b0 and ADC maps), the volume of interest, the ADC histogram and quantitative histogram parameters, and output colours were also adjusted in conjunction with input from radiologists.

Prior to commencing the studies described in results chapters of this thesis, we developed a preliminary version of MIROR suitable for research use. At this stage, MIROR allowed radiologists to draw a ROI on a b0 image that could be transferred to a matched ADC map, and could measure the volume of the defined ROI, perform statistical analysis on the ROI values, create a histogram, and extract and store histogram parameters such as median and different percentile ADC values, skewness, kurtosis and entropy in a repository.

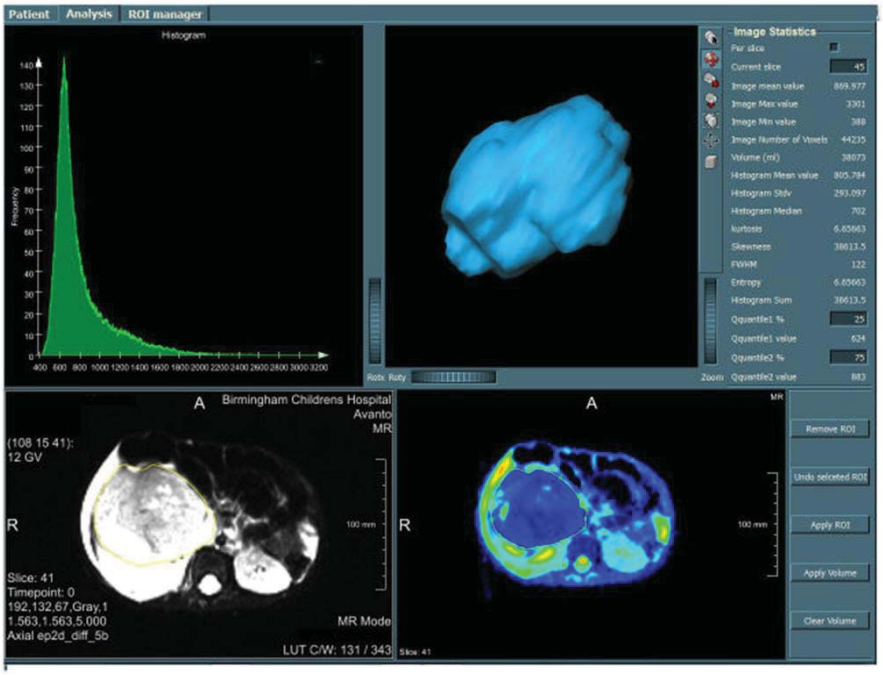

Figure 3.1. MIROR graphical user interface patient view depicting analysis of a malignant Wilms tumour. The ROI is drawn on a high-resolution b0 image and overlaid on the corresponding parametric ADC map. An ADC histogram (top left) and volumatic representation of the tumour (top right) are generated.

The refinement, further development and evaluation of MIROR for clinical use is described in the body of the thesis. In addition to design, evaluation and translation, this research contributed to development of the CDSS through recruitment of patients whose tumours formed part of the inbuilt repository, maintaining a clinical database of patient details including serial imaging, treatments and outcome, and drawing ROIs from which ADC histograms were generated for benign and malignant tumours and individual tumour types.

3.2.2.2. ROI construction

Whole tumour (WT) ROIs were drawn manually around solid tumours on high-resolution b0 images by a clinician and refined by a consultant radiologist (KF, 10 years' experience) Alterations to ROIs were made following consensus of the two individuals. ROIs were transferred to a matched ADC map and an embedded image registration component of MIROR ensured alignment of parametric maps and imported image data. Conventional MR images guided delineation of tumour at each consecutive tumour-containing slice, excluding peri-tumoural oedema. To minimise partial volume effect, only sections where tumour was >50% of the adjacent more central slice and at least 3 cm^2 were included. The entire tumour volume including cystic and necrotic areas was included in the ROI to determine representative data for heterogeneous tumours. This process was repeated for images acquired following neo-adjuvant chemotherapy. Figure 3.2. depicts a WT ROI constructed within MIROR.

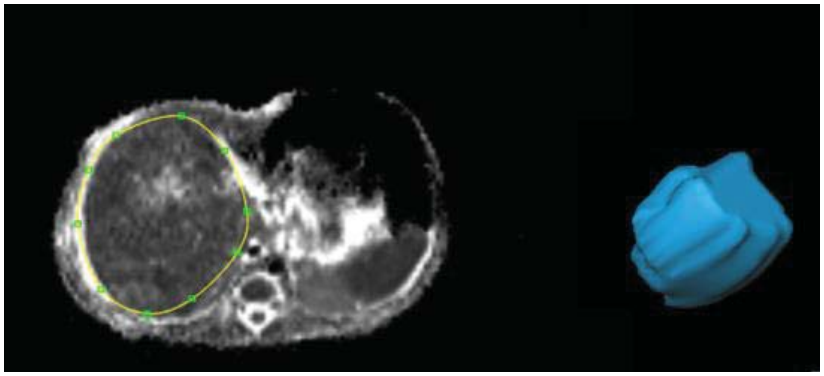

Figure 3.2. A Whole Tumour (WT) ROI constructed within MIROR (Wilms Tumour)

A second ROI was drawn around the largest single axial slice (SS) in a subset of tumours to ascertain the optimum method of ROI construction for inter-rater reproducibility and discrimination between benign and malignant lesions. A second consultant radiologist (SA, 1 years' experience) drew WT and SS ROIs blind to the results of first radiologist to allow comparison of histogram parameters between the two raters and the two techniques.

3.2.3 Computation of ADC and IVIM Modeling of the DW Data

Post-processing was performed in MIROR. ADC values were computed using a monoexponential linear fit of the b-values 0 and 1000 s/mm^2. IVIM modelling was carried out for all cases where six b-values had been acquired. An algorithm for IVIM analysis using biexponential fitting was developed using Python (v. 2.7), enabling calculation of D and f parameters (Le Bihan et al., 1988). Linear regression was performed using high b-values (>100 s/mm^2), to calculate the D parameter from the gradient of fit as perfusion effects are negligible at high b values when $D^* >> D$ (Taouli et al., 2016). The f parameter was deduced from the same fit, by extrapolating the fit to the *y* axis and taking the difference from the intercept to the b0 signal. D^* was not calculated due to the large errors involved, particularly as the study involved a comparison of longitudinal data.

Advanced histogram analysis of the overlaid ROI on voxel-by-voxel parametric maps was performed in MIROR using its quantitative and statistical analysis components. The area under the histogram was normalized to unity to dissociate histogram parameters from lesion size. For each patient, tumour volume and ADC and IVIM parameter median, 15th, 25th, 75th and 95th centiles, skewness, kurtosis, volume and entropy were calculated and exported for detailed analysis.

3.2.4 Visual interpretation of ADC histograms

The morphology or shape of histograms can be described in terms of skewness, kurtosis and entropy. Skewness is a measure of symmetry: a histogram with a symmetrical or normal distribution is characterised by two halves which mirror one another, whereas one with a skewed distribution is asymmetrical. A right-skewed distribution is also termed positively-skewed and has a tail on the right, whereas a left or negatively-skewed distribution has a tail

on the left (Figure 3.3). Skewness can be quantified to define the extent to which a distribution differs from the normal distribution.

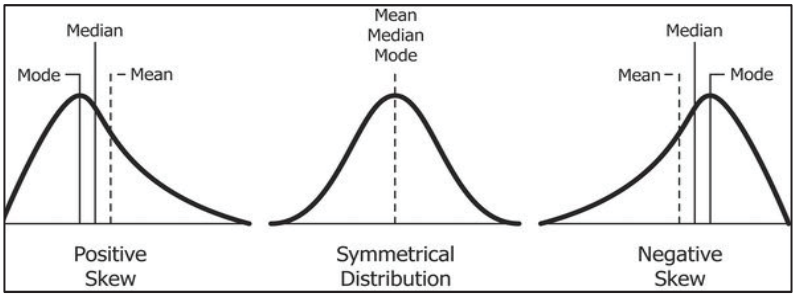

Figure 3.3. Histogram Skewness

Kurtosis is a measure of how peaked a histogram appears: a histogram with a standard normal distribution has kurtosis of 3. Increased kurtosis (>3) is visuallised as a thin 'bell' with a high peak, whereas decreased kurtosis (<3) is seen as a broadened peak with a 'thickening' of the tails of the histogram (Figure 3.4.)

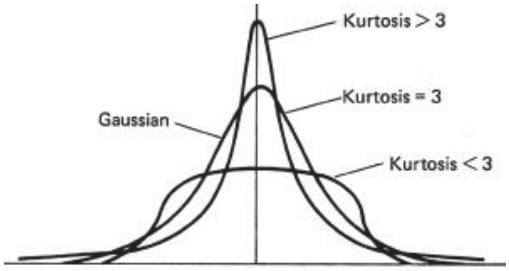

Figure 3.4. Kurtosis

Entropy is a measure of disorder, with the entropy of a historgram reflecting an estimation of its randomness. Entropy can be thought of as a measure of the sharpness of the peak of a histogram, as shown in Figure 3.5.

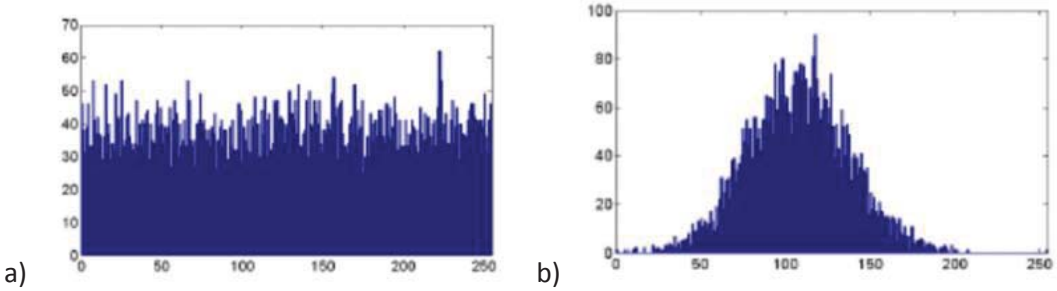

Figure 3.5. Entropy. Histogram a) shows a higher entropy than histogram b).

3.3. Brain Tumours

3.3.1 MRI and MR Spectroscopy acquisition

Single-voxel MRS was acquired on children presenting with radiological features suggestive of a brain tumour as standard diagnostic imaging prior to treatment or surgical intervention. MRS was performed on one of three MR scanners, two 1.5T (GE Signa Excite, or Siemens Avanto) or one 3T (Phillips Interna Achieva) following conventional MRI, including axial T1 and T2-weighted, diffusion EPI and fluid-attenuated inversion recovery and post-contrast T1-weighted sequences. At 1.5T, a single-voxel MRS protocol was used with point-resolved spectroscopy (PRESS) localization, short echo time (TE) 30 ms, repetition time (TR) 1500ms. Cubic voxels had 1.5 cm or 2 cm side length, acquiring 256 or 128 repetitions respectively. At 3T, a short echo time 35 ms and repetition time 2000ms were used, with cubic voxels of side length 1.3 cm, 1.5 cm or 2 cm and 196, 128 and 196 repetitions respectively.

MRI confirmed accurate voxel placement within solid tumour, avoiding cysts, necrosis and non-tumoural tissue and located >3mm from bone, scalp and air. As MR spectra can appear different if voxels are placed over high or low-grade elements within the same tumour, it was ensured that placement was over the solid enhancing tumour component if possible, which should correspond to the most malignant section.

3.3.2 MRS Processing

Spectroscopy processing was performed using standard scanner software exported to hospital clinical PACS (Agfa IMPAX 6.5.2.2016). The majority of raw data were also processed using TARQUIN (Totally Automatic Robust Quantitation in NMR) v3.2.2 (Wilson et al.,

2011). Example MR spectra processed using scanner software and TARQUIN are shown in Figure 3.6.

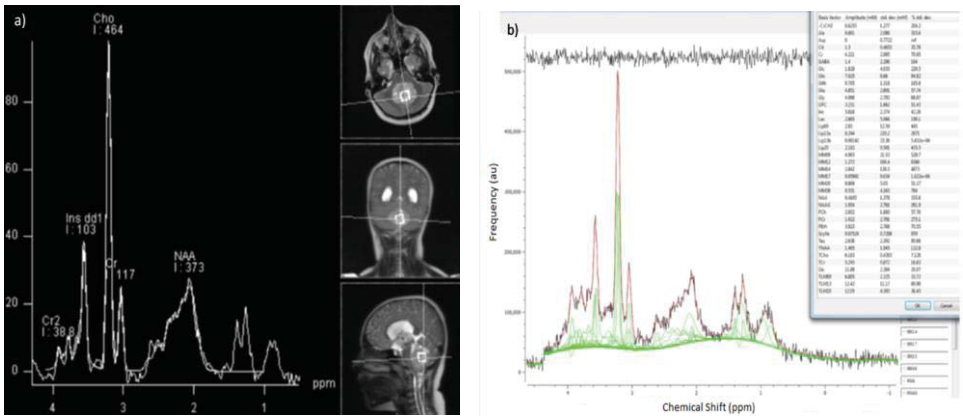

Figure 3.6. Example MR spectra processed using scanner software (a) and TARQUIN (b)

Raw MRS data were sent from scanners to a research and advanced applications PACS (Pukka J DICOM explorer version 6.1.1) and exported to a dedicated server for processing with results added back to that PACS system. Data were made available to radiologists through the automatic export to the hospital clinical PACS. Processing provided a graphical magnetic resonance spectrum (MRS) and tissue metabolite profile, as depicted in Figure 3.6.

3.4. MRS interpretation by Radiologists

Radiologists in Birmingham Children's Hospital were invited to attend one of two 1.5 hour teaching sessions on the theory and interpretation of MRS, conducted by a researcher (K.M.) and expert spectroscopist and paediatric oncologist (A.P.). The information in this section summarises the content of those sessions.

3.4.1. Quality control

As with all imaging investigations, quality of MRS must be assessed prior to interpretation. Radiologists were taught to perform a visual quality control assessment of all MR spectra included in the studies described in this thesis. There are two main aspects to determining if a spectrum meets quality control criteria:

1) Assessing the proportion of tumour and other tissues in the voxel. The spectrum obtained will be a combination of the spectra from these tissues, and normal brain in particular contains many metabolites.

2) Assessing the spectral quality itself – signal:noise ratio (SNR), line width, phasing, baseline and artefact. For this, it is important to determine if the choline peak is at least 5 times that of the noise, and if the choline and creatine peaks are well separated.

Figure 3.7. Examples of MR spectra failing quality control (Harris et al., 2007)

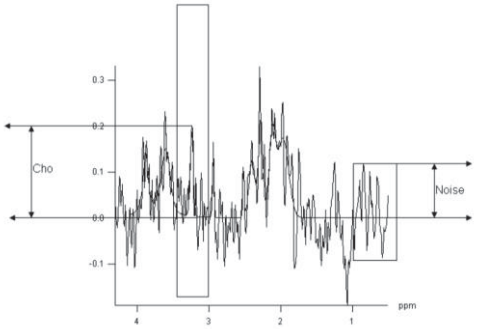

A) Example of poor SNR. The choline peak is less than 5 times that of the noise. The poor SNR may be due to voxel placement over cyst or too few averages for voxel size. In this example, the large lipid peaks are due to voxel placement over scalp.

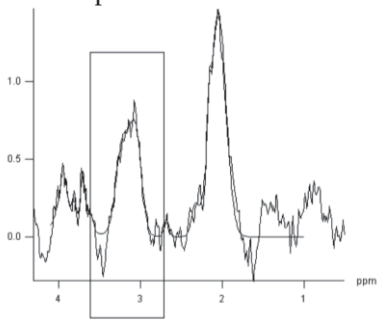

B) Example of poor line width. Choline and creatine peaks are coalesced. Poor line width may be due to voxel placement close to bone, or heterogeneity within the voxel. In this example, the voxel placement includes normal brain as suggested by high N-acetyl aspartate.

3.4.2. Instructions for use of mean MR spectra

Mean MR spectra are derived from combining data from all spectra obtained from tumours of a certain type in a certain location at a specified field strength. Mean spectra vary considerably between tumour types. In the example mean spectra below (infratentorial pilocytic astrocytoma at 1.5T) (Figure 3.8.), mean metabolite peaks are depicted by a solid black line, with standard deviation represented by grey shading. The number of cases from which the mean spectrum is determined is provided, with spectra being more accurate when containing data from a large number of cases.

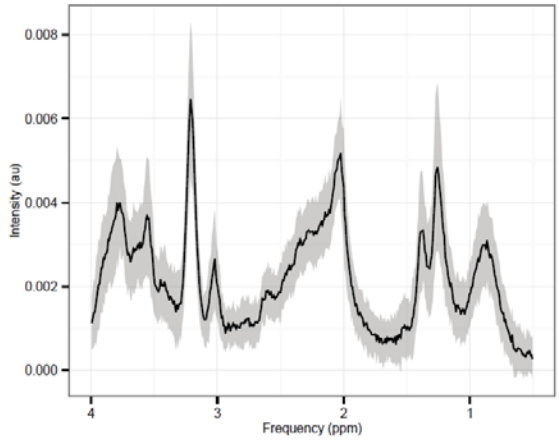

Figure 3.8. Example mean MR spectrum (n=15) – pilocytic astrocytoma

Radiologists were advised to reduce their differential diagnosis as much as possible on clinical features and conventional imaging prior to using mean MR spectra to facilitate diagnosis. It is thought that MRS is most likely to be helpful if radiologists have two candidate diagnoses with very different mean spectra than if they are looking for a match from the spectra of a large set of diagnoses each with slightly different spectra.

Radiologists were provided with a booklet containing mean MR spectra for common tumour types in different locations (supratentorial and infratentorial) at 1.5T and 3T, which was

designed and compiled as part of this PhD (Appendix 3). The following instructions for use of mean spectra to facilitate diagnosis were provided:

1. Formulate a list of differential diagnoses using clinical features and conventional imaging sequences
2. Assess data quality of case spectrum:
   - Is the voxel positioned correctly?
   - Are the SNR and line width acceptable?
3. Compare the mean spectra from the main differential diagnoses to that of the case spectrum

Radiologists were taught that differences in mean spectra are accounted for by location (supratentorial or infratentorial), echo times and field strength (1.5T or 3T).

3.5. Histopathology

Histopathology reports for all biopsied or surgically excised body and brain tumours were obtained from the official hospital results reporting system (Sunquest ICE Desktop Live, version 541). Results of first authorised histopathology reports, central review, and alterations in initial histopathological diagnosis were documented. The time from initial imaging and biopsy or surgery to definitive histopathological diagnosis was recorded. Unbiopsied cases and those with inconclusive histopathology were reviewed, and the reasons for lack of biopsy or tissue diagnosis were documented.

3.6. Reference Standard for Body and Brain Tumour Diagnosis

Body tumours were diagnosed by histopathological review of tissue obtained through biopsy or following surgical resection, with diagnosis confirmed by the Solid Tumour Multi-Disciplinary Team (MDT). The Solid Tumour MDT consisted of paediatric oncologists, paediatric radiologists, paediatric surgeons, clinical oncologists and histopathologists The reference standard for brain tumour diagnosis was the Paediatric Neuro-Oncology MDT consensus diagnosis, incorporating clinical information, MRI, MRS, histopathology, second opinion, genetics and follow-up information about treatment response and tumour behaviour. The Neuro-Oncology MDT consisted of paediatric oncologists, paediatric radiologists in part specializing in neuroradiology, neurosurgeons, clinical oncologists and histopathologists. Consensus diagnosis was confirmed once clinical course had been established at study end.

3.7. Statistical analysis

Statistical analysis was performed using SPSS Statistics (v. 23, Chicago, IL) and MiniTab (v. 17.1) software.

3.7.1. Statistics used in body tumour analysis

ADC and IVIM histogram parameters (median ADC, skewness, kurtosis, entropy and 5^{th}, 15^{th}, 25^{th}, 75^{th} and 95^{th} centile values) are continuous variables and not normally distributed. The Mann-Whitney U and Kruskal-Wallis tests were used to perform comparison of differences in non-normally distributed histogram parameters between two tumour types or between individual tumours at diagnosis. $P<0.05$ was taken as indicating statistical significance.

The issue of multiple comparisons was considered, given concurrent evaluation of various ADC percentile values, skewness, kurtosis and entropy. The area under the ROC curve (AUC) was examined to assess diagnostic abilities of ADC median and attempt identify a cut-off value for differentiating benign from malignant lesions, aiming to maximize the sum of sensitivity and specificity.

Comparisons of ADC and IVIM histogram parameters (median, skewness, kurtosis, entropy and 15^{th}, 25^{th} and 75^{th} centile values) from pre- and post-chemotherapy parameters were performed using the Wilcoxon signed rank test with $p<0.05$ considered statistically significant. The Wilcoxon signed ranked test is used for paired analyses of non-normally distributed data. Histogram shift in response to treatment was analyzed through comparing changes in median, 15^{th}, 25^{th} and 75^{th}centiles, skewness, kurtosis and entropy to identify the optimal parameters for identifying response to chemotherapy. Correlations between change in tumor volume and histogram parameters were ascertained using Spearman rank correlation. Pre-treatment ADC and IVIM parameters and change in tumour volume and histogram parameters in survivors and patients who had died were analyzed and compared. The volume of highly malignant tumour pre- and post-chemotherapy was compared and reviewed in context of clinical course.

To assess significance of inter-rater variability of ADC histogram parameters, comparison of not normally distributed data (median, 15^{th}, 25^{th}, 75^{th} and 95^{th} percentile ADC) was performed using the Wilcoxon test. The Friedman test compared the WT and SS methods of ROI construction for determining ADC parameters for each radiologist separately, and investigated any interaction between method and inter-rater variability. The Mann-Whitney U

test was used to compare ADC histogram parameters of benign and malignant tumour groups determined from WT and SS ROI construction.

Assessment of inter-rater variability of ROI construction was performed using Bland Altman Statistics. Bland-Altman plots (Figure 3.9.) with limits of inter-observer agreement (mean difference +/- 1.96 x standard deviation) were constructed to analyse ADC histogram parameter reproducibility between radiologists and WT and SS methods of ROI construction.

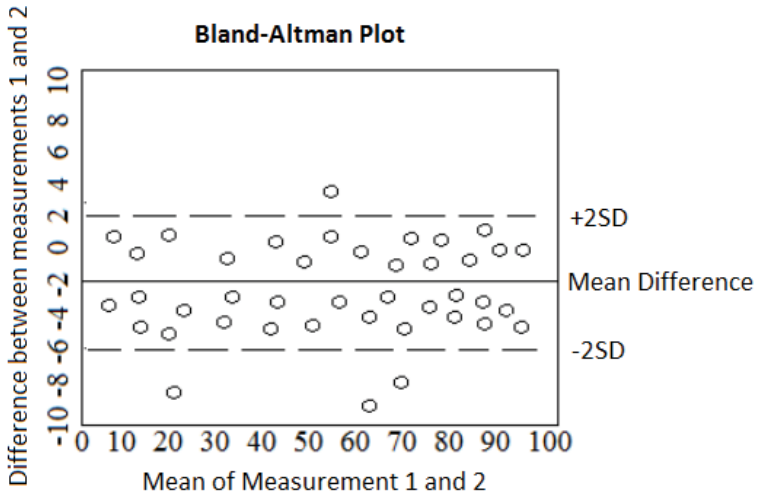

Figure 3.9. Example Bland-Altman Plot used to assess inter-rater agreement and estimate bias. The line of mean difference indicates bias resulting from systematic differences between the two readers. This example demonstrates a randomly distributed error with the majority of points falling within the 2SD cut-off, suggesting a high level of inter-rater agreement.

3.7.2. Statistics used in brain tumour analysis

Comparison of post-MRI and post-MRS diagnosis with MDT consensus determined how many cases were correctly diagnosed in accordance with the reference standard at each stage. Accuracy of MRI +/- MRS for each category of brain tumour (all locations, and supratentorial, and infratentorial) was made through estimates of sensitivity. Proportions were reported with 95% confidence intervals calculated from the Binomial distribution. McNemar's test was used to determine if MRS had a statistically significant effect on correct

diagnosis compared with MRI alone. Significance of direction of change towards improvement with MRS was established using the McNemar Ordered Category test of Directional Change, and increase in radiologists' agreement on correct diagnoses was assessed using the Bhapkar Chi-squared test (Bhapkar, 1966).

Chapter 4: Diffusion-Weighted Imaging and ADC Histogram Analysis in the Diagnosis of Solid Childhood Body Tumours

4.1. Introduction

As different types of solid paediatric tumours have overlapping imaging characteristics, non-invasive discrimination of benign from malignant lesions can be difficult using conventional MRI alone (Abdel Razek et al., 2012). Diffusion-Weighted Imaging (DWI) has shown promise in facilitating non-invasive diagnosis of paediatric tumours through calculation of ADC (mm^2/s), a quantitative measure of diffusion with an inverse relationship with cellularity (Kralik et al., 2014). Studies have shown median ADC of malignant paediatric body lesions to be significantly lower than benign lesions (Abdel Razek et al., 2009; Kocaoglu et al., 2010), with recent research suggesting ADC can characterise tumours and differentiate between tumour types (Abdel Razek et al., 2009; Kocaoglu et al., 2010).

ADC histograms, constructed by drawing a region of interest (ROI) around a tumour, could provide additional visual and quantifiable information about imaged tissue through demonstrating peaks that correspond to distinct cellular subpopulations (Hales et al., 2015). Although median ADC provides an overall measure of average cellularity across a lesion, tumours are heterogeneous masses consisting of a mixture of histological cell types interspersed with cysts and necrosis. Visual interpretation of histogram shape may add value to information obtained from conventional imaging, and calculating quantitative histogram parameters such as ADC values at different centiles, skewness, kurtosis and entropy could facilitate more detailed and objective tumour characterisation. Whole tumour ADC histogram analysis has shown promise in diagnosing and grading paediatric brain lesions (Bull et al., 2012), differentiating tumour type and grade in adults (Pereira et al., 2015; Mimura et al., 2016; Hao et al., 2016) and characterising the cellular composition of Wilms tumours following induction chemotherapy (Hales et al., 2015).

The measured DW signal is influenced by perfusion in addition to diffusion, which can limit the reliability of the ADC measurement. The intravoxel incoherent motion (IVIM) model uses information from multi b-value DWI to separate the pure diffusion component (D) from pseudodiffusion (D*) arising from microcirculatory perfusion, and allows calculation of a perfusion fraction (f) reflecting signal from the vasculature (Le Bihan et al., 1988). D* is not commonly reported in the literature as it is difficult to determine accurately. Although IVIM provides additional information for tumour characterisation, acquisition and analysis are more complex than ADC, which can be calculated from only two b-values. IVIM parameters can be helpful in discriminating benign from malignant lesions in adults (Kang et al., 2014; Klauss et al., 2016), but additional value over ADC has not been established in children.

There is a paucity of evidence evaluating ADC or IVIM histogram analysis for discriminating benign from malignant paediatric tumours or distinguishing tumour type at diagnosis. Research is needed to determine the added value of visual interpretation of DWI histograms and quantitative analysis of histogram parameters over conventional MR imaging, and establish how to present this information to clinicians to facilitate clinical decision-making.

Developing a clinical decision support system (CDSS), MIROR, could make complex information from DWI histogram analysis more accessible and comprehensible for clinicians. Building a tumour repository within MIROR incorporating information from statistical parameters found to differ significantly between benign and malignant tumour groups would allow development of a diagnostic tool to facilitate tumour classification through comparison of new cases with data representative of different tumour types.

This chapter aimed to explore the role of visual interpretation and quantitative analysis of ADC histograms in discriminating benign from malignant solid tumours in children, and ascertain the potential for differentiating tumour type. The potential additional value of IVIM analysis will also be explored. A further aim was to develop MIROR as a CDSS through creating a repository of benign and malignant tumours with which future cases could be compared to facilitate classification.

4.2. Methods

4.2.1. Patients

Children with solid tumours (ages 0-16 years) undergoing diagnostic MRI with DWI at Birmingham Children's Hospital from June 2012 - September 2016 were eligible for inclusion in this observational study. Data were acquired both retrospectively and prospectively. Patients with lymphatic malformations were excluded because of characteristic findings on routine MRI.

4.2.2. MRI and DWI acquisition

Patients underwent 1.5T MR examination using the imaging protocol described in Methods, Chapter 3. DWI was acquired using between two and six b-values (b = 0, 50, 100, 150, 600, 1000 s/mm^2). Total scan duration ranged from 1 min 37 sec to 2 min 42 sec for two b-values (b = 0 and b = 1000 s/mm^2 for ADC calculation), and up to 7 min 32 sec to acquire all six necessary for IVIM analysis.

4.2.3. Image analysis

MRI datasets including ADC maps were transferred into MIROR, where ROIs were drawn around the entire solid tumour on high-resolution b0 images after review of the whole conventional MRI set by an experienced radiologist (KF, 10 years' experience) and overlaid on matched parametric ADC maps.

Advanced histogram analysis was performed in MIROR. All patients were imaged with at least the two b-values necessary for ADC histogram analysis. IVIM analysis was performed in a subset of patients in whom all six b-values had been acquired, obtaining histograms for the parameters D and f. Mean ADC histograms for benign and malignant tumours, and for individual tumour types, were created using pooled data and visually compared. ADC and IVIM histogram parameters including median, 5^{th}, 15^{th}, 25^{th}, 75^{th} and 95^{th} percentile values, skewness, kurtosis and entropy were calculated and compared between groups.

4.2.4. Development of MIROR as a CDSS

MIROR was developed as a clinical decision support system (CDSS) for DWI of body tumours children using this tumour cohort. Information derived from statistical analysis of ROIs of parametric ADC maps of individual benign and malignant tumours was extracted and stored in the repository for future comparison with new cases.

4.2.5. Statistical analysis

Comparisons of non-normally distributed data (median, 5^{th}, 15^{th} 25^{th}, 75^{th} and 95^{th} centile ADC or IVIM parameters, skewness, kurtosis and entropy) from pre-treatment images of benign and malignant tumours were analyzed using the Mann-Whitney U test, with $p<0.05$

considered statistically significant. Sample sizes for individual tumour types were too small to make statistical comparisons meaningful or reliable. Area under the ROC curve (AUC) analysis was used to assess diagnostic ability of ADC median as a representative parameter and attempt to identify a cut-off value for malignancy.

4.3. Results

4.3.1. Patient demographics

Fifty-five children were identified, of which fifty (37 malignant and 13 benign tumours) were recruited. Five patients were excluded because of incomplete images (n=2), inadequate size (n=2), and diagnosis of lymphatic malformation (n=1). Demographic data for all patients is shown in Table 4.1. A subset of forty-two patients (32 malignant and 10 benign tumours) had multi-b-value DWI data available as required for IVIM analysis.

Table 4.1. Demographic data of all patients (cases with IVIM in brackets)

Lesion	Cases (IVIM)	Mean age, range (yrs)	Sex (F/M)
Malignant	**37 (32)**	**3.94 (0.03-11.82)**	**16/21**
Wilms' tumour	14 (9)		
Neuroblastoma	11 (11)		
Hepatoblastoma	4 (4)		
Rhabdomyosarcoma	3 (2)		
Rhabdoid	2 (2)		
Clear cell sarcoma	1 (1)		
Ewing's sarcoma	1 (1)		
Germ cell	1 (1)		
Osteosarcoma	1 (0)		
Benign	**13 (10)**	**3.63 (0.03 – 14.22)**	**6/7**
Liver haemangioma	1 (1)		
Ganglioneuroma	4 (3)		
Mesoblastic nephroma	2 (1)		
Lipoma	1 (1)		
Infantile myofibromatosis	1 (1)		
Haematocolpos	1 (0)		
Vascular malformation	1 (1)		
Ovarian immature teratoma	1 (1)		
Abscess	1 (1)		

An example T2-weighted MRI, ADC map, ROI and corresponding ADC histogram from a 3 year-old patient with a Wilms tumour is shown in Figure 4.1.

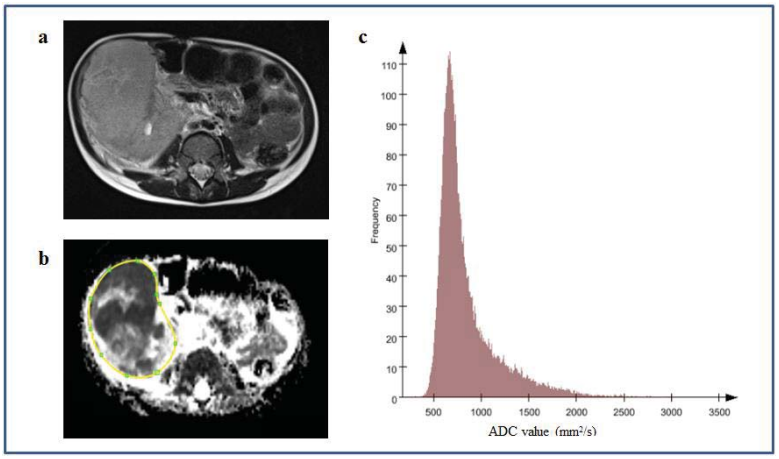

Figure 4.1. a-c. Example ROI and corresponding ADC histogram: Wilms tumour. MRI shows a heterogeneous tumour arising from the right kidney. Solid components restrict diffusion. ADC map was obtained and a whole-tumour ROI selected (b). The corresponding histogram (c) appears shifted to the left and positively skewed with a sharp peak, as reflected through quantitative values obtained: ADC median 0.74 x 10^{-3} mm^2/s, skewness 0.0238, kurtosis 2.18, and entropy 6.83.

4.3.2. ADC Histograms of benign and malignant tumours

Mean ADC histograms of benign and malignant tumours appear morphologically different, as shown in Figure 4.2. The pooled mean histogram of malignant tumours is shifted to the left, positively skewed and peaked with a higher kurtosis, whereas that of benign tumours is shifted to the right, negatively skewed, and flatter with a lower kurtosis.

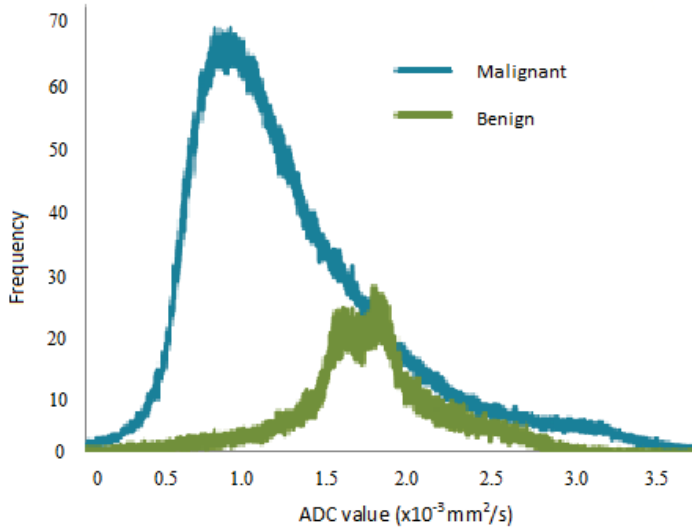

Figure 4.2. The morphological differences between pooled mean histograms of benign (n=13) and malignant (n=37) tumours. The mean is represented by the solid line, and Standard Deviation (SD) by the shaded area.

Mean pooled histograms of individual tumour types also different visually (Figure 4.3.), indicating potential value of ADC histogram analysis in distinguishing tumour type in a larger cohort.

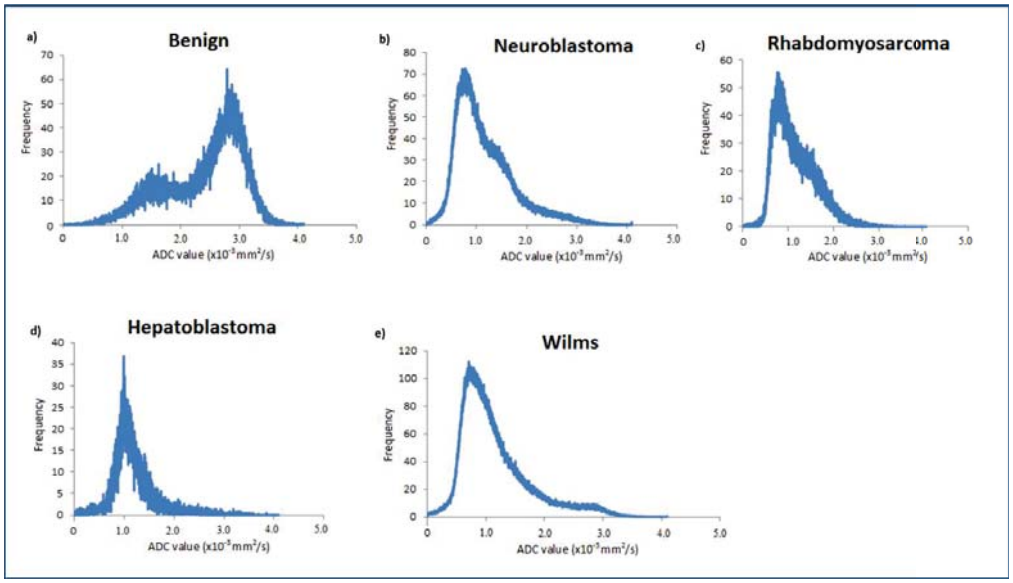

Figure 4.3. The morphological differences in appearance of mean pooled histograms of benign tumours (n=13), neuroblastoma (n=11), rhabdomyosarcoma (n=3), hepatoblastoma (n=4) and Wilms tumours (n=14).

4.3.3. Quantitative discrimination between Malignant and Benign Childhood Tumours using ADC

Quantitative differences in ADC histogram parameters between benign and malignant tumours are shown in Table 4.2. As the median volume of benign lesions was significantly less than malignant ones, histograms were normalised to an area of unity.

Malignant tumours demonstrated significantly lower median, 5^{th}, 15^{th}, 25^{th}, and 75^{th} centile ADC values, more positive skewness, higher kurtosis and higher entropy than benign lesions. ADC centile values at the extreme right of histograms did not differ significantly between benign and malignant tumours, with no significant difference between 95^{th} centile ADC values. Detailed histogram parameters from ADC maps of benign and malignant tumours are summarised in Table 4.2. Comparison of histogram parameters (median ADC, skewness, kurtosis and entropy) of benign and malignant tumours is shown in box plots (Figure 4.4.).

Table 4.2. Comparison of ADC histogram parameters between benign and malignant childhood tumours

	Malignant (n=37)	**Benign (n=13)**	**P value**
Volume* (ml)	31791 (624-149554)	4943 (376-142436)	0.006*
ADC median*	0.97 (0.42-1.57)	1.57 (0.73-2.64)	0.015*
ADC 5%*	0.55 (0.30-1.00)	0.98 (0.22-1.37)	0.008*
ADC 15%*	0.71 (0.35-1.11)	1.07 (0.39-1.54)	0.005*
ADC 25%*	0.75 (0.39-1.29)	1.37 (0.52-2.17)	0.001*
ADC 75%*	1.31 (0.47-1.93)	1.68 (0.93-2.92)	0.011*
ADC 95%	1.99 (0.86-2.87)	1.91 (1.21-3.23)	0.514
Skewness*	0.0226 (0.0139-0.0269)	-0.0006 (-0.023-0.0292)	<0.001*
Kurtosis*	2.22 (1.99-2.25)	2.03 (1.80-2.03)	<0.001*
Entropy*	7.27 (5.79-7.84)	6.80 (6.22-7.67)	0.05*

Data are presented as median and range; asterisks denote statistical significance $p<0.05$.
The unit for ADC value is x 10^{-3} mm^2/s

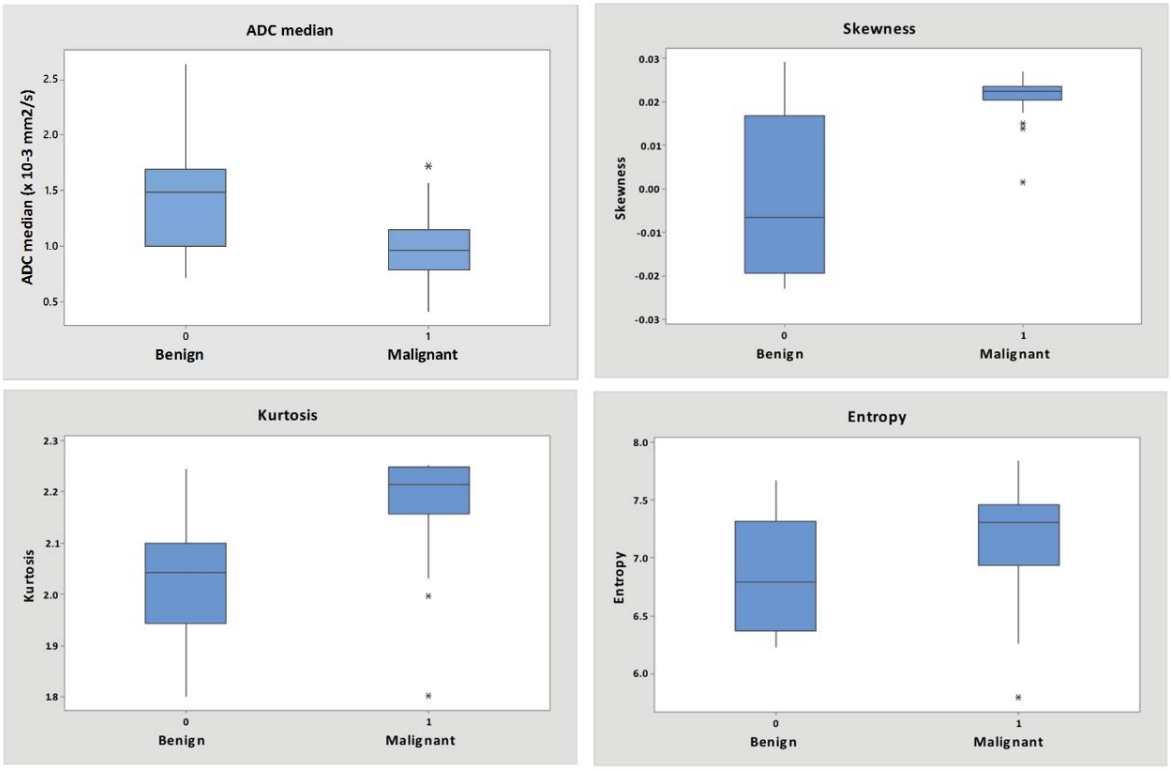

Figure 4.4. Box plots show comparison of ADC histogram parameters (ADC median, skewness, kurtosis and entropy) for benign and malignant paediatric tumours. Line in box represents the median, height of the box represents the interquartile range, whiskers are the lowest and highest data points within 1.5 interquartile range, and asterisks indicate outliers.

4.3.3. Quantitative discrimination between Malignant and Benign Childhood Tumours using IVIM parameters

The differences in ADC and IVIM histogram parameters D and f between benign and malignant tumours in the subset of patients undergoing IVIM analysis is shown in Table 4.

Table 4.3. Comparison of benign (n = 10) and malignant (n = 32) lesions with ADC, D and f histogram parameters

Parameter	**Mann-Whitney test**		
	ADC	**D**	**F**
Median	0.001*	0.049*	0.320
5%	0.005*	0.056	0.919
15%	0.003*	0.051	0.543
25%	0.002*	0.045*	0.248
75%	0.007*	0.052	0.494
95%	0.202	0.112	0.760
Skewness	<0.001*	0.018*	0.122
Kurtosis	<0.001*	0.740	0.631
Entropy	0.036*	0.081	0.965

Asterisks denote statistical significance p<0.05

In this subset of cases, both ADC and D were lower in malignant tumours. There was a significant difference in all ADC histogram parameters between benign and malignant tumours other than 95th centile, with the latter demonstrating significantly lower median, 5th, 15th, 25th, and 75th percentile ADC, and higher kurtosis, skewness and entropy. Significant differences in the D parameter were only observed through lower median and 25th percentile and higher skewness in malignancy. There were no significant differences in any measure of the f parameter between benign and malignant lesions.

4.3.4. Quantitative discrimination between malignant tumour types

It was not possible to discriminate individual malignant tumour types in this small cohort. Given the small numbers involved, it was inappropriate to look for statistically significant differences in ADC histogram parameters between individual malignant tumour types or attempt to construct accurate predictive models. Patients with Wilms tumours, neuroblastomas, hepatoblastomas and rhabdomyosarcomas had ADC median values of 0.90, 0.96, 1.00, and 1.02 x 10^{-3} mm^2/s, kurtosis of 2.21, 2.25, 2.23 and 2.10, and skewness of 0.0229, 0.0227, 0.0224 and 0.0183 respectively.

4.3.5. Differentiating neuroblastoma from ganglioneuroma

Of clinical relevance, malignant neuroblastoma (n=11) appears distinguishable from benign ganglioneuroma (n=4) through morphologically different ADC histograms, with those of the former demonstrating left shift with significantly lower median, 5th, 15th, 25th and 75th centile ADC, more positive skewness and higher kurtosis. Entropy did not differ significantly. The small group sizes imply this pattern needs confirmation with more cases. Example ADC histograms of neuroblastoma and ganglioneuroma are shown in Figures 4.5a and b, with detailed histogram parameters presented in Table 4.3.

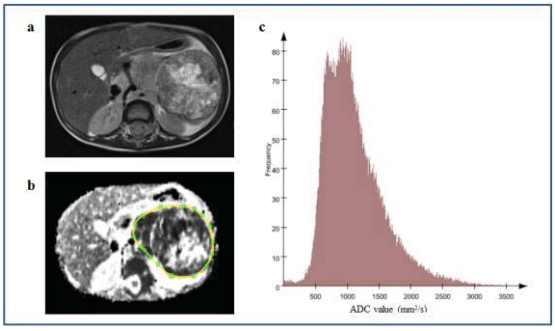

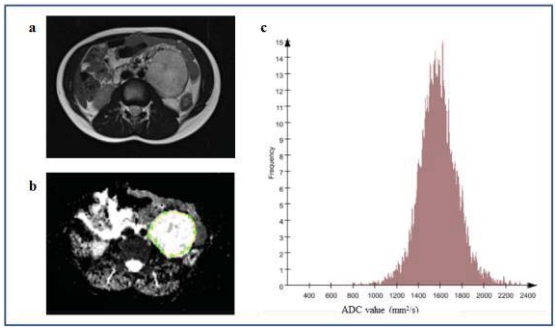

Figure 4.5.a Neuroblastoma **b.** Ganglioneuroma

4.5.a. A 2 year-old girl with a left sided neuroblastoma. Axial T2-weighted image (a) shows a large abdominal mass lying anterior to the left kidney. ADC map was obtained and a whole-tumour ROI selected (b). The corresponding histogram of the neuroblastoma (c) is shifted to the left and positively skewed, as reflected by ADC median 0.99 x 10^{-3} mm^2/s, skewness 0.0217, kurtosis 2.25 and entropy 7.47

4.5.b. A 6 year-old boy with a left-sided ganglioneuroma. Axial T2-weighted image (a) shows a well-defined round mass in the left side of the abdomen. The mass enhances heterogeneously and does not restrict diffusion. ADC map was obtained and a whole-tumour ROI selected (b). The corresponding histogram of the ganglioneuroma (c) is shifted to the right and negatively skewed as reflected by ADC median 1.58 x 10^{-3} mm^2/s, skewness -0.0196, kurtosis 2.029 and entropy 6.50.

Table 4.4. Comparison of ADC histogram parameters between neuroblastoma and ganglioneuroma

	Neuroblastoma (n=11)	Ganglioneuroma (n=4)	P value
Age*	1.48 (0.05-5.63)	7.45 (0.79-9.72)	0.01*
Volume (ml)	17642 (624-75125)	3870 (376-24196)	0.117
ADC median*	0.96 (0.63-1.31)	1.64 (1.40-1.91)	0.004*
ADC 5%*	0.53 (0.31-0.82)	0.99 (0.86-1.29)	0.004*
ADC 15*	0.64 (0.42-0.89)	1.23 (1.03-1.35)	0.004*
ADC 25%*	0.72 (0.54-0.99)	1.42 (1.26-1.49)	0.004*
ADC 75%*	1.31 (0.91-1.92)	1.92 (1.54-2.26)	0.009*
ADC 95%	1.83 (1.34-2.86)	2.19 (1.74-2.57)	0.296
Skewness*	0.0227 (0.0179-0.0269)	-0.0192 (-0.0230 -0.0136)	0.004*
Kurtosis*	2.25 (2.029-2.25)	2.04 (1.95-2.10)	0.009*
Entropy	7.37 (6.26-7.81)	6.59 (6.22-7.55)	0.19

Data are presented as median and range; asterisks denote statistical significance $p<0.05$.
The unit for ADC value is x 10^{-3} mm^2/s.

4.3.4. ROC curve analysis

The representative parameter median ADC has an AUC of 0.77; 95%CI 0.69-0.87; p=0.001) in differentiating benign from malignant lesion, with a 1.01 x10^{-3} cut-off value yielding sensitivity 80.1%, specificity 81.2%. The ROC curve is shown in Figure 4.6.

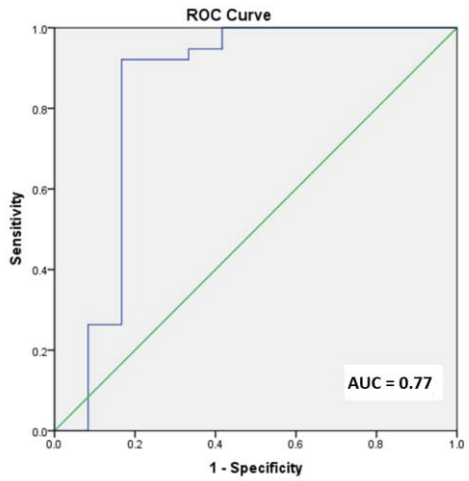

Figure 4.6. ROC curve analysis for ADC median distinguishing benign from malignant tumours

4.3.5. Development of MIROR Tumour Repository and as a CDSS

The statistical information derived from ADC histogram analysis of individual benign and malignant tumour cases was incorporated into the tumour repository within MIROR to allow its development as a CDSS and diagnostic tool. Following this study, MIROR contained a repository of 13 benign and 37 malignant tumours from which comparisons can be made with new cases to facilitate discrimination. Statistical data concerning histogram parameters found to be significantly different between benign and malignant tumour groups were incorporated into the diagnostic tool to allow comparison of values from new cases with those in the repository, displayed as box-plots. The CDSS output generated is shown in Figure 4.7.

a) Malignant

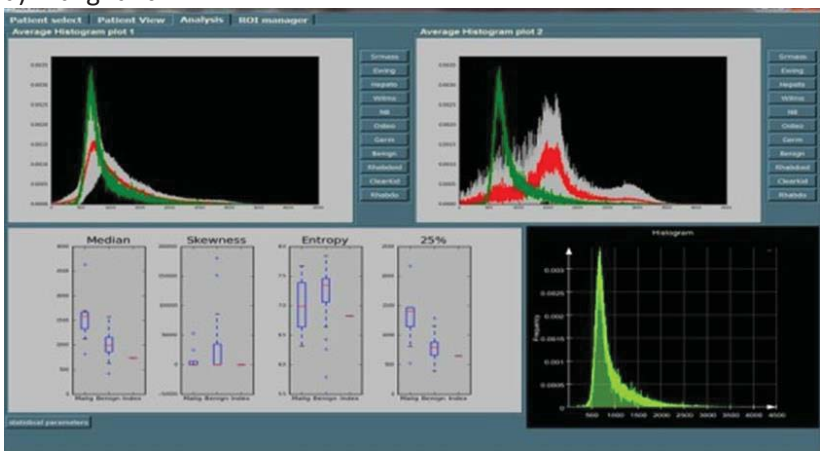

b) Benign

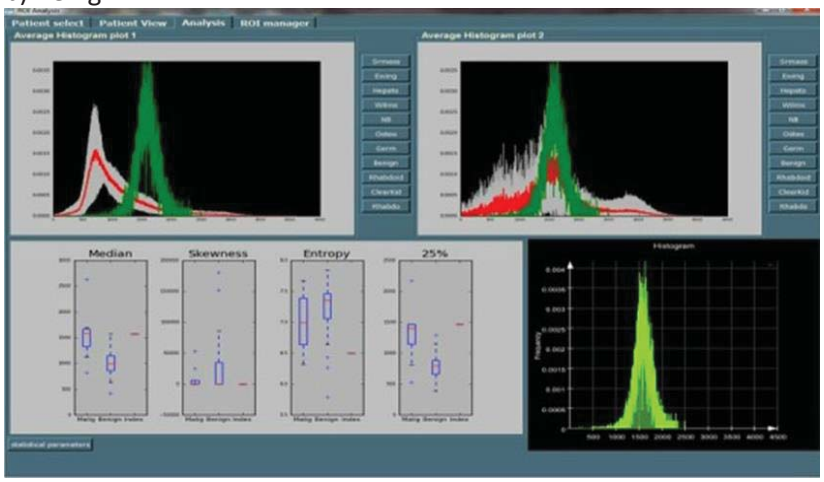

Figure 4.7. MIROR user-interface analysis tab, demonstrating MIROR as a decision support system to differentiate benign from malignant tumours. The green histogram line represents the index case, and the red line and grey area represent the mean and standard deviation of malignant (a) and benign tumours (b) respectively. The example box-plots compare median, 25th percentile, skewness and entropy values of the index case with tumour types in the repository.

4.4. Discussion.

ADC histograms derived from benign and malignant paediatric body tumours are different, which is apparent both through visual interpretation of histogram shape and through quantitative analysis of ADC histogram parameters. The morphological differences between ADC histograms of benign and malignant tumours could potentially be used in clinical practice, with visual interpretation of ADC histograms enhancing radiological interpretation of DWI and facilitating non-invasive diagnosis. Quantitative histogram parameters, such as

ADC percentile values, skewness and kurtosis, were significantly different between benign and malignant lesions. IVIM analysis does not confer any additional advantage over the more easily acquired and clinically applicable ADC. Incorporating the statistical information acquired in a repository within MIROR has contributed to development a clinical decision support system (CDSS) aiming to facilitate discrimination of benign and malignant tumours in clinical practice.

Visual interpretation of ADC histograms or quantitative analysis of histogram parameters has not previously been used to discriminate childhood tumours. Paediatric studies evaluating mean or median ADC (Kocaoglu et al., 2010; Lope et al., 2010) do not account for tumour heterogeneity, which cannot be conferred though a global parameter. Macroscopic and microscopic intra-lesional necrotic and cystic areas may impact ADC, with necrotic components demonstrating high values, and cysts a range of values reflecting haemorrhage, mucinous and serous fluids. Rather than simply providing a numerical ADC value, histogram-based evaluation elucidates visual information and statistical features that reflect overall histological tumour characteristics and may be useful for qualitative and quantitative radiological evaluation.

ADC histograms of malignant tumours were more positively skewed than those of benign tumours; this was apparent visually and confirmed as statistically significant on quantitative analysis. Positive skewness could equate to high cellularity reflected by dense population of the left end of the histogram, with more pixels with low ADC lying left of the mean but supportive tissue giving a long tail at high ADC values. Similar findings have been reported in adults (Suo et al., 2014), with higher grade tumours demonstrating more positively skewed histograms than lower grade lesions (Pereira et al., 2015).

The finding of a visually apparent and significantly higher kurtosis in ADC histograms in malignant tumours, with a distinct peak and rapid decline, implies more uniform cellularity. Homogeneous tumours with uniform arrangement of malignant cells have a steep histogram peak, whereas heterogeneous lesions with cystic, necrotic or haemorrhagic components show low kurtosis (Takahashi et al., 2015). Studies in adults have reported significantly higher kurtosis in malignant (Suo et al., 2014) and high-grade tumours (Pereira et al., 2015).

Statistical parameters representing the left side of the histogram may be most discriminatory of tumour type as more aggressive components are represented by lower ADC centiles. The extreme right may correspond to non-malignant tissue included in the whole-tumour ROI, such as normal renal tissue or stromal components. We found ADC centiles representing the extreme left of the histogram (5^{nd}-25^{th} centile) significantly different between malignant and benign lesions, whereas those corresponding to the extreme right (95^{th} centile) were not. The adult literature has reported high levels of significance of 10% ADC (Mimura et al., 2016) in discriminating benign from malignant lesions, with a report of ADC parameters representing the left side of the histogram distinguishing degrees of differentiation of hepatic malignancy (Drevelegas et al., 2016).

ADC histogram analysis performed better than IVIM in differentiating benign and malignant tumours. Although discrimination was possible with certain parameters derived from histogram analysis of IVIM D, robustly significant differences in ADC were consistently observed across all percentiles (other than 95^{th}) and descriptors of histogram shape. The f parameter did not reach significance, which may be due to the variation in vascularity between tumours in our cohort. As ADC is influenced by both D and D*, the combination of diffusion and perfusion into a single parameter may allow for its higher diagnostic

performance. The excellent comparative performance of ADC has important implications for clinical practice as quantitative ADC analysis is far simpler and quicker to perform than IVIM, and may be more easily incorporated into the clinical workflow.

It is important to consider clinical application of ADC histogram analysis and potential to add value to conventional imaging. Distinguishing between tumours with similar morphological appearances on conventional MRI, such as neuroblastoma and ganglioneuroma, or Wilms and rhabdoid tumours, would be of considerable clinical benefit. We were able to show clearly visually apparent and quantifiably significant differences in ADC histogram parameters between neuroblastomas and ganglioneuromas. This should be interpreted cautiously given small numbers involved, but nonetheless is a promising finding warranting further investigation. ADC was found to be significantly lower in neuroblastoma than ganglioneuroma in a small paediatric study (Gahr et al., 2011), and further work is needed to establish the role of histogram analysis in this area.

The possibility of translating research findings into clinical practice is an important consideration when determining added value of advanced imaging techniques. ADC values derived from b0 and 1000 s/mm^2 values calculated by scanner software were used as these are readily available to radiologists and reflect what is currently possible in a clinical setting. Incorporating DWI data into MIROR as a CDSS may prove a valuable way of integrating advanced ADC histogram analysis into the diagnostic pathway and allowing objective classification according to quantifiable parameters. Prospective testing is necessary to ascertain the added value of ADC histogram analysis through MIROR over conventional MRI in differentiating benign from malignant childhood tumours in clinical practice.

Study limitations should be considered. Groups of benign and malignant tumours are unbalanced, and the current version of MIROR was developed with a limited set of retrospective data. There were insufficient cases of individual malignant tumour types to explore the role of these techniques in differentiating tumour type. Future work will involve adding new tumours to the continually evolving repository within MIROR to improve the predictive ability of identified biomarkers for benign and malignant lesions.

4.5. Conclusions

ADC histograms of benign and malignant tumours are morphologically and quantifiably different. ADC histograms of malignant lesions are shifted to the left, with more positive skewness and higher kurtosis than benign tumours. Incorporation of this data into MIROR has facilitated its development as a CDSS and diagnostic tool to make ADC histogram analysis accessible and comprehensible to clinicians in the future. Prospective evaluation is needed to validate these promising findings and integrate this new technique into clinical practice.

Chapter 5: Prospective Validation of the Added Value of Diffusion-Weighted Imaging and ADC Histogram Analysis in Differentiating Benign from Malignant Solid Childhood Tumours

5.1. Introduction

Incorporating information from quantitative ADC histogram analysis into the clinical decision-making process could facilitate confident non-invasive diagnosis of solid paediatric body tumours. Earlier work described in this thesis suggests both visual interpretation of ADC histograms and quantitative analysis of derived parameters could assist radiological discrimination of benign from malignant tumours. Radiologists currently use DWI clinically in a purely qualitative manner to help tumour characterisation, reviewing and commenting on diffusion restriction as a possible marker of malignancy. Although quantitative ADC histogram analysis may provide a more objective evaluation of the diffusion characteristics of an imaged lesion and confer valuable additional information regarding its malignancy, the techniques involved are not yet validated and remain unavailable clinically.

Work described in Chapter 4 shows ADC histograms for benign and malignant tumours appear morphologically different, with visually observable variances substantiated by significant quantitative differences in parameters related to histogram shape. Histograms of malignant tumours tend to be positively skewed, with left shift and high kurtosis, whereas those of benign tumours are comparatively negatively skewed and shifted to the right with a lower kurtosis. Visual comparison of the histogram of an undiagnosed tumour with mean histograms of benign and malignant lesions could thus facilitate tumour categorisation.

Quantitative histogram parameters may provide additional information to aid classification. It was shown in Chapter 4 that malignant tumours have significantly lower median, 5^{th}, 15^{th}, 25^{th} and 75^{th} centile ADC values, higher kurtosis, more positively skewed histograms and higher entropy than benign lesions. Although increasingly recognised in the adult literature (Pereira et al., 2015; Mimura et al., 2016; Hao et al., 2016), no study has prospectively

evaluated the added value of either visual interpretation of ADC histograms, or parameters derived from quantitative ADC histogram analysis, over conventional MRI in discriminating benign from malignant paediatric solid tumours at diagnosis.

The advanced imaging data necessary for ADC histogram analysis is complex to acquire and interpret, forming a barrier to its clinical use. Clinical decision support systems (CDSSs) facilitate interpretation and analysis of novel MRI techniques through presenting information to clinicians in a clear and intelligible way. As previously described, a modular medical image region of interest analysis tool and repository (MIROR) is being developed by our research team as a CDSS for automatic processing and classification of advanced MRI data (Zarinabad et al., 2018). MIROR uses advanced quantitative analysis to evaluate multi b-value DWI data and compare it with results from previous cases stored within a repository, the formation of which is described in Chapter 4.

MIROR could potentially guide clinicians through ADC histogram analysis in real time, enabling integration of this technique into clinical practice. A clinician can draw a ROI around a tumour and derive an ADC histogram, from which parameters such as median and various percentile ADC values, skewness, kurtosis and entropy are extracted and stored. MIROR allows visual comparison of a case histogram with mean histograms of benign and malignant tumours, and comparison of quantitative histogram parameters with those previously shown to discriminate between tumour types. CDSS cross-validation of MIROR has shown high sensitivity and specificity in discriminating between benign and malignant tumours using quantitative histogram parameters, with median, 15% and 75% ADC highly discriminatory (Zarinabad et al., 2018). Quantitative values for skewness, kurtosis and entropy show promise in this area, but further work is required to determine robust

discriminatory cut-off values for these more novel descriptors. Additional information derived from ADC histogram analysis may add value to that obtained through conventional imaging to facilitate diagnosis, particularly in more difficult or ambiguous cases.

This chapter aimed to prospectively evaluate the added value of quantitative ADC histogram analysis using MIROR as a CDSS in aiding clinicians to non-invasively discriminate between benign and malignant solid paediatric tumours. Both visual interpretation of ADC histogram shape and quantitative analysis incorporating previously published values of median, 15% and 75% ADC for benign and malignant tumours (Zarinabad et al., 2018) were investigated.

5.2. Methods

5.2.1. Patients

Children aged 0-16 with solid lesions having imaging characteristics sufficiently suggestive of malignancy to require discussion at the Solid Tumour Multidisciplinary Team Meeting (MDT) were eligible for inclusion in this prospective study. All included children underwent diagnostic MRI with DWI at Birmingham Children's Hospital between February 2017 and July 2018. Exclusion criteria were treatment prior to imaging, incomplete MRI, and lack of available DWI for advanced analysis. Thirty-three children were included.

5.2.2. Magnetic resonance imaging acquisition and analysis

Patients underwent 1.5T MR examination with multi b-value DWI using the imaging protocol described in Methods, Chapter 3. MRI datasets including ADC maps were transferred to local research PACS prior to upload into MIROR for further analysis.

5.2.3. Determination of added diagnostic value of quantitative ADC histogram analysis

Two radiologists (SA, 1 year experience and KF, 10 years' experience) reviewed all imaging and ADC histogram outputs. Radiologists were given information about the age and gender of each child and their clinical presentation, and asked to sequentially view 1) conventional imaging sequences and 2) DWI and ADC maps processed using scanner software, as currently performed in routine clinical practice. Radiologists were asked to comment at each stage as to whether the lesion appeared benign or malignant and whether they would recommend biopsy. A list of up to four differential diagnoses was requested at each stage. All reporting was undertaken independently and blind to histopathological and final diagnoses.

Radiologists used MIROR to construct a whole tumour ROI guided by conventional imaging, and derived an ADC histogram with quantitative ADC parameters. Following 3) visual comparison of the ADC histogram of the index case with mean histograms of benign and malignant tumours from the MIROR repository, radiologists were asked to determine whether the lesion was benign or malignant, whether biopsy was recommended, and to provide a revised list of differential diagnoses. Radiologists were finally asked to 4) compare the quantitative median, 15^{th} and 75^{th} percentile ADC of the lesion calculated in MIROR with previously determined median values for benign and malignant tumours (Zarinabad et al., 2018).

Factors contributing to the clinical decision-making process in discriminating benign from malignant lesions were documented for each case. A semi-structured interview was conducted at study end to determine radiologists' perception of the added value and clinical applicability of ADC histogram analysis and MIROR as a CDSS.

Figure 5.1. shows an example of the decision support system within MIROR for differentiating between benign and malignant tumours. Example mean histograms from the repository for benign and malignant tumours are shown in Figure 5.2.

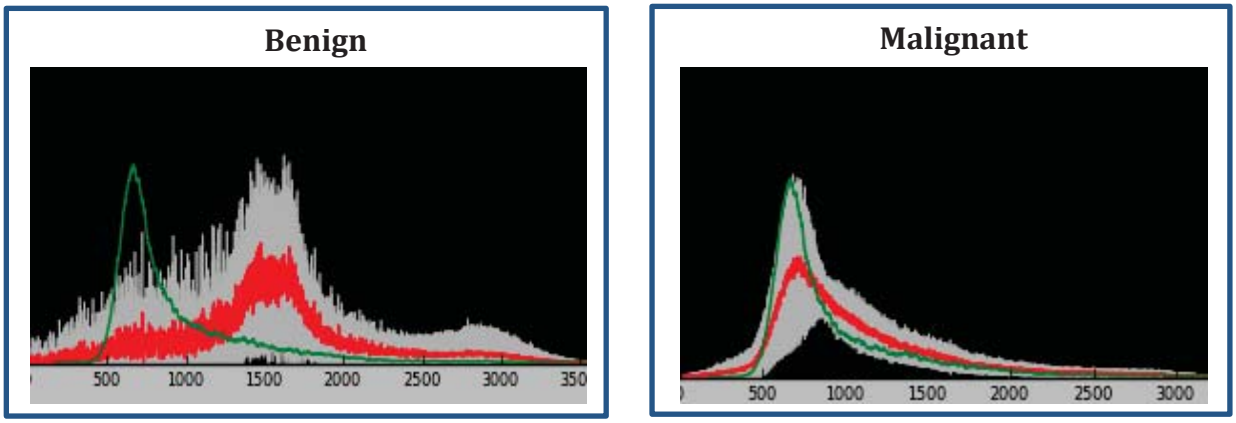

Figure 5.1. Extracts from the CDSS within MIROR for differentiating between benign and malignant tumours (The GUI for benign v malignant is shown in Chapter 4, Figure 4.7). The index case histogram (green) is superimposed on mean histograms for benign and malignant tumours (mean = red line; standard deviation = grey shaded area). In this example of a Wilms tumour, it can be seen that the green index case histogram closely matches the mean histogram for malignant tumours.

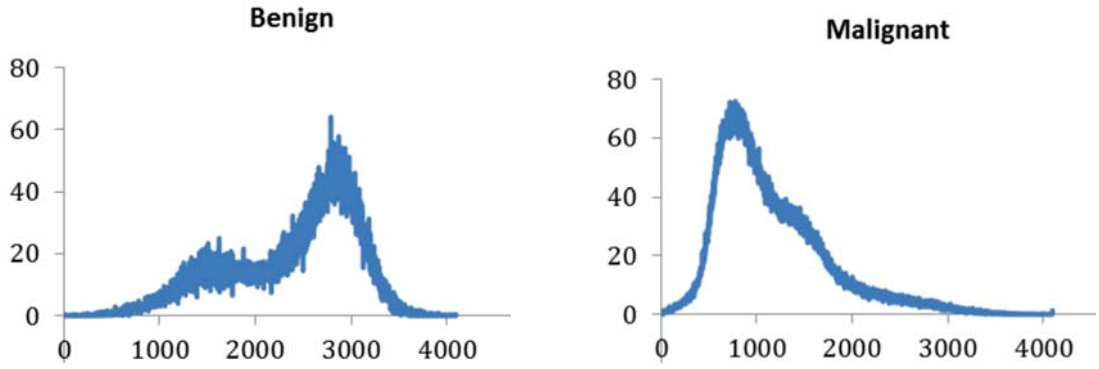

Figure 5.2. Example mean histograms for benign and malignant tumours. The histogram for benign tumours has a negative skew and is shifted to the right, whereas that of the malignant tumours has a positive skew and is shifted to the left.

5.2.4. Statistical analysis

Accuracy of conventional MRI and MRI+ADC histogram analysis in terms of correct classification of benign and malignant tumours was ascertained through estimates of sensitivity, following averaging the percentage of correct diagnoses made by the two

radiologists. McNemar's test determined if ADC histogram analysis had a statistically significant effect on correct diagnosis compared with MRI alone. The Kruskal-Wallis test was used to compare reference ADC histogram parameters with those from the prospective cohort.

5.3. Results

Thirty-two children were recruited. One was excluded for lack of conclusive diagnosis, leaving 31 for analysis of which 20 were malignant and 11 benign. Patient demographics and tumour details are presented in Table 5.1.

Table 5.1. Demographic data of all patients

Tumour	Median age, years (range)	Gender	Diagnosis	Patients, n
Benign	3.51 (0.03-14.22)	F= 8; M= 4	Ganglioneuroma	1
			Nephroblastomatosis	2
			Mesoblastic nephroma	1
			Vascular malformation	2
			Ovarian dermoid	1
			Splenic cyst	1
			Tuberculoma	1
			Intra-abdominal extrapulmonary sequestration	1
			Kaposiform haemangioendothelioma	1
				11
Malignant	3.85 (0.02-11.82)	F= 8; M= 12	Neuroblastoma	6
			Rhabdoid tumor	2
			Rhabdomyosarcoma	2
			Wilms tumour	4
			Germ cell tumour	1
			LCH	2
			Ewing Sarcoma	1
			Fibrosarcoma	1
			Retiform Sertoli-Leydig cell tumour	1
				20

Histological confirmation of diagnosis was available for 30 of the 31 tumours, a median of 38 (range 2-298) days after initial imaging. Diagnosis of intra-abdominal pulmonary sequestration was made clinically in the remaining case.

5.3.1. Classification of Benign and Malignant Childhood Tumours

The percentage of tumours correctly classified as benign or malignant using conventional imaging (MRI and DWI) and with addition of ADC histogram analysis, initially involving visual interpretation of ADC histogram shape and then following review of quantitative ADC parameters, is shown in Table 5.2.

Table 5.2. Percentage of tumours correctly classified as benign or malignant using conventional imaging (MRI and DWI) and with addition of ADC histogram analysis

	Conventional MRI		**ADC histogram analysis**	
	MRI alone	**+ conventional DWI**	**+ visual ADC histogram**	**+ quantitative histogram parameters**
All tumours (31)	77%	79%	90%	90%
Malignant (20)	100%	100%	100%	100%
Benign (11)	36%	41%	73%	73%

Percentages given are averages of results of the two radiologists

The diagnosis of benign and malignant lesions after conventional MRI was accurate in 79% of all cases, increasing to 90% with addition of ADC histogram analysis (Table 5.2). Of benign tumours, 41% were correctly diagnosed with MRI alone with 73% correctly diagnosed after MRI and visual interpretation of the ADC histogram. There was no further improvement in classification following review of quantitative histogram parameters. All malignant tumours were correctly diagnosed on conventional MRI alone. ADC histogram

analysis had a statistically significant effect on correct diagnosis for all cases (+11%) ($p = 0.04$)) and for benign tumours (+ 34%) ($p = 0.014$) (McNemar's Test). The improvement in diagnostic accuracy following review of conventional DWI available through scanner software did not reach significance. None of the cases incorrectly diagnosed after MRI + ADC histogram analysis had previously been correctly diagnosed after MRI alone.

Following conventional MRI alone a splenic cyst, two vascular malformations and a ganglioneuroma were correctly diagnosed as benign by both radiologists. Addition of conventional DWI through review of ADC maps resulted in further correct benign diagnosis of nephrogenic rests by radiologist 2. Following visual interpretation of ADC histograms, both radiologists correctly re-diagnosed benign ovarian dermoid, mesoblastic nephroma and tuberculoma with radiologist 1 also correctly re-classifying extrapulmonary sequestration and radiologist 2 kaposiform haemangioendothelioma.

ADC histogram analysis was not performed in two cases, infantile fibrosarcoma and nephrogenic rests, as it was not possible to visualise the lesions clearly enough to construct an ROI. Although the infantile fibrosarcoma was correctly classified as malignant by both radiologists based on conventional imaging appearances, the nephrogenic rests were correctly diagnosed as benign by radiologist 2 only following review of qualitative DWI.

5.3.2. Recommendations for biopsy

The radiologists' recommendations for the need for biopsy to confirm benign or malignant diagnosis at each stage in the diagnostic pathway are shown in Table 5.3.

Table 5.3. Recommendations for biopsy

	Conventional MRI		Quantitative ADC histogram analysis	
	MRI alone	**+ conventional DWI**	**+ visual ADC histogram**	**+ quantitative histogram parameters**
All tumours (31)	97%	97%	90%	90%
Malignant (20)	100%	100%	100%	100%
Benign (11)	91%	91%	73%	73%

Percentages given are averages of the two radiologists

Information from DWI and ADC histogram analysis resulted in a significant 18% reduction in the number of recommendations for biopsy in patients with benign lesions (91% to 73%) ($p = 0.03$), although the 7% reduction for all cases (97% to 90%) did not reach significance ($p = 0.06$) (McNemar's Test). On MRI appearances alone, biopsy was recommended in all but one benign lesion, a splenic cyst. Visual ADC histogram analysis allowed further conclusive confirmation of benign diagnosis in an ovarian dermoid tumour and a tuberculoma without recommendation for biopsy. Review of quantitative histogram parameters did not prevent recommendation of any further biopsies. There were no inappropriate recommendations to avoid biopsy in any malignant tumours.

5.3.3. Quantitative ADC Histogram Parameters

The reference values for median, 15% and 75% ADC of benign and malignant lesions included in the MIROR repository, and the values obtained from the tumours in this prospective cohort, are shown in Table 5.4. The Kruskal-Wallis test revealed no significant differences between reference ADC histogram parameters derived from the original cohort and those derived prospectively from patients involved in this study.

Table 5.4. Median, 15th and 75th percentile ADC of the original reference cohort (13 benign, 37 malignant) and prospectively acquired cases (11 benign, 20 malignant).

	Malignant	Benign
ADC median reference	0.97 (0.42-1.57)	1.57 (0.73-2.64)
ADC median prospective	1.06 (0.72-1.77)	1.52 (1.11-2.33)
ADC 15% reference	0.71 (0.35-1.11)	1.07 (0.39-1.54)
ADC 15% prospective	0.70 (0.11-0.98)	0.99 (0.13-1.51)
ADC 75% reference	1.31 (0.47-1.93)	1.68 (0.93-2.92)
ADC 75% prospective	1.67 (0.3-3.04)	1.91 (0.3-2.59)

Data are presented as median and range
The unit for ADC value is x 10^{-3} mm^2/s.

5.3.4. Factors contributing to radiological diagnosis

The shape of the histogram curve was documented as being a helpful contributing factor in diagnosis of 23 of the 28 cases (82%) correctly classified. Quantitative ADC parameters were reported to provide useful additional confirmatory information in eight, but did not change diagnosis in any case.

5.3.5. Examples of cases in which quantitative ADC histogram analysis provided added value

Individual cases in which review of information provided from ADC histogram analysis provided potential added clinical value are described below.

Benign Tumours:

Case 1. Ovarian Dermoid Tumour

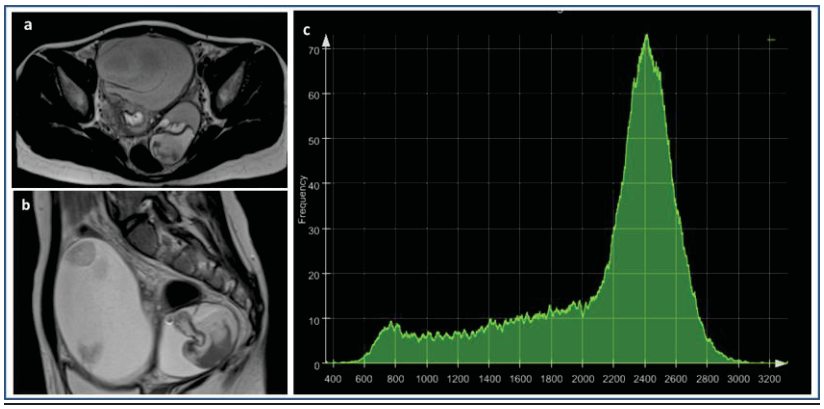

Figure 5.3. Ovarian dermoid misdiagnosed as germ cell tumour

Axial (a) and sagittal (b) T2-weighted MR images of a 10 year-old girl who presented with a large, complex supravesical pelvic mass which consisted of cystic and solid components. This was misdiagnosed as malignant by both radiologists following review of conventional MR imaging, with a primary differential diagnosis of a well-differentiated germ cell tumour. Visual ADC histogram interpretation (c) led to confident diagnosis of benign ovarian dermoid with recommendation not to biopsy, which was further confirmed quantitatively by a high median ADC (2.33).

Case 2. Mesoblastic nephroma

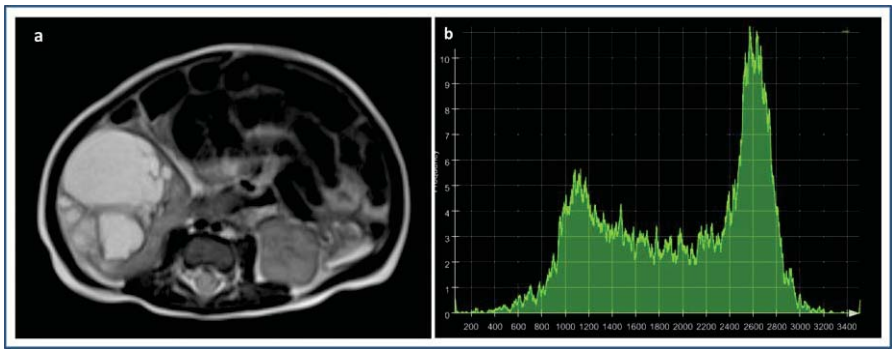

Figure 5.4. Mesoblastic nephroma initially misdiagnosed as probable malignancy

Axial T2-weighted MRI (a) of a 1 month-old baby with an antenatally diagnosed multicystic lesion arising from the right kidney. Both radiologists diagnosed malignancy after review of

conventional MRI, but were confident this was a benign lesion following visual ADC histogram analysis (b).

Case 3. Tuberculoma

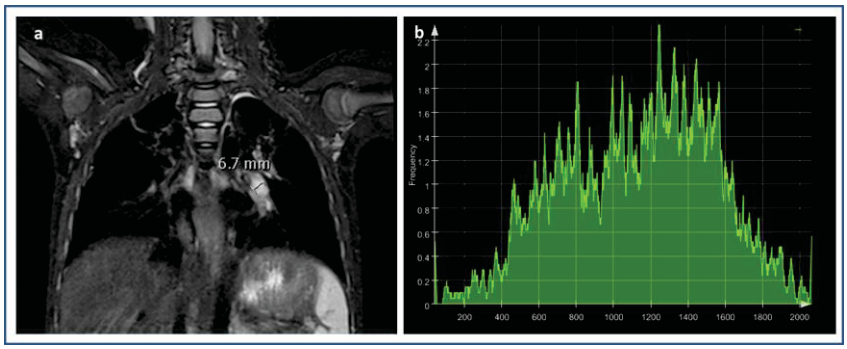

Figure 5.5. Tuberculoma initially misdiagnosed as likely Ewing Sarcoma

Coronal (a) T2-weighted MR images of a 5 year old boy demonstrating a heterogeneous mass on the left chest wall centred around costochondral junction of the left fifth rib, showing moderate restriction of diffusion and mixed contrast enhancement. The mass extended superficially and internally into the thorax, and was associated with collapse of the adjacent lung. This was initially misdiagnosed as a malignant lesion on MRI by both radiologists, with a primary differential of Ewing Sarcoma. After visual interpretation of the ADC histogram (b), a confident benign diagnosis was made by both radiologists without recommendation for biopsy.

Case 4. Kaposiform haemangioendothelioma

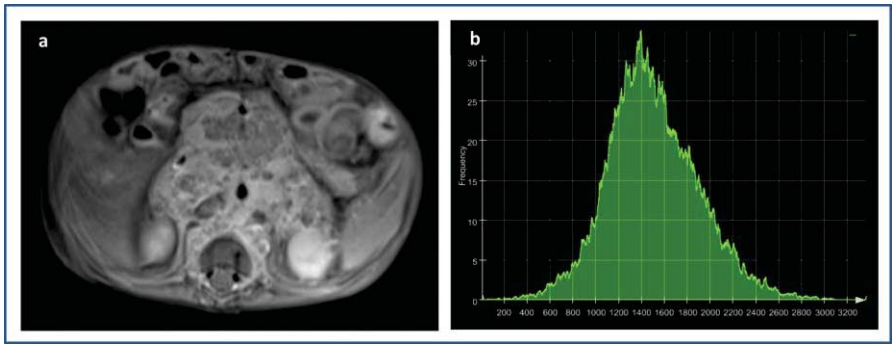

Figure 5.6. Kaposiform haemangioendothelioma misdiagnosed as probable neuroblastoma

T2-weighted axial MRI (a) of a 6 month-old baby who presented with bleeding tendencies, melaena and a large abdominal mass revealed a large, complex, heterogeneous reteroperitonal mass with no restriction of diffusion, with peritoneal involvement that encased the abdominal vasculature and appeared to invade the left kidney. Both radiologists misdiagnosed this as a malignant lesion on conventional MRI, with a primary differential diagnosis of neuroblastoma. Radiologist 2 made a diagnosis of a benign tumour following review of the ADC histogram (b), whereas radiologist 1 still considered the lesion to be malignant. This is interesting as kaposiform haemangioma is a benign tumour with locally aggressive features, reflected by the histogram demonstrating appearances intermediate between benign and malignant lesions.

Malignant Tumours

For comparison, an example MR image and corresponding ADC histogram for a malignant extrarenal Wilms Tumour is shown in Figure 5.7.

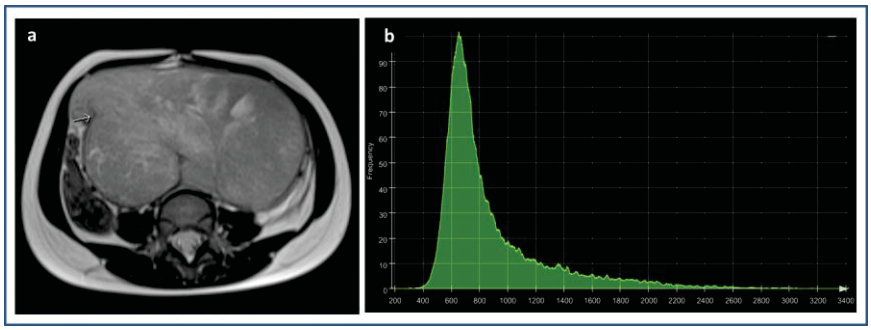

Figure 5.7. Extrarenal Wilms Tumour

T2-weighted MRI (a) of a 5 year-old girl who presented with a lower abdominal mass demonstrating a large, lobulated lesion of uncertain origin extending into the pelvis. Differential diagnosis included sarcoma or an extra adrenal neuroblastoma. The corresponding ADC histogram (b) is typical of malignancy, in accordance with the histopathological diagnosis of extrarenal Wilms tumour.

5.3.6. Misdiagnosis following ADC histogram analysis

One benign tumour, nephroblastomatosis, remained misclassified as malignant by both radiologists following ADC histogram analysis. An MR image for this case and the corresponding ADC histogram are shown in Figure 5.8.

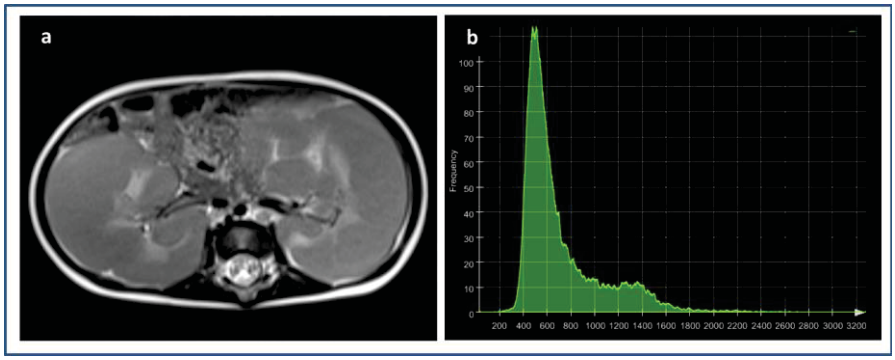

Figure 5.8. Nephroblastomatosis misdiagnosed as malignancy

Axial T-2 weighted MRI (a) of a 7 month-old girl who presented with an abdominal mass revealed numerous large, rounded masses arising from the renal cortex of both kidneys bilaterally, causing massive renal enlargement. Both radiologists felt MRI appearances were consistent with either large nephroblastic rests or Wilms tumours and recommended biopsy. Review of the ADC histogram (b), which is typical of a malignant lesion, led to misdiagnosis of malignancy by both radiologists. Nephroblastomatosis is a pre-malignant condition, which may be reflected in the malignant appearance of the corresponding histogram.

5.3.7. Radiologist Interview

Radiologists reported finding ADC histogram analysis a valuable diagnostic tool in non-invasive differentiation of benign from malignant paediatric tumours, with additional information from an extra modality confirming or refuting the provisional diagnosis made through conventional imaging. The main clinical benefit was increasing diagnostic confidence, with potential to avoid biopsy in cases with high certainly of being benign. The major disadvantage was that constructing a whole tumour ROI is time-consuming,

particularly in large tumours, and not always practical in a busy clinical setting. Clinical scenarios deriving most potential added value were confirming provisional diagnosis of benign tumours, diagnosing malignant tumour type as more mean histograms are acquired, and classifying unusual tumours. The least benefit was conferred in very typical cases for which diagnosis is straightforward on conventional imaging and clinical features alone. MIROR was considered a potentially user-friendly, comprehensive and clinically applicable CDSS.

Although both visual interpretation of histogram shape and review of quantitative parameters were considered helpful, there was a preference for visual interpretation. Radiologists reported a reluctance to rely on numerical parameters in view of the considerable overlap in reference values for benign and malignant tumours. Constructing a whole tumour ROI added up to 10 minutes to reporting time: this was acceptable if facilitating a difficult diagnosis, but quicker techniques such as single slice ROIs would greatly aid clinical application if results were as accurate. Further addition of mean histograms for individual tumour types was cited as potentially clinically advantageous to enable comparison of an index histogram with those of malignant tumours within the differential.

5.4. Discussion

This study suggests quantitative ADC histogram analysis is a promising technique to facilitate non-invasive discrimination of benign from malignant paediatric solid tumours in clinical practice. The accuracy and confidence of radiological diagnosis of benign lesions increased sequentially with addition of information from conventional DWI and visual interpretation of ADC histogram shape, with fewer biopsies recommended to confirm diagnosis at each step in the proposed diagnostic pathway. Addition of quantitative numerical

histogram parameters did not further increase diagnostic accuracy. The CDSS MIROR allowed presentation of complex data in a comprehensive and intelligible way, facilitating discrimination between benign and malignant tumours through comparison of new cases with information in the repository. ADC histogram analysis was well accepted by radiologists and considered a potentially valuable and clinically applicable additional diagnostic tool.

ADC histogram analysis was found to add most clinical value in confirmation of diagnosis of benign lesions. All malignant tumours in this cohort were classified correctly as malignant using conventional MRI, leaving no possibility for improvement through incorporation of additional information. A higher amount of uncertainty was observed in initial diagnosis of benign tumours, with only 41% correctly diagnosed on MRI alone. The diagnostic accuracy in the benign group increased significantly when using the information provided by MIROR, with 73% of benign tumours correctly diagnosed following visual interpretation of the ADC histogram. Biopsy recommendations in benign lesions decreased with the additional information as diagnostic confidence increased.

Visual interpretation of ADC histogram shape conferred the most added diagnostic value and was reported by radiologists to be more useful than additional numerical information about histogram parameters. This suggests illustrative graphical depiction may be the most appropriate way to present complex DWI data to radiologists, whose daily work involves interpretation of images rather than numerical data. The considerable degree in overlap between reference values for benign and malignant lesions may have contributed to the reluctance of radiologists to rely on quantitative parameters sufficiently to change their diagnosis.

The morphological differences apparent in ADC histograms of benign and malignant paediatric tumours have also been described in tumours in adults. Benign and malignant breast tumours have been retrospectively discriminated through whole-tumour ADC histogram analysis, with significantly lower median, minimum, 25^{th}, 75^{th} and 90^{th} percentile ADC and higher skewness, kurtosis and entropy in malignancy (Suo et al., 2016). Similar findings have been reported in differentiating benign and malignant orbital tumours (Xu at al., 2016). Although quantitative histogram parameters and median ADC have been shown to prospectively discriminate benign from malignant salivary gland tumours with high sensitivity and specicifity (Miland et al., 2017), there are, at the time of writing, no reports of prospective evaluation of the added diagnostic value of visually observable differences in ADC histograms of benign and malignant lesions.

The CDSS MIROR has potential to facilitate use of quantitative ADC histogram analysis in a clinical setting, delivering decision support to allow clinicians to interpret the information provided. The increasing amount of complex MRI information available can be overwhelming for clinicians, and inherent difficulties with interpretation and analysis may prove an obstacle to implementation and clinical use. Making data from advanced MRI techniques accessible and comprehensible is an important clinical goal to improve decision-making. As a diagnostic tool, MIROR allows users to extract morphological features and statistical information about a defined region, and compare it with relevant findings available in its repository to predict outcome for the index case. Radiologists reported finding ADC histogram analysis using MIROR easy to perform and interpret. ROI construction, generation of an index case ADC histogram and subsequent visual interpretation and comparison with reference histograms from the repository was considered straightforward and possible to incorporate into the clinical workflow with minimal training.

Confident radiological diagnosis of paediatric solid tumours at the time of initial imaging has potential to enhance patient care. Histopathological diagnosis requires an invasive procedure such as biopsy or surgical resection, and was unavailable for a median of 38 days after imaging in this cohort. Biopsy could be avoided completely if a confident non-invasive diagnosis were made in a benign lesion that did not require resection on clinical grounds. As the available repository for different malignant tumour types grows, accurate discrimination of malignant tumours that appear similar on conventional MRI may be possible. This could help prevent misdiagnosis and inappropriate treatment, as can occur with Wilms and renal rhabdoid tumours given recent recommendations to avoid biopsy in most suspected cases of the former (CCLG, 2018). Availability of clearly presented and comprehensible information about tumour characteristics in multidisciplinary meetings prior to confirmation of histopathological diagnosis would be a particularly valuable aid to diagnostic and management decisions.

Although quantitative ADC histogram analysis has considerable potential, there are limitations inherent to the technique. It is not always possible to clearly define a lesion and draw a ROI, as demonstrated by the radiologist being unable to construct ROIs in two cases in this cohort, an infantile fibrosarcoma and nephrogenic rests. The time taken to draw a whole-tumour ROI in large tumours (up to 10 minutes) may form a barrier to use in a busy clinical setting. Establishing quicker ROI techniques that convey similar information in a robust but more time-efficient manner, such as single-slice ROIs, is an important aim for the future to improve clinical applicability.

It is important to consider cases in which ADC histogram analysis was not helpful to identify scenarios in which additional caution should be taken in interpreting results. One benign

lesion, nephroblastomatosis, remained misdiagnosed as malignant following visual and quantitative ADC histogram interpretation. This was an unusual case involving a 7 month-old baby presenting with bilateral kidney enlargement and multiple homogeneous renal lesions. Although nephroblastomatosis was diagnosed histologically ("undifferentiated blastema together with scattered epithelial lined tubules in keeping with nephroblastomatosis"), clinical uncertainty remained as to whether this constituted a Wilms tumour or nephroblasomatosis. It is possible that this clinical atypia reflected unusual tumour characteristics, with the corresponding ADC histogram appearing more characteristic of malignancy. The child was treated with vincristine and actinomycin, to which she subsequently showed a good response.

A second case, kaposiform haemangioendothelioma, was diagnosed as malignant by radiologist 1 but benign by radiologist 2 following review of the ADC histogram, which displayed intermediate malignant and benign features. Kaposiform haemangioendothelioma is a locally aggressive vascular tumour, which may appear atypical of a benign lesion due to its aggressive behaviour, the influence of the vascular component on diffusion, and the possibility of artefact from bleeding into the tumour. Similarly, adult studies of DWI in identifying malignancy have reported misclassification of liver hemangioma (Feuerlein et al., 2009). ADC histograms of vascular lesions should be interpreted cautiously given the magnetic properties of static blood, and the impact of perfusion as capillary and sinusoidal blood flow in vessels contributes to a large IVIM component. As this could be assessed using the intravoxel incoherent motion (IVIM) model (Le Bihan et al., 1988), IVIM analysis may be helpful in facilitating diagnosis of vascular lesions and should be explored in future studies.

Limitations to this study include the small sample size and unbalanced groups of benign and malignant tumours. Confirmation of findings should be performed in a larger cohort of tumours with additional evaluation by other radiologists. Whilst ADC has been shown to be robust across different scanners (Grech-Sollars et al, 2015), evaluation in a multicentre setting would aid clinical adoption. Future work should further explore the use of quantitative parameters with the aim of developing robust automated prediction models and their presentation to radiologists in a manner which fits with clinical practice.

5.5. Conclusions

Additional information from ADC histogram analysis provided to clinicians through the CDSS MIROR can allow for better and more informed non-invasive discrimination of benign and malignant body tumours in children than possible through interpretation of conventional MRI alone. Visual interpretation of ADC histogram shape was well accepted by radiologists, who found the technique clinically applicable and potentially valuable as an additional tool to confirm or refute a provisional diagnosis of malignancy. As the main barrier to clinical implementation in routine practice is the time involved in drawing whole tumour ROIs, validation of more limited methods of ROI construction would be helpful to ascertain accuracy and reproducibility of less labour intensive techniques that may be more easily applied in a clinical setting.

Chapter 6: Evaluating Chemotherapeutic Response of Paediatric Solid Tumours Using Diffusion-Weighted MRI and Quantitative ADC Histogram Analysis

6.1. Introduction

Chemotherapeutic response of paediatric solid malignant tumours is generally assessed through measuring change in size on conventional imaging. If a tumour becomes smaller it is assumed to have responded to treatment, whereas if it remains static or increases in size non-response is presumed. Size is a relatively crude measure as tumour shrinkage can take weeks or months to become apparent and does not always reflect change at a cellular level (Olsen, 2015). Some tumours, such as stromal-predominant Wilms tumours which differentiate into more mature stromal or mesenchymal types (Anderson et al., 2002), demonstrate minimal tumour shrinkage despite good histological response. The lack of reduction or increase in size seen on conventional imaging can erroneously suggest that treatment has been ineffective (Pizzo et al., 2016).

Additional information provided through diffusion-weighted imaging (DWI) could aid non-invasive monitoring of oncological response and potentially add value in these difficult cases. As discussed in earlier chapters, highly cellular solid malignant tumours restrict diffusion, reflected quantitatively by low ADC values. A reduction in cellularity and an increase in histological differentiation with chemotherapy should lead to a corresponding increase in ADC (Kocaoglu and Bulakbasi, 2016). There are reports in the literature of significant increase in mean ADC of paediatric osteosarcoma, neuroblastic and abdominal tumours following chemotherapy (Demir et al., 2015; Neubauer et al., 2017; Oka et al., 2010; McDonald et al., 2011). Monitoring ADC changes during treatment could facilitate clinical decision-making through allowing on-going risk stratification and identification of non-responders.

ADC histograms, which provide visual and quantitative information about cellular subpopulations within heterogeneous tissue, may demonstrate a morphological shift as tumour tissue changes in response to treatment. In stromal-type Wilms tumours, for example, the predominant viable tissue subpopulation demonstrates a positive shift in mean ADC after chemotherapy as it differentiates into more mature tissue (Hales et al., 2015). Visual comparison of ADC histograms obtained at diagnosis with those obtained after treatment, and quantitative analysis of ADC histogram parameters, may facilitate radiological evaluation of treatment response. Although increasingly recognised in the adult literature (Mimura et al., 2016; Kyriazi et al., 2011), there has been little research evaluating the role of histogram analysis for assessing oncological response in childhood solid tumours.

Although the IVIM parameters D and f have not facilitated discrimination between benign and malignant childhood tumours (Meeus et al., 2017), they have been found to be useful markers of tumour response in adult studies (Xiao et al., 2015). In view of this, the role of IVIM analysis in monitoring chemotherapeutic response in childhood tumours should be investigated.

As described in earlier chapters, a clinical decision support system (CDSS), MIROR, is being developed by our research team for automatic processing of DWI data to facilitate discrimination between benign and malignant tumours (Zarinabad et al., 2018). MIROR can allow comparison and superimposition of serial ADC histograms from individual cases. ADC histogram analysis is a potential tool for monitoring chemotherapeutic response, both through visual comparison of serial histograms and through review of changes in quantitative histogram parameters with treatment.

This chapter aimed to evaluate the added value of visual interpretation of ADC histograms and parameters derived from quantitative ADC and IVIM histogram in determining chemotherapeutic response of malignant paediatric solid tumours, and compare this with changes in tumour volume. A further aim was to explore and validate MIROR as a CDSS for monitoring treatment response.

6.2. Methods

6.2.1. Patients

Children aged 0-16 years with solid body tumours imaged with MRI with DWI at diagnosis and following neo-adjuvant chemotherapy at Birmingham Children's Hospital between 2012 and 2016 were included. Patients were recruited prospectively following presentation during the study period and retrospectively after searches of computerized records.

6.2.2. Magnetic resonance imaging acquisition

MRI was conducted at diagnosis and following chemotherapy using a 1.5T scanner following the imaging protocol described in Chapter 3, Methods. DWI was acquired using between two and six b-values (b = 0, 50, 100, 150, 600, 1000 s/mm^2), with a total scan duration ranging from 1 min 37 sec to 7 min 32 sec.

6.2.3. Image analysis

Whole tumour (WT) ROIs were drawn manually around the solid tumour on pre- and post-treatment images in MIROR (Zarinabad et al., 2018) and refined by a consultant radiologist (KF, 10 years' experience). MIROR was adapted to allow comparison of tumours and ADC histograms before and after treatment through ROI construction on serial images, with

superimposition of pre and post treatment histograms allowing response assessment through visual comparison of shift and change in shape.

6.2.4. Calculation of ADC and IVIM Modeling

Post-processing was performed in MIROR, with IVIM modelling conducted for all cases in which six b-values had been acquired to allow calculation of D and f parameters. Advanced histogram analysis of the ROI overlaid on parametric maps was performed. Tumour volume, ADC and IVIM parameter median, 15^{th}, 25^{th} and 75^{th} centiles, skewness, kurtosis and entropy were calculated and compared for each case to determine the most useful parameters for clinical use in monitoring chemotherapeutic response.

Tumour response was categorized using RECIST criteria (Eisenhauer et al., 2009) according to conventional imaging parameters. The volume of highly malignant tumour was calculated as the volume of tissue with median ADC values $<1.01 \times 10^{-3}$ mm^2/s, a cut-off determined from earlier work on ADC regarding histogram characteristics of benign and malignant lesions described in Chapter 4. Differences in total and highly malignant tumour volume, quantitative ADC and IVIM values and histogram parameters before and after chemotherapy were calculated and compared.

6.2.5. Statistical analysis

Comparisons of pre- and post-chemotherapy ADC and IVIM histogram parameters were performed using the Wilcoxon signed-rank test, with significance taken as $p<0.05$. Spearman rank correlation ascertained correlations between change in total and highly malignant tumour volume and individual histogram parameters. Pre-treatment ADC and IVIM

parameters and change in tumour volume and histogram parameters in patients who had died and survivors were compared. The highly malignant tumour volume pre- and post-chemotherapy was compared and reviewed in the context of clinical course. Patients were considered individually to determine the added value of ADC and IVIM histogram analysis in specific clinical scenarios.

6.3. Results

6.3.1. Patient demographics and imaging

A computerized search of medical records identified 29 children (15 males, 14 females) with solid malignant tumours who had undergone MRI with multi b-value DWI at diagnosis and following induction chemotherapy. Children recruited to the study were aged between 2 months and 9.26 years (median, 3.53 years). IVIM analysis was performed on all but one patient for whom post-treatment DWI did not include all 6 b-values. Demographic information is shown in table 6.1.

Table 6.1. Demographic data of all patients

Lesion	Cases	Median age, range (yrs)	Sex (F/M)
Malignant Tumours	**29**	**3.53 (0.2-9.26)**	**15/14**
Clear cell sarcoma	1		
Ewing's sarcoma	1		
Hepatoblastoma	4		
Rhabdomyosarcoma	5		
Wilms tumour	8		
Neuroblastoma	10		

Children were imaged at diagnosis and following neo-adjuvant chemotherapy with a median time interval of 76 days (range 41-224 days) between scans. An example MIROR output for superimposition of pre- and post-treatment histograms for a Wilms tumour, demonstrating shift to the right with treatment, is shown in Figure 6.1.

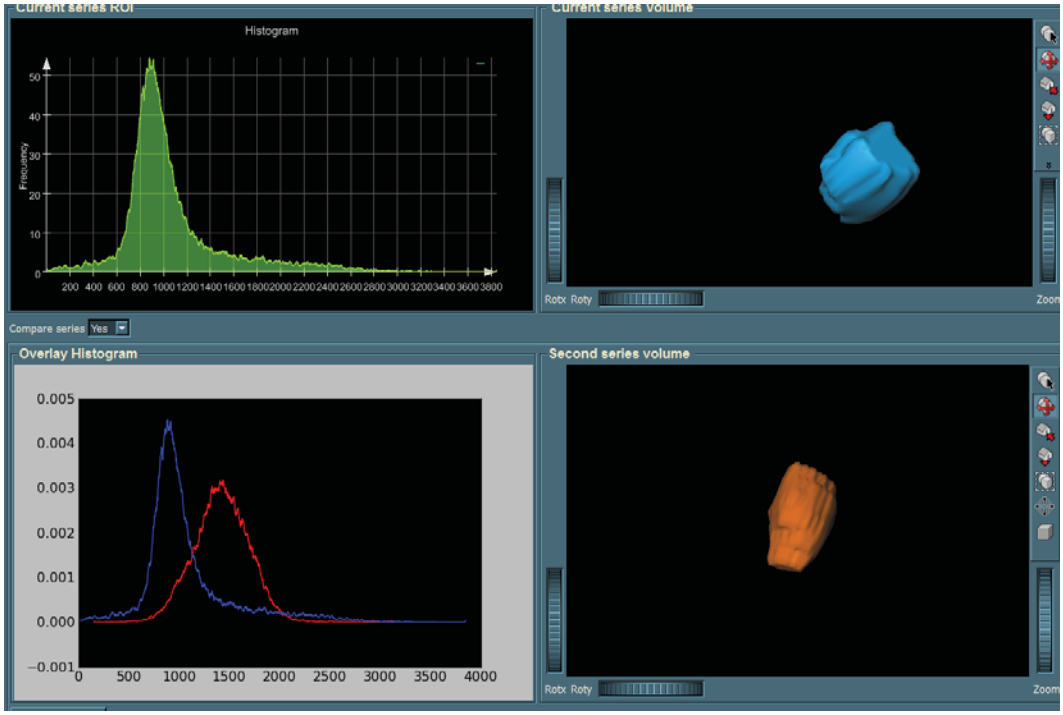

Figure 6.1. MIROR output showing superimposition of pre- (blue) and post-treatment (red) histograms (Wilms Tumour) (bottom left). The pre-treatment histogram (top left), pre-treatment volume (top right) and post-treatment volume (bottom right) are also displayed on this GUI.

A whole tumour region of interest (ROI) was drawn around diagnostic and post-treatment images of a Wilms tumour on a b0 image prior to overlay on a corresponding parametric apparent diffusion coefficient (ADC) map. The ADC histograms derived from pre- and post-treatment imaging were superimposed to allow visual comparison. In the example above, it can be seen that the post-treatment histogram (red) is morphologically different and shifted to the right compared to the pre-treatment histogram (blue).

6.3.2. Morphological observable differences in histogram shape

Morphological differences in shape were apparent when comparing histograms visually before and after chemotherapy. Histograms shifted to the right following chemotherapy corresponding to an increase in ADC values. This is shown in Figure 6.2, which demonstrates

the change in pooled ADC histogram shape for Wilms tumours, and was observed consistently across all tumour types.

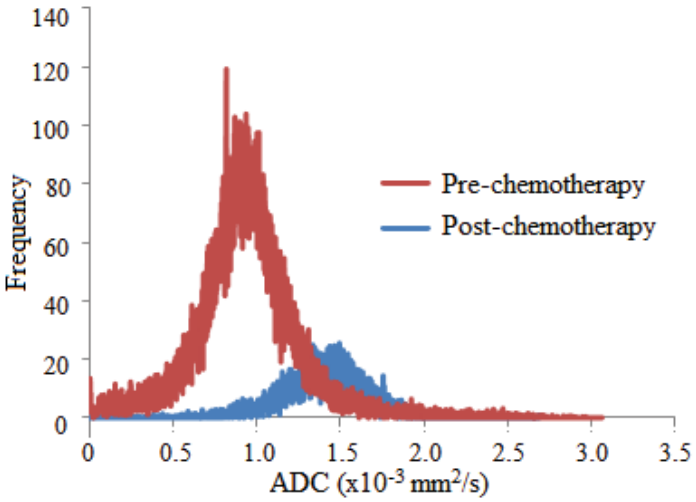

Figure 6.2. Change in pooled ADC histogram shape following chemotherapy (Wilms tumours). It can be seen that, compared with the pre-treatment histogram (red), the post-treatment histogram (blue) is shifted to the right in accordance with the corresponding increase in ADC values, with a reduction in kurtosis and a greater skew to the right.

Table 6.2. describes diagnosis, volume, pre- and post-chemotherapy ADC values, treatment and clinical outcome of included cases.

Table 6.2. Legend: RECIST Criteria: PR – partial response (>30% size reduction); CR – complete response (no residual tumour); SD – stable disease (<30% size reduction or <20% size increase); PD – progressive disease (>20% size increase); A – alive; D – died; Rapid COJEC: C=cisplatin, O=vincristine, J=carboplatin, E=etoposide, C=cyclophosphamide; IVADo: I=ifosfamide, V=vincristine, A=dactinomycin, Do=doxorubicin; VA: V=vincristine, A=dactinomycin; VIDE: V=vincristine, I=ifosfamide, D=doxorubicin, E=etoposide; Carbo/etop: Carboplatin, etoposide; ActinoD : Actinomycin D

Table 6.2. Diagnosis, volume, pre- and post-chemotherapy ADC values, treatment and clinical outcome

Diagnosis	Volume at diagnosis (ml)	Volume after treatment (ml)	Percentage volume change	RECIST response category	Pre-treatment median ADC ($x10^{-3}mm^2/s$)	Post-treatment median ADC ($x10^{-3}$ mm^2/s)	Percentage ADC increase	Treatment given	Clinical outcome
Hepatoblastoma	115	41	-63%	PR	1.11	1.37	+19%	Cisplatin x 2	A
Hepatoblastoma	779	106	-86%	PR	1.02	1.46	+30%	Cisplatin x 2	A
Hepatoblastoma	112	181	+61%	PD	0.95	1.42	+33%	Cisplatin x 2	A
Hepatoblastoma	307	21	-93%	PR	0.98	0.95	-3%	Cisplatin x 2	A
Neuroblastoma	917	86	-91%	PR	1.31	1.38	+5%	COadJEC x 8	A
Neuroblastoma	106	101	-5%	SD	0.96	0.85	-13%	Carbo/etop x 2	A
Neuroblastoma	551	66	-88%	PR	0.89	0.92	+3%	COJEC x 8	A
Neuroblastoma	178	17	-90%	PR	0.63	1.17	+46%	COJEC x 7	D
Neuroblastoma	337	181	-46%	PR	0.99	1.89	+48%	COJEC x 8	A
Neuroblastoma	204	62	-70%	PR	0.99	1.20	+18%	COJEC x 6	D
Neuroblastoma	249	6	-98%	PR/CR	0.79	0.66	-20%	COJEC x 8	A
Neuroblastoma	26	1	-96%	PR/CR	0.88	1.19	+26%	COJEC x 8	A
Neuroblastoma	27	2	-93%	PR/CR	0.75	1.17	+36%	Carbo/etop x 3	A
Neuroblastoma	425	8	-98%	PR/CR	1.06	1.28	+17%	COJEC x 6	D
Rhabdomyosarcoma	653	209	-68%	PR	1.02	1.12	+9%	IVADoVVx 2;IVADo x1	A
Rhabdomyosarcoma	385	41	-89%	PR	2.19	2.47	+11%	IVADoV x2;IVADo x 2	A
Rhabdomyosarcoma	13	0.5	-96%	PR/CR	0.72	1.03	+30%	IVAVVx 2; IVA x 1	A
Rhabdomyosarcoma	136	51	-63%	PR	1.39	1.70	+18%	IVAVV x 2; IVA x 1	A
Rhabdomyosarcoma	154	31	-80%	PR	0.93	0.80	-16%	VAVV x 3	A
Wilms	101	43	-57%	PR	0.95	1.27	+25%	AV x 1	D
Wilms	476	90	-81%	PR	0.68	1.19	+43%	VAV x 2	A
Wilms	1008	343	-66%	PR	1.05	1.63	+36%	VAV x 2	A
Wilms	1132	169	-85%	PR	1.18	1.03	-15%	Vinc+Dactino+Dox x1	D
Wilms	464	238	-49%	PR	0.74	0.98	+24%	VAV x 2	A
Wilms	542	35	-94%	PR	0.86	1.29	+33%	VAV x 1	A
Wilms	1037	193	-81%	PR	1.26	1.79	+30%	Vinc/ActinoD/Vincx1	A
Wilms	446	40	-91%	PR	0.89	0.99	+10%	Vinc/ActinoD/Vincx 2	A
Clear Cell Kidney	81	105	+30%	PD	0.69	1.41	+51%	Vinc+Dactin+Dox x1	A
Ewing's	105	21	-80%	PR	0.79	1.84	+57%	VIDE x 6	A

6.3.3. Changes in ADC histogram parameters following chemotherapy

ADC values following chemotherapy were significantly higher than at diagnosis. There were significant increases in ADC mean (+0.23 x 10^{-3} mm^2/s (0.13; 0.33)), ADC median (+0.31 $\times 10^{-3}$ mm^2/s (0.20; 0.42)), ADC 15% (+0.24 x $10^{-3}$$mm^2/s$ (0.15; 0.31)), ADC 25% (+0.29$\times 10^{-3}$ mm^2/s (0.17, 0.38)) (all $p<0.0001$) and ADC 75% (+0.24$\times 10^{-3}$ mm^2/s (0.11; 0.37)($p=0.001$)). Kurtosis decreased significantly by -0.11 (-0.19, -0.04) ($p=0.002$) and entropy by -0.20 (-0.39, -0.03) ($p=0.021$). The decrease in skewness of -0.0076 (-0.0187, 0.0016) did not reach significance ($p=0.08$). ADC and histogram parameters before and after chemotherapy are shown in Table 6.3, with median values across tumour types demonstrated in Table 6.4.

Table 6.3. Pre- and post-chemotherapy volume, ADC measurements and histogram parameters

Parameter	Pre-treatment (median and range)	Post-treatment (median and range)	Change (95% CI)	Significance
Volume* (ml)	307 (13-1132)	51 (0.5, 343)	-256 (-83%) (-156, -410)	<0.0001
Volume highly malignant* (ml)	208 (10-620)	17 (0.01-139)	-191 (-92%)	<0.0001
ADC Mean*	1.04 (0.78, 2.12)	1.27 (0.69, 2.43)	+0.23 (0.13, 0.33)	<0.0001
ADC Median*	0.95 (0.63, 2.19)	1.26 (0.66, 2.47)	+0.31 (0.20, 0.42)	<0.0001
ADC 15%*	0.62 (0.43, 1.54)	0.86 (0.58, 1.72)	+0.24 (0.15; 0.31)	<0.0001
ADC 25%*	0.75 (0.54, 1.79)	1.04 (0.45, 2.19)	+0.29 (0.17, 0.38)	<0.0001
ADC 75%*	1.24 (0.9, 2.49)	1.48 (0.90, 2.69)	+0.24 (0.11, 0.37)	=0.001
Skewness	0.0228 (0.0008, 0.0429)	0.0152 (-0.0379, 0.0474)	-0.0076 (-0.0187, 0.0016)	=0.08
Kurtosis*	2.21 (1.8, 2.25)	2.08 (1.8, 2.26)	-0.11 (-0.19, -0.04)	=0.002
Entropy*	7.17 (6.26, 7.84)	6.97 (4.94, 7.70)	-0.20 (-0.39, -0.03)	=0.021

ADC unit = x10^{-3} mm^2/s; * denotes significance ($p<0.05$)

Table 6.4. Change in volume and ADC parameters in individual tumour types

Change in Parameter	Hepato-blastoma (4)	Neuro-blastoma (10)	Wilms (8)	Rhabdo-myosarcoma (5)	Clear Cell (1)	Ewings (1)	Total
Volume (%)	-87%	-90%	-81%	-83%	+29%	-80%	-82%
Highly malignant volume (%)	-93%	-85%	-85%	-72%	-92%	-98%	-92%
ADC Median	+0.41	+0.21	+0.44	+0.28	+0.72	+1.04	+0.31
ADC 15%	+0.42	+0.24	+0.38	+0.26	+0.64	+1.02	+0.30
ADC 25%	+0.42	+0.27	+0.34	+0.22	+0.52	+1.03	+0.29
ADC 75%	+0.37	+0.02	+0.48	+0.19	+0.54	+0.60	+0.24
Skewness	-0.029	+0.0046	+0.0011	+0.0045	-0.0221	-0.0616	-0.0076
Kurtosis	-0.25	-0.11	-0.14	+0.01	-0.29	+0.06	-0.11
Entropy	-0.18	-0.39	+0.05	-0.18	-0.24	-0.36	-0.20

ADC unit = $x10^{-3}$ mm^2/s

6.3.4. Changes in IVIM histogram parameters following chemotherapy

Histogram parameters for IVIM D changed significantly following chemotherapy. IVIM D percentile values were significantly higher following chemotherapy than at diagnosis, with significant increases in median ($p<0.0001$), 15^{th} ($p<0.0001$), 25^{th} ($p<0.0001$) and 75^{th} centile ($p<0.0001$) D. Significant reductions were seen in kurtosis ($p=0.002$) and skewness ($p=0.016$), and although entropy also decreased this did not reach significance ($p=0.168$). IVIM f parameters did not change significantly following chemotherapy. Median changes in ADC, IVIM D and f histogram parameters are shown in Table 6.5.

Table 6.5. Changes in ADC and IVIM histogram parameters following chemotherapy

Change Following Chemotherapy	ADC (n=29)	D (n=28)	f (n=28)
Mean	0.23 (<0.0001)	0.22 (<0.0001)	2.53 (=0.108)
Median	0.31 (<0.0001)	0.32 (<0.0001)	2.5 (=0.13)
15%	0.30 (<0.0001)	0.28 (<0.0001)	2.0 (=0.18)
25%	0.29 (<0.0001)	0.24 (<0.0001)	1.0 (=0.178)
75%	0.24 (=0.001)	0.26 (<0.0001)	4.0 (=0.122)
Skewness	-0.0076 (=0.08)	-0.01033 (=0.016)	0.004904 (=0.223)
Kurtosis	-0.11 (=0.002)	-0.15 (=0.002)	0.03 (=0.114)
Entropy	-0.20 (=0.021)	-0.12 (=0.168)	0.004 (=0.223)

ADC unit = $x10^{-3}$ mm^2/s; f = %

6.3.5. Relationship of ADC and IVIM histogram parameters to volume change

Median tumour volume decreased significantly after chemotherapy by 83% (256ml) from 307 to 51ml (range 98% reduction to 62% increase) ($p<0.0001$). The median volume of highly malignant tumour defined as ADC <1.01 $x10^{-3}mm^2/s$ also decreased significantly by 92% (191ml) from 208 (range 10.2-620mls) to 17ml (range 0.01ml-139ml) ($p<0.0001$). There was no correlation between change in total or highly malignant tumour volume and change in ADC or IVIM histogram parameters.

6.3.6. Relationship of change in volume, ADC and IVIM parameters to survival

In this cohort, 5 patients died and 24 survived: these are small numbers and groups are very unbalanced so observations pertaining to survival should be interpreted cautiously. Survival outcome was not related to change in volume, RECIST criteria, or change in ADC or IVIM parameters. Reduction in overall tumour volume was categorised as PR on RECIST criteria in all 5 patients who died. Of 24 surviving patients, 21 had PR, 1 had SD and 2 had PD. ADC or IVIM histogram parameters were not significantly different between those who died and those who survived as demonstrated in Table 6.6.

Table 6.6 Change in volume and ADC histogram parameters in survivors and non-survivors

Outcome (n)	Δ ADC median	Δ ADC 15%	Δ ADC 75%	Δ Skewness	Δ Kurtosis	Δ Entropy	Δ Volume	Δ Volume highly malignant	RECIST category
Survived (24)	0.31	0.33	0.31	-0.00522	-0.16	0.03	-81%	-92%	PR=21 SD=1 PD=2
Died (5)	0.38	0.31	0.35	0.00029	-0.12	-0.26	-87%	-95%	PR=5
P value	0.62	0.49	0.90	0.76	0.80	0.32	0.85	0.53	N/A

ADC unit = $x10^{-3}$ mm^2/s

6.3.7. Change in highly malignant tumour volume and ADC histogram parameters in RECIST-defined progressive disease

Progression according to RECIST criteria with increase in total tumour size was observed in two patients. One was a hepatoblastoma that increased in volume by 39% from 112 to 182ml, the other a clear cell sarcoma of the kidney, which enlarged by 23% from 81 to 105ml. The size increases were interpreted as tumour progression and prompted intensification of treatment followed by surgical resection.

Superimposition and visual comparison of the ADC histograms obtained before and after chemotherapy (Figure 6.3) reveals marked morphological changes suggestive of evolution of imaged tissue. Quantitative ADC histogram analysis revealed that although total tumour volume increased, in both cases the volume of highly malignant tumour characterised by ADC <1.01 $x10^{-3}$ mm^2/s decreased prior to treatment intensification. There was a reduction in the highly malignant component of hepatoblastoma by 71% from 79 to 23ml, while the highly malignant sector of clear cell sarcoma decreased by 92% from 66 to 5.3ml. Both tumours demonstrated an increase in ADC values suggestive of oncological response with respective increases in median ADC of 0.47 and 0.72 $x10^{-3}$ mm^2/s. Both patients remain well and are in remission two years after completion of treatment.

Figure 6.3. Pre- and post-treatment histograms of **a)** hepatoblastoma and **b)** clear cell sarcoma of the kidney with RECIST-defined progression on treatment.

a. Hepatoblastoma

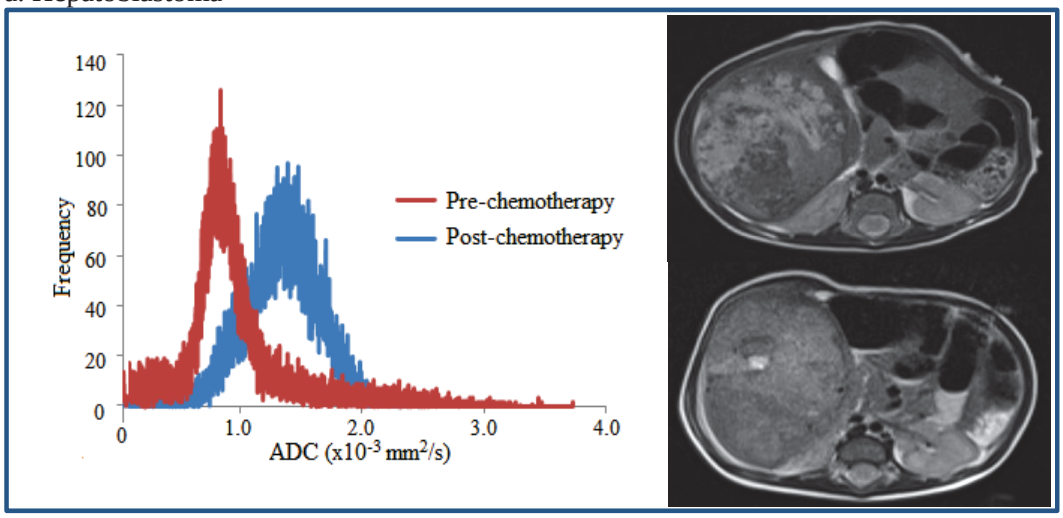

a) The hepatoblastoma increased in volume by 39% during neo-adjuvant chemotherapy. ADC histogram analysis revealed a 71% reduction in the highly malignant tumour component, characterised by ADC <1.0 x$10^{-3}$$mm^2$/s, from 79 to 23ml. There was a corresponding increase in ADC median of 0.47 x$10^{-3}$$mm^2$/s.

b). Clear Cell Sarcoma of Kidney

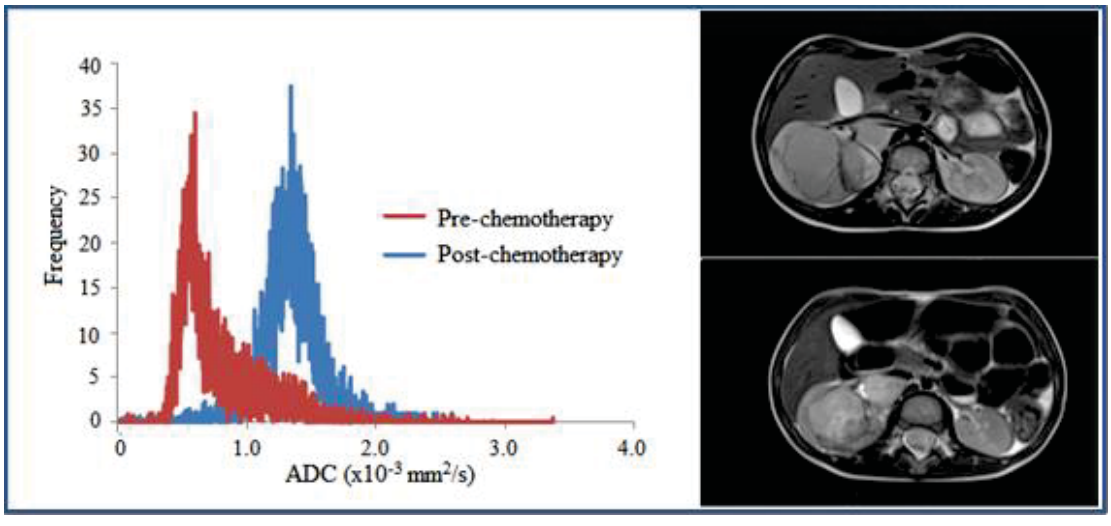

b) The clear cell sarcoma of the kidney enlarged by 23% during induction chemotherapy. There was a decrease in the highly malignant tumour component by 92%, from 66 to 5.3ml. The median ADC increased by 0.72 x$10^{-3}$$mm^2$/s.

6.4. Discussion

This work suggests ADC and IVIM histogram analysis have potential to provide promising non-invasive biomarkers of oncological response in solid paediatric tumours. Analysis revealed observable visual changes in histogram shape and significant quantitative differences in histogram parameters following treatment, including increases in ADC and D. Presenting this complex data through MIROR made it accessible and visually interpretable to clinicians, suggesting this decision support system may facilitate future integration of advanced quantitative imaging into clinical paediatric practice.

Visual comparison of histograms obtained at diagnosis and after treatment revealed marked morphological differences in shape and a shift to the right corresponding to oncological response. The quantitative changes in histogram parameters related to shape and significant decreases in kurtosis and entropy were clearly apparent visually. Research in adults assessing early treatment response in cervical cancer also demonstrated observable visual changes in ADC histogram shape and significant quantitative differences in histogram parameters (Meng et al., 2017) including decreases in skewness, kurtosis and entropy (Meng et al., 2016). Presenting this complex quantitative information in a clear and visual way to radiologists via MIROR through provision of comparative pre- and post-treatment histograms could facilitate incorporation of ADC histogram analysis into clinical practice, providing an additional tool for non-invasive evaluation of treatment response.

Evidence in the literature suggests ADC and DWI reflect chemotherapeutic response in individual categories of childhood solid tumours (Demir et al., 2015; Neubauer et al., 2017; Oka et al., 2010). This study provides additional evidence that these ADC histogram analysis-derived biomarkers show similar properties across multiple tumour types. The

significant increase in median ADC in this cohort corresponds to findings of two pediatric studies showing a similar rise in neuroblastic tumours (Demir et al., 2015; Neubauer et al., 2017). It also supports findings of studies showing significant increase in median ADC in a paediatric abdominal tumours, (McDonald et al., 2011), significantly higher average and minimum ADC in osteosarcoma after chemotherapy (Oka et al., 2010), and reports of positive shift in mean ADC in histogram analysis of stromal-type Wilms tumours following treatment (Hales et al., 2015).

IVIM is a relatively new technique that has not been particularly studied in paediatric oncology. There are no reports of the value of IVIM histogram analysis in monitoring chemotherapeutic response in children. The observation that IVIM D behaved in a similar way to ADC suggests short acquisition and a mono-exponential fitting model is sufficient for clinical use. This finding is important for integrating quantitative DWI into clinical practice as it is quicker and easier to obtain data using only 2 b-values than it is to perform multi b–value DWI and analysis with bi-exponential fitting. Data acquisition with a shorter scanning time improves clinical applicability and feasibility of use in the paediatric population.

IVIM f did not change significantly following chemotherapy. This is interesting as decrease in tumour vascularity with treatment should equate to a reduction in f, which relates to the tissue perfusion fraction. The f parameter is, however, dependent on factors other than vascularity, being also influenced by tissue heterogeneity and complex interactions within the microcirculatory network (Le Bihan., 2017). Chemotherapeutic response is characterised by an increase in heterogeneity that has an opposing effect to vascularity on f and may explain the lack of change observed. Studies of IVIM in cervical cancer found significant differences in ADC and D, but not D* or f, between responders and non-responders (Wang et al., 2016).

Understanding the exact meaning of f and the factors that influence it requires further research.

It was not possible to characterise chronological changes in ADC or IVIM parameters in this study as patients were imaged for a second time after an average of 71 days of treatment. It has been reported that ADC and D increase throughout chemo-radiotherapy, whereas f and D* increase initially before a later decrease at around 4 weeks into treatment (Zhu et al., 2017). It is possible that an early increase in f occurred in patients in this study and was negated by a later decrease. As patients were scanned as part of routine management additional early imaging to observe trends was not feasible, but further research including serial imaging could be conducted to investigate this further.

Novel imaging biomarkers provide additional information to change in tumour size which could be helpful clinically in terms of monitoring treatment response and adjusting treatment accordingly (Therasse et al., 2000). Absence of correlation with volume change suggests ADC and IVIM histogram parameters reflect different underlying tumour properties and could potentially be used in a multivariate model as independent markers of treatment response. Size reduction has limitations as a surrogate response marker (Olsen, 2015). Measurement of tumour size is relatively crude and error prone (Husband et al., 2004) and shrinkage does not always translate to improved survival. Change in tumour volume in patients in this study did not differ between survivors and non-survivors, although it must be noted that nor did any DWI histogram parameters. Tumour shrinkage generally occurs late and is relatively insensitive to early treatment effects (Miller et al., 1981). ADC, either assessed through visual interpretation of histograms or as quantitative measurements, may be a valuable early response marker as increases precede change in size (Kocaoglu and

Bulakbasi, 2016). As some tumours respond to chemotherapy through differentiation rather than shrinkage, size reduction does not always equate to treatment response. Additionally, novel agents developed to target specific metabolic pathways rather than resulting in size reduction require different measures of efficacy (Harry et al., 2010).

There was no correlation between changes in ADC and IVIM histogram parameters and reduction in tumour volume. This substantiates earlier research demonstrating no correlation between volume reduction and ADC increase in neuroblastic tumours (Demir et al., 2015). The tumour properties reflected by DWI and tumour volume may be different, with potential for development of a multivariate model incorporating quantitative DWI in combination with size and tumour-specific markers to provide an accurate overall reflection of response.

A reduction in the highly malignant component of a tumour could occur with treatment while overall volume remains unchanged. Tumours are heterogeneous masses comprised of highly malignant tissue interspersed with other components such as stroma, necrotic tissue and cystic regions. Tumour response apparent through change in cellular composition would not be reflected through size measurement. Following review of the literature (Gahr et al., 2011; Kocaoglu and Bulakbasi, 2016; Gawande et al., 2013) and work previously described in this thesis differentiating benign from malignant tumours, an ADC cut-off of 1.01 $x10^{-3}mm^2/s$ was selected to calculate the volume of highly malignant tissue within a tumour. ADC histogram analysis demonstrated a reduction in highly malignant tumour volume in all patients in this cohort. Interestingly, the volume of highly malignant tumour decreased in both patients who demonstrated an overall increase in tumour size on treatment, with both ADC histograms demonstrating a characteristic shift to the right and morphological change in shape following chemotherapy. Both children did well clinically, suggesting treatment was

effective despite this initial tumour growth. This suggests a potential role for ADC histogram analysis in the further investigation of patients with apparent tumour progression according to size criteria prior to treatment intensification.

This small single centre study has demonstrated promising results for ADC and IVIM histogram analysis as potential imaging biomarkers of chemotherapeutic response in paediatric solid tumours. There are, however, limitations and larger, prospective, well-powered studies with longer follow-up times are necessary to provide outcome data and information about clinical utility (McShane et al., 2005). The sample size in this study was small and the cohort consisted of a wide mix of tumour types. Survival could not be used as an outcome measure as treatment was generally effective with few deaths and longitudinal data available is insufficient. It is very possible that early changes in ADC and IVIM parameters were missed given the long time interval between diagnostic and follow-up imaging: further work incorporating serial scans would be helpful to explore chronological changes more fully. It was not possible to explore correlations between post-treatment histopathology and histogram parameters or volume change. There is no standardised way of reporting histopathological response across several tumour types, and although histological interpretation was attempted data procured were unfortunately insufficient for meaningful analysis. Further research including robust measures of histopathological response should be performed.

6.5. Conclusion

This study has demonstrated that visual ADC histogram interpretation and quantitative ADC and IVIM histogram analysis are promising non-invasive biomarkers of chemotherapeutic response of childhood solid tumours, conferring additional information to that obtained

through measuring change in size to facilitate clinical decision-making. The imaging parameters analysed show similar properties across a range of paediatric tumour types. This technique can easily be applied in a clinical setting as most important information can be obtained through short image acquisition. The CDSS MIROR allowed clinicians to interpret, analyse and compare MR images and complex ADC and IVIM histogram data in an accessible and comprehensible way.

Chapter 7: Inter-Rater Variability of Different Methods of ROI Construction for ADC Histogram Analysis

7.1. Introduction

The optimum method for determining a Region of Interest (ROI) for quantitative ADC histogram analysis has not yet been established in the literature. Some studies have included the entire tumour volume with and without cystic (Kocaoglu et al., 2010; Abdel Razek et al., 2009; Humphries et al., 2007) and necrotic (Littooij et al., 2015; McDonald et al., 2011) areas, others have drawn several small ROIs in the solid component of a tumour (Gawande et al., 2013; Oka et al., 2010), and drawing a single ROI around the largest axial slice has also been proposed. It is important to determine a robust methodology of ROI construction that is clinically applicable, reproducible and that provides representative information about tissue characteristics of a lesion.

The previous chapters have used whole tumour (WT) ROIs for ADC histogram analysis, ensuring maximum sampling of tumour regions. In theory, histogram analysis from a WT ROI should reflect heterogeneity better than selective sampling (Woo et al., 2014a), with "fitting" of histogram peaks allowing characterization of the various composite tissue types within a lesion. Constructing a WT ROI is, however, labour intensive and time consuming, making application difficult in a busy clinical setting. Drawing a single ROI around the largest single axial slice (SS) would be more practical and applicable clinically if found to yield similar results. Drawing small ROIs drawn in the solid tumour component may be influenced by sampling bias and would only convey information about regions demonstrating the most restricted diffusion.

Assessment of inter-rater variability is important to ascertain the reproducibility and validity of results obtained from different methods of ROI construction. Studies have demonstrated excellent intra- and inter-rater reliability of ADC measurement from whole tumour (WT)

ROIs (Jerome et al., 2016; Littooij et al., 2015), but there is little evidence for reproducibility of ADC histogram parameters derived from other methods of ROI construction.

This chapter explores the inter-rater variability of whole tumour (WT) and single slice (SS) ROIs, and the variability of ADC histogram parameters obtained by the two different construction methods. The aim is to formulate recommendations for the optimum ROI methodology for ADC histogram analysis of paediatric solid tumours in clinical practice.

7.2. Methods

7.2.1. Patients

A representative sample of patients with malignant and benign tumours was selected from those previously recruited for the study carried out in Chapter 4.

7.2.2. MRI and DWI acquisition

Patients underwent 1.5T MR examination with DWI using the imaging protocol described in Methods, Chapter 3.

7.2.3. Image analysis and assessment of inter-observer variability of whole tumour and single slice ROIs

For each patient, whole tumour (WT) ROIs were drawn around the entire solid tumour on high-resolution b0 images using MIROR by two consultant radiologists (KF, 10 years' experience; SA, 1 year experience) and overlaid on matched ADC maps. Single slice (SS)

ROIs were then drawn around the largest axial tumour slice. Each radiologist was blind to the ROIs drawn by the other.

ADC histogram parameters (median, 15^{th}, 25^{th}, 75^{th} and 95^{th} percentile ADC) derived from WT and SS ROIs from the two radiologists were compared to assess inter-rater variability. These parameters were selected for comparison as they represent the distribution of histogram values obtained from an ROI and are widely reported in the literature. Variability between methods was determined through comparing ADC histogram parameters obtained from WT with those derived from SS ROIs.

7.2.4. Statistical analysis

To assess significance of variability of histogram parameters produced by the two radiologists, comparison of not normally distributed data (median, 15^{th}, 25^{th}, 75^{th} and 95^{th} percentile ADC) was performed using the Wilcoxon test. The non-parametric Friedman test was used on ADC parameters to compare the WT and SS methods for each radiologist separately, and on differences between radiologists' results to determine any interaction between method and inter-rater variability. ADC histogram parameters of benign and malignant tumour groups determined from WT and SS ROI construction were compared using the Mann–Whitney U test using averages of the two radiologists' values. Statistical significance was taken as $p < 0.05$.

Bland-Altman plots with limits of inter-observer agreement (mean difference +/- 1.96 x standard deviation) were constructed to analyse ADC histogram parameter reproducibility between radiologists and WT and SS methods of ROI construction.

7.3. Results

7.3.1. Patient demographics

A representative sample of 20 patients with malignant and 12 with benign tumours were selected for this study. Demographic data is shown in Table 7.1.

Table 7.1. Demographic data of all patients

Tumour	Median age, years (range)	Gender	Diagnosis	Patients, n
Benign	3.82 (0.03-14.22)	F=6; M=6	Liver haemangioma	1
			Ganglioneuroma	3
			Mesoblastic nephroma	2
			Lipoma	1
			Infantile myofibromatosis	1
			Haematocolpos	1
			Vascular malformation	1
			Ovarian immature teratoma	1
			Abscess	1
			Total	**12**
Malignant	3.19 (0.03-11.82)	F= 8; M= 12	Wilms' tumour	5
			Neuroblastoma	5
			Hepatoblastoma	4
			Rhabdomyosarcoma	3
			Rhabdoid	2
			Germ cell	1
			Total	**20**

.

7.3.2. Inter-rater variability between radiologists for ADC histogram parameters obtained using WT and SS ROIs

There were no statistically significant differences between radiologists for any ADC parameter for either whole tumour or single slice ROIs (Wilcoxon Signed Rank Test). Table 7.2 shows the median inter-radiologist difference and 95% confidence intervals for each ADC histogram parameter both as an absolute value and as a percentage of the median, demonstrating the radiologists differed by at most 2% for any characteristic with no significant differences.

Table 7.2. The inter-radiologist difference (+ 95% CI) for each ADC histogram parameter, both as an absolute value and as a percentage of the median (n=32)

Sample	Absolute difference	Percentage difference	p-value
Whole Tumour			
ADC median	0.0193 (-0.0435, 0.0035)	1.4 (-4.59, 0.716)	0.114
ADC 15%	0.0123 (-0.0395, 0.0125)	1.18 (-4.64, 1.60)	0.385
ADC 25%	0.0145 (-0.041, 0.007)	1.27 (-4.59, 0.95)	0.250
ADC 75%	0.008 (-0.047, 0.0415)	0.45 (-4.30, 3.03)	0.594
ADC 95%	0.004 (-0.081, 0.0625)	0.09 (-4.99, 3.40)	0.874
Single Slice			
ADC Median	0.0035 (-0.017, 0.0075)	0.29 (-2.15, 0.55)	0.524
ADC 15%	0.004 (-0.0205, 0.0075)	0.39 (-2.48, 0.92)	0.495
ADC 25%	0.0035 (-0.0165, 0.0075)	0.31 (-1.89, 0.79)	0.484
ADC 75%	0.0005 (-0.0255, 0.0145)	0.12 (-1.75, 1.03)	0.801
ADC 95%	0.003 (-0.0385, 0.017)	0.21 (-2.12, 0.76)	0.645

The unit for ADC value is x 10^{-3} mm^2/s.

7.3.3. Variability between ADC histogram parameters obtained following WT and SS methods of ROI construction

The ADC histograms for individual tumours obtained using either a WT or a SS ROI appeared visually identical (Figure 7.1). The Friedman test revealed no significant differences between any ADC parameters obtained using single slice and whole tumour methods for either radiologist ($p>0.05$). There was no interaction between inter-rater difference and method ($p >0.05$).

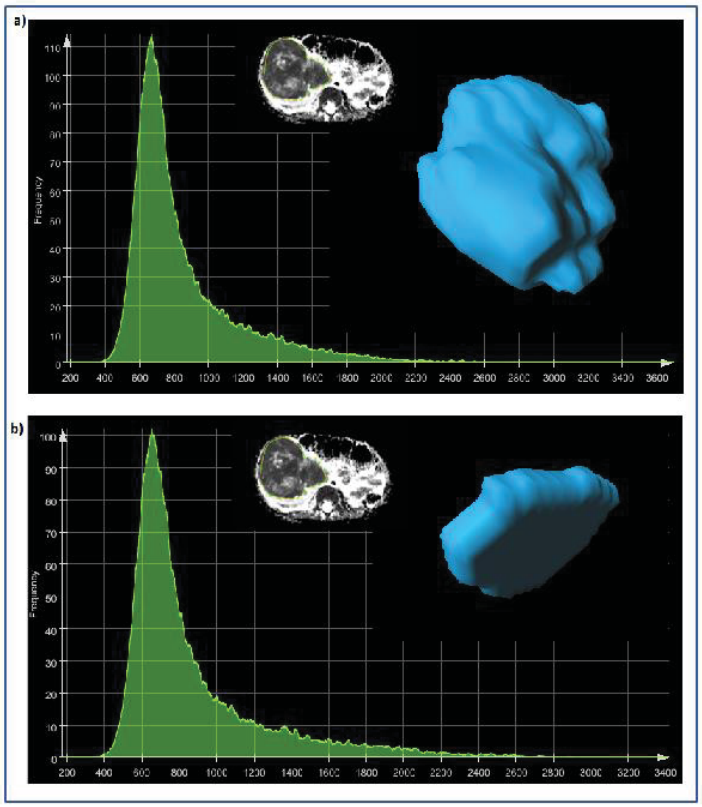

Figure 7.1. ADC histograms obtained using WT (a) and SS (b) ROIs for an individual tumour (Wilms tumour), demonstrating almost identical appearance of the two histograms.

Table 7.3. The difference between ADC parameters obtained using WT and SS ROIs for the two radiologists (n=32)

	ADC Median		**ADC 15%**		**ADC 25%**		**ADC 75%**		**ADC 95%**	
	Rad 1	Rad 2	Rad 1	Rad 2	Rad 1	Rad 2	Rad 1	Rad 2	Rad 1	Rad 2
WT	1.08	1.12	0.81	0.77	0.89	0.89	1.48	1.44	2.03	1.95
SS	1.08	1.11	0.81	0.76	0.88	0.88	1.47	1.44	2.02	1.95
P-value	0.86	0.48	0.724	0.07	0.74	0.07	0.48	0.72	0.48	0.59

The unit for ADC value is x 10-3 mm2/s.

7.3.4. Time taken to draw WT and SS ROIs

The average time taken to draw a WT ROI was 10.6 minutes (range 2.3 to 15.9 minutes), whereas SS ROIs were drawn in an average time of 34 seconds (range 24 seconds to 1.3 minutes). Constructing ROIs around small, discrete, homogeneous lesions (e.g. lipoma) was less time consuming than constructing ROIs around large, diffuse, heterogeneous masses (e.g. neuroblastoma)

7.3.5. Differences in ADC histogram parameters obtained using WT and SS ROIs between benign and malignant tumours

The different ADC parameters obtained using WT and SS ROIs between Benign and Malignant tumour groups were compared (Mann-Whitney Test), using averages of the values obtained by the two radiologists. For both methods of ROI construction, there were strongly significant differences in all ADC parameters between benign and malignant tumours, other than 95% ADC.

Table 7.4. The difference between ADC parameters obtained using WT and SS ROIs for Benign and Malignant tumour groups (n = 64)

	ADC Median		**ADC 15%**		**ADC 25%**		**ADC 75%**		**ADC 95%**	
	WT	SS	WT	SS	WT	SS	WT	SS	WT	SS
Benign	1.55	1.56	1.13	1.17	1.27	1.36	1.67	1.67	1.90	1.98
Malignant	1.03	1.02	0.74	0.72	0.83	0.81	1.33	1.36	1.98	1.97
P-value	0.009	0.004	0.024	0.043	0.011	0.014	0.039	0.02	0.48	0.755

The unit for ADC value is x 10-3 mm2/s.

7.3.6. Bland-Altman Analysis

Bland-Altman analysis showed that inter-rater reproducibility and reproducibility of the two different methods of ROI construction were acceptable for all ADC histogram parameters. This is demonstrated in Figure 7.2 using the representative example of Median ADC.

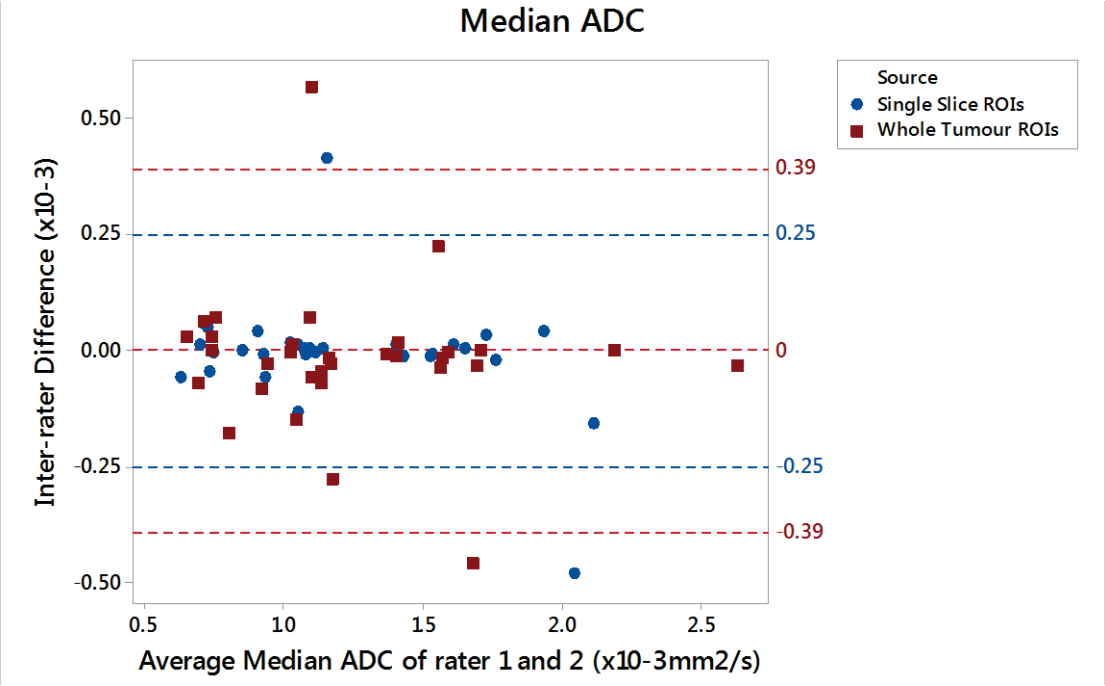

Figure 7.2. Bland-Altman plot of inter-rater difference versus average median ADC of the two radiologists for WT and SS ROIs

Inter-rater agreement and agreement between methods of ROI construction were good, with all but four cases falling within the limits of agreement. There was no significant correlation between Mean Difference and Median ADC of raters 1 and 2 (Pearson correlation -0.217, p = 0.085).

The four cases that fell outside the limits of inter-rater agreement (mean difference +/- 1.96 x standard deviation) were a SS and WT vascular malformation, a SS mesoblastic nephroma, and a WT ganglioneuroma. The vascular malformation and ganglioneuroma were very small lesions (26 mls and 3.4 mls respectively, compared with a mean overall tumour volume of

378 mls). The two radiologists drew the SS mesoblastic nephroma differently, as one included an area the other did not feel was representative of tumour within the ROI.

7.4 Discussion

This study suggests ADC histogram parameters obtained using quantitative DWI are reproducible, user-independent, robust to methodology of ROI construction, and provide information about tissue characteristics of the imaged lesion. Inter-rater reproducibility of both WT and SS ROIs was excellent, with no significant difference in any ADC histogram parameter between radiologists using either method. The virtually identical visual appearance in ADC histograms, and lack of observed significant difference between histogram parameters obtained using WT and SS ROIs, suggest these two methods provide essentially equivalent results and may be interchangeable. ADC histogram parameters of benign and malignant tumours obtained by both radiologists were significantly different using both WT and SS ROIs, suggesting tumour classification as benign or malignant would be unaffected by radiologist or method of ROI construction.

It is important to formulate recommendations for the optimum method of ROI construction for clinical use of quantitative DWI given the heterogeneity of methodology described in the literature. The high inter-rater reproducibility of ADC histogram parameters concurs with reports of WT ROI reproducibility (Jerome et al., 2016; Littooij et al., 2015), and provides reassuring evidence that accurate results may be obtained from different raters. Constructing WT ROIs is labour-intensive, taking our radiologists on average 10.6 minutes but up to 15.9 minutes to draw, which could be a barrier to implementation in a busy clinical setting. Employing simpler methods of ROI construction, such as single slice axial (SS) ROIS, which are easier and less time-consuming to construct (taking 34 seconds on average), would

improve practical applicability. Our finding that SS ROIs are reproducible and provide similar information to WT ROIs has important implications for clinical practice.

The only histogram parameter that was not significantly different between benign and malignant tumours was 95th percentile ADC, obtained by both WT and SS ROIs. This reflects findings described in Chapter 4, and makes biological sense as ADC parameters reflecting the extreme right of the histogram represent more cystic tumour components, whereas the lower ADC percentile values at the left of the histogram reflect the more highly malignant tumour component.

It is important to consider cases for which ADC histogram parameters were not reproducible to understand the limitations of these techniques. Of the four cases that fell outside the Bland-Altman defined limits of inter-rater agreement, two were WT ROIs and two SS, suggesting that one method of ROI construction is not inherently less reproducible than the other. The three tumours involved were a vascular malformation (WT and SS), mesoblastic nephroma (SS) and ganglioneuroma (WT). The comparatively small size of the vascular malformation and ganglioneuroma may have contributed to the variability in parameters produced. The mesoblastic nephroma was complex and difficult to characterise, with the two radiologists interpreting the tumour margins differently when constructing the SS ROI. This indicates that caution should be exercised when reviewing results from small or complex tumours, and the limitations of ROI construction in these scenarios should be reviewed further.

7.5. Conclusions

Inter-rater reproducibility of both WT and SS ROIs is excellent, and ADC histogram parameters derived from SS or WT ROIs do not differ significantly. The significant

differences between ADC histogram parameters of benign and malignant lesions were apparent across raters and methods. In view of these findings, we recommend construction of a single ROI around the largest axial tumour slice to obtain a preliminary ADC histogram and quantitative ADC histogram parameters for clinical use. As this technique is relatively quick, user-independent and clinically applicable, use of SS ROIs may facilitate integration of advanced DWI and ADC histogram analysis into routine clinical practice in the future.

Chapter 8: Diagnostic Accuracy and Added Value of Qualitative Radiological Review of MRS in Evaluation of Childhood Brain Tumours

8.1. Introduction

Magnetic Resonance Imaging (MRI) is the standard imaging investigation for children with a suspected brain tumour, but there is paucity of evidence for its diagnostic accuracy (Orphanidou-Vlachou et al., 2013; Panigrahy et al., 2006). Conventional MRI cannot always allow accurate identification of tumour type or grade (Panigrahy et al., 2010; Arle et al., 1997; Panigrahy et al., 2006; Law et al., 2003; Orphanidou-Vlachou et al., 2013; Shiroishi et al., 2015) or conclusive differentiation of neoplastic from indolent lesions (Panigrahy and Bluml, 2009; Panigrahy et al., 2010; Moller-Hartmann et al., 2002). Definitive diagnosis is currently made by histopathology following biopsy or surgical resection (Louis et al., 2007). Accurate early non-invasive diagnosis could improve patient care through guiding surgical decision-making, allowing timely treatment planning and informing family discussions.

Magnetic Resonance Spectroscopy (MRS) has potential to improve diagnosis and characterisation of brain tumours through non-invasive measurement of metabolite profiles (Panigrahy et al., 2006; Davies et al., 2008; 2010b). Pathologically different tumour types that appear morphologically similar on MRI display different key metabolic features on MRS (Hollingworth et al., 2006; Preul et al., 1996; Panigrahy et al., 2010). MRS is not currently used routinely in all paediatric centres, partly as there has been little formal evaluation of diagnostic utility, and few radiologists are trained in its quantitative evaluation.

Despite evidence for technical feasibility and diagnostic accuracy (Davies et al., 2008; Wang et al., 1995; Vicente et al., 2013; Arle et al., 1997), few studies have evaluated how MRS can add value to conventional paediatric radiological reporting (Shiroishi et al., 2015). Prospective studies of the added diagnostic value of MRS in paediatric oncology are lacking, with little systematic comparison with conventional MRI. Research is needed to evaluate the

diagnostic impact and added value of MRS over MRI alone in this patient population and integrate the technique into the diagnostic pathway. Exploring methods of MRS interpretation that may be adopted by radiologists without complicated quantitative interpretation or sophisticated computer software could facilitate incorporation into clinical practice.

The aim of this chapter was to evaluate prospectively the added diagnostic value of MRS in combination with conventional radiological reporting in children's brain tumour diagnosis in routine clinical practice. A further objective was to determine whether MRS is equally helpful for all brain tumour types and identify clinical scenarios with potential to improve patient care.

8.2 Methods

8.2.1. Participants

Children <16 years of age presenting to Birmingham Children's Hospital between December 2015 and 2017 with radiological features suggestive of a brain tumour were eligible for inclusion. Participants formed a consecutive series with data collected prospectively and recruitment prior to MRS and Paediatric Neuro-Oncology Multidisciplinary Team (MDT) consensus diagnosis. All 52 cases with MRI and MRS available prior to histopathological diagnosis were included. Ethical approval was granted and written informed parental consent obtained. Cases without diagnosis confidently established by the MDT were excluded.

8.2.2. MRI and MR Spectroscopy

The index test was single-voxel MRS, acquired as standard diagnostic imaging prior to treatment or surgical intervention. MRS was performed at 1.5T or 3T following conventional MRI, which confirmed voxel placement entirely within solid tumour. The imaging protocol is as described in the Methods, Chapter 3. Spectroscopy processing provided a graphical magnetic resonance spectrum and tissue metabolite profile using standard scanner software, with the majority of raw data also processed using TARQUIN v3.2.2 (Wilson et al., 2011) prior to export to hospital clinical PACS (Agfa IMPAX 6.5.2.2016).

8.2.3. Reference Standard: Multidisciplinary Team (MDT) Consensus Diagnosis

The reference standard was Paediatric Neuro-Oncology Multidisciplinary Team (MDT) consensus diagnosis, incorporating clinical information, MRI, MRS, histopathology, second opinion, genetics and follow-up information about treatment response and tumour behaviour. Consensus diagnosis was confirmed once clinical course had been established at study end.

Sub-analysis was performed using histopathology as an alternative reference standard, excluding cases without conclusive histopathology. Histopathology is an accepted but imperfect diagnostic gold standard: sampling error may occur, particularly in heterogeneous tumours, and rare or atypical lesions may be misdiagnosed. Some tumours remain unbiopsied or exhibit characteristic clinical or radiological features precluding need for tissue diagnosis.

8.2.4. Conventional MRI and MRS interpretation: Radiologists

Three consultant paediatric radiologists who form part of the Neuro-Oncology MDT reported conventional and advanced imaging. Radiologist 1 (LM) had over 15 years' experience in

paediatric neuroradiology and local and national brain tumour research, Radiologist 2 (AO) was an established member of the MDT (6 years) and Radiologist 3 (BP) a newly appointed consultant (3 years). Reporting was undertaken blind to final histopathological and reference diagnoses, independent from the other two radiologists.

For each case, information was provided about age, gender and clinical presentation. Radiologists sequentially viewed conventional imaging followed by MRS processed using scanner software or TARQUIN where available. Index case spectra were visually compared with mean spectra for common paediatric brain tumours presented in a booklet provided (Appendix 3). Each radiologist gave up to four differential diagnoses based on MRI alone, rating their certainty of being correct on a scale 1-10. This was repeated after visually interpreting MRS. Principal MRI / MRI+MRS diagnosis was taken as that with highest certainty.

8.2.5. Independent MRS interpretation: Spectroscopist

An expert spectroscopist and paediatric oncologist (AP, 15 years' experience), blind to radiological, histopathological and reference diagnoses, independently sequentially interpreted MRS with no information other than voxel location images, followed by adding radiologists' differential diagnoses. Up to four diagnoses with certainty ratings were given at each stage. All interpreters recorded whether MRS was suitable for analysis.

8.2.6. Histopathology

Histopathology was interpreted by an independent histopathologist (IN, 10 years' experience) as routine clinical practice prior to documentation on an official hospital reporting system (Sunquest ICE Desktop Live, v.541).

8.2.7. Radiologist Interviews

Semi-structured interviews (10-15 minutes duration) were performed at study end to determine radiologists' perceptions of the added value of MRS in the diagnostic pathway. Interviews included open questions regarding radiologists' use of MRS in clinical practice, their perceptions of the added value of MRS as a diagnostic tool, clinical scenarios for which it was most and least helpful, disadvantages and problems encountered, and how information available could be improved through provision of additional tools or training. Interviews were recorded, transcribed and coded, and thematic analysis performed.

8.2.8. Statistical analysis

Comparison of post-MRI and post-MRS diagnosis with MDT consensus diagnosis determined how many cases were correctly diagnosed in accordance with reference standard at each stage. Accuracy of MRI +/- MRS for each category of brain tumour (all locations, supratentorial and infratentorial) was made through estimates of sensitivity. Results of individual radiologists were analyzed, with inter-observer variability calculated (Chi-squared test). McNemar's test determined if MRS significantly improved individual radiologists' proportion of correct diagnoses. Significance of direction of change towards improvement with MRS (McNemar Ordered Category test of Directional Change) and increase in radiologists' agreement on correct diagnoses (Bhapkar Chi-squared test) were assessed (Bhapkar, 1966).

Cases were reviewed individually to determine the proportion where MRS added value through radiologists changing an incorrect to a correct diagnosis, increasing subjective certainty of a correct diagnosis, or reducing the number of differentials considered. Added value of expert spectroscopist interpretation was ascertained through reviewing cases with

correct diagnoses confirmed and those correctly re-diagnosed following spectroscopist review. Incorrectly diagnosed cases were evaluated and reasons documented.

8.2.9. Study Protocol

The study protocol and workflow is illustrated in Figure 8.1.

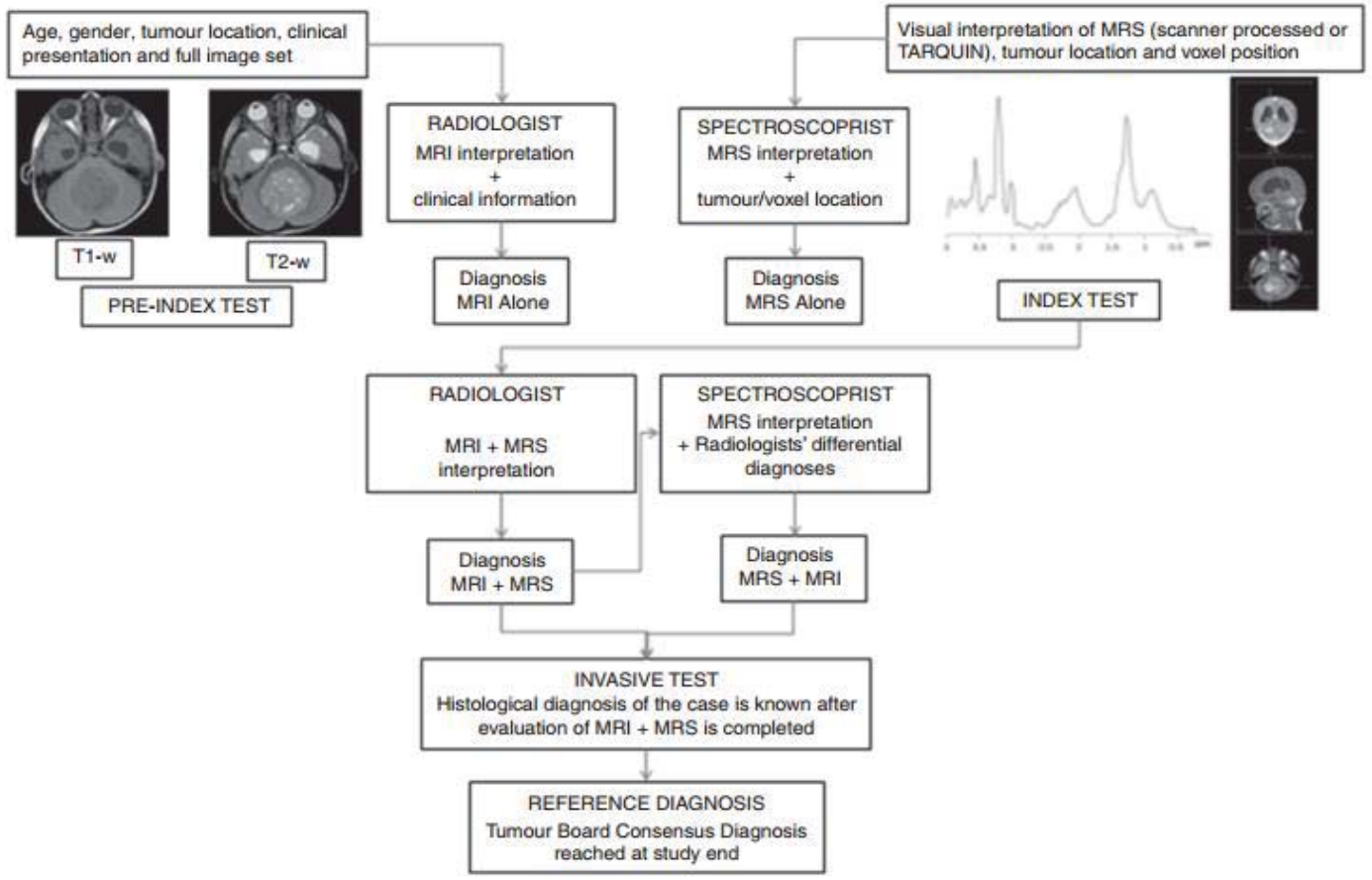

Figure 8.1. Study protocol and workflow

MRS was interpreted independently by 1) radiologists and 2) an expert spectroscopist. All readers were blinded to the reference standard of MDT consensus diagnosis and final histopathology.

Radiologists determined diagnosis in two stages:

1. MRI interpretation in combination with clinical information
2. MRS interpretation in combination with MRI results and clinical information (index test)

The spectroscopist performed a similar process:

1. MRS interpretation blind to clinical and radiological information (but knowing tumour location and voxel position)
2. MRS interpretation with the differential diagnosis made by radiologists

8.3. Results

8.3.1. Patient demographics

Diagnostic MRS was performed on 52 patients following initial imaging. One case was excluded for lack of MDT consensus diagnosis. Ages ranged from a fetus at an antenatal age of 36 weeks gestation to 15 years (median 6.9 years), 27 were male. Tumours were located in the posterior fossa (PF) (27), supratentorially (22) and in the brainstem (2). Breakdown of cases by reference diagnosis is described in Table 8.1 with detailed clinical information in Table 8.2. Participant flow is depicted in Figure 8.2.

Of our patient cohort, 35 (69%) individuals had undergone previous imaging that had detected a CNS lesion prior to routine reimaging including MRS using the standard diagnostic tumor protocol described. Of these 35, 24 (47%) were performed externally, of which 7 were CTs, 16 MRIs, and 1 an antenatal ultrasound. Of the 11 (22%) previouslyimaged at Birmingham Children's Hospital, 6 were for epilepsy, 1 requested by endocrinology, and 2 emergency scans performed after hours.

Table 8.1. Tumour types and patient demographics

Tumour Type (TB Consensus Diagnosis)	**Number**
Medulloblastoma	9
Ependymoma	4
Pilocytic Astrocytoma	13
ATRT	3
Pineoblastoma	1
Germinoma	2
NGGCT	1
Craniopharyngioma	1
Atypical Choroid Plexus Papilloma	1
Diffuse Astrocytoma	2
Central neurocytoma	1
Pituitary adenoma	1
Low grade glioma	1
Tectal plate glioma	3
Ganglioglioma	1
Ewing Sarcoma of occiput	1
Rhabdomyosarcoma skull base	1
Non-tumour	5
Total	**51**
Age, years (median, range)	6.9 (36/40-15y)
Male: female	27:24
Tumour Location	PF = 27; ST = 22; BS = 2

PF, posterior fossa; ST, supratentorial; BS, brainstem

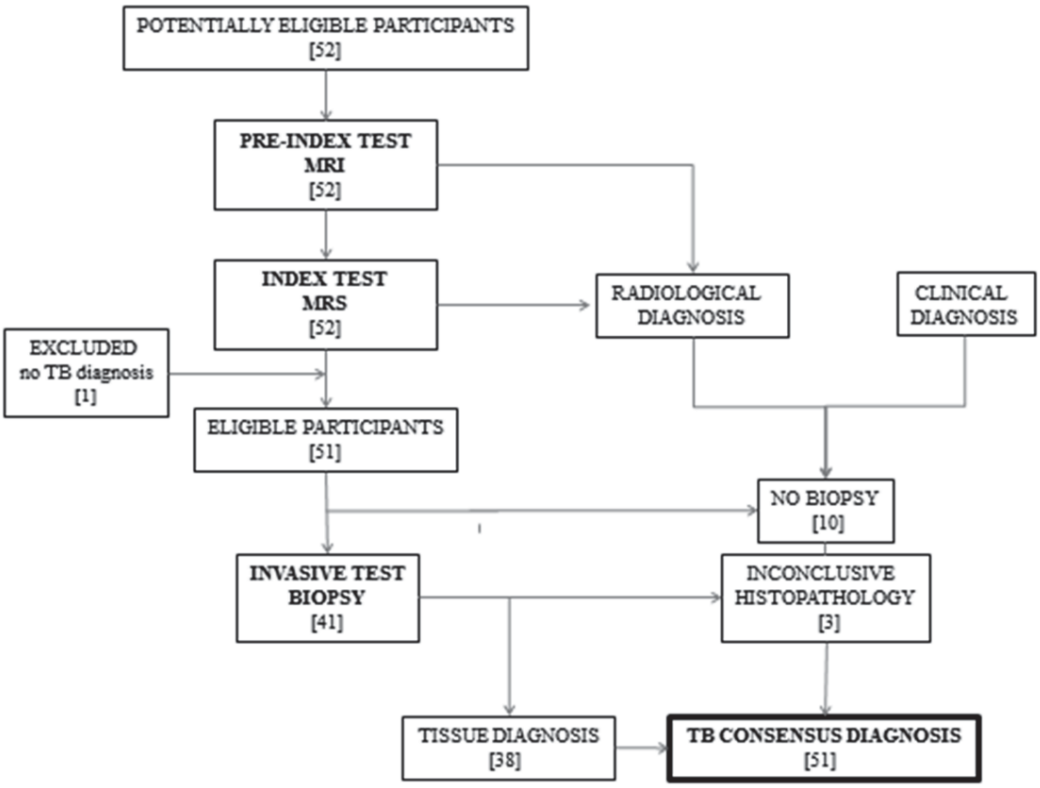

Figure 8.2. Flow of participants (all cases)

Table 8.2. Tumour types and clinical and demographic characteristics of study population (n=51)

Sex	Age	Presenting Symptoms	Tumour Location	Diagnosis Method	Consensus Diagnosis
Histopathology available n = 38					
M	2	Vomiting and ataxia (2 weeks)	ST, Third ventricular primary, metastases	EB (endoscopic)	ATRT
F	13	Ataxia (2 months)	PF	OS	Pilocytic Astrocytoma
M	2	Left sided torticollis and ataxia	PF	OS	Pilocytic Astrocytoma
M	2	Ataxia (1 month)	PF	OS	Medulloblastoma
F	7	Unsteadiness	PF	OS	Medulloblastoma
F	2	Deteriorating gait	ST, Pineal region	OB	Pineoblastoma
F	2	Unwell, off feeds, lethargic	PF, leptomeningeal	OB	ATRT
M	3	New onset squint	PF	OS	Medulloblastoma
M	10	Headaches and vomiting	ST, Suprasellar	OB	Germinoma
M	3	Headaches	PF, Superior cerebellum	OB	Pilocytic Astrocytoma
M	36wk(AN)	Antenatal USS finding	PF	OS (post-mortem)	Medulloblastoma
M	9	Headaches and vomiting	PF	OS	Medulloblastoma
M	1.8	Nausea and vomiting	PF	OS	ATRT
M	12	Unsteadiness (2 months)	PF, Left cerebellum	OS	Pilocytic Astrocytoma
F	10	Recurrent headaches	PF, IVth ventricle	OS	Medulloblastoma
F	12	Headaches	ST, Pituitary fossa	OS	Pituitary adenoma
F	9	Vomiting	PF, floor IVth ventricle	OS	Medulloblastoma
M	1	Haemophilia A, SOL PF	PF	OS	Pilocytic Astrocytoma
F	8	Headaches and vomiting	PF	OS	Pilocytic Astrocytoma
M	2	Unsteadiness and falls	PF	OB	Ewing Sarcoma of occiput
F	7	Headaches and vomiting	PF	OS	Pilocytic Astrocytoma
M	9	Headaches and vomiting	PF	OS	Pilocytic Astrocytoma
M	19	Headaches and vomiting	PF	OS	Medulloblastoma
F	7	Headaches and vomiting	PF	OS	Pilocytic Astrocytoma
F	11	Headaches and diplopia	ST, right basal ganglia	OS	Pilocytic Astrocytoma
M	8	Right sided weakness	ST, right parietal	OS	Anaplastic Ependymoma
F	15	Generalized tonic clonic seizure	ST, parietal lobe	OS	Grade II partial diffuse astrocytoma
M	7	Focal seizure	ST, occipital lobe	OS	Gangliocytoma
M	4	Not documented	ST, infratemporal fossa	OS	Rhabdomyosarcoma skull base
M	10	Headaches, papilloedema	ST, medial aspect left trigone	OS	Atypical choroid plexus carcinoma
F	2	Cough, swallowing problem	PF	OS	Ependymoma
M	9	Vomiting (6 weeks)	PF	OS	Ependymoma
M	5	Headaches and vomiting	PF	OS	Pilocytic Astrocytoma
M	5	Visual impairment	ST, suprasellar	OB	Craniopharyngioma
F	3	Headaches	PF	OS	Ependymoma
M	0.5	Failure to thrive	ST, hypothalamus	OB	Pilocytic astrocytoma
F	13	Headaches, visual disturbance	ST, intraventricular	OS	Central neurocytoma
M	5	Headaches and vomiting	PF	OS	Medulloblastoma
Unbiopsied n = 10					
M	9	Epilepsy	ST, Thalamus	C	Non-tumour
F	2	Unsteadiness (10 days)	PF, Left inferior cerebellar peduncle	C	Demyelination
F	11	New onset focal epilepsy	ST, Left parietal lobe	C	Tectal Plate Glioma
M	3	Autism and bedwetting	ST, Tectal plate	C	Tectal Plate Glioma
F	8	Incidental finding	BS	C	Pontine Pilocytic Astrocytoma
M	11	Left sided eye pain	PF	C	Diffuse Astrocytoma
F	8	Headaches and vomiting	ST, left superior temporal	C	Focal cortical dysplasia
F	6	Endocrine referral: polyuria/polydipsia	ST, suprasellar	C	Non-germinomatous germ cell tumour
M	13	Epilepsy tumor protocol	ST, right para-hippocampal gyrus	C	Low Grade Glioma
M	10	Developmental delay	ST, tectal plate	C	Tectal Plate Glioma
Inconclusive histopathology n = 3					
F	5	Clumsy and ataxic	BS	OB: C – 2nd histopath inconclusive	Ganglioglioma
M	14	Vomiting and occipital headache	ST, pineal	OB: C – 2nd histopath inconclusive	Germinoma
F	2	Right hemiparesis and facial droop	ST, left thalamus	OB: C - 2nd histopath inconclusive	Infarction

PF, posterior fossa; ST, supratentorial; BS, brainstem
C, clinical; F, female; M, male; OB, open biopsy; OS, open surgery; SB, stereotactic biopsy

8.3.2. Diagnostic Accuracy of MRI and MRI+MRS

Table 8.3 shows radiologists' combined and individual sequential diagnostic accuracy of principal diagnosis, followed by accuracy of spectroscopist interpretation.

Table 8.3. Diagnostic accuracy of radiologists following MRI alone and MRS+MRS, and spectroscopist interpretation of MRS alone and MRS+differentials

	Number of Patients	Correct MRI alone	Correct MRI+MRS	Correct MRS alone	Correct MRS + differentials
		RADIOLOGISTS		**SPECTROSCOPIST**	
By Location (all tumours)					
PF/BS	29	80%	88%	78%	78%
ST	22 (18 analyzable[a])	62%	68%	59% (72% analyzable[a])	68% (83% analyzable[a])
By Radiologist (all tumours)					
Rad 1	51	73%	78%	-	-
Rad 2	51	65%	71%	-	-
Rad 3	51	71%	83%	-	-
All Tumours	**51 (47 analyzable[a])**	**69%**	**77%**	**69% (75% analyzable[a])**	**75% (81% analyzable[a])**
Tumours with histopathological diagnosis only					
All Tumours	38	74%	81%	68% (72% analyzable[a])	73% (78% analyzable[a])

PF Posterior Fossa; ST Supratentorial/; BS Brainstem

[a]Analyzable MRS = Passed or borderline QC, or interpretable despite failing QC (n=47)

8.3.2. Diagnostic Accuracy

8.3.2.1. Radiologists

There was no significant inter-observer difference between radiologists' diagnostic accuracy using conventional MRI (p=0.67, Chi-squared test). Principal MRI diagnosis was correct in 69% of cases, increasing to 77% with MRS.

MRI+MRS resulted in significantly more additional correct diagnoses than MRI alone (p=0.03, McNemar Ordered Category Test of Directional Change). Median changes in accuracy and 95% confidence intervals for Radiologist 1 (most experienced), 2 and 3 respectively following addition of MRS were +5.8% (-0.03-0.14; p=0.25) +5.8% (-0.06-0.18; p=0.45) and +11.8% (0.01-0.26; p=0.03) (McNemar's Test). Direction of change was towards improvement for all radiologists, reaching significance for Radiologist 3. There was significant increase in radiologists' agreement on correct diagnosis with addition of MRS (p=0.046, Bhapkar chi-squared test) (Bhapkar, 1966). There was no increase in radiologists' agreement when diagnosis was incorrect

8.3.2.2. Spectroscopist

Four cases were excluded from independent spectroscopy analysis as MRS failed QC. Spectroscopist interpretation was correct in 69% all cases (75% of 47 suitable for analysis) increasing to 75% (81% with analyzable MRS) following provision of radiologists' differentials.

8.3.3. Added clinical value of MRS

Radiologists' review of MRS added value in 73% cases (37/51) through replacing incorrect with correct diagnosis, increasing certainty of diagnosis when correct, or reducing the number of differentials considered. Spectroscopist review accurately diagnosed a further 10%, with a total of 83% of patients (42/51) incurring added value through a combination of radiologist and spectroscopist interpretation of MRS.

The 27% (14/51) for which MRS did not benefit radiologists had either failed QC, or were rare or atypical tumours without comparator mean MRS or conclusive local histopathology. Spectroscopist review correctly diagnosed five of these difficult cases.

Spectroscopist review confirmed correct radiological diagnosis in 70% (36/51) of all cases, or 77% of the 47 spectra suitable for analysis. Diagnosis was not attempted in four cases (8%) where MRS failed QC. Of 11 cases (22%) where the spectroscopist was incorrect, five had inconclusive histopathology and were diagnosed following central histopathological review, two had inconclusive histopathology post central review and one was unbiopsied. Reasons for misdiagnosis of the remaining three were unclear, although each MRS was atypical for tumour type. Radiologists diagnosed these three tumours correctly on MRI, suggesting clinical management would not have been adversely altered and highlighting the importance of integrating all forms of information prior to formulating a conclusive diagnosis.

Review of tumours incorrectly diagnosed on MRI subsequently re-diagnosed correctly following MRS suggests where added value may be incurred in the clinical pathway. In the posterior fossa, visual MRS interpretation improved radiologists' diagnostic accuracy of medulloblastoma (89% to 96%), pilocytic astrocytoma (72% to 82%), ATRT (50% to 100%), and diffuse astrocytoma (67% to 100%), with further improvement in ependymoma (89% to 100%) following spectroscopist review. Supratentorially, radiologists' diagnosis of ependymoma (0 to 33%) and tectal plate glioma (89% to 100%) improved after MRS, with spectroscopist review improving ATRT (0 to 100%) and diffuse astrocytoma (0 to 100%). Spectroscopist review also increased diagnostic accuracy of lesions that were not primary CNS tumours and non-tumours (67% to 100%) in all locations.

Tumour types with improvement in accuracy of principal diagnosis following radiologist or spectroscopist review of MRS are shown in Table 8.4.

Table 8.4. Tumour types with improvement in accuracy of principal diagnosis following MRS

Tumour Type	Correct MRI alone (R)	Correct MRI+ MRS (R)	Correct MRS+dd (S)
Posterior Fossa			
Medulloblastoma	89%	96%	67%
Ependymoma	89%	89%	100%
Pilocytic Astrocytoma	72%	82%	82%
ATRT	50%	100%	100%
Diffuse Astrocytoma	67%	100%	0%
Non-Tumour	67%	67%	100%
Ewing Sarcoma of occiput[a]	33%	33%	100%
Supratentorial			
ATRT	0%	0%	100%
Diffuse Astrocytoma	0%	0%	100%
Tectal plate glioma	89%	100%	100%
Ependymoma	0%	33%	0%
Rhabdomyosarcoma skull base[a]	67%	67%	100%
Non-Tumour	67%	67%	100%

R = Radiologists; S = Spectroscopist; dd = differential diagnosis
[a]Correct diagnosis = not primary CNS lesion

8.3.4. Quality Control

Of 51 MRS, 36 (71%) met quality control (QC) standards. Nine (17.5%) were borderline for reasons of inclusion of normal brain within the voxel, poor voxel placement, poor shimming, phasing or line-width, unacceptable baseline, or low signal-to-noise ratio. Six (11.5%) failed QC (voxel placement over bone, poor phasing), of which two still provided sufficient information for spectroscopist analysis. Interpretation was not attempted in the remaining four.

Of 45 spectra obtained at 1.5T, 32 (71%) passed QC, compared to four of six (67%) 3T spectra. TARQUIN processing was available in 47, leading to four additional MRS being of

acceptable quality. One of four MRS processed by scanner software only failed QC. Comparison between MRS processed using scanner software and using TARQUIN may be seen in Figure 8.3.

a) b)

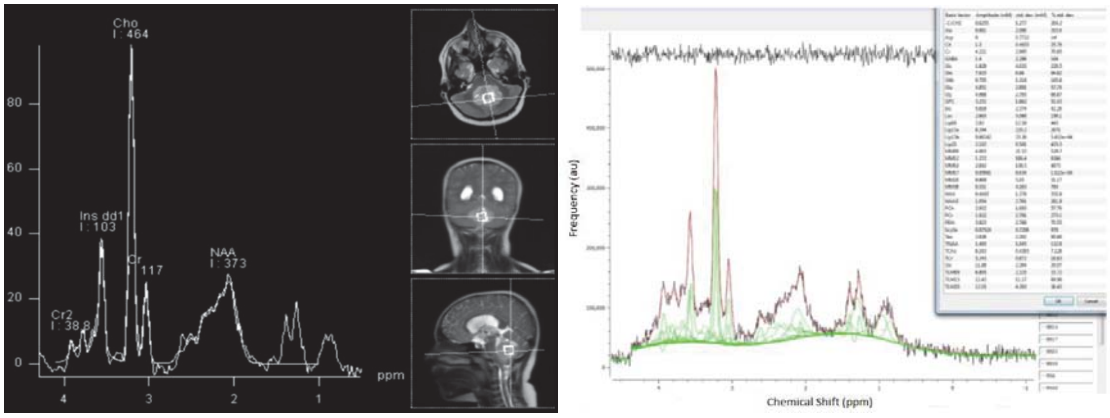

Figure 8.3. MRS processed using scanner software (a) and using TARQUIN (b)
MRS from a patient with medulloblastoma processed using scanner software (a) and using TARQUIN (b). Metabolite concentrations and their Crammer Rao lower bounds are listed in the box on the right of the TARQUIN output.

The spectroscopist correctly diagnosed eight of nine borderline quality spectra. Of six failing QC, two were correctly diagnosed with a third identified as hemorrhagic tumor. Tumours with uninterpretable MRS were diagnosed subsequently as germinoma, NGGCT and pituitary adenoma. All radiologists correctly diagnosed the germinoma and NGGCT on conventional imaging, and two identified pituitary adenoma.

8.3.5. Adverse events resulting from MRS

One case, a supratentorial central neurocytoma, was correctly diagnosed by one radiologist on MRI but subsequently misdiagnosed following MRS. No other tumours correctly diagnosed with conventional imaging were misdiagnosed.

8.3.6. Histopathology

Availability of histopathology is shown in Figure 8.4.

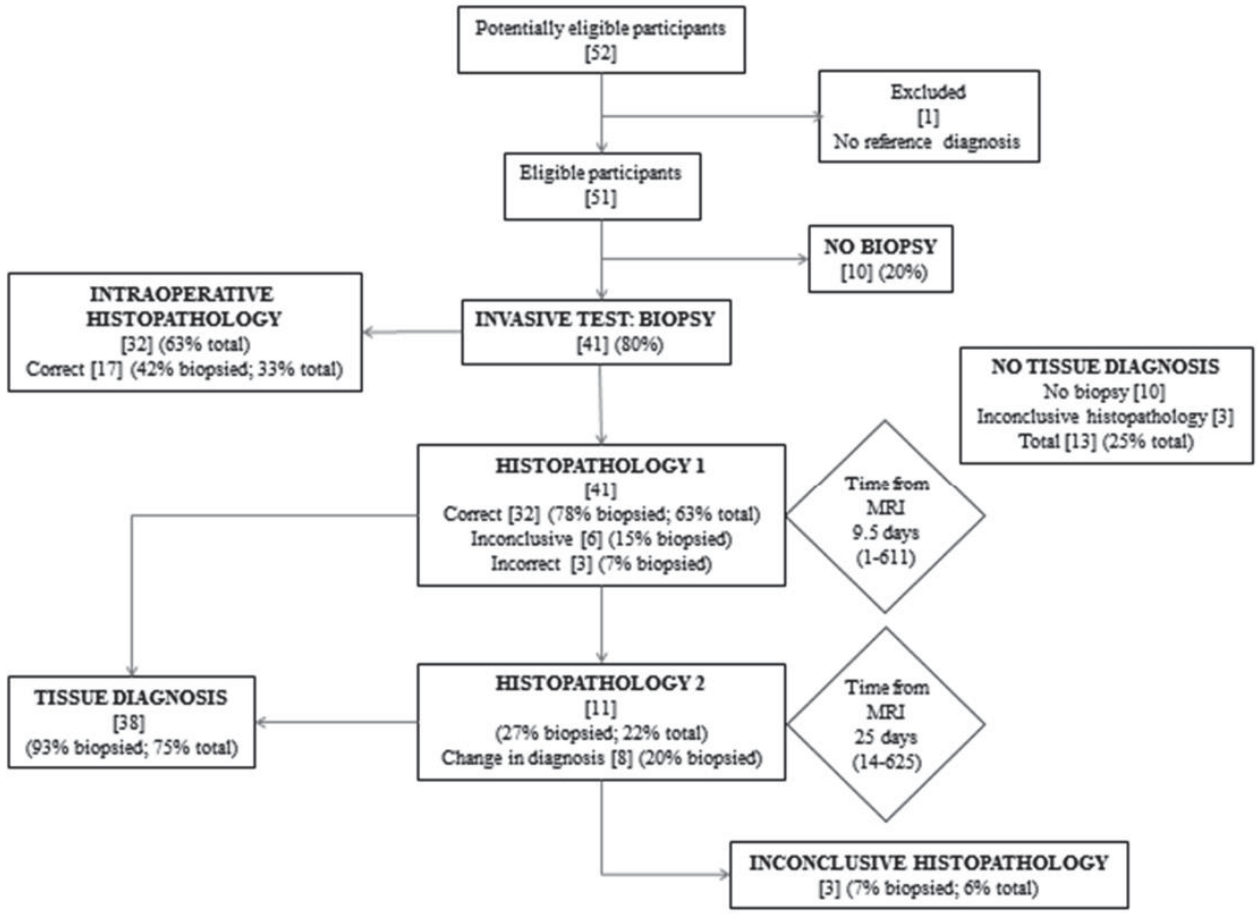

Figure 8.4. Availability of histopathology

Of 51 patients, 80% (41/51) underwent surgical intervention. Histopathological diagnosis was achieved in 75% (38/51); the remaining 25% lack tissue diagnosis. Intraoperative histopathology accorded with MDT consensus diagnosis in 42% biopsied (33% all) cases. First histopathology was correct in 78% of those biopsied (63% all), incorrect in 7% and inconclusive in 15%. Central review was requested in 27%, resulting in change of diagnosis in 20% with 7% remaining inconclusive.

First histopathology was available a median of 9.5 days (range 1-611) following MRI, or 6 days (0-30) post-surgery. Second histological opinion yielded results a median 25 (14-625) days following imaging, with treatment commencing after a median of 31 (11-78) days.

8.3.7. Histopathological Diagnosis Subgroup Analysis

Subgroup analysis was performed in 38 patients with histopathological diagnosis using this alternative reference standard (see Table 8.2. for patient demographics). Radiologists correctly diagnosed 74% of this subgroup using MRI alone, increasing to 81% with MRS (Table 8.3). The 7% increase in accuracy was comparable to 8% observed overall. Spectroscopist MRS interpretation was accurate in 74%, or 78% excluding 2 uninterpretable spectra.

8.3.8. Examples of cases in which MRS improved diagnostic accuracy and management

Examples of cases in which diagnostic accuracy and management were improved following MRS are presented in Figures 8.5. and 8.6.

Case 1. ATRT

An 8 week-old baby presented with a 48-hour history of decreased feeding and lethargy on a background of a 2-week history of increasing head circumference and left eye deviation. CT revealed a posterior fossa mass, and MRI confirmed the presence of a large, lobulated, heterogenous tumour occupying and expanding the fourth ventricle. The lesion included both solid and cystic components, demonstrating patchy enhancement, intermediate to low signal on FLAIR and restricted diffusion. There was evidence of hydrocephalus with grossly dilated ventricles bilaterally. Enhancement along the cord suggested disseminated spinal disease.

Initial differential radiological diagnoses included ependymoma, medulloblastoma and ATRT. Spectroscopy favoured ATRT with low N-acetyl aspartate, high choline and lipid. The chance of cure was very small in the context of metastatic disease in such a young child. Although intensive chemotherapy could have been an option, the baby was too small to

harvest stem cells and would most likely not tolerate treatment. The Paediatric Neuro-Oncology MDT discussed offering palliative treatment from the outset, but the decision was made to perform a biopsy to confirm histological diagnosis prior to formulating a definitive management plan. Pathology reported INI-1 negative undifferentiated embryonal tumour, confirming ATRT. A palliative course was followed, and the baby died 2 weeks later.

This case is an example in which a confident non-invasive diagnosis could have spared an invasive diagnostic procedure in a patient for whom palliative care and maintaining quality of life was appropriate. Using conventional MR imaging alone, radiologists 1 and 2 misdiagnosed this case as ependymoma with certainties of 50% and 60% respectively. Radiologist 3 correctly diagnosed ATRT with certainty of 60%. Incorporation of MRS information resulted in a change in the list of differential diagnoses to ATRT alone with increases in certainties to 80%, 90% and 90%.

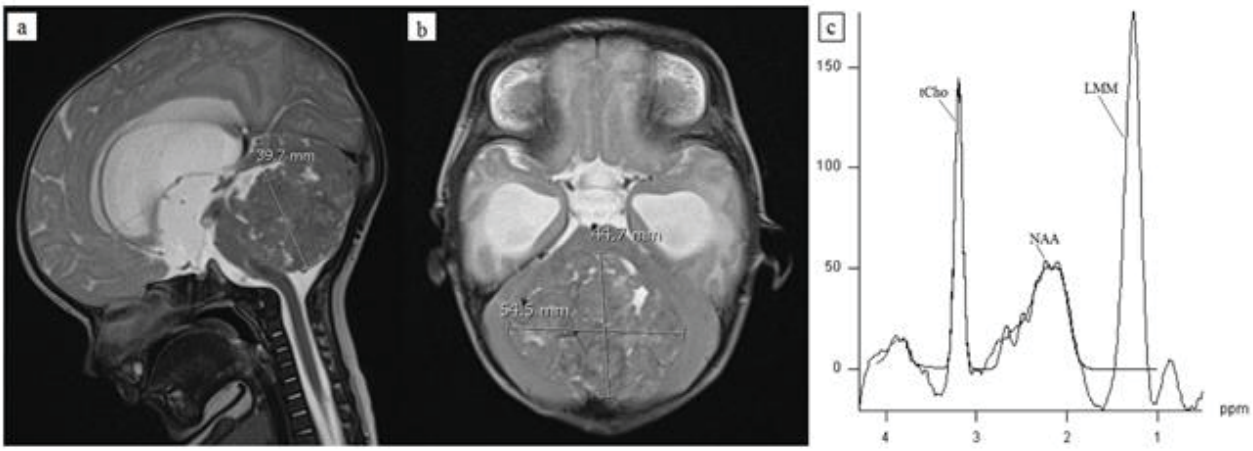

Figure 8.5. ATRT**.** T2-weighted sagittal and axial (a) MR images of an 8 week old baby with a metastatic posterior fossa lesion. Initial differential radiological diagnoses included ependymoma, medulloblastoma and ATRT. MRS (b) favoured ATRT with low NAA, high tCho and LMM, subsequently confirmed following open biopsy.
tCo Total choline, NAA N-acetyl aspartate, LMM Lipids and Macromolecules

Case 2. Medulloblastoma

Antenatal ultrasound revealed a large congenital posterior fossa tumour in a fetus at 36 weeks gestation. Antenatal MRI with MR spectroscopy was performed to further characterize the lesion and guide management. Conventional MRI revealed a large posterior fossa mass containing a 26mm cyst along the superior aspect, with dilatation of the third and lateral ventricles.

Visual inspection of the MRS available on hospital PACS processed by Siemens software revealed a spectrum dominated by total choline and lipids (particularly the lipid peak at 1.3ppm) consistent with a malignant brain tumour. Other metabolite features included a peak around 3.6ppm and a broad feature between 2.0 and 2.5ppm. Overall, the spectrum was consistent with a medulloblastoma. The mother was counselled accordingly, and a management plan was put in place for transfer to Birmingham Children's Hospital for definitive care post-delivery. The baby sadly died following appropriate palliation. Post-mortem histological review confirmed medulloblastoma.

This case is an example in which accurate non-invasive diagnosis was used to guide timely management planning and inform antenatal discussions at a time of considerable distress. Reviewing MRI alone, our radiologists misdiagnosed this tumour as teratoma, ATRT and germ cell tumour, with certainties of 60%, 60% and 50% respectively. Following review of MRS, all three correctly diagnosed medulloblastoma with certainties of 60%, 60% and 80%.

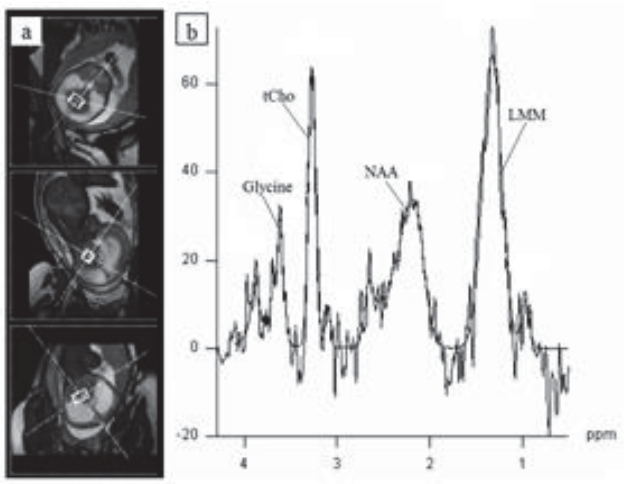

Figure 8.6. Medulloblastoma. Antenatal MR images (a) of a 36 week gestation fetus with a large congenital posterior fossa tumor. Initial MR appearances were suggestive of teratoma, ATRT or germ cell tumor. MRS (b), dominated by choline and lipids with a glycine peak at 3.6ppm, was consistent with medulloblastoma confirmed following post-mortem histopathology.
tCo Total choline, NAA N-acetyl aspartate, LMM Lipids and Macromolecules

8.3.9. Radiologist Interviews

Radiologists found MRS a supportive tool to refine diagnoses reached through conventional imaging, particularly in differentiating posterior fossa tumours with overlapping imaging characteristics such as ependymoma and medulloblastoma. Review of choline facilitated classification of ambiguous lesions as malignant or indolent. Aggressive features in conservatively managed lesions were identified using choline, lipids and lactate, with usual MRS suggesting atypia. In addition to facilitating definitive diagnosis of new tumour types, radiologists described using MRS to diagnose recurrence through comparing spectra at follow up with those obtained at diagnosis. Radiologists found MRS increasingly helpful as they gained experience with its interpretation, and reported being confident to visually interpret spectra in 5-10 minutes.

The main difficulty reported with using MRS in clinical practice was quality control (QC) issues due to poor voxel placement, inclusion of normal brain, calcification and artefact. MRS did not allow definitive diagnosis of rare supratentorial tumours, particularly those lacking comparator mean spectra. Despite this, one radiologist reported finding unusual MRS features useful in alerting to the possibility of a rare or atypical tumour.

Radiologists considered the provision of additional decision support tools, such as a booklet containing mean or example spectra for a wide range of possible tumour types, or a computer-based programme, would be helpful to integrate MRS into clinical practice. They felt improving their own ability to interpret and verify the quality of MRS was more important than reliance on a computer output. MRS was described as "an important tool in the radiology toolbox", used to supplement conventional imaging and support clinical decisions based on a range of sources of information, rather than a modality to be used in isolation.

The main comments from the spectroscopist were that TARQUIN processing led to additional MRS being of acceptable quality in cases where scanner processing did not pass QC standards, and that formal discussion with radiologists (rather than just being provided with a differential diagnosis and MRS) would provide optimal diagnostic accuracy.

8.4. Discussion

Visual interpretation of MRS improved accuracy of pre-therapeutic diagnosis for all participating radiologists, adding further value through confirmation of correct MRI diagnoses, narrowing broad differentials and increasing inter-rater agreement. Expert spectroscopist review verified correct diagnoses and allowed characterisation of more

difficult cases. These are clinically important outcomes given the challenge in formulating therapeutic decisions based on uncertainty and the potential of accurate early diagnosis of childhood brain tumours to improve patient care.

Non-invasive diagnosis of posterior fossa tumours may be sufficiently robust to recommend treatment planning prior to histopathological confirmation. Radiologists correctly identified 88% of all posterior fossa tumours using MRS, similar to earlier reports from our institution (Davies et al., 2008) with the majority of misdiagnosed tumours in this location being rare lesions. This has important implications for clinical practice. Identification of medulloblastomas from diagnostic imaging would allow early radiotherapy referral, and non-invasive diagnosis of ependymomas could guide surgical planning given the importance of complete resection of this tumour type. Correct diagnosis of all indolent lesions after spectroscopist review suggests avoidance of biopsy may be reasonable if MRS is typical of non-tumour.

All tumours irrespective of location, diagnosis or quality of MRS were included in this study to reflect the diversity usually seen in clinical practice. Increased diagnostic accuracy was more marked in posterior fossa than supratentorial lesions. The former consist of a limited number of tumour types that can be accurately discriminated using computer-based classifiers (Wang et al., 1995; Arle et al., 1997; Davies et al., 2008; Vicente et al., 2013), whereas the latter are histologically diverse, including rare tumour subtypes without comparator mean spectra. Reflecting the proportion of rare tumours in the paediatric population accounts for the lower diagnostic accuracy seen in this study than in those of common posterior fossa lesions (Wang et al., 1995; Arle et al., 1997; Davies et al., 2008; 2010b; Vicente et al., 2013). Although quality control (QC) issues limit implementation of MRS, it was interesting to note

that our spectroscopist could derive useful diagnostic information from even poorer quality spectra. Spectroscopist visual interpretation of MRS passing QC was 81% accurate, comparable with reports in the literature of an increase in diagnostic accuracy following spectroscopist review of MRS from 63% to 87% (Shiroishi et al., 2015).

The potential role of MRS in the diagnostic pathway can be demonstrated through the sequence of imaging interpretation described in this study. Radiologists at Birmingham Children's Hospital review conventional MR imaging and formulate a list of differential diagnoses, and then use MRS as a supportive and confirmatory tool seeking expert spectroscopist opinion if diagnosis remains uncertain. Conventional imaging is sufficient to diagnose lesions with distinct radiological features (e.g. craniopharyngioma). Radiologists' review of MRS adds value in the diagnosis of common tumours with overlapping imaging characteristics, such as posterior fossa medulloblastoma and ATRT. Expert spectroscopist opinion can further improve diagnosis of difficult cases, with atypical lesions including misdiagnosed ependymoma, pontine pilocytic astrocytoma, supratentorial ATRT and non-primary CNS tumours accurately diagnosed at this stage.

Although MRS is intended to complement rather than replace tissue diagnosis, histopathology is an imperfect diagnostic gold standard with several limitations. Many paediatric tumours are located in central vital structures and providing representative tissue samples through biopsy of such lesions is difficult. Awaiting histopathological confirmation of diagnosis can result in treatment delay, which is important to avoid in this vulnerable patient group as outcomes may be affected. Advanced imaging would be particularly valuable in tumours not amenable to biopsy or those with inconclusive histopathology. Over 25% of this cohort lacked tissue diagnosis, with management of these patients determined on

radiological and clinical features alone. Although MRS may influence consensus diagnosis, with potential incorporation bias using this as a reference standard, subgroup analysis against histopathology including only cases with histopathological confirmation revealed similar net improvement in accuracy. MDT diagnoses were verified through clinical course rather than simply accepted as correct following MRI and MRS.

It is important to consider potential adverse effects of MRS on diagnosis and clinical decision-making. A central neurocytoma diagnosed correctly by MRI was subsequently misdiagnosed as a diffuse astrocytoma. Although this is a rare tumour type that did not have comparator mean spectra, it was correctly identified following spectroscopist review. Spectroscopist analysis was incorrect in three tumours correctly diagnosed by radiologists on conventional imaging (medulloblastoma, pilocytic astrocytoma and craniopharyngioma). MRS of all these lesions was atypical of tumour type, highlighting the importance of interpretation in the context of all available information. Other misdiagnosed lesions were rare and difficult to diagnose on histology.

Making MRS widely clinically available is an important objective to improve patient care. The techniques described in this chapter are readily applicable without additional infrastructure. The MRS protocol used involves single-voxel acquisition and visual interpretation, each adding around 5 minutes to examination and reporting times. It is generally accepted that optimal analysis of MRS data requires fitting to a linear combination of metabolite basis functions, which was not available through scanner software used in this study. One barrier to using platform independent software has been the difficulty of handling MRS raw data. This is, however, becoming easier as demonstrated by the use of a PACS linked to a server running TARQUIN software, making results available to users in real time.

In this study, TARQUIN analysis was more robust to clinical data of variable quality than scanner processed MRS, increasing the number of cases providing useful information. Clinicians also appreciated clarification regarding metabolite assignment available through TARQUIN. Complex spectroscopy methods with longer acquisition times (e.g. MRSI/CSI), sophisticated decision support software and automated classifiers may improve accuracy (Wang et al., 1995; Arle et al., 1997; Davies et al., 2008; Vicente et al., 2013), but are not routinely available and are challenging to implement clinically.

As radiologists are not formally trained to quantitatively evaluate MRS, it is important to present easily interpretable information for clinical use taking into account working practices. Radiologists at Birmingham Children's Hospital incorporate visual MRS interpretation into routine practice, comparing the MRS profile from an index case with a repository of mean spectra from common tumour types, and report finding MRS a helpful tool to confirm or refute diagnoses made through conventional imaging. This is encouraging as it suggests widespread implementation of the technique is a realistic objective. Expert spectroscopist support for difficult cases and centers with less experience could potentially be provided through central radiological review. Developing usable classifiers and decision support systems for radiologists may improve MRS interpretation and is a key aim for the future.

It is important to acknowledge limitations of this study design. It is difficult in a single centre to ensure complete blindness of radiologists to patients' clinical course. Bias may have been introduced as not all cases were reported contemporaneously, although final histopathological and consensus diagnoses were not revealed until study end. Results of this single-centre study may not be generalizable to institutions with less spectroscopic or more paediatric neuroradiological expertise and robust prospective multi-centre evaluation is required.

Although Birmingham Children's Hospital is one of the largest centres in the UK with an established neuro-oncology MDT and imaging research programme, participating radiologists were not all experienced in MRS interpretation. Our least experienced radiologist demonstrated greatest improvement, indicating visual MRS interpretation may benefit those with less expertise with modest training requirements.

8.5. Conclusion

In conclusion, this study demonstrates MRS can add diagnostic value in clinical practice, both through visual interpretation by radiologists and expert spectroscopy review. Further prospective multi-centre studies are needed to validate these findings in a range of clinical settings and formulate recommendations to incorporate MRS into the diagnostic pathway to improve patient care. Work is also needed to evaluate the therapeutic impact of MRS and determine its added value in clinical decision-making in paediatric neuro-oncology to improve outcomes for children with brain tumours.

Chapter 9: Evaluation of the Therapeutic Impact of MRS in Management of Paediatric Brain Lesions in Clinical Practice

9.1. Introduction

MRS has been shown to add diagnostic value in a clinical setting. As shown in Chapter 8, visual interpretation of MRS by radiologists and expert spectroscopist review can improve the accuracy of non-invasive diagnosis of childhood brain tumours compared with that obtained through conventional MRI. Although there is evidence that MRS can enhance conventional radiological reporting at diagnosis (Murphy et al., 2002; Julia-Sape et al., 2012; Galanaud et al., 2006; Shiroishi et al., 2015), there has been little work assessing its impact on other forms of management decisions or its therapeutic impact in clinical practice (Lin et al., 1999; Moller-Hartmann et al., 2002).

There are a number of additional potential clinical roles for MRS in paediatric neuro-oncology. MRS could be used to guide biopsy to target the highly malignant component of heterogeneous lesions, identify unusual or aggressive high grade tumours through characteristic features such as high lipids (Wilson et al., 2013; Vicente et al., 2013; Astrakas et al., 2004) and choline (Marcus et al., 2007) and facilitate surgical planning through accurate pre-operative diagnosis. Confident non-invasive diagnosis of indolent lesions could negate the need for biopsy. It could also be possible to diagnose relapse or metastases that display similar metabolic features to the primary lesion (Gill et al., 2013) and differentiate progression from pseudoprogression or treatment induced changes. Studies are needed to quantify the extent to which MRS enhances clinical decision-making for children with brain tumours to facilitate optimal integration into diagnostic and management pathways.

The aim of this chapter was to review clinical use of MRS in a single centre, establish added value in non-invasive diagnosis and clinical decision-making and investigate potential impact on patient care.

9.2. Methods

9.2.1. Patients

All 69 children referred to the Paediatric Neuro-Oncology Multidisciplinary Team (MDT) at Birmingham Children's Hospital with a suspected brain tumour following imaging with MRI and MRS between January 2014 and 2016 were included in this observational study.

9.2.2. MRI and MR Spectroscopy

Single-voxel MRS was performed as diagnostic imaging prior to surgical intervention or treatment. MRS was acquired on one of three MR scanners (1.5T GE Signa Excite, 1.5T Siemens Avanto 3T Philips Interna Achieva) after conventional MRI using the protocol described in the Methods Chapter 3. Spectroscopy was processed using standard scanner software exported to hospital PACS (Agfa IMPAX 6.5.2.2016), with raw spectroscopy data processed using TARQUIN v3.2.2 (Wilson et al., 2011) for research use.

9.2.3. Multidisciplinary Team (MDT) Diagnosis

The Paediatric Neuro-Oncology MDT reviewed all patients. Decisions regarding diagnosis and management were made following review of clinical information, conventional imaging, MRS and histopathology. MDT discussions, clinical questions and decisions were contemporaneously documented in detail in real time by an experienced medical secretarial team and reviewed by clinicians prior to storage. Diagnostic reference standard was the diagnosis agreed by the MDT at study end, verified through clinical course. Tumours with diagnoses confirmed on histopathology were classified according to the WHO Classification of Tumours of the Central Nervous System 2007 (Louis et al., 2007). Those lacking histopathological diagnosis were assigned a diagnosis from a predefined list (see Table 8.1.).

9.2.4. Radiologists

The radiologists reporting imaging in this study were consultant paediatric radiologists (n = 10), seven of whom had a special interest in neuroradiology through involvement in a relevant clinical study board, with 3 responsible for reporting images at Neuro-Oncology MDT meetings. Radiologists commonly discuss cases with colleagues prior to issuing formal reports which are uploaded onto the hospital PACS. The majority of diagnostic imaging in children presenting with suspected brain tumours was reported by paediatric radiologists with an interest in paediatric neuroradiology. MRI scans from patients presenting out of hours were preliminarily reported by the consultant paediatric radiologist on duty, but usually reviewed by a radiologist with an interest in neuroradiology prior to release of the official imaging report. All MRI and MRS included in this study were reviewed by a paediatric radiologist with an interest in neuroradiology as part of the MDT.

9.2.5. Conventional MRI interpretation

Conventional MRI scans were reported by a consultant paediatric radiologist prior to availability of histopathology. Official imaging reports were retrospectively reviewed to obtain the primary contemporaneous radiological diagnosis. Radiological diagnosis was defined as 'correct' (certain) if the only documented diagnosis on the imaging report exactly corresponded to that determined by the MDT at study end, and 'partially correct' (uncertain) if this was first in a list of differentials or reported as a query. An 'incorrect' MRI diagnosis was where the MDT diagnosis was in a list of differentials but not first, or not listed. Cases with no documented radiological diagnosis were excluded.

9.2.6. MRS interpretation

Contemporaneous MRS interpretation prior to availability of histopathology was taken from imaging and MDT reports, inter-clinician correspondence and medical records. Documented MDT discussions and clinical correspondence were reviewed to identify clinical questions answered using information from spectroscopy. Cases in which MRS facilitated diagnosis, helped answer a specific clinical question, or influenced management or outcome were examined in detail and recorded.

MRS data processed using scanner software and uploaded to the hospital PACS were available at the time of initial MRI reporting. The accepted system for radiological reporting at Birmingham Children's Hospital is to view and interpret conventional MRI first, then follow this by adding information from visual interpretation of MRS. Diagnostic considerations are documented at each stage and included in the radiology report, making it possible to form a clear distinction of the contribution made by MRS to the diagnostic process. The interpretation of MRS used clinically was made through visualization of the spectra in the great majority of cases. Spectroscopy processing was undertaken using standard scanner software and exported to hospital PACS in all cases described. Raw spectroscopy data processed using TARQUIN were available in a subset of patients as part of a research study. Contemporaneous MRS interpretation in clinical practice was mainly via visual interpretation by radiologists of the scanner-processed spectra via PACS, with some support provided by visual inspection of the TARQUIN processed spectra. Although radiologists did not tend to use TARQUIN for metabolite quantitation they anecdotally found individual metabolite fits provided by TARQUIN useful. Detailed interpretation of MRS by expert clinicians and researchers from the hospital Children's Brain Tumour Research Team was requested on a subset of 14 patients.

9.2.7. Histopathology

Histopathology reports were obtained from the official hospital results reporting system (Sunquest ICE Desktop Live, version 541).

9.2.8. Statistical analysis

'Correct' and 'partially correct' MRI reports were combined to determine the percentage of patients with accurate radiological diagnosis made on conventional imaging alone. 'Correct' MRI reports were interpreted as implying diagnostic certainty, whereas 'partially correct' reports implied uncertainty. Non-invasive diagnoses corresponding to those determined by the MDT following addition of MRS were totalled to determine the accuracy of MRI combined with MRS. The number of 'partially correct' radiology reports confirmed by MRS reflected the increase in diagnostic certainty.

Comparison of post-MRI and post-MRS diagnosis with the reference diagnosis determined how many more cases were diagnosed correctly. Proportions were reported with 95% confidence intervals calculated from the Binomial distribution. McNemar's test determined if MRS had a statistically significant effect on correct diagnosis compared with MRI alone. Accuracy of MRI +/- MRS for each tumour category (all locations, supratentorial, infratentorial and brainstem) was made through estimates of sensitivity.

9.3. Results

9.3.1. Demographics

Five cases were excluded for lack of documented MRI diagnosis, with 64 patients included in the analysis. The patients' ages ranged from 1 month to 16 years (median 9 years), 40 were male and 24 female. All cases had their diagnosis reviewed by the local MDT. The

breakdown of cases by MDT diagnosis with corresponding histopathological confirmation can be seen in Table 9.1.

Table 9.1. Multidisciplinary Team (MDT) Diagnoses

MDT Diagnosis	Number	Histopathology diagnosis available	Central Histopathology Review requested	Histopathology inconclusive
Supratentorial	**40**	**24**	**8**	**4**
Anaplastic Astrocytoma	1	1	0	0
ATRT	3	3	0	0
Diffuse astrocytoma	1	1	1	0
DNET	3	2	1	0
Germinoma	1	0	0	0
Glioblastoma multiforme	1	1	0	0
Mixed germ cell tumour	1	1	0	0
Meningioma	1	0	0	0
Teratoma	2	2	0	0
Optic pathway glioma	2	0	0	0
Pilocytic astrocytoma	4	4	0	0
Pilomyxoid astrocytoma	1	1	1	0
Pituitary macroadenoma	1	1	1	0
Supratentorial PNET	2	2	2	0
Supratentorial ependymoma	1	1	0	0
Non-malignant: 2=cortical dysplasia, 1=pineal cyst, 1=epidermoid cyst, 6= incidental lesions	10	2	0	0
Diagnosis Uncertain: 1= ?astroblastoma, 2=?tectal plate glioma, 2=?LGG	5	0	0	4 (1 unbiopsied)
Posterior Fossa	**17**	**14**	**0**	**0**
Medulloblastoma	6	6	0	0
Ependymoma	1	1	0	0
Pilocytic Astrocytoma	7	7	0	0
Non-malignant (incidental lesions)	3	0	0	0
Brainstem	**7**	**1**	**0**	**0**
DIPG	5	1	0	0
Low Grade Glioma	2	0	0	0
Total	**64**	**39 (61%)**	**8 (8/39= 21%)**	**4 (4/39 = 10%)**

9.3.2. Histopathology

Of 64 patients, biopsy or surgical resection was performed in 43 (67%). Conclusive histopathological diagnosis was available in 39 (61% of all patients, 91% biopsied patients) a median of 12 (4–40) days following imaging or nine (0-16) days post-biopsy. Central histopathology review was requested and undertaken in eight samples (19%) in which there was diagnostic uncertainty, leading to minor change in diagnoses in seven (16%). Histopathology was inconclusive in four biopsied patients (15%), one due to sampling error and three due to atypical histopathological appearance. Of all patients, 25 (39%) were managed without histopathological diagnosis. Availability of histopathological diagnosis for brain lesions is shown in Figure 9.1.

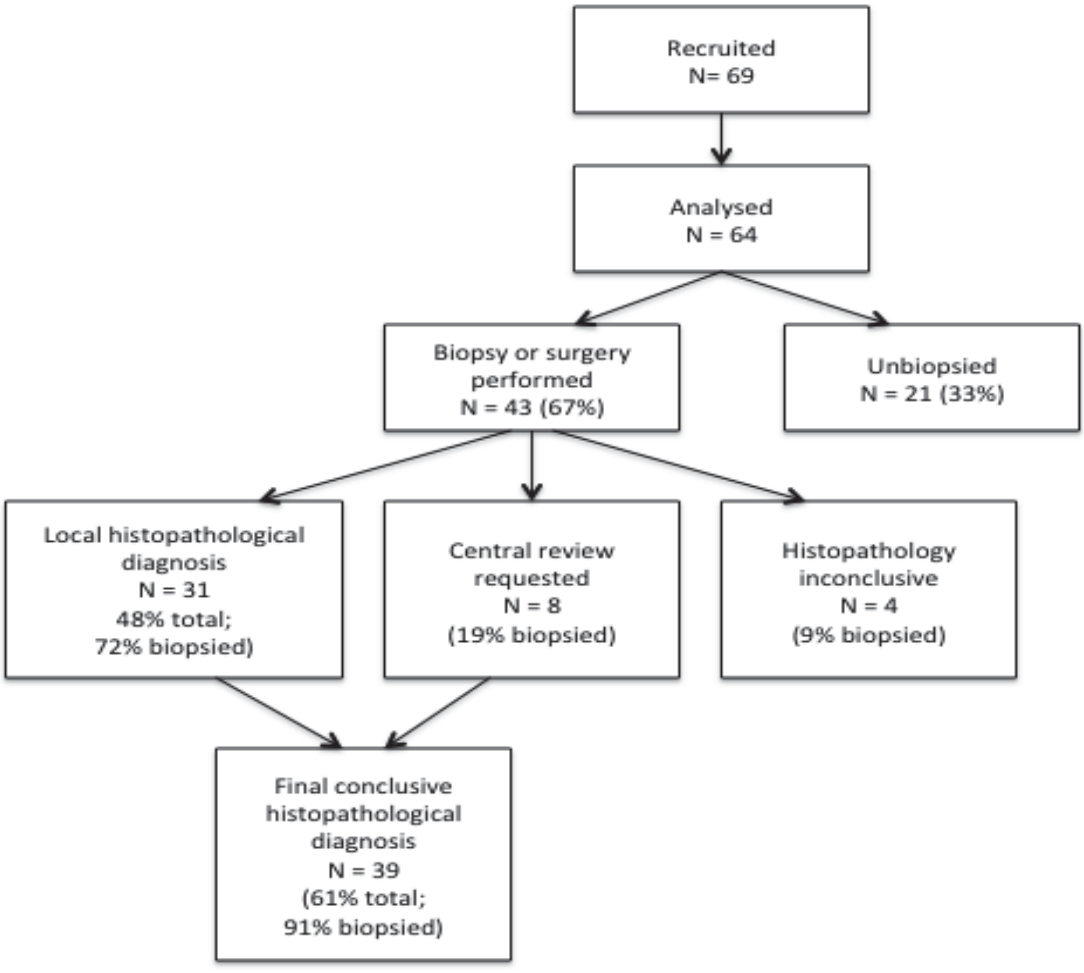

Figure 9.1. Consort chart. Availability of histopathology diagnosis for CNS lesions

9.3.3. MRS Quality Control

Of the 64 MRS studies performed, 11 (17%) failed quality control (QC). Of these, 5 did not meet standards for voxel placement and contained predominantly normal brain or necrotic tumour, 2 were incorrectly configured, 2 had poor signal:noise ratio, 1 had poor line-width secondary to intratumoral calcification and 1 was uninterpretable due to presence of blood products.

9.3.4. Non-invasive diagnosis using MRI alone and following addition of MRS

The principal MRI diagnosis was accurate in terms of exact accordance with the reference standard of diagnosis agreed by the MDT at study end in 38 of 64 patients (59% sensitivity), increasing to 47 (73% sensitivity) with addition of MRS (Table 9.2.). Nine of these 47 cases (19.1%: 95%CI (9.1%, 33.3%)) had been incorrectly diagnosed with MRI alone. MRS had a statistically significant effect on correct diagnosis for all tumour types ($p = 0.012$) (McNemar's Test). None of the 17 cases incorrectly diagnosed after MRS and MRI had been correctly diagnosed after MRI alone.

Of 40 supratentorial tumours, 17 (43% sensitivity) were correctly diagnosed with MRI alone with 24 (60% sensitivity) correctly diagnosed after MRS and MRI. Seven of the 24 (30.4%: 95%CI (13.2%, 52.9%)) were incorrectly diagnosed with MRI alone. None of 16 cases incorrectly diagnosed after MRS and MRI had previously been diagnosed correctly using MRI alone. McNemar's test shows a significant MRS effect on correct diagnosis ($p = 0.016$). The other tumour types in the posterior fossa and brainstem are too small in number for separate statistical consideration. Radiological diagnosis using MRI alone was accurate in 15 of 17 posterior fossa (88%) and six of seven brainstem (86%) tumours increasing to 16 (94%) and 17 (100%) respectively with addition of information from MRS.

Of the 38 accurate diagnoses made using MRI alone, 18 (28%) were certain ('correct') and 20 (31%) uncertain ('partially correct'). Following addition of MRS, confidence increased in 14 (37%) accurate MRI diagnoses with none incorrectly re-diagnosed. Addition of MRS resulted in an increase in confidence in correct MRI diagnosis in 41%, 27% and 50% of supratentorial, posterior fossa and brainstem lesions respectively. MRS identified both ependymomas preoperatively, neither of which were diagnosed on conventional MRI. Table 9.3. provides detailed analysis of diagnosis at each stage of the diagnostic pathway.

Table 9.2. Diagnosis of CNS lesions by location using MRI alone, MRI+MRS and histopathology

	Supratentorial	**Posterior Fossa**	**Brainstem**	**Total**
N	40	17	7	64
Accurate MRI diagnosis[a]	17 (43%)	15 (88%)	6 (86%)	38 (59%)
MRI diagnosis 'correct' (certain)	6 (15%)	9 (53%)	3 (43%)	18 (28%)
Accurate MRI+MRS diagnosis	24 (60%)	16 (94%)	7 (100%)	47 (73%)
Accurate MRI diagnoses with increased certainty following MRS	7/17 (41%)	4/15 (27%)	3/6 (50%)	14 (37%)
MRI diagnosis 'incorrect' or 'inconclusive' correctly diagnosed by MRS	8/23 (35%)	1/2 (50%)	1/1 (100%)	10/26 (38%)
MRS diagnosis 'incorrect'	2 (5%)	0	0	2 (3%)
Appropriate change in management after MRS	17 (43%)	2 (12%)	4 (57%)	23 (36%)
Biopsy/resection	26 (65%)	16 (94%)	1 (14%)	43 (67%)
Histopathological diagnosis available	24 (60%)	14 (82%)	1 (14%)	39 (61%)
Central histopathology review requested	8 (31% samples)	0	0	8 (19%)
Histopathology inconclusive	4 (15% samples)	0	0	4 (9%)

[a]Accurate MRI diagnosis = total 'correct' (certain) and 'partially correct'(uncertain)

Table 9.3. Diagnosis of CNS lesions by tumour type using MRI alone, MRI+MRS and histopathology

Multidisciplinary Team Diagnosis	Number	Total 'correct' MRI	Total 'partially correct' MRI	Total 'correct'+'partially correct' MRI	Total 'incorrect' or 'inconclusive' MRI	Total correct MRI+MRS	Total 'partially correct' MRI confirmed by MRS	Total 'incorrect' or 'inconcluvie' MRI correctly diagnosed by MRS	MRS 'incorrect'	Change in management resulting from MRS
Supratentorial	**40**	**6**	**11**	**17**	**23**	**24**	**7**	**8**	**2**	**17**
Anaplastic Astrocytoma	1	0	0	0	1	0	0	0	**0**	n=1: MRS confirmed high grade lesion: guided MDT decision to aim for complete resection
ATRT	3	0	0	0	3	0	0	0	1 (ependymoma)	n=1: Incorrect MRS diagnosis – did not alter management
Diffuse astrocytoma	1	0	1	1	0	1	0	0	0	n=1: MRS used to successfully guide biopsy of a heterogeneous lesion (CSI)
DNET	3	0	1	1	2	3	1	2	0	n=1: MRS suggestive of DNET (high mIns) avoided biopsy
Germinoma	1	1	0	1	0	1	0	0	0	
Glioblastoma multiforme	1	0	0	0	1	0	0	0	0	
Mixed germ cell tumour	1	0	1	1	0	1	1	0	0	n=1: MRS used to answer clinical question regarding diagnosis of bifocal or metastatic disease. Bifocal disease diagnosed resulting in treatment with proton beam RT rather than CSI.
Meningioma	1	1	0	1	0	1	0	0	0	
Teratoma	2	1	0	1	1	2	0	1	0	
Optic pathway glioma	2	1	1	2	0	2	1	0	0	n=1: metastatic OPG diagnosis uncertain using MRI alone. Confirmation with MRS allowed commencement of LGG protocol without biopsy.

Pilocytic astrocytoma	4	1	1	2	2	2	0	0	0	
Pilomyxoid astrocytoma	1	0	0	0	1	0	0	0	0	
Pituitary macroadenoma	1	0	0	0	1	0	0	0	0	
Supratentorial PNET	2	0	1	1	1	1	0	0	1 (ependymoma)	n=1: Incorrect MRS diagnosis – did not alter management
Supratentorial ependymoma	1	0	0	0	1	1	0	1	0	n=1: MRS suggested ependymoma, guided surgical planning to aim for complete resection
Non-malignant: (2=cortcal dysplasia, 1=pineal cyst, 1=epidermoid cyst, 6= incidental lesions)	10	1	5	6	4	9	4	4	0	n=8: Confident diagnosis of benign lesions made with addition of MRS. These diagnoses were uncertain using MRI alone. Avoided biopsy in 8 patients
Diagnosis Uncertain: (1= ?astroblastoma, 2=?tectal plate glioma, 2=?low grade glioma	5	0	0	0	5	0				n=2: Unusual MRS in ? astroblastoma and ? tectal plate glioma alerted to unusual pathology. Close monitoring enabled early detection of aggressive course. n=2:MRS suggestive of low grade lesions in 2 ? low grade gliomas – MDT decision to observe
Posterior Fossa	**17**	**9**	**6**	**15**	**2**	**16**	**4**	**1**	**0**	**2**
Medulloblastoma	6	3	3	6	0	6	2	0	0	0
Ependymoma	1	0	1	1	0	1	1	0	0	n=1: Confirming ependymoma preoperatively allowed surgical planning of complete resection. Intraoperative histopathology was inconclusive in this case.
Pilocytic Astrocytoma	7	6	1	7	0	7	1	0	0	

Non-malignant (incidental lesions)	3	0	1	1	2	1	0	1	0	n=1: Avoidance of biopsy in non-malignant lesion
Brainstem	**7**	**3**	3	**6**	**1**	**7**	**3**	**1**	**0**	**4**
DIPG	5	3	2	5	0	5	2	0	0	n=2: confirmation of DIPG diagnosis when MRI uncertain, allowed family discussions and referral to RT
Low Grade Glioma	2	0	1	1	1	2	1	1	0	n=2: Atypical MRS profile of pontine lesions alerted clinicians to diagnosis of LGG rather than DIPG. No radiotherapy given. n=1 observed (stable), n=1 treated on LGG protocol (stable)
Total	**64**	**18 (28%)**	**20 (31%)**	**38 (59%)**	**26 (41%)**	**47 (73%)**	**14 (14/38 = 37%)**	**10 (10/26 = 38%)**	**2**	**23 (36%)**

9.3.4. Lesions without histopathological diagnosis

Of all patients, 25 (39%) lacked histopathological diagnosis. Of these, 21 (84%; 33% all patients) were unbiopsied and four (16%) reported as inconclusive (one due to sampling error, three due to atypical histopathological appearance). MDT consensus diagnosis was reached in 21 (84%) of these patients, with diagnostic uncertainty remaining in four (16%). MRS contributed to diagnosis in 17 (68%) of this group, modifying it in three (12%). Management was influenced by MRS in 13 (52%) of these patients through avoiding biopsy (n=10), revision of diagnosis with subsequent appropriate management (n=1), and alerting to high-grade behaviour of lesions initially thought to be low grade (n=2). For diagnosis of CNS lesions managed without histopathology, see Tables 9.4. and 9.5.

Table 9.4. Diagnostic pathway of CNS lesions managed without histopathology

Reason for lack of histopathological diagnosis	Tumour Location	Multidisciplinary Team (MDT) Diagnosis	Diagnosis facilitated by MRS	Initial diagnosis modified by MRS	Management changed by MRS
Unbiopsied n=21 (33% all patients)	Supratentorial n=14; Posterior fossa n=1 Brainstem n=6	Indolent lesions n=11 (incidental lesions n=9, cortical dysplasia n=2)	n=9 indolent lesions MRS confirmed non-malignancy n=2 indolent lesions MRS unavailable – decision for conservative management based on conventional imaging	n=9 confirmed diagnosis: conventional MRI diagnosis uncertain	n=9 confident MRS diagnosis of non-tumour avoided biopsy in indolent lesions
		Optic pathway glioma n=2	n=1: Confirmed optic pathway glioma (metastatic)	n=1 confirmed diagnosis: conventional MRI diagnosis uncertain	n=1: Avoided biopsy in metastatic optic pathway glioma in patient with multiple comorbidities.
		DNET n=1	n=1: Confirmed DNET (high mIns)	n=1 confirmed diagnosis: conventional MRI diagnosis uncertain	
		Germinoma n=1	MRS diagnosis not documented		
		DIPG n=4	n=2: Confirmed DIPG (conventional MRI diagnosis uncertain)	n=2 confirmed diagnosis: conventional MRI diagnosis uncertain	
		Low grade glioma n = 2	n=2: Confirmed low grade glioma	n=1 confirmed diagnosis: conventional MRI diagnosis uncertain n=1 Re-diagnosis. Pontine lesion misdiagnosed as DIPG by MRI reclassified as LGG following MRS. Atypical MRS profile was suggestive of LGG. Diagnosis of LGG was verified through clinical course.	n=1: pontine lesion misdiagnosed as DIPG using MRI alone was reclassified as LGG following MRS. The child was treated on the LGG protocol and remains stable 16months after diagnosis.

Inconclusive histopathology n = 4 (6% all patients)	Supratentorial n=4	? tectal plate glioma n=2; ? astoblastoma n=1; ? low grade glioma n=1	n=1: Alerted to high grade tumour (?astroblastoma) in lesion initially thought low grade on conventional MRI and histopathology n=1: Confirmed low grade glioma where MRI diagnosis uncertain	n=2 Unusual MRS profiles alerted clincians to unusual tumour types. n=1: MRI diagnosis of tectal plate glioma. Histopathology inconclusive. Atypical MRS profile indicated tectal plate glioma unlikely. n=1: MRI diagnosis of tectal plate glioma. Histopathology inconclusive (?low grade glioma.: Central review ?astroblastoma). MRS profile not typical of tectal plate or low grade glioma alerting clinicians to unusual high grade tumour type.	n=1: MRI diagnosis tectal plate glioma. Atypical MRS profile resulted in close observation and early detection of increase in size. n=1: MRI diagnosis tectal plate glioma. MRS profile unusual alerting clinicians to unusual tumour type. Close monitoring enabled early detection of rapid increase in size and metastatic spread.
Total n=25 (39% all patients)		**21 (21/25 = 84%) (consensus TB diagnosis)**	**17 (17/25 = 68%) (MRS facilitated diagnosis)**	**3 (3/25 = 12%) (MRS modified diagnosis)**	**13 (13/25 = 52%) (MRS altered management)**

Table 9.5. Diagnosis of CNS lesions managed without histopathology

	Percentage (number)	Notes
Number of patients without histopathology	39% (25)	
MDT consensus diagnosis reached	84% (21)	Diagnostic uncertainty: 16% (4)
MRS contributed to MDT diagnosis	68% (17)	MRS modified diagnosis: 12% (3)
MRS influenced management	52% (13)	-Avoiding biopsy (10) -Revision of diagnosis with subsequent appropriate management (1) -Alerting to high-grade behaviour of lesions initially thought low grade (2).

9.3.5. Indolent lesions

Indolent lesions were diagnosed in 13 patients (20%), all of which were subsequently verified on clinical course. Non-invasive diagnosis of incidental tumours and cortical dysplasia was made in 11 patients (85%), with MRS making a major contribution to 10 (91%) of these diagnoses. A major contribution describes a case in which diagnosis was unclear prior to addition of MRS interpretation, but information from MRS allowed formulation of a clear diagnosis and management plan. The diagnosis of whether the tumour was indolent in these 11 cases was not clear from MRI interpretation alone, but review of MRS allowed the diagnosis to be made with confidence. MRI alone suggested a diagnosis of non-malignant lesion in 6 cases (46%), none of which were certain (all "partially correct"). There was no misclassification of malignant lesions as indolent using MRS.

Histopathology was available in 2 of these 13 patients, confirming an arteriovenous malformation in one and a pigmented epidermoid cyst in the other. The arterioveous malformation was seen on imaging as a hyperdense lesion on the dorsal aspect of the pons with a ring of T1 enhancement and visible patchy hemosiderin. Imaging features

were suggestive of pontine cavernoma, but concerns regarding possible underlying pathology led to national multidisciplinary review with the recommendation for biopsy. The epidermoid cyst was confirmed histopathologically following surgical resection of a posterior fossa lesion with associated gross symptomatic hydropcephalus. Table 9.6. provides details of diagnosis of indolent lesions.

Table 9.6. Diagnosis of indolent lesions

	Number	**Percentage**
Number of indolent lesions	13 (Supratentorial 10; Posterior Fossa 3)	20% total
Indolent lesions diagnosed non-invasively	11	85%
Indolent lesions diagnosed following MRI alone	6 (all "partially correct")	46%
Indolent lesions diagnosed following MRI+MRS	10	77%
Malignant lesions misclassified as indolent using MRS	0	0
Indolent lesions biopsied	2 (AV malformation; epidermoid cyst)	15%
Management changed by MRS	10 (avoided biopsy)	10/11 unbiopsied = 91% non-invasive diagnoses confirmed using MRS

9.3.6. Treatment

Treatment was initiated a median of 28 (1–364) days following initial imaging. In 10 patients (seven medulloblastomas; two diffuse intrinsic pontine gliomas (DIPG); one glioblastoma multiforme) first line treatment with radiotherapy commenced a median of 45.5 (13-53) days after imaging, or 43.5 (31-49) days after surgery. In medulloblastoma, the median time from surgery to radiotherapy was 45 days (31-49), longer than the recommended standard of 28-41 days recommended to confer good prognosis.

9.3.7. MRS and clinical management

MRS influenced clinical management in 36% of cases (23 patients) through avoiding and guiding biopsy, aiding tumour characterisation, facilitating diagnosis in cases without histopathology, surgical planning, and identifying unusual tumour types.

9.3.8. Examples of cases in which MRS influenced clinical management

The following cases are examples of patients in which MRS influenced or improved clinical management. Conventional MR images and corresponding MRS profiles are demonstrated to illustrate the information conveyed through the two complementary imaging modalities, and the role of MRS in guiding clinical decision-making.

Case 1. Determining biopsy site in a heterogeneous lesion (Figure 9.2.)

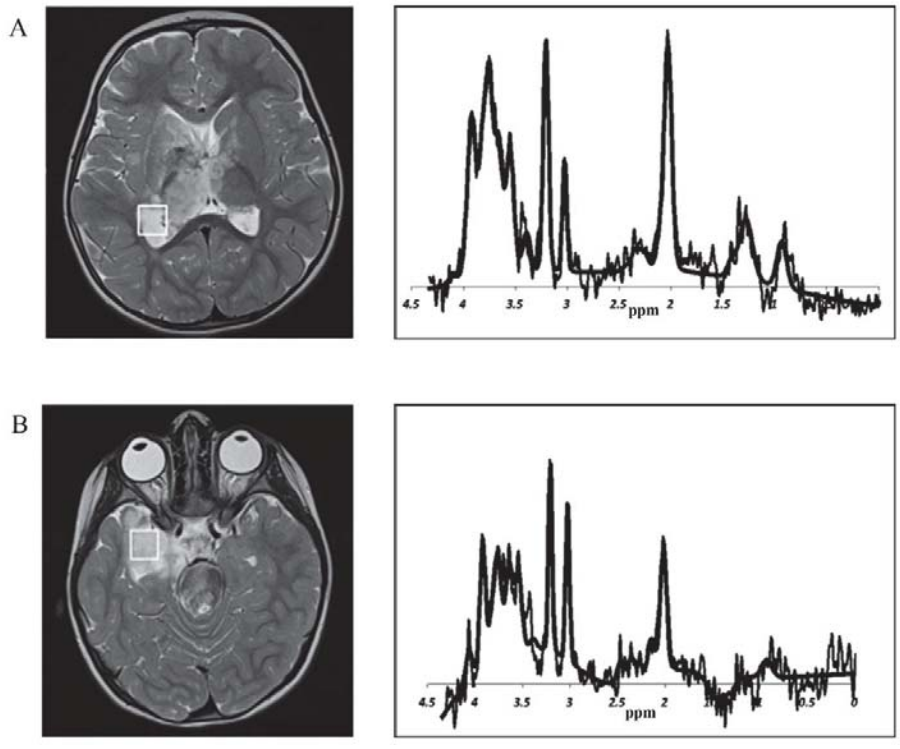

Figure 9.2. Determining biopsy site in a heterogeneous lesion
A) Right thalamus and trigone
B) Medial temporal lobe

MRI of a 2-year old girl revealed a diffuse, heterogeneous CNS lesion affecting the right thalamus and trigone (A) and medial temporal lobe (B). Although the right trigone was a more surgically accessible biopsy site it was unclear if this contained representative tumour, or very diffuse infiltrating tumour and oedema unlikely to provide positive histopathology. Accessing the medial temporal lobe, which looked more typical of tumour on conventional imaging, necessitated a more invasive procedure with higher risk of morbidity. To aid decision-making repeat MRI with spectroscopy was performed over potential biopsy sites, revealing increased choline:creatine ratio over the right thalamus and trigone suggestive of representative tumour tissue. The overall MRS in this region was suggestive of a childhood low-grade glioma. Successful biopsy of this area with minimal morbidity yielded histopathological diagnosis of low-grade glioma.

Case 2. Exclusion of metastatic disease: bifocal, mixed germ cell tumour (Figure 9.3.)

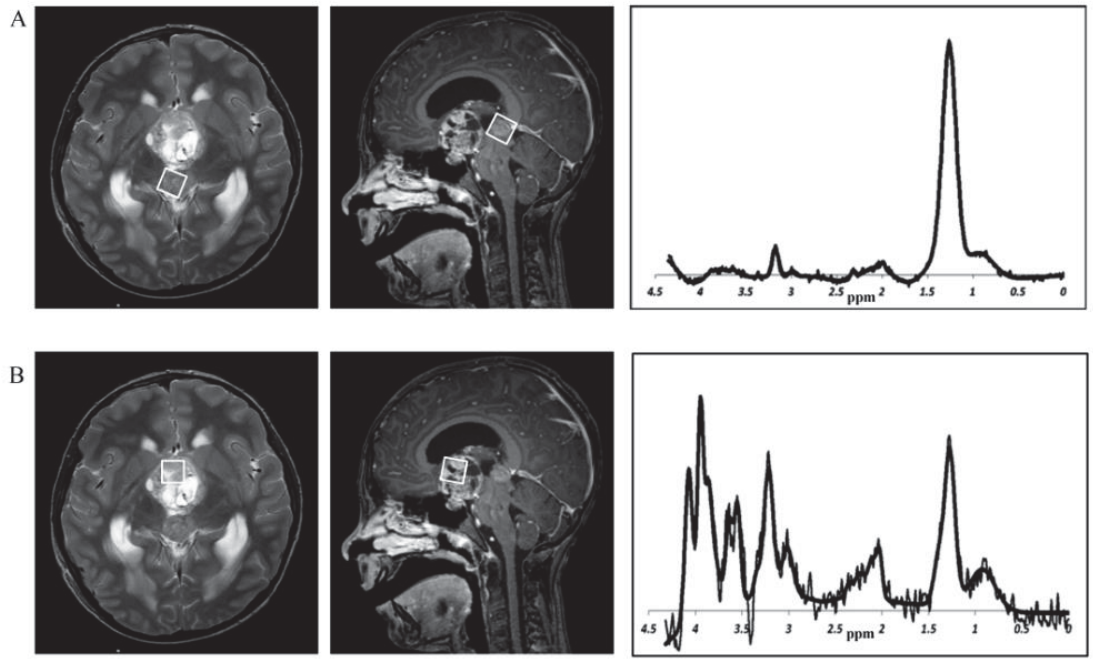

Figure 9.3. Exclusion of metastatic disease in a bifocal, mixed germ cell tumour
A) Pineal component
B) Suprasellar component

MRI of a 9-year old boy revealed a bifocal midline tumour radiologically consistent with a mixed germ cell tumour with possible metastatic disease. MRS profiles of two components this tumour appeared very different. The homogeneous pineal component (A) had a spectrum typical of germinoma, whereas the heterogeneous suprasellar component (B) had a profile suggestive of the secreting component of a germ cell tumour. MRS thus facilitated exclusion of metastatic disease in favour of bifocal germ cell tumour without the need for biopsy of the pineal lesion. Metastatic germ cell tumour would have required cranio-spinal irradiation (CSI) whereas the diagnosis of bifocal germ cell tumour allowed monitoring of the suprasellar lesion without CSI initially. Rapid life-threatening suprasellar tumour progression subsequently necessitated surgical resection. The patient was later referred for focal proton beam radiotherapy instead of CSI.

Case 3. Pre-operative diagnosis facilitating surgical planning (Figure 9.4.)

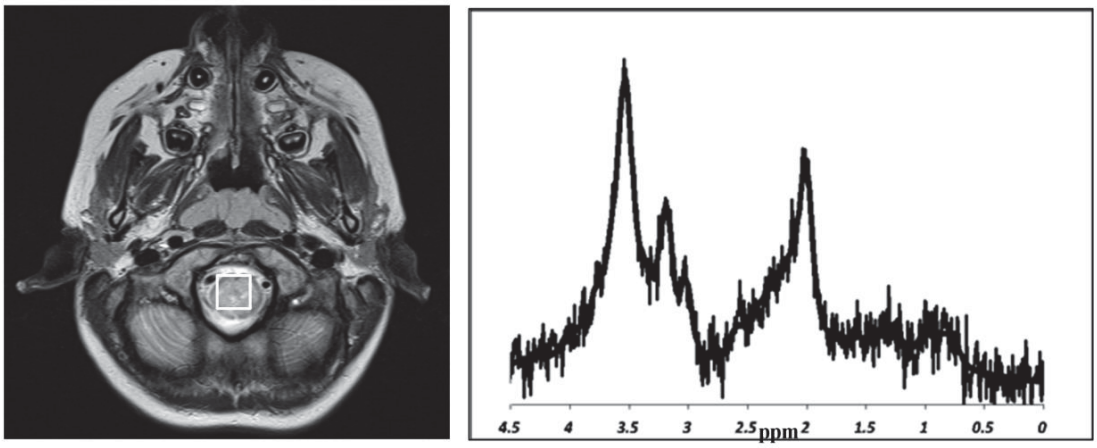

Figure 9.4. Pre-operative diagnosis facilitating surgical planning

MRI of a 9-year old boy with an underlying diagnosis of neurofibromatosis type 2 (NF2) revealed an infratentorial lesion radiologically consistent with pilocytic astrocytoma or ependymoma. The tumour was diagnosed pre-operatively as an

ependymoma using information from MRS, allowing surgical planning for complete resection. Interestingly, although high myo-inositol on MRS of this case supported a diagnosis of ependymoma, intraoperative histopathology did not support this. The final histopathological diagnosis confirmed ependymoma.

Case 4. Identification of high-grade, unusual tumour types in cases with inconclusive histopathology (Figure 9.5.)

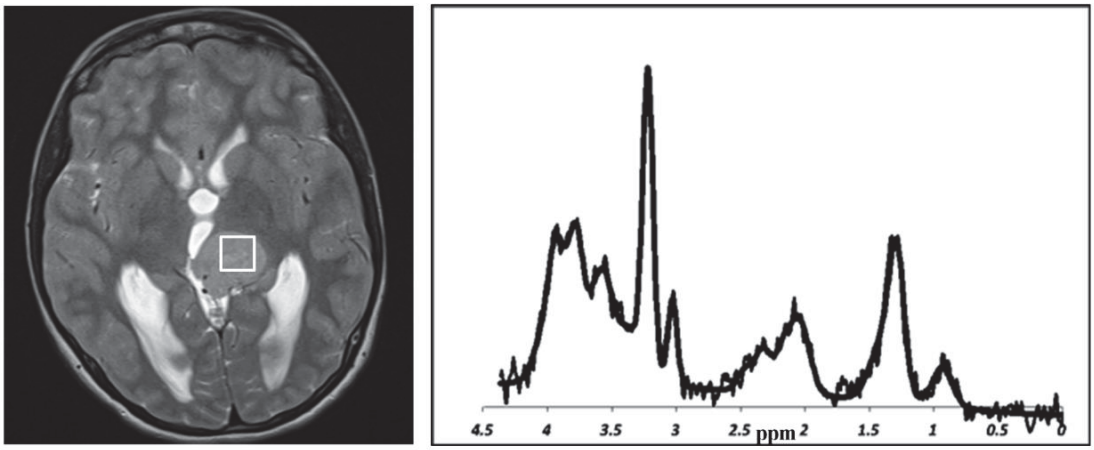

Figure 9.5. Identification of high-grade, unusual tumour types in a case with inconclusive histopathology

MRI of a 13-year old girl revealed a supratentorial tumour of uncertain diagnosis. Although a definitive diagnosis was not made following biopsy, the lesion demonstrated histological features consistent with a low-grade tumour. MRS demonstrated high-grade features of high choline, low N-acetyl aspartate and high lipids. This unusual MRS profile alerted clinicians to the possibility of rare tumour type and possible sampling error on biopsy, which was later confirmed. Close monitoring allowed early detection of rapid growth and metastatic spread. This tumour followed an aggressive course and was diagnosed as a probable astroblastoma following central review.

9.3.9. Incorrect MRS diagnoses

Two incorrect diagnoses were made using MRS (ATRT and supratentorial PNET both misdiagnosed as ependymoma). Neither was correctly diagnosed on MRI and management was not altered. MRS diagnosis was not documented in 18 cases (28%), and unsuitable for analysis in two (3%) due to tumour calcification and poor line-width.

9.4. Discussion

This study indicates that MRS can guide clinical decision-making in paediatric neuro-oncology through provision of information unavailable from conventional imaging. Visual interpretation of MRS resulted in improved accuracy and confidence in non-invasive diagnosis of paediatric brain tumours in real time in clinical practice. In addition to facilitating diagnosis of tumour type, MRS allowed confident identification of indolent lesions with avoidance of biopsy and its associated comorbidities. The additional information provided also influenced patient management through guiding biopsy of heterogeneous tumours, aiding tumour characterisation, allowing diagnosis in cases without histopathological confirmation and identifying unusual and aggressive tumour types.

This is the first study evaluating the impact of MRS on clinical decision-making in paediatric neuro-oncology. The degree of improvement in diagnostic accuracy from that obtained with MRI alone (59%) to that following MRS (73%) is similar to other reports (Arle et al., 1997; Shiroishi et al., 2015). Work described in chapter 7 found addition of MRS improved non-invasive diagnostic accuracy for paediatric brain tumours at all locations from 69% to 77%. The slightly higher accuracies in this

earlier work may be explained by the higher level of neuroradiological expertise of the three participating radiologists, all of whom formed part of the Neuro-Oncology MDT, compared to radiologists in this study who were not pre-selected and had more varied neuroradiology experience. The work described in this chapter investigated the impact of MRS on clinical practice in real time, capturing the complexities and limitations of radiological reporting and decision-making in a clinical setting.

This study aimed to reflect clinical practice through describing added value of MRS in unselected CNS lesions, incorporating challenges of variable neuroradiology experience and data quality. Radiologists in Birmingham Children's Hospital perform visual interpretation of MRS profiles generated through scanner software prior to availability of TARQUIN analysis. This is advantageous as information is available to clinicians in real time, but is a limitation in terms of optimising diagnostic accuracy. Studies have shown improved accuracy using sophisticated data analysis techniques and automated classifiers (Vicente et al., 2013; Wang et al., 1995; Arle et al., 1997; Davies et al., 2008), but these are currently unavailable for clinical use. Making classifiers and decision support systems widely available may improve MRS interpretation and allow its use in centres with less expertise. Supporting clinical practice is a key objective to allow routine implementation of MRS to improve patient care and is an important aim for the future. Indeed the incorporation of MRS into MIROR is currently being undertaken.

The limitations of histopathology as gold standard for brain tumour diagnosis have previously been described. In this cohort, 15% histopathology samples were reported as inconclusive and 19% required central review, and the delay of a median of 12

days from imaging to histopathological confirmation potentially translated into delay in initiating treatment. Median time from surgery to radiotherapy in medulloblastoma was 45 days, longer than the recommendation of 28-41 days to confer good prognosis in standard risk patients. It is important to consider the potential for reducing time-to-treatment conferred through accurate non-invasive diagnosis with MRS, particularly with emergence of proton therapy where times from decision to treatment initiation may be longer due to the centralisation of services.

This retrospective study was limited by completeness of contemporaneous documentation of both MRI and MRS interpretation and the clinical decisions that ensued. This may have resulted in under-reporting of both diagnostic accuracy and the impact of MRS on management decisions. There is, unfortunately, no current standardization in either radiological reporting or recording the decisions of the MDT. As there is an inevitable lack of precision in information documented in a retrospective study where recording standards were not predetermined, future prospective studies should use specific recording standards to overcome this limitation. It is not uncommon for a radiologist to give a broad differential even in light of a more certain suspicion, possibly resulting in a greater number of "partially correct" outcomes. As it is difficult to make management decisions based on broad differentials, it could be argued that MRS added value to the clinical decision-making process through narrowing the long list of possibilities made from conventional imaging and confirming the correct diagnosis. Follow-up time is relatively short, the longest being 2 years post-diagnosis, and it is possible that MDT diagnosis may be reviewed in some cases at a later date.

A further limitation is that this study included a small number of cases managed at a single centre, cautioning against generalization of results to centres with different levels of expertise and processes. The results described reflect practice in Birmingham Children's Hospital, one of the largest institutions in the United Kingdom with a well-established, specific Neuro-Oncology MDT, an active imaging research program, and well established interest in advanced MRI techniques such as MRS. Clinicians also have the opportunity for support with MRS interpretation from an active research team and expert clinicians. This may limit the ease with which these results can be replicated by institutions with less spectroscopy experience. This study should be repeated in other institutions, preferably in a prospective manner, where definitions and recoding standards can be agreed prior to acquiring data. A number of patients in this study lacked histopathological diagnosis, reflecting clinical practice. Although it is more challenging to make a definitive diagnosis on cases without histology, MDT diagnoses were verified through clinical course rather than simply being accepted as correct following MRI and MRS. Clinical course on follow-up is an important element of confirming the diagnosis for unbiopsied lesions: no lesion diagnosed as indolent by the MDT, for example, subsequently demonstrated aggressive behaviour.

Benefits of MRS in this patient cohort included guidance for management for lesions lacking histopathology, and support of decisions for observation rather than biopsy following MRS suggestive of indolence. A limitation of an observational study is that it cannot be certain that patients would not have been managed in the same way without MRS. Contemporaneous documentation did, however, reveal MRS to provide additional useful clinical information contributing to the clinical decisions made, and

it could be argued that inclusion of a modality providing reassurance adds value to clinical decision-making regarding observation of benign lesions. Multi-parametric imaging will not replace tumour tissue analysis in the majority of cases, but having a more accurate diagnosis early in the patient pathway can have some major advantages. Surgical strategies can be influenced, plans can be made in a more timely manner even if they need refining at a later date, and discussions with the family can proceed.

There is a paucity of research into the optimum way to implement MRS into diagnostic and management pathways. Added value of MRS over conventional imaging in therapeutic decision-making has not been evaluated prospectively in the paediatric population in a multicentre setting and studies are needed in this area. Further work with longer follow up times and clear outcome measures is needed to evaluate the impact of MRS on patient management and clinical outcomes.

9.5. Conclusion

MRS provides information to facilitate clinical decision-making additional to that available through conventional radiological methods. There is potential to improve patient outcomes through accurate early non-invasive diagnosis, avoiding biopsy of indolent lesions, aiding tumour characterisation and facilitating early treatment planning. There has been considerable progress in development and evaluation of MRS in paediatric oncology. Integration into clinical practice could help guide important management decisions and individualise treatment. Further multicentre research is needed to define the optimum use of MRS in a clinical setting and

integrate this technique into routine clinical practice to improve care of children with cancer.

Chapter 10: Conclusions and Future Work

10.1. Conclusions

This thesis has demonstrated that functional imaging has potential to add value to diagnosis and treatment monitoring in paediatric oncology compared with conventional MRI alone. Presentation of complex information derived from DWI and ADC histogram analysis through a clinical decision support system (CDSS), MIROR, and provision of visually interpretable comparator mean MR spectra, were well received by radiologists and applicable in a clinical setting. Incorporating these techniques into clinical practice has potential to facilitate clinical decision-making and ultimately improve patient care.

Quantitative DWI and ADC histogram analysis could facilitate non-invasive diagnosis of paediatric solid body tumours as histograms of benign and malignant tumours are morphologically and quantifiably different. Histograms of malignant tumours appear shifted to the left, more positively skewed and peaked than those of benign lesions, reflected numerically by significantly lower ADC percentile values and higher skewness and kurtosis. Parameters obtained from more complex IVIM analysis did not perform as well as ADC. The information described could be made accessible and comprehensible for clinicians through MIROR, a CDSS developed as an integral part of this research. Calculating mean ADC histograms for benign and malignant tumours from data stored within a continually updated repository could facilitate diagnosis of new cases through allowing visual comparison of index and mean histograms.

Visual interpretation of ADC histograms significantly improved prospective non-invasive radiological discrimination of benign from malignant body tumours over

conventional MRI alone. Following morphological comparison of the ADC histogram of an index case with mean histograms derived from the MIROR repository, the percentage of benign tumours correctly diagnosed improved from 45% to 73%, with no malignant tumours incorrectly diagnosed. The technique was well received by radiologists, who considered ADC histogram analysis using MIROR a clinically applicable and potentially valuable additional diagnostic tool to confirm or refute a provisional diagnosis of malignancy.

Quantitative ADC and IVIM histogram analysis are promising non-invasive biomarkers of chemotherapeutic response of childhood solid tumours, conferring additional information to measuring change in size. Visual interpretation of ADC histograms revealed a shift to the right and marked morphological changes in shape following treatment, reflected through significant quantitative differences in parameters including increases in ADC and D. Imaging biomarkers analysed show similar properties across a range of paediatric tumour types. MIROR allowed clinicians to interpret, analyse and compare MR images and complex ADC and IVIM histogram data through superimposition of pre- and post-treatment histograms and provision of comparator quantitative parameters.

ADC histogram analysis provides reproducible, user-independent data that is robust to methodology of ROI construction and accurately reflects tissue characteristics of the imaged lesion. Inter-rater reproducibility of both whole-tumour (WT) and single-slice (SS) ROIs is excellent, and histogram-derived parameters from SS ROIs enable classification of benign and malignant tumours as well as those derived from WT ROIs. As WT ROI construction is labour-intensive and time-consuming, construction

of a single ROI around the largest axial tumour slice can be recommended to obtain an ADC histogram for clinical use. This technique is time-efficient, user-independent and clinically applicable, which may facilitate integration of quantitative ADC histogram analysis into clinical practice.

Qualitative radiological review of single voxel ^{1}H-MRS can improve accuracy of non-invasive diagnosis of paediatric brain tumours and add value in the diagnostic pathway. Radiologists' principal MRI diagnosis was correct in 69% of an unselected cohort of childhood CNS lesions, increasing to 77% with MRS with significantly improved inter-rater agreement. Non-invasive diagnosis of posterior fossa tumours with MRS may be sufficiently accurate (88%) to recommend treatment planning prior to histopathological confirmation. MRS added further value through radiologists' increased certainty of correct diagnosis and reduced number of differentials, with additional expert spectroscopist review proving helpful in characterisation of difficult cases.

In addition to improving non-invasive diagnosis, MRS can add therapeutic value to conventional imaging and facilitate clinical decision-making in paediatric neuro-oncology. MRS has potential to enhance patient care through avoiding biopsy of indolent lesions, aiding tumour characterisation and facilitating earlier family discussions and treatment planning. Integration into clinical practice can help guide important management decisions and individualise treatment.

10.2. Development of MIROR as a CDSS

This research has contributed to the development, refinement and evaluation of MIROR as a CDSS suitable for integration into clinical practice. This involved working closely with radiologists to determine clinical usability, with feedback incorporated into the on-going design process to develop a tool based on the needs of those intended to utilise it. Although work to date has predominantly involved analysis of advanced DWI data, there is potential to incorporate modules for analysis of other imaging information, such as MR spectroscopy. Availability of a user-friendly and flexible CDSS that encompasses a variety of medical image analysis techniques and post-processing methods could facilitate uptake of advanced MRI in a real-time clinical setting.

MIROR has potential to guide clinicians through the implementation and analysis of advanced imaging techniques in real-time and engender clinical acceptance through translational applications. The current version has a user-friendly graphical user interface that allows clinicians to draw a region of interest (ROI) around a tumour and measure morphologic properties such as size, shape and volume. Statistical data analysis of the ROI overlaid on advanced ADC parametric maps allows derivation of an ADC histogram, from which parameters such as median, entropy, skewness, kurtosis and various centile values are extracted and stored. The self-archiving repository allows continual expansion with acquisition of new tumour cases, and on-going improvement of prediction accuracy of available biomarkers in the database. MIROR provides decision support to aid diagnosis through allowing visual comparison of a case histogram with mean histograms of benign and malignant tumours stored within the repository, and can also be used to compare sequentially

acquired histograms from an individual case to monitor changes with treatment and ascertain degree of chemotherapeutic response.

10.3. Future Work

The work in this thesis has highlighted several areas for future research. Establishment of quantitative reference values for descriptive parameters of ADC histogram shape, such as skewness, kurtosis and entropy, may provide useful additional information for diagnosis of malignancy in body tumours. Sophisticated multi-variate analysis techniques could facilitate discrimination between benign and malignant lesions, and more cases are needed to build adequate predictive models and determine cut-off values, which should be validated for clinical use. Further research with larger tumour cohorts and prospective testing is needed to determine robust quantitative measures that may be employed in a fully automated CDSS, the development of which is an important aim for the future.

The potential for mean ADC histograms of individual types of malignant tumours to facilitate tumour-specific non-invasive diagnosis should be evaluated. Acquisition of sufficient cases from which to determine robust representative examples and calculate reference histogram parameters will be possible through continuing growth of the MIROR tumour repository. Research is needed to determine whether histogram analysis may identify high-risk tumours and provide prognostic information. The role in determining chemotherapeutic response requires further study, including prospective validation in a larger patient cohort through links to clinical trials with well-specified treatment protocols, exploring changes early in the course of treatment, and correlating histogram parameters with histopathology. Longer follow-up times

are required to determine outcome and survival associations with identified biomarkers. Exploration of the role of IVIM in diagnosis and treatment monitoring is another aim, particularly additional value of the perfusion factor f. It is also important to evaluate MIROR and the ROI techniques recommended in a multicentre setting to establish whether results obtained in our single centre are reproducible and widely applicable.

Despite the growing body of evidence for the added diagnostic and therapeutic value of MRS, further work is needed to define its optimum use in clinical practice and make clear recommendations for incorporation into diagnostic and therapeutic pathways. Prospective multi-centre studies with standardised acquisition and analysis protocols are needed to validate findings for the added value of MRS in a range of clinical settings. The acquisition of mean, location-specific MR spectra for rare tumour types and providing example spectra at higher field strengths is important on-going work. Developing usable classifiers and CDSSs for radiologists is a key future aim to improve MRS interpretation and clinical integration. Expansion of the functionality of MIROR will include addition of more embedded advanced quantitative analysis options for MRS, with addition of real-time interactive machine learning to optimise use of available information.

The studies described in this thesis are an important base for further larger multicentre prospective studies allowing subgroup analysis and collection of outcome-related data. Further work is needed to continue integration of these promising new techniques into clinical practice, evaluate their applicability and reproducibility in a

multicentre setting, and formulate recommendations for incorporation into diagnostic and therapeutic pathways.

10.4. Summary of findings

This thesis demonstrates that diffusion weighted imaging with quantitative ADC histogram analysis is a valuable adjunct to conventional imaging in diagnosis and treatment monitoring of solid childhood body tumours. Single voxel magnetic resonance spectroscopy adds value to information provided through MRI in non-invasive diagnosis and therapeutic management of paediatric CNS lesions. Presentation of information derived from these advanced imaging techniques in a visual manner through a CDSS (MIROR) improves accessibility and clinical applicability, potentially allowing use in real-time in a clinical setting to improve care of children with cancer.

11. References

Abdel Razek, A.A.K., Gaballa, G., Elhawarey, G., et al. (2009) Characterization of pediatric head and neck masses with diffusion-weighted MR imaging. **European radiology**, 19 (1): 201–208

Abdel Razek, A.A.K., Soliman, N. and Elashery, R. (2012) Apparent diffusion coefficient values of mediastinal masses in children. **European Journal of Radiology**, 81 (6): 1311–1314

Alibek, S., Cavallaro, A., Aplas, A., et al. (2009) Diffusion weighted imaging of pediatric and adolescent malignancies with regard to detection and delineation: initial experience. **Academic radiology**, 16 (7): 866–871

Anderson, J., Slater, O., McHugh, K., et al. (2002) Response without shrinkage in bilateral Wilms tumor: significance of rhabdomyomatous histology. **Journal of pediatric hematology/oncology**, 24 (1): 31–34

Arle, J.E., Morriss, C., Wang, Z.J., et al. (1997) Prediction of posterior fossa tumor type in children by means of magnetic resonance image properties, spectroscopy, and neural networks. **Journal of neurosurgery**, 86 (5): 755–761

Astrakas, L., Ye, S., Zarifi, M., et al. (2006) The clinical perspective of large scale projects: a case study of multiparametric MR imaging of pediatric brain tumors. **Oncology reports**, 15 Spec no.: 1065–1069

Astrakas, L.G., Zurakowski, D., Tzika, A.A., et al. (2004) Noninvasive magnetic resonance spectroscopic imaging biomarkers to predict the clinical grade of pediatric brain tumors. **Clinical cancer research : an official journal of the American Association for Cancer Research**, 10 (24): 8220–8228

Barker, P.B., Hearshen, D.O. and Boska, M.D. (2001) Single-voxel proton MRS of the human brain at 1.5T and 3.0T. **Magnetic resonance in medicine**, 45 (5): 765–769

Bartha, R., Megyesi, J.F. and Watling, C.J. (2008) Low-grade glioma: correlation of short echo time 1H-MR spectroscopy with 23Na MR imaging. **AJNR. American journal of neuroradiology**, 29 (3): 464–470

Battal, B., Akgun, V. and Kocaoglu, M. (2012) Diffusion-weighted MRI beyond the central nervous system in children. **Diagnostic and interventional radiology (Ankara, Turkey)**, 18 (3): 288–297

Bhapkar, V.P. (1966) A Note on the Equivalence of Two Test Criteria for Hypotheses in Categorical Data. **Journal of the American Statistical Association**, 61 (313): 228–235

Bluml, S., Panigrahy, A., Laskov, M., et al. (2011) Elevated citrate in pediatric astrocytomas with malignant progression. **Neuro-oncology**, 13 (10): 1107–1117

Bossuyt, P.M., Reitsma, J.B., Bruns, D.E., et al. (2003) The STARD statement for reporting studies of diagnostic accuracy: explanation and elaboration. The Standards for Reporting of Diagnostic Accuracy Group. **Croatian medical journal**, 44 (5): 639–650

Bottomley, P.A. (1987) Spatial localization in NMR spectroscopy in vivo. **Annals of the New**

York Academy of Sciences, 508: 333–348

Bull, J.G., Saunders, D.E. and Clark, C.A. (2012) Discrimination of paediatric brain tumours using apparent diffusion coefficient histograms. **European radiology**, 22 (2): 447–457

Calvar, J.A., Meli, F.J., Romero, C., et al. (2005) Characterization of brain tumors by MRS, DWI and Ki-67 labeling index. **Journal of neuro-oncology**, 72 (3): 273–280

Castillo, M., Kwock, L. and Mukherji, S.K. (1996) Clinical applications of proton MR spectroscopy. **AJNR. American journal of neuroradiology**, 17 (1): 1–15

Castillo, M., Smith, J.K. and Kwock, L. (2000) Correlation of myo-inositol levels and grading of cerebral astrocytomas. **AJNR. American journal of neuroradiology**, 21 (9): 1645–1649

Chan, J.H., Tsui, E.Y., Luk, S.H., et al. (2001) Diffusion-weighted MR imaging of the liver: distinguishing hepatic abscess from cystic or necrotic tumor. **Abdominal imaging**, 26 (2): 161–165

Children's Cancer and Leukaemia Group. (2018) Recommendations for the use of paediatric tumour biopsy. Available at: https://www.cclg.org.uk/write/MediaUploads/Member%20area/Treatment%20guidelines/Recommendations_for_use_of_renal_tumour_biopsy_Feb_2018.pdf

Clementi, V., Tonon, C., Lodi, R., et al. (2005) Assessment of glutamate and glutamine contribution to in vivo N-acetylaspartate quantification in human brain by (1)H-magnetic resonance spectroscopy. **Magnetic resonance in medicine**, 54 (6): 1333–1339

Costello, L.C., Franklin, R.B. and Narayan, P. (1999) Citrate in the diagnosis of prostate cancer. **The Prostate**, 38 (3): 237–245

Davies, N.P., Arvanitis, T.N., Auer, D., et al. (2010a) Multicentre prospective classification of childhood brain tumours based on 'H MRS metabolite profiles. **In: Neuro-Oncology. (**pp. II32 - II32). Oxford Univ Press Inc. (2010)

Davies, N.P., Wilson, M., Harris, L.M., et al. (2008) Identification and characterisation of childhood cerebellar tumours by in vivo proton MRS. **NMR in Biomedicine**, 21 (8): 908–918

Davies, N.P., Wilson, M., Natarajan, K., et al. (2010b) Non-invasive detection of glycine as a biomarker of malignancy in childhood brain tumours using in-vivo 1H MRS at 1.5 tesla confirmed by ex-vivo high-resolution magic-angle spinning NMR. **NMR in Biomedicine**, 23 (1): 80–87

Davies, N.P., Manias, K.A., Wilson, M.,., et al. (2016) Prospective evaluation of MRS-based classification of childhood cerebellar tumours (unpublished)

de Graaf, R.A. (2009) In Vivo NMR Spectroscopy: Principles and Techniques. **Academic radiology**, 16 (7): 866–871

Demir, S., Altinkaya, N., Kocer, N.E., et al. (2015) Variations in apparent diffusion coefficient values following chemotherapy in pediatric neuroblastoma. **Diagnostic and interventional radiology (Ankara, Turkey)**, 21 (2): 184–188

Dredger, S.M., Kothari, A., Morrison, J., et al. (2007) Using participatory design to develop

(public) health decision support systems through GIS. **International journal of health geographics**, 6: 53

Drevelegas, K., Nikiforaki, K., Constantinides, M., et al. (2016) Apparent Diffusion Coefficient Quantification in Determining the Histological Diagnosis of Malignant Liver Lesions. **Journal of Cancer**, 7 (6): 730–735

Eisenhauer, E.A., Therasse, P., Bogaerts, J., et al. (2009) New response evaluation criteria in solid tumours: revised RECIST guideline (version 1.1). **European journal of cancer (Oxford, England : 1990)**, 45 (2): 228–247

Federau, C., Maeder, P., O'Brien, K., et al. (2012) Quantitative measurement of brain perfusion with intravoxel incoherent motion MR imaging. **Radiology**, 265 (3): 874–881

Feuerlein, S., Pauls, S., Juchems, M.S., et al. (2009) Pitfalls in abdominal diffusion-weighted imaging: how predictive is restricted water diffusion for malignancy. **AJR. American journal of roentgenology**, 193 (4): 1070–1076

Gahr, N., Darge, K., Hahn, G., et al. (2011) Diffusion-weighted MRI for differentiation of neuroblastoma and ganglioneuroblastoma/ganglioneuroma. **European Journal of Radiology**, 79 (3): 443–446

Galanaud, D., Nicoli, F., Chinot, O., et al. (2006) Noninvasive diagnostic assessment of brain tumors using combined in vivo MR imaging and spectroscopy. **Magnetic resonance in medicine**, 55 (6): 1236–1245

Garcia-Gomez, J.M., Luts, J., Julia-Sape, M., et al. (2009) Multiproject-multicenter evaluation of automatic brain tumor classification by magnetic resonance spectroscopy. **Magma (New York, N.Y.)**, 22 (1): 5–18

Gauvain, K.M., McKinstry, R.C., Mukherjee, P., et al. (2001) Evaluating pediatric brain tumor cellularity with diffusion-tensor imaging. **AJR. American journal of roentgenology**, 177 (2): 449–454

Gawande, R.S., Gonzalez, G., Messing, S., et al. (2013) Role of diffusion-weighted imaging in differentiating benign and malignant pediatric abdominal tumors. **Pediatric radiology**, 43 (7): 836–845

Gill, S.K., Wilson, M., Davies, N.P., et al. (2014) Diagnosing relapse in children's brain tumors using metabolite profiles. **Neuro-oncology**, 16 (1):156-164

Govindaraju, V., Young, K. and Maudsley, A.A. (2000) Proton NMR chemical shifts and coupling constants for brain metabolites. **NMR in Biomedicine**, 13 (3): 129–153

Grachev, I.D. and Apkarian, A.V. (2000) Chemical heterogeneity of the living human brain: a proton MR spectroscopy study on the effects of sex, age, and brain region. **NeuroImage**, 11 (5 Pt 1): 554–563

Grech-Sollars M., Hales P.W., Miyazaki K., et al. (2015) Multi-centre reproducibility of diffusion MRI parameters for clinical sequences in the brain. **NMR in Biomedicine**, 28 (4): 468-85

Hales, P.W., Olsen, O.E., Sebire, N.J., et al. (2015) A multi-Gaussian model for apparent

diffusion coefficient histogram analysis of Wilms' tumour subtype and response to chemotherapy. **NMR in Biomedicine**, 28 (8): 948–957

Hao, Y., Pan, C., Chen, W., et al. (2016) Differentiation between malignant and benign thyroid nodules and stratification of papillary thyroid cancer with aggressive histological features: Whole-lesion diffusion-weighted imaging histogram analysis. **Journal of magnetic resonance imaging : JMRI**, 44 (6):1546-1555

Harris, L.M., Davies, N., MacPherson, L., et al. (2007) The use of short-echo-time 1H MRS for childhood cerebellar tumours prior to histopathological diagnosis. **Pediatric radiology**, 37 (11): 1101–1109

Harris, L.M., Davies, N.P., MacPherson, L., et al. (2008) Magnetic resonance spectroscopy in the assessment of pilocytic astrocytomas. **European Journal of Cancer**, 44 (17): 2640–2647

Harris, L.M., Davies, N.P., Wilson, S., et al. (2011) Short echo time single voxel 1H magnetic resonance spectroscopy in the diagnosis and characterisation of pineal tumours in children. **Pediatric blood & cancer**, 57 (6): 972–977

Harry, V.N., Semple, S.I., Parkin, D.E., et al. (2010) Use of new imaging techniques to predict tumour response to therapy. **The Lancet. Oncology**, 11 (1): 92–102

Hattingen, E., Delic, O., Franz, K., et al. (2010) (1)H MRSI and progression-free survival in patients with WHO grades II and III gliomas. **Neurological research**, 32 (6): 593–602

Hattingen, E., Raab, P., Franz, K., et al. (2008) Myo-inositol: a marker of reactive astrogliosis in glial tumors? **NMR in Biomedicine**, 21 (3): 233–241

Hipp, S.J., Steffen-Smith, E., Hammoud, D., et al. (2011) Predicting outcome of children with diffuse intrinsic pontine gliomas using multiparametric imaging. **Neuro-oncology**, 13 (8): 904–909

Hirai, T., Kitajima, M., Nakamura, H., et al. (2011) Quantitative blood flow measurements in gliomas using arterial spin-labeling at 3T: intermodality agreement and inter- and intraobserver reproducibility study. **AJNR. American journal of neuroradiology**, 32 (11): 2073–2079

Hollingworth, W., Medina, L.S., Lenkinski, R.E., et al. (2006) A Systematic Literature Review of Magnetic Resonance Spectroscopy for the Characterization of Brain Tumors. **American Journal of Neuroradiology**, 27 (7): 1404–1411

Howe, F.A. and Opstad, K.S. (2003) 1H MR spectroscopy of brain tumours and masses. **NMR in Biomedicine**, 16 (3): 123–131

Humphries, P.D., Sebire, N.J., Siegel, M.J., et al. (2007) Tumors in pediatric patients at diffusion-weighted MR imaging: apparent diffusion coefficient and tumor cellularity. **Radiology**, 245 (3): 848–854

Husband, J.E., Schwartz, L.H., Spencer, J., et al. (2004) Evaluation of the response to treatment of solid tumours - a consensus statement of the International Cancer Imaging Society. **British Journal of Cancer**, 90 (12): 2256–2260

Ichikawa, T., Erturk, S.M., Motosugi, U., et al. (2006) High-B-value diffusion-weighted MRI in

colorectal cancer. **AJR. American journal of roentgenology**, 187 (1): 181–184

Ichikawa, T., Erturk, S.M., Motosugi, U., et al. (2007) High-b value diffusion-weighted MRI for detecting pancreatic adenocarcinoma: preliminary results. **AJR. American journal of roentgenology**, 188 (2): 409–414

Jerome, N.P., Miyazaki, K., Collins, D.J., et al. (2017) Repeatability of derived parameters from histograms following non-Gaussian diffusion modelling of diffusion-weighted imaging in a paediatric oncological cohort. **European radiology**, (1):345-353

Jiru, F. (2008) Introduction to post-processing techniques. **European Journal of Radiology**, 67 (2): 202–217

Julia-Sape, M., Coronel, I., Majos, C., et al. (2012) Prospective diagnostic performance evaluation of single-voxel 1H MRS for typing and grading of brain tumours. **NMR in Biomedicine**, 25 (4): 661–673

Kang, K.M., Lee, J.M., Yoon, J.H., et al. (2014) Intravoxel incoherent motion diffusion-weighted MR imaging for characterization of focal pancreatic lesions. **Radiology**, 270 (2): 444–453

Kim, J.-H., Chang, K.-H., Na, D.G., et al. (2006) 3T 1H-MR spectroscopy in grading of cerebral gliomas: comparison of short and intermediate echo time sequences. **AJNR. American journal of neuroradiology**, 27 (7): 1412–1418

Klauss, M., Mayer, P., Maier-Hein, K., et al. (2016) IVIM-diffusion-MRI for the differentiation of solid benign and malign hypervascular liver lesions-Evaluation with two different MR scanners. **European Journal of Radiology**, 85 (7): 1289–1294

Klose, U. (2008) Measurement sequences for single voxel proton MR spectroscopy. **European Journal of Radiology**, 67 (2): 194–201

Knutsson, L., van Westen, D., Petersen, E.T., et al. (2010) Absolute quantification of cerebral blood flow: correlation between dynamic susceptibility contrast MRI and model-free arterial spin labeling. **Magnetic resonance imaging**, 28 (1): 1–7

Kocaoglu, M. and Bulakbasi, N. (2016) Monitorization of chemotherapy response using diffusion-weighted imaging in neuroblastoma. **Diagnostic and interventional radiology (Ankara, Turkey)**, 22 (1): 108

Kocaoglu, M., Bulakbasi, N., Sanal, H.T., et al. (2010) Pediatric abdominal masses: diagnostic accuracy of diffusion weighted MRI. **Magnetic resonance imaging**, 28 (5): 629–636

Koh, D.-M., Collins, D.J. and Orton, M.R. (2011) Intravoxel incoherent motion in body diffusion-weighted MRI: reality and challenges. **AJR. American journal of roentgenology**, 196 (6): 1351–1361

Koh, D.-M., Takahara, T., Imai, Y., et al. (2007) Practical aspects of assessing tumors using clinical diffusion-weighted imaging in the body. **Magnetic resonance in medical sciences : MRMS : an official journal of Japan Society of Magnetic Resonance in Medicine**, 6 (4): 211–224

Koh, D.M., Brown, G., Riddell, A.M., et al. (2008) Detection of colorectal hepatic metastases

using MnDPDP MR imaging and diffusion-weighted imaging (DWI) alone and in combination. **European radiology**, 18 (5): 903–910

Kovanlikaya, A., Panigrahy, A., Krieger, M.D., et al. (2005) Untreated pediatric primitive neuroectodermal tumor in vivo: quantitation of taurine with MR spectroscopy. **Radiology**, 236 (3): 1020–1025

Kralik, S.F., Taha, A., Kamer, A.P., et al. (2014) Diffusion imaging for tumor grading of supratentorial brain tumors in the first year of life. **AJNR. American journal of neuroradiology**, 35 (4): 815–823

Kyriazi. S., Collins, D.J., Messiou, C., et al. (2011) Metastatic ovarian and primary peritoneal cancer: assessing chemotherapy response with diffusion-weighted MR imaging—value of histogram analysis of apparent diffusion coefficients. **Radiology**, 261: 182–192.

Laigle-Donadey, F., Doz, F. and Delattre, J.-Y. (2008) Brainstem gliomas in children and adults. **Current opinion in oncology**, 20 (6): 662–667

Law, M., Yang, S., Wang, H., et al. (2003) Glioma grading: sensitivity, specificity, and predictive values of perfusion MR imaging and proton MR spectroscopic imaging compared with conventional MR imaging. **AJNR. American journal of neuroradiology**, 24 (10): 1989–1998

Le Bihan, D., Breton, E., Lallemand, D., et al. (1988) Separation of diffusion and perfusion in intravoxel incoherent motion MR imaging. **Radiology**, 168 (2): 497–505

Le Bihan, D. (2017) What can we see with IVIM MRI? **NeuroImage**. available online: https://doi.org/10.1016/j.neuroimage.2017.12.062

Lehnhardt, F.-G., Bock, C., Rohn, G., et al. (2005) Metabolic differences between primary and recurrent human brain tumors: a 1H NMR spectroscopic investigation. **NMR in Biomedicine**, 18 (6): 371–382

Lin, A., Bluml, S. and Mamelak, A.N. (1999) Efficacy of proton magnetic resonance spectroscopy in clinical decision making for patients with suspected malignant brain tumors. **Journal of neuro-oncology**, 45 (1): 69–81

Littooij, A.S., Humphries, P.D. and Olsen, O.E. (2015) Intra- and interobserver variability of whole-tumour apparent diffusion coefficient measurements in nephroblastoma: a pilot study. **Pediatric radiology**, 45 (11): 1651–1660

Londono, A., Castillo, M., Armao, D., et al. (2003) Unusual MR spectroscopic imaging pattern of an astrocytoma: lack of elevated choline and high myo-inositol and glycine levels. **AJNR. American journal of neuroradiology**, 24 (5): 942–945

Lope, L.A., Hutcheson, K.A. and Khademian, Z.P. (2010) Magnetic resonance imaging in the analysis of pediatric orbital tumors: utility of diffusion-weighted imaging. **Journal of AAPOS : the official publication of the American Association for Pediatric Ophthalmology and Strabismus / American Association for Pediatric Ophthalmology and Strabismus**, 14 (3): 257–262

Louis, D.N., Ohgaki, H., Wiestler, O.D., et al. (2007) The 2007 WHO classification of tumours of the central nervous system. **Acta neuropathologica**, 114 (2): 97–109

Mansson, S., Johansson, E., Magnusson, P., et al. (2006) 13C imaging-a new diagnostic platform. **European radiology**, 16 (1): 57–67

Marcus, K.J., Astrakas, L.G., Zurakowski, D., et al. (2007) Predicting survival of children with CNS tumors using proton magnetic resonance spectroscopic imaging biomarkers. **International journal of oncology**, 30 (3): 651–657

Martin, A.J., Liu, H., Hall, W.A., et al. (2001) Preliminary assessment of turbo spectroscopic imaging for targeting in brain biopsy. **AJNR. American journal of neuroradiology**, 22 (5): 959–968

Mazaheri, Y., Vargas, H.A., Akin, O., et al. (2012) Reducing the influence of b-value selection on diffusion-weighted imaging of the prostate: evaluation of a revised monoexponential model within a clinical setting. **Journal of magnetic resonance imaging : JMRI**, 35 (3): 660–668

McDonald, K., Sebire, N.J., Anderson, J., et al. (2011) Patterns of shift in ADC distributions in abdominal tumours during chemotherapy-feasibility study. **Pediatric radiology**, 41 (1): 99–106

McRobbie, D. W., Moore, E. A., Graves, M. J. & Prince, M. R. (2007) MRI From Picture To Proton, 2nd edn (Cambridge University Press, Cambridge).

McShane, L.M., Altman, D.G., Sauerbrei, W., et al. (2005) Reporting recommendations for tumor marker prognostic studies (REMARK). **Journal of the National Cancer Institute**, 97 (16): 1180–1184

Meeus, E.M., Zarinabad, N., Manias, K.A., et al. (2018) Diffusion-weighted MRI and intravoxel incoherent motion model for diagnosis of pediatric solid abdominal tumors. **Journal of magnetic resonance imaging : JMRI**, 47(6):1475-1486

Meng, J., Zhu, L., Zhu, L., et al. (2016) Apparent diffusion coefficient histogram shape analysis for monitoring early response in patients with advanced cervical cancers undergoing concurrent chemo-radiotherapy. **Radiation oncology**, 11 (1): 141

Meng, J., Zhu, L., Zhu, L., et al. (2017) Histogram analysis of apparent diffusion coefficient for monitoring early response in patients with advanced cervical cancers undergoing concurrent chemo-radiotherapy. **Acta radiologica**, 58(11):1400-1408.

Milad, P., Elbegiermy, M., Shokry, T., et al. (2017) The added value of pretreatment DW MRI in characterization of salivary glands pathologies. **American Journal of Otolaryngology**, 38(1):13-20.

Miller, A.B., Hoogstraten, B., Staquet, M., et al. (1981) Reporting results of cancer treatment. **Cancer**, 47 (1): 207–214

Mimura, R., Kato, F., Tha, K.K., et al. (2016) Comparison between borderline ovarian tumors and carcinomas using semi-automated histogram analysis of diffusion-weighted imaging: focusing on solid components. **Japanese journal of radiology**, 34 (3): 229–237

Moller-Hartmann, W., Herminghaus, S., Krings, T., et al. (2002) Clinical application of proton magnetic resonance spectroscopy in the diagnosis of intracranial mass lesions. **Neuroradiology**, 44 (5): 371–381

Murphy, M., Loosemore, A., Clifton, A.G., et al. (2002) The contribution of proton magnetic resonance spectroscopy (1HMRS) to clinical brain tumour diagnosis. **British journal of neurosurgery**, 16 (4): 329–334

Neubauer, H., Evangelista, L., Hassold, N., et al. (2012) Diffusion-weighted MRI for detection and differentiation of musculoskeletal tumorous and tumor-like lesions in pediatric patients. **World journal of pediatrics : WJP**, 8 (4): 342–349

Neubauer, H., Li, M., Muller, V.R., et al. (2017) Diagnostic Value of Diffusion-Weighted MRI for Tumor Characterization, Differentiation and Monitoring in Pediatric Patients with Neuroblastic Tumors. **RoFo**, 189 (7):640-650

Ng WH, Lim T. (2008) Targeting regions with highest lipid content on MR spectroscopy may improve diagnostic yield in stereotactic biopsy. **Journal of Clinical Neuroscience,** 15(5):502-506

Oka, K., Yakushiji, T., Sato, H., et al. (2010) The value of diffusion-weighted imaging for monitoring the chemotherapeutic response of osteosarcoma: a comparison between average apparent diffusion coefficient and minimum apparent diffusion coefficient. **Skeletal radiology**, 39 (2): 141–146

Olsen, O.E. (2015) Why measure tumours? **Pediatric radiology**, 45 (1): 35–41

Opstad, K.S., Bell, B.A., Griffiths, J.R., et al. (2009) Taurine: a potential marker of apoptosis in gliomas. **British Journal of Cancer**, 100 (5): 789–794

Orphanidou-Vlachou, E., Auer, D., Brundler, M.A., et al. (2013) 1H magnetic resonance spectroscopy in the diagnosis of paediatric low grade brain tumours. **European Journal of Radiology**, 82 (6): e295–e301

Orphanidou-Vlachou, E., Kohe, S.E., Brundler, M.-A., et al. (2018) Metabolite Levels in Paediatric Brain Tumours Correlate with Histological Features. **Pathobiology : journal of immunopathology, molecular and cellular biology**, 85 (3): 157–168

Panigrahy, A. and Bluml, S. (2009) Neuroimaging of pediatric brain tumors: from basic to advanced magnetic resonance imaging (MRI). **Journal of child neurology**, 24 (11): 1343–1365

Panigrahy, A., Krieger, M.D., Gonzalez-Gomez, I., et al. (2006) Quantitative short echo time 1H-MR spectroscopy of untreated pediatric brain tumors: preoperative diagnosis and characterization. **AJNR. American journal of neuroradiology**, 27 (3): 560–572

Panigrahy, A., Nelson, M.D.J. and Bluml, S. (2010) Magnetic resonance spectroscopy in pediatric neuroradiology: clinical and research applications. **Pediatric radiology**, 40 (1): 3–30

Peet, A.C., Arvanitis, T.N., Leach, M.O., et al. (2012) Functional imaging in adult and paediatric brain tumours. **Nature reviews. Clinical oncology**, 9 (12): 700–711

Peet, A.C., Davies, N.P., Ridley, L., et al. (2007) Magnetic resonance spectroscopy suggests key differences in the metastatic behaviour of medulloblastoma. **European Journal of Cancer**, 43 (6): 1037–1044

Pereira, J.A.S., Rosado, E., Bali, M., et al. (2015) Pancreatic neuroendocrine tumors:

correlation between histogram analysis of apparent diffusion coefficient maps and tumor grade. **Abdominal imaging**, 40 (8): 3122–3128

Pizzo, P.A., Poplack, D.G., Adamson, P. C., et al. (2016). *Principles and practice of pediatric oncology*.

Poretti, A., Meoded, A. and Huisman, T.A.G.M. (2012) Neuroimaging of pediatric posterior fossa tumors including review of the literature. **Journal of magnetic resonance imaging : JMRI**, 35 (1): 32–47

Pouwels, P.J., Brockmann, K., Kruse, B., et al. (1999) Regional age dependence of human brain metabolites from infancy to adulthood as detected by quantitative localized proton MRS. **Pediatric research**, 46 (4): 474–485

Preul, M.C., Caramanos, Z., Collins, D.L., et al. (1996) Accurate, noninvasive diagnosis of human brain tumors by using proton magnetic resonance spectroscopy. **Nature medicine**, 2 (3): 323–325

Proisy, M., Bruneau, B., Rozel, C., et al. (2015) Arterial spin labeling in clinical pediatric imaging. **Diagnostic and interventional imaging**, 97 (2):151-8

Provencher, S.W. (2001) Automatic quantitation of localized in vivo 1H spectra with LCModel. **NMR in Biomedicine**, 14 (4): 260–264

Ricci, P.E., Pitt, A., Keller, P.J., et al. (2000) Effect of voxel position on single-voxel MR spectroscopy findings. **AJNR. American journal of neuroradiology**, 21 (2): 367–374

Rosen, Y. and Lenkinski, R.E. (2007) Recent advances in magnetic resonance neurospectroscopy. **Neurotherapeutics : the journal of the American Society for Experimental NeuroTherapeutics**, 4 (3): 330–345

Ross, B. and Bluml, S. (2001) Magnetic resonance spectroscopy of the human brain. **The Anatomical record**, 265 (2): 54–84

Rumboldt, Z., Camacho, D.L.A., Lake, D., et al. (2006) Apparent diffusion coefficients for differentiation of cerebellar tumors in children. **AJNR. American journal of neuroradiology**, 27 (6): 1362–1369

Sankar, T., Caramanos, Z., Assina, R., et al. (2008) Prospective serial proton MR spectroscopic assessment of response to tamoxifen for recurrent malignant glioma. **Journal of neuro-oncology**, 90 (1): 63–76

Seymour, Z.A., Panigrahy, A., Finlay, J.L., et al. (2008) Citrate in pediatric CNS tumors? **AJNR. American journal of neuroradiology**, 29 (5): 1006–1011

Shiroishi, M.S., Panigrahy, A., Moore, K.R., et al. (2015) Combined MRI and MRS improves pre-therapeutic diagnoses of pediatric brain tumors over MRI alone. **Neuroradiology**, 57 (9): 951–956

Suo, S.-T., Chen, X.-X., Fan, Y., et al. (2014) Histogram analysis of apparent diffusion coefficient at 3.0 T in urinary bladder lesions: correlation with pathologic findings. **Academic radiology**, 21 (8): 1027–1034

Suo, S., Zhang, K., Cao, M., et al. (2016) Characterization of breast masses as benign or malignant at 3.0T MRI with whole-lesion histogram analysis of the apparent diffusion coefficient. **Journal of magnetic resonance imaging : JMRI,** 43 (4): 894-902.

Takahashi, M., Kozawa, E., Tanisaka, M., et al. (2015) Utility of histogram analysis of apparent diffusion coefficient maps obtained using 3.0T MRI for distinguishing uterine carcinosarcoma from endometrial carcinoma. **Journal of magnetic resonance imaging : JMRI**, 43 (6): 1301–1307

Taouli, B., Beer, A.J., Chenevert, T., et al. (2016) Diffusion-Weighted Imaging Outside the Brain: Consensus Statement From an ISMRM-Sponsored Workshop. **Journal of Magnetic Resonance Imaging**, 44 (3): 521–540

Tate, A.R., Underwood, J., Acosta, D.M., et al. (2006) Development of a decision support system for diagnosis and grading of brain tumours using in vivo magnetic resonance single voxel spectra. **NMR in Biomedicine**, 19 (4): 411–434

Therasse, P., Arbuck, S.G., Eisenhauer, E.A., et al. (2000) New guidelines to evaluate the response to treatment in solid tumors. European Organization for Research and Treatment of Cancer, National Cancer Institute of the United States, National Cancer Institute of Canada. **Journal of the National Cancer Institute**, 92 (3): 205–216

Tzika, A.A., Astrakas, L.G., Zarifi, M.K., et al. (2003) Multiparametric MR assessment of pediatric brain tumors. **Neuroradiology**, 45 (1): 1–10

Tzika, A.A., Astrakas, L.G., Zarifi, M.K., et al. (2004) Spectroscopic and perfusion magnetic resonance imaging predictors of progression in pediatric brain tumors. **Cancer**, 100 (6): 1246–1256

van der Graaf, M. (2010) In vivo magnetic resonance spectroscopy: basic methodology and clinical applications. **European biophysics journal : EBJ**, 39 (4): 527–540

Vicente, J., Fuster-Garcia, E., Tortajada, S., et al. (2013) Accurate classification of childhood brain tumours by in vivo (1)H MRS - a multi-centre study. **European journal of cancer (Oxford, England : 1990)**, 49 (3): 658–667

Wang, Y., Chen, Z.E., Nikolaidis, P., et al. (2011) Diffusion-weighted magnetic resonance imaging of pancreatic adenocarcinomas: association with histopathology and tumor grade. **Journal of magnetic resonance imaging : JMRI**, 33 (1): 136–142

Wang, Y.-C., Hu, D.-Y., Hu, X.-M., et al. (2016) Assessing the Early Response of Advanced Cervical Cancer to Neoadjuvant Chemotherapy Using Intravoxel Incoherent Motion Diffusion-weighted Magnetic Resonance Imaging: A Pilot Study. **Chinese medical journal**, 129 (6): 665–671

Wang, Z., Sutton, L.N., Cnaan, A., et al. (1995) Proton MR spectroscopy of pediatric cerebellar tumors. **AJNR. American journal of neuroradiology**, 16 (9): 1821–1833

Warren, K.E. (2004) NMR spectroscopy and pediatric brain tumors. **The oncologist**, 9 (3): 312–318

Warren, K.E., Frank, J.A., Black, J.L., et al. (2000) Proton magnetic resonance spectroscopic imaging in children with recurrent primary brain tumors. **Journal of clinical oncology :**

official journal of the American Society of Clinical Oncology, 18 (5): 1020–1026

White, C.M., Pope, W.B., Zaw, T., et al. (2014) Regional and voxel-wise comparisons of blood flow measurements between dynamic susceptibility contrast magnetic resonance imaging (DSC-MRI) and arterial spin labeling (ASL) in brain tumors. **Journal of neuroimaging : official journal of the American Society of Neuroimaging**, 24 (1): 23–30

Wilson, M., Cummins, C.L., MacPherson, L., et al. (2013) Magnetic resonance spectroscopy metabolite profiles predict survival in paediatric brain tumours. **European Journal of Cancer**, 49 (2): 457–464

Wilson, M., Gill, S.K., MacPherson, L., et al. (2014) Noninvasive detection of glutamate predicts survival in pediatric medulloblastoma. **Clinical cancer research : an official journal of the American Association for Cancer Research**, 20 (17): 4532–4539

Wilson, M., Reynolds, G., Kauppinen, R.A., et al. (2011) A constrained least-squares approach to the automated quantitation of in vivo (1)H magnetic resonance spectroscopy data. **Magnetic resonance in medicine**, 65 (1): 1–12

Woo, S., Cho, J.Y., Kim, S.Y., et al. (2014a) Histogram analysis of apparent diffusion coefficient map of diffusion-weighted MRI in endometrial cancer: a preliminary correlation study with histological grade. **Acta radiologica (Stockholm, Sweden : 1987)**, 55 (10): 1270–1277

Woo, S., Lee, J.M., Yoon, J.H., et al. (2014b) Intravoxel incoherent motion diffusion-weighted MR imaging of hepatocellular carcinoma: correlation with enhancement degree and histologic grade. **Radiology**, 270 (3): 758–767

Xiao , Y., Pan, J., Chen, Y., et al. (2015) Intravoxel Incoherent Motion-Magnetic Resonance Imaging as an Early Predictor of Treatment Response to Neoadjuvant Chemotherapy in Locoregionally Advanced Nasopharyngeal Carcinoma. Medicine, 94 (24): e973

Xu, X.Q., Hu, H., Su, G.Y., (2016) Utility of histogram analysis of ADC maps for differentiating orbital tumors. **Diagnostic Interventional Radiology.**, 22 (2) :161-7.

Yamasaki, F., Kurisu, K., Satoh, K., et al. (2005) Apparent diffusion coefficient of human brain tumors at MR imaging. **Radiology**, 235 (3): 985–991

Yamashita, Y., Kumabe, T., Higano, S., et al. (2009) Minimum apparent diffusion coefficient is significantly correlated with cellularity in medulloblastomas. **Neurological research**, 31 (9): 940–946

Yeom, K.W., Mobley, B.C., Lober, R.M., et al. (2013) Distinctive MRI features of pediatric medulloblastoma subtypes. **AJR. American journal of roentgenology**, 200 (4): 895–903

Zarinabad, N., Meeus, E.M., Manias, K., et al. (2018) Automated Modular Magnetic Resonance Imaging Clinical Decision Support System (MIROR): An Application in Pediatric Cancer Diagnosis. **JMIR medical informatics**, 6 (2): e30

Zhu, L., Zhu, L., Wang, H., et al. (2017) Predicting and Early Monitoring Treatment Efficiency of Cervical Cancer Under Concurrent Chemoradiotherapy by Intravoxel Incoherent Motion Magnetic Resonance Imaging. **Journal of computer assisted tomography**, 41 (3): 422–429

APPENDIX 1

Core Multimodal Protocol (Brain)
SIOPE Brain Imaging Group

Modality		**MRS**			**Diffusion**				**Perfusion**			
Description		**SVS (short-TE)**			**DTI**				**DSC - T2***			
Sequence		**PRESS**			**EPI**				**GRE**			
		Param	**Value**	**Value**	**Param**	**Value**	**Param**	**Value**	**Param**	**Value**	**Param**	**Value**
Fixed		Field	1.5 T	3 T	Field	1.5T	Field	3T	Field	1.5T	Field	3T
		TR (ms)	1500	2000	FOV (mm)	240	FOV (mm)	211	FOV (mm)	240x240x95	FOV (mm)	240x240x105
		Vector length	2048	2048	Acq matrix	96x96	Acq matrix	96x96	Acq matrix	96x96x19	Acq matrix	96x96x30
		TE (ms)	30		Resolution	2.5 isotropic	Resolution (mm)	2.2 isotropic	Orientation	axial	Orientation	axial
					Coverage	whole brain	Coverage	whole brain	Sense	2	Sense	2
					b factor	1000	b factor	1000	Temp resoln	1.49x60	Temp resoln	1.86sx60
Variable		TE (ms)		30 - 35	TR (ms)	min	TR (ms)	min	Sequence	FE-EPI	Sequence	FE-EPI
		VOI (ml)	3.4 - 8 (to fit tumour)	2.2 - 8 (to fit tumour)	TE (ms)	min (fix BW?)	TE (ms)	min (fix BW?)	TE (ms)	40ms	TE(ms)	40ms
		BW (kHz)	2 or 2.5 kHz	2 or 2.5 kHz	Grad dirs	15+	Grad dirs	15+	TR (ms)	min	TR(ms)	min
		Aves(WS)	128 - 256	64 - 196	NSA (b=0)	1(3)	NSA (b=0)	1 (3)	flip angle	20 deg	flip angle	20 deg
		Aves (W)	8 - 16	8 - 16	Speed-up	x2	Speed-up	x2	Injection rate	3ml/sec	Injection rate	3ml/sec
					Partial Fourier		Partial Fourier		Gd-DTPA	0.1mmol/Kg 50% as pre bolus	Gd-DTPA	0.1mmol/Kg 50% as pre bolus
Time (mins)	**Set-up**		3	3					2		2	
	Acq		3.4 - 6.6	2.3 - 6.7					2		2	
	Total		6.4 - 9.6	5.3 - 9.7	5		3		4		4	
	Total	**minimum at 3T - 8.3 mins + DSC**										

APPENDIX 2

Core Multimodal Protocol (Body)

Modality	**Diffusion**	
Description	**DWI**	
Sequence	**Multi-Slice EPI (1.5T)**	
	Param	**Value**
Fixed	FOV (mm)	250 x 172
	Slice Thickness (mm)	5
	Matrix	192 x 132
	b factor	0,50,100,300,600,1000
	Orientation	Axial
Variable	TR (ms)	5700
	TE (ms)	92
	BW (Hz/Px)	1371
	NSA	1
	Slice Thickness (5mm)	5
	Gap (mm)	5
Time (mins)	Set-up	0
	Acq	4.5-7 depending on number of slices
	Total	4.5-7 depending on number of slices

APPENDIX 3

Interpretation of Magnetic Resonance Spectroscopy Booklet

Functional Imaging Group

The Birmingham Children's Hospital NHS Trust

Interpretation of Magnetic Resonance Spectroscopy

Diagnosing Brain Tumours in Children

Brain Tumour Research Group

Birmingham Children's Hospital

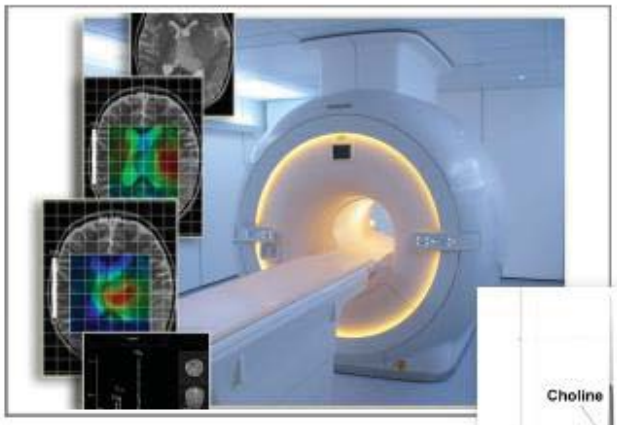

UNIVERSITY OF BIRMINGHAM

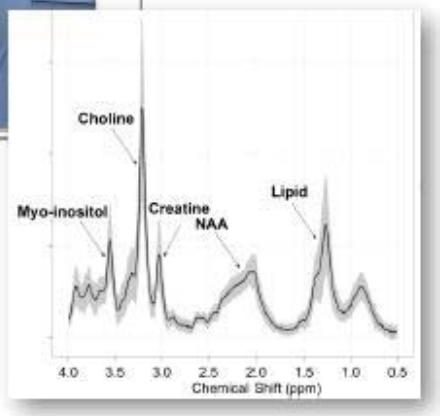

2015

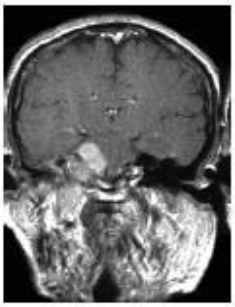

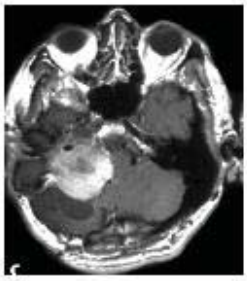

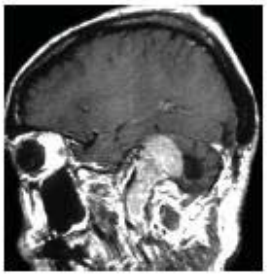

NHS National Institute for Health Research

MAGNETIC RESONANCE SPECTROSCOPY
VERSION 2; JANUARY 2016

1

Contents

SECTION 1
Understanding MRS

MRS in the diagnosis of paediatric brain tumours

1H-Magnetic resonance spectroscopy (MRS) is a non-invasive technique that can help discriminate between different types and grades of brain tumour. It measures the chemical composition of tissue, providing information about high concentration intermediary metabolites such as choline (involved in membrane synthesis), N-acetyl aspartate (neuronal marker) and mobile lipids (apoptosis and necrosis). This information is presented as a graph with a series of peaks, each of which corresponds to a certain metabolite.

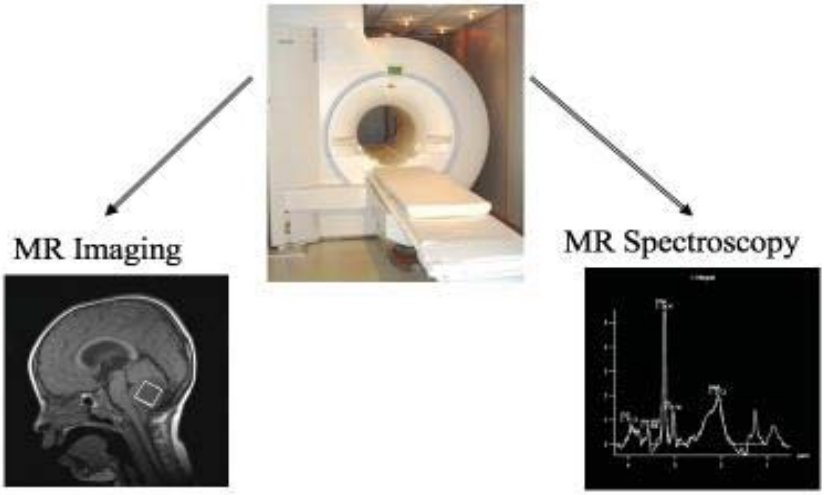

The appearance of an MR spectrum depends on the protocol used to acquire it. MRS protocols vary in choice of echo time and single versus multi voxel acquisition. Single voxel spectroscopy acquires MRS data from a single region of interest, and has been used successfully in children in multicentre studies (1). Multi voxel spectroscopy (also called chemical shift imaging (CSI) or magnetic resonance spectroscopic imaging (MRSI)) involves acquiring data simultaneously over a 2D or 3D grid of voxels. This provides improved classification of heterogeneous tumours but is more technically demanding, less reproducible and more difficult to quantify reliably.

Background to MRS

MRS may be used in combination with conventional imaging techniques to support the diagnosis of childhood brain tumours. Brain tumours in children are histologically diverse entities with overlapping and heterogeneous imaging features. Diagnosis is difficult based on conventional imaging alone, leading to reliance on histopathological information obtained using invasive procedures. Chemical profiles are a useful diagnostic aid as different tumour types display characteristic patterns of metabolite levels (2-4). Studies in adults have found MRS improves the accuracy of non-invasive diagnosis of brain tumours (5). Combining MRS with pattern recognition has given diagnostic precision comparable to histopathology in a multi-centre setting (6). Pattern recognition of MRS profiles has also been shown to be a useful diagnostic aid in children (2,3).

Quantitative interpretation of MRS metabolite levels can facilitate non-invasive tumour categorisation. Brain tumours generally have high levels of choline and lactate and reduced N-acetyl aspartate (NAA) (3,7). Individual metabolites may be used quantitatively to determine tumour type. High grade tumours have high total levels of choline (Cho), lipids (8) and glycine (4), while taurine has a strong association with primitive neuroectodermal tumours (9) and medulloblastomas (2,3). Creatine (Cr) is significantly lower in pilocytic astrocytomas than in other paediatric brain tumours ($p<0.000001$) (2).

Paediatric pilocytic astrocytomas, medulloblastomas and ependymomas have been accurately classified using MRS in a number of studies (3,7,10,11). Metabolite ratios of NAA:Cho and Cr:Cho differentiated these tumours in 26 children with an accuracy of 0.85 (10), and using ratios of NAA, Cho and Cr in 33 patients had an accuracy of 0.88 (7). An automated method fitting MRS data of 35 patients using Linear Discriminant Analysis (LDA) differentiated these tumours with an accuracy of 0.93 (3). A multi-national study including 78 paediatric patients also demonstrated significant differences in metabolite concentrations of these malignancies, with diagnostic classifiers having an accuracy of 0.98 discriminating the three types of tumour (11).

MRS can facilitate diagnosis of tumour subgroups and detect subtle differences between paediatric low grade gliomas. These tumours are often grouped together for treatment, but vary considerably in terms of anatomical location, histopathology, age at diagnosis and prognosis. The concentrations of key metabolites such as choline and myoinositol are significantly different in glioneuronal and glial tumours and other histological subtypes of low grade glioma ($p<0.05$) (12). There are also significant differences in metabolite profiles of pilocytic astrocytomas and unbiopsied optic pathway gliomas depending on neurofibromatosis type I status and location ($p<0.05$) (12). As low grade gliomas are often unbiopsied and treatment response differs between tumour types, forming an accurate non-invasive diagnosis could improve outcomes for these patients.

There is evidence that MRS provides added value in diagnosing brain tumours in adults in clinical practice (2,5,13-15). A recent retrospective study found including MRS in the pre-operative diagnosis of paediatric brain tumours significantly improved accuracy of radiological diagnosis over MRI alone (16). MRI was used to retrospectively diagnose untreated brain tumours in 60 patients, and both MRS and MRI were used by radiologists for a further 60 cases. The former group were correctly diagnosed in 63% of cases compared to 87% in the latter group ($p<0.005$). Using MRS data to reinterpret imaging from the former group resulted in a significant increase in accuracy to 87% ($p<0.05$) (16). The added value of MRS compared with conventional radiology was also found in a retrospective study of 30 paediatric brain tumour patients (Davies et al).

Interpreting MRS Metabolites in Normal Brain

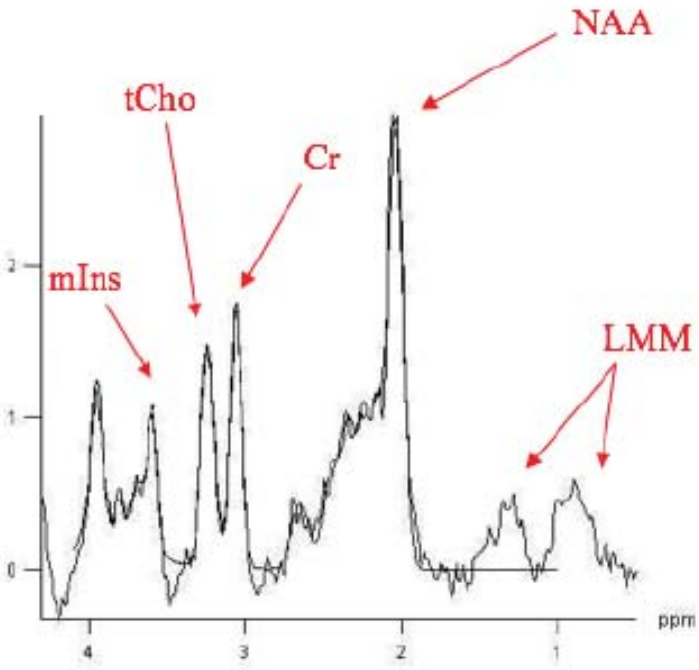

- Myoinositol (mIns) - role uncertain
- Total Choline (tCho) - cell turnover
- Creatine (Cr) - energy state
- N-Acetyl-Aspartate (NAA) - neurons
- Lipids/Macromolecule (LMM) - apoptosis and necrosis

Peet, Archives Dis Child. 2008

Metabolites are seen as peaks on a magnetic resonance spectrum, with different metabolites occurring at different ppm, or points along the x-axis. The area under the peak represents the concentration of that metabolite.

Metabolite locations in ppm

- 3.6: Myo-Inositol (mIns)
- 3.2: Total Choline (tCho)
- 3.0: Creatine (Cr)
- 2.0: N-Acetyl-Aspartate (NAA)
- 0.8, 1.2: Lipids/Macromolecule (LMM)

Key Features of Normal Brain

Straight line can be drawn up through mIns, tCho, Cr and NAA

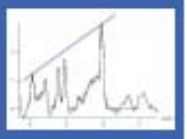

- Low mIns
- Cr peak higher than tCho peak
- High NAA
- Low LMM

Data Quality

As with all imaging investigations, quality must be assessed prior to interpretation.

There are two main aspects:

1) Assess the proportion of tumour and other tissues in the voxel. The spectrum will be a combination of the spectra from these tissues. Normal brain in particular contains many metabolites.

Voxel Placement

- Away from bone > 3mm
- Away from scalp lipid > 3mm
- Do not include normal brain
- Include as little cyst and CSF as possible

Always make sure the voxel placement is saved for future reference.

2) Assess the spectral quality itself – signal:noise ratio (SNR), line-width, phasing, baseline, artefacts.

Example of poor SNR
Noise at 0ppm <5 times Cho

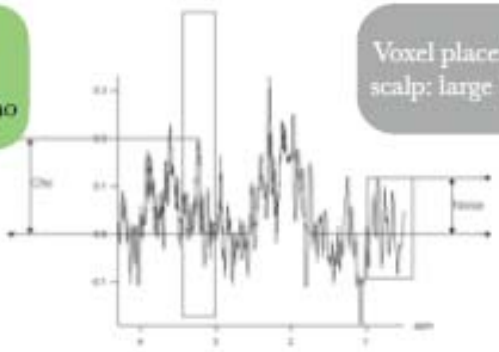

Voxel placement over scalp: large lipid peaks

Poor SNR: Placement over cyst or too few averages for voxel size

Example of poor line width
Cho and Cr peak coalesced

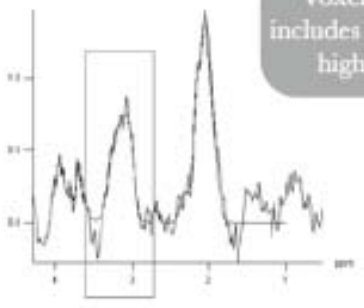

Voxel placement includes normal brain: high NAA, Cr

Poor linewidth: Placement close to bone, or heterogeneity within voxel

Does the spectrum meet quality control criteria?

- Is the choline peak at least 5 times that of the nose?
- Are choline and creatine peaks well separated?

If not, the spectrum may not be suitable for analysis.

Use of Mean Spectra

Mean spectra vary considerably between tumour types. Reducing the differential diagnosis as much as possible on the clinical features and conventional imaging helps greatly. MRS is more likely to help if you have two candidate diagnoses which have very different mean spectra than if you look for a match from the spectra of a large set of diagnoses each with slightly different mean spectra.

The number of cases the mean spectra are determined from is provided. Spectra are more accurate where there are a large number of cases.

The dark line is the mean spectrum, the grey shading is the standard deviation.

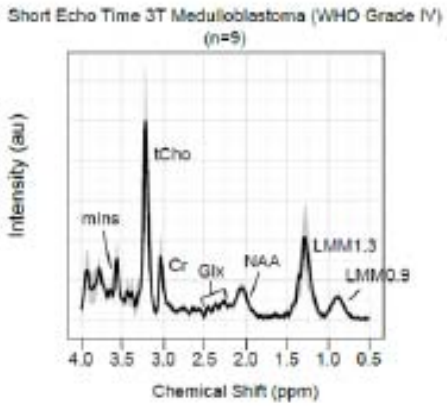

Steps for Use of Mean Spectra to Facilitate Diagnosis

1. Formulate a list of differential diagnoses using clinical features and conventional imaging sequences
2. Assess data quality of case spectrum:
   - Is the voxel positioned correctly?
   - Are the SNR and line width acceptable?
3. Compare the mean spectra from the main differential diagnoses to that of the case spectrum

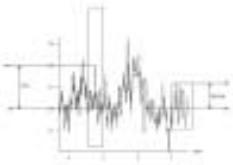

Differences in mean spectra are accounted for by:
- Location: supratentorial or infratentorial
- Echo times (short or long TE)
- Field strength: 1.5T or 3T

It is important to realise that spectra look different when acquired at different echo times (TE) and field strengths:

- Echo times - eg the lactate doublet is upright at 30ms but inverted at 135ms, myoinositol is less readily seen at 135ms and a single peak around 3.6ppm is more likely to be attributed to glycine.
- Field strengths - eg myoinositol is essentially one peak at 1.5T but two at 3T when short echo times are used, NAA is more easily seen at 3T since the broad glutamate feature between 2.0 and 2.5ppm overlaps less with it.

Example of Use of MRS for Diagnosis

Clinical Case

- 4 year old boy
- 2 month history of headaches and lethargy
- Progressive nausea and vomiting
- New onset of ataxia

Conventional MRI

T2 Weighted   T1 Weighted

Posterior Fossa Tumour

Differential Diagnosis
- Medulloblastoma
- Ependymoma

Additional Information from MRS

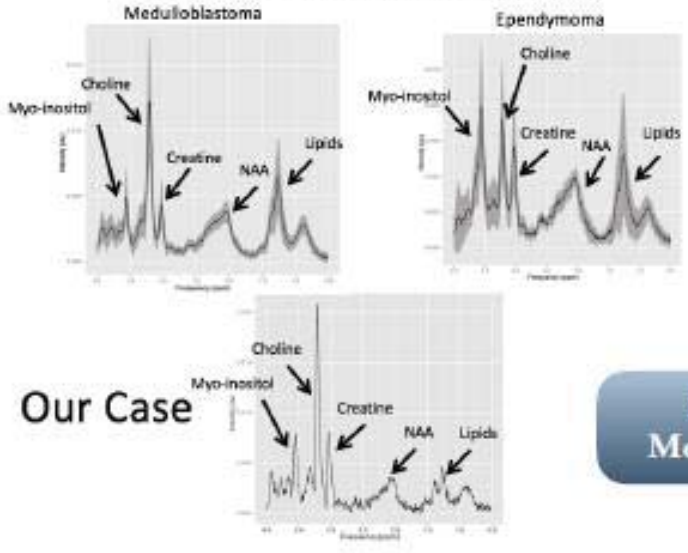

Final Diagnosis: Medulloblastoma

SECTION2

Mean Spectra

Normal Brain

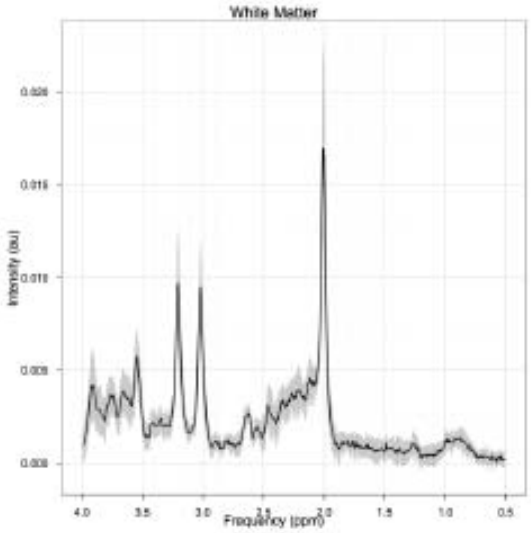

Normal Brain Key Features

- Low mIns
- High NAA
- Low LMM

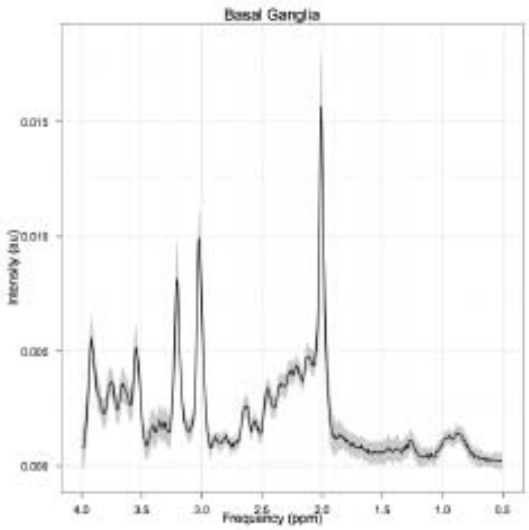

Astrocytomas

Diffuse Astrocytoma

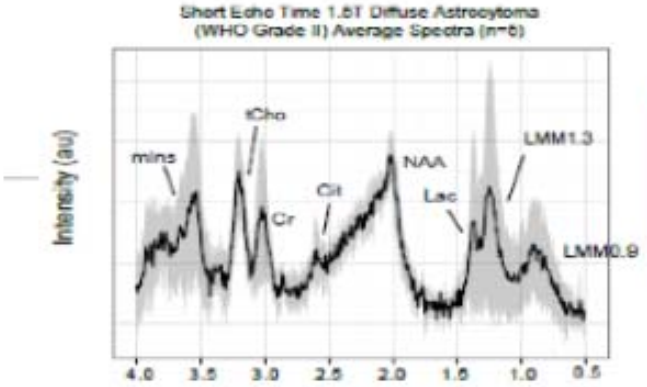

Diffuse Astrocytoma Key Features

- May have a noisy spectrum

Anaplastic Astrocytoma

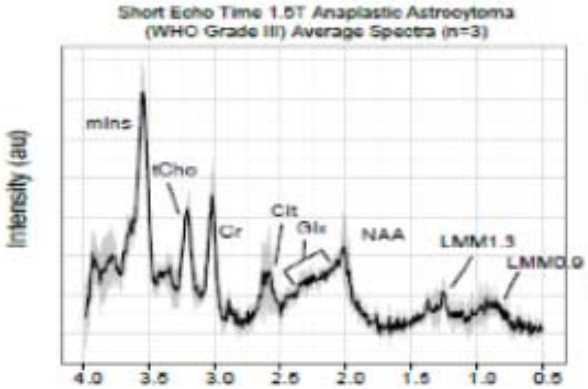

Anapaestic Astrocytoma Key Features

- High mIns
- High creatine
- Prominent citrate
- Low lactate

Glioblastoma Multiforme

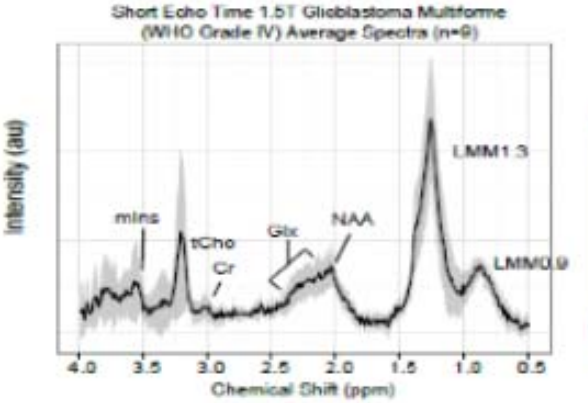

GBM Key Features

- Low mIns
- Low NAA peak (plus broad Glx peak)
- High LMM at 1.3ppm

Pilocytic Astrocytoma

All locations

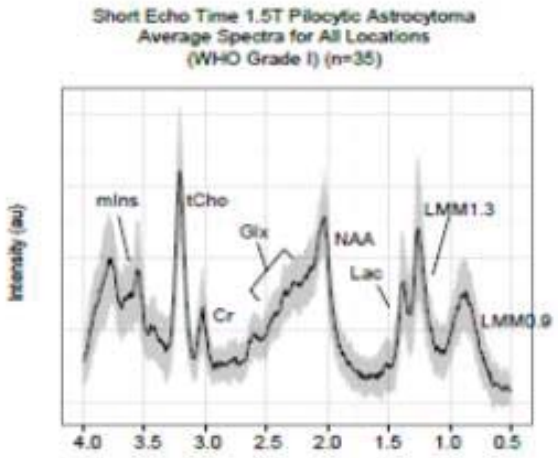

Pilocytic Astrocytoma Key Features

- Low Cr
- High NAA peak (similar to normal brain)
- Lactate readily detected

Supratentorial

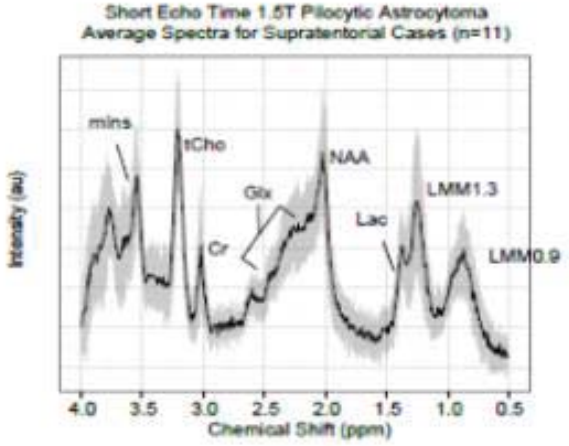

Pilocytic Astrocytomas vary in mIns concentration between locations

Infratentorial

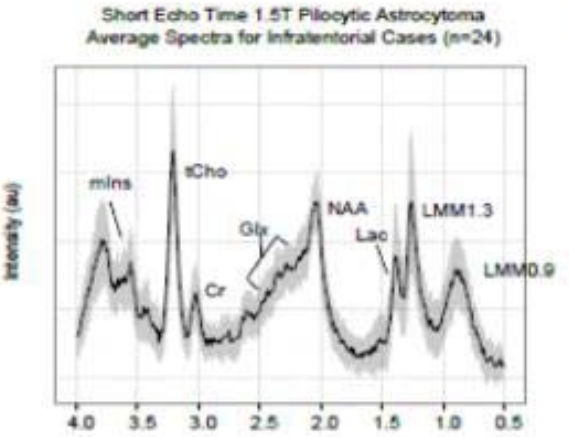

Atypical Teratoid Rhabdoid Tumours

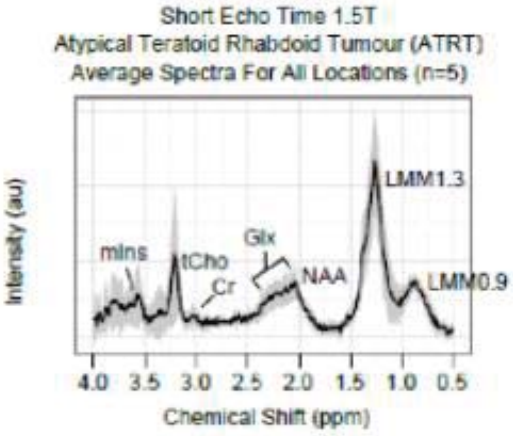

ATRT
Key Features

- Low mIns
- Low Cr
- High LMM at 1.3ppm

Choroid Plexus Tumours

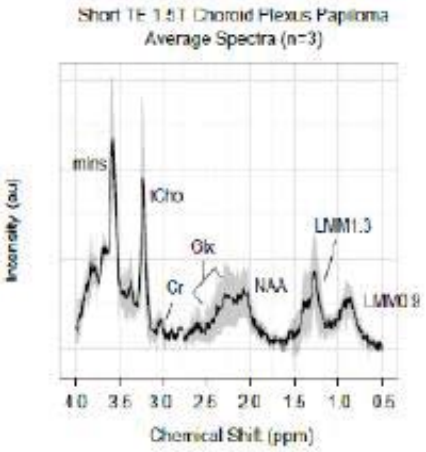

CPP
Key Features

- High mIns
- High tCho
- Low Cr
- Low NAA

CNS PNET

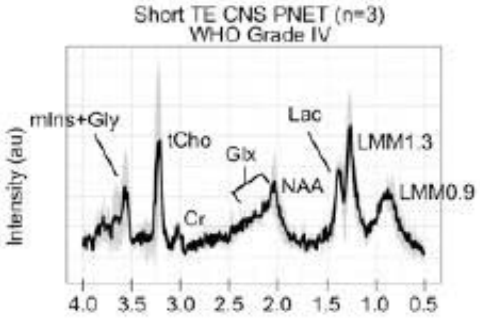

Craniopharyngioma

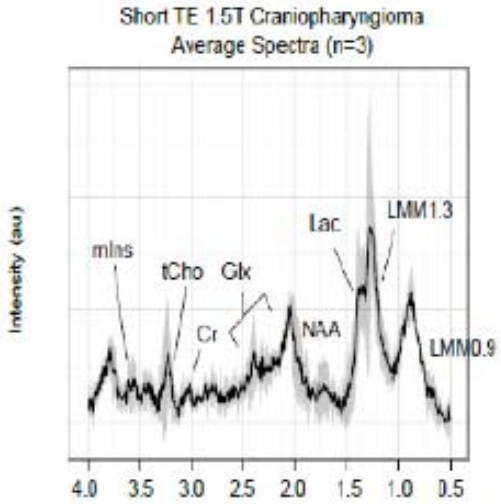

Craniopharyngioma Key Features

- Low Cr
- Low tho
- Low Glx

Diffuse Intrinsic Pontine Glioma

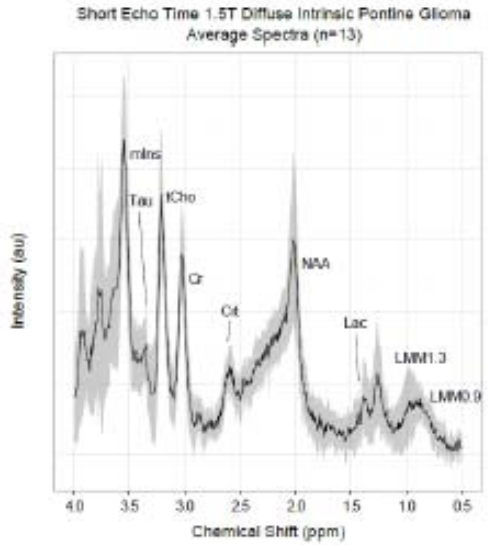

DIPG Key Features

- High mIns
- High citrate at 2.6ppm
- High NAA with narrow peak
- Low lactate
- Low LMM

Ependymoma

All locations

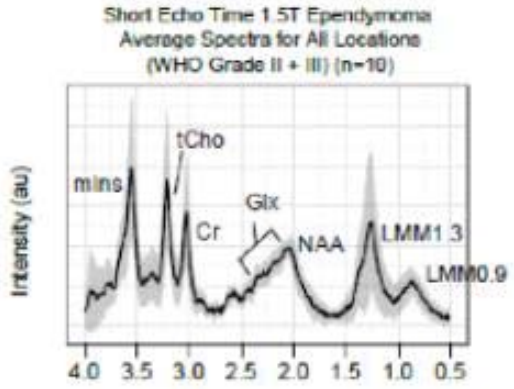

All locations

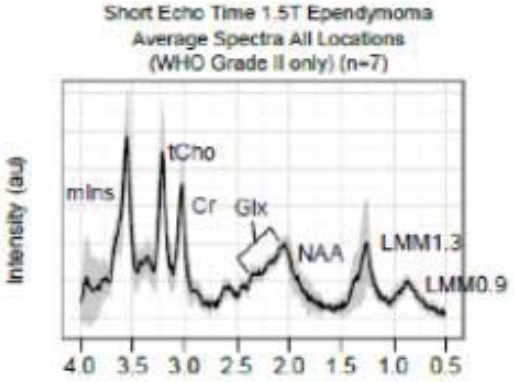

All locations

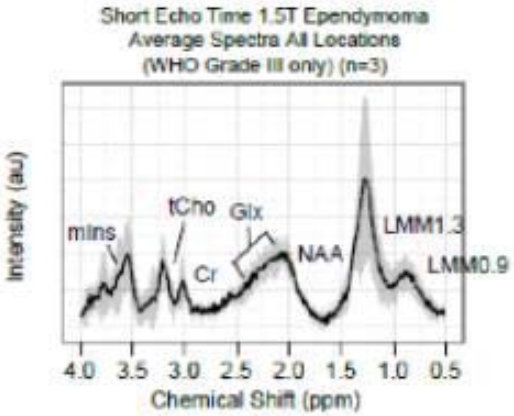

Ependymoma Key Features

- High mIns peak
- Low NAA peak (plus broad Glx peak)
- High lactate

Ependymomas vary in mIns, creatine and lipid levels between grade

- Low mIns in Grade III
- Lipids dominant in Grade III
- Lower creatine in higher grade

Ganglioglioma

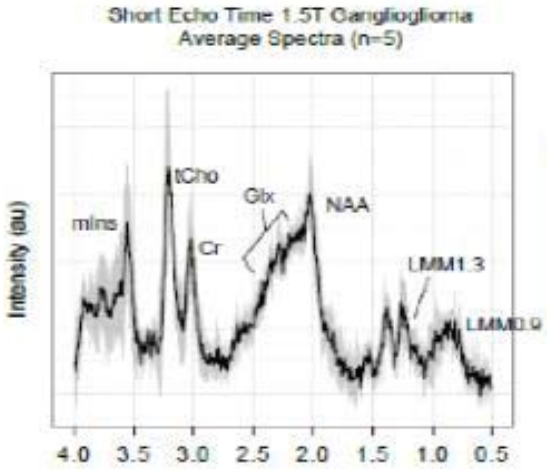

Ganglioglioma Key Features

- Low LMM at 1.3ppm

Germinoma

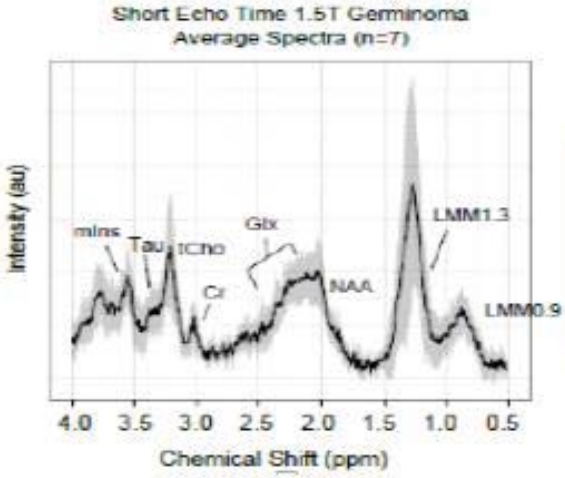

Germinoma Key Features

- Low mIns
- Detectable Taurine
- High glutamate+glutamine (Glx)
- High LMM at 1.3ppm

Medulloblastoma

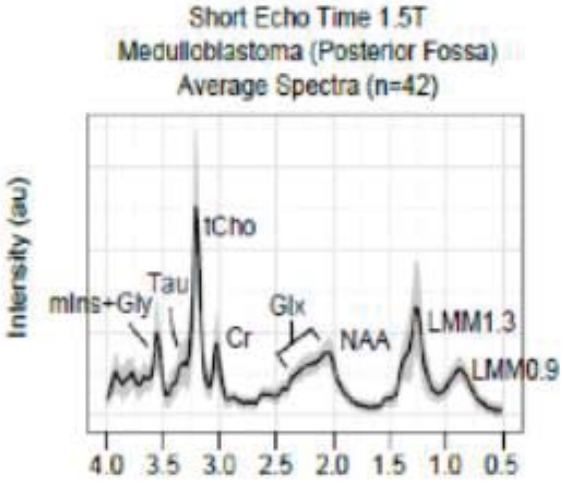

Medulloblastoma
Key Features

- Low mIns
- Presence of Taurine ("shoulder") at 3.3-3.4ppm
- High tCho with narrow peak
- Broad Glx peak without narrow NAA peak
- High LMM

Supratentorial PNET

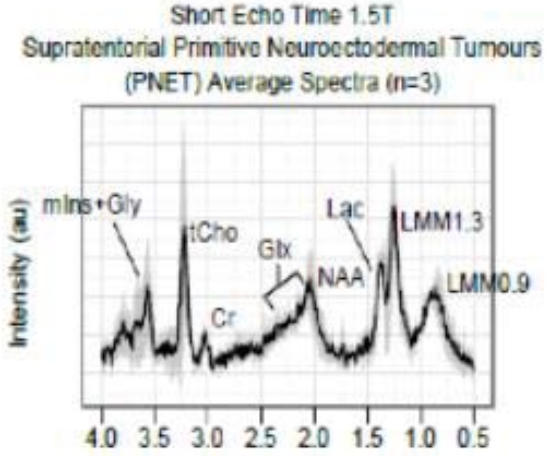

3T and Long TE Spectra

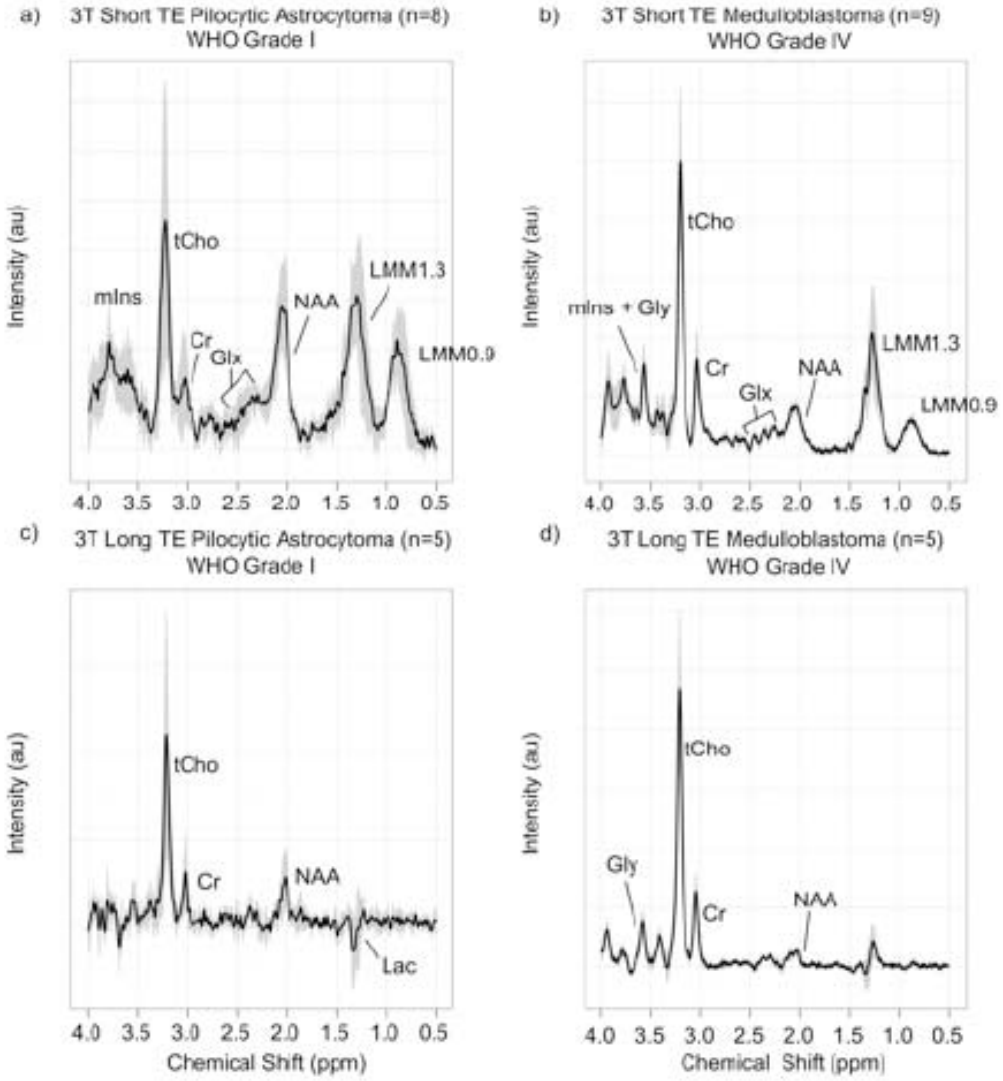

Differentials for Posterior Fossa Tumours

Ependymoma

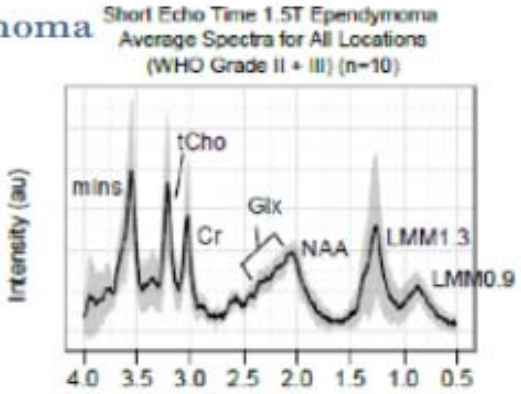

Ependymoma Key Features

- High mIns peak
- Low NAA peak (plus broad Glx peak)
- High lactate

Medulloblastoma

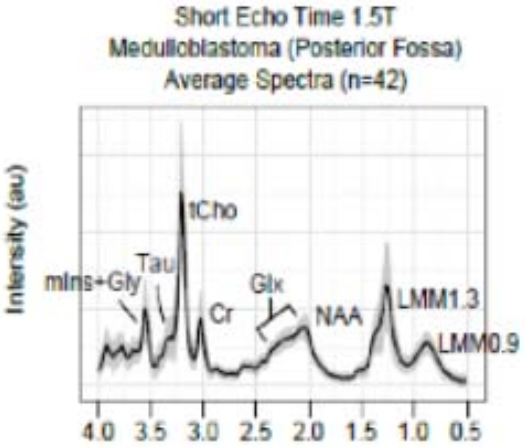

Medulloblastoma Key Features

- Low mIns
- Presence of Taurine ("shoulder") at 3.3-3.4ppm
- High tCho with narrow peak
- Broad Glx peak without narrow NAA peak
- High LMM

Pilocytic Astrocytoma

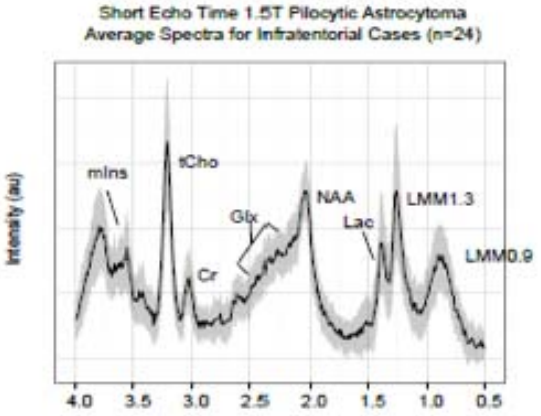

Pilocytic Astrocytoma Key Features

- Low Cr
- High NAA peak (similar to normal brain)
- Lactate readily detected

Differentials for Supratentorial Tumours

Pilocytic Astrocytoma

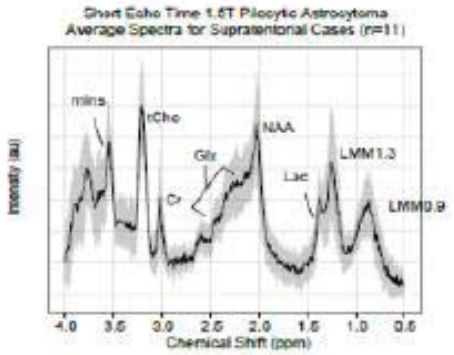

Pilocytic Astrocytoma Key Features

- Low Cr
- High NAA peak (similar to normal brain)
- Lactate readily detected

Ependymoma

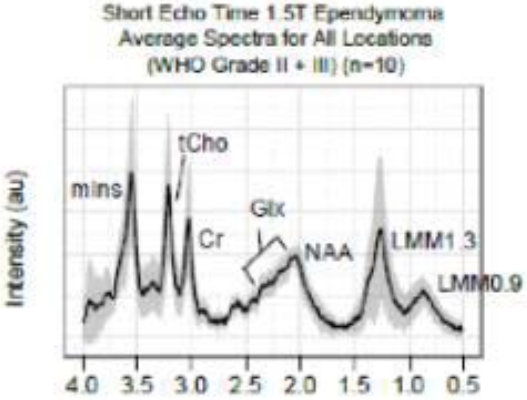

Ependymoma Key Features

- High mIns peak
- Low NAA peak (plus broad Glx peak)
- High lactate

Glioblastoma Multiforme

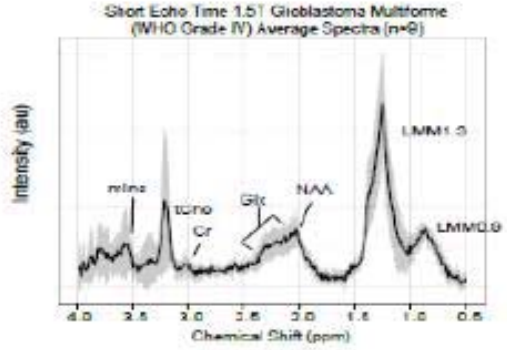

GBM Key Features

- Low mIns
- Low NAA peak (plus broad Glx peak)
- High LMM at 1.3ppm

Differentials for Other Tumours

Medulloblastoma

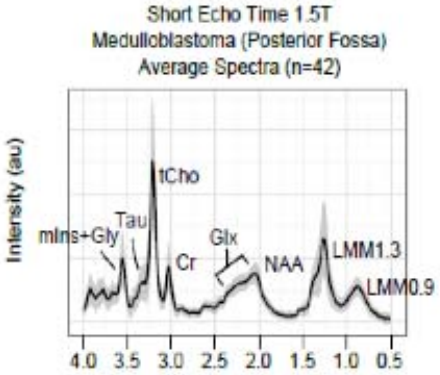

Medulloblastoma Key Features

- Presence of Taurine ("shoulder") at 3.3-3.4ppm
- High tCho with narrow peak
- Broad Glx peak without narrow NAA peak
- Variable LMM

Supratentorial PNET

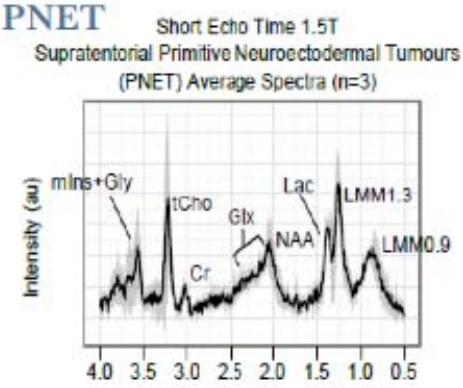

Atypical Teratoid Rhabdoid Tumours

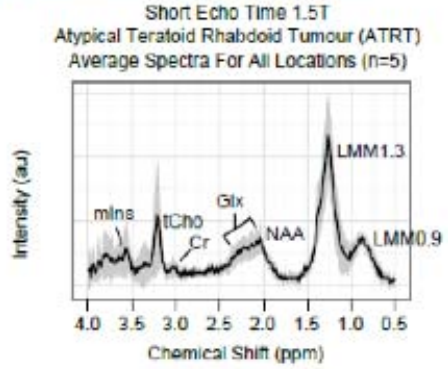

ATRT Key Features

- Low mIns
- Low Cr
- High LMM

REFERENCES

1. Davies NP, Arvanitis TN, Auer D, French A, Grazier R, Grundy R, et al. MULTICENTRE PROSPECTIVE CLASSIFICATION OF CHILDHOOD BRAIN TUMOURS BASED ON 'H MRS METABOLITE PROFILES. In: NEURO-ONCOLOGY (pp II32 - II32) OXFORD UNIV PRESS INC (2010). OXFORD UNIV PRESS INC; 2010 Jun 1.

2. Panigrahy A, Krieger MD, Gonzalez-Gomez I, Liu X, McComb JG, Finlay JL, et al. Quantitative short echo time 1H-MR spectroscopy of untreated pediatric brain tumors: preoperative diagnosis and characterization. AJNR Am J Neuroradiol. 2006 Mar;27(3):560–72.

3. Davies NP, Wilson M, Harris LM, Natarajan K, Lateef S, MacPherson L, et al. Identification and characterisation of childhood cerebellar tumours by in vivo proton MRS. NMR in Biomedicine. John Wiley & Sons, Ltd; 2008 Oct 1;21(8):908–18.

4. Davies NP, Wilson M, Natarajan K, Sun Y, MacPherson L, Brundler MA, et al. Non-invasive detection of glycine as a biomarker of malignancy in childhood brain tumours using in-vivo 1H MRS at 1.5 tesla confirmed by ex-vivo high-resolution magic-angle spinning NMR. NMR in Biomedicine. 2010 Jan; 23(1):80–7.

5. Julia-Sape M, Coronel I, Majos C, Candiota A-P, Serrallonga M, Cos M, et al. Prospective diagnostic performance evaluation of single-voxel 1H MRS for typing and grading of brain tumours. NMR in Biomedicine. 2012 Apr;25(4):661–73.

6. Garcia-Gomez JM, Luts J, Julia-Sape M, Krooshof P, Tortajada S, Robledo JV, et al. Multiproject-multicenter evaluation of automatic brain tumor classification by magnetic resonance spectroscopy. MAGMA. 2009 Feb;22(1):5–18.

7. Arle JE, Morriss C, Wang ZJ, Zimmerman RA, Phillips PG, Sutton LN. Prediction of posterior fossa tumor type in children by means of magnetic resonance image properties, spectroscopy, and neural networks. J Neurosurg. 1997 May;86(5):755–61.

8. Astrakas LG, Zurakowski D, Tzika AA, Zarifi MK, Anthony DC, De Girolami U, et al. Noninvasive magnetic resonance spectroscopic imaging biomarkers to predict the clinical grade of pediatric brain tumors. Clin Cancer Res. 2004 Dec;10(24):8220–8.

9. Kovanlikaya A, Panigrahy A, Krieger MD, Gonzalez-Gomez I, Ghugre N, McComb JG, et al. Untreated pediatric primitive neuroectodermal tumor in vivo: quantitation of taurine with MR spectroscopy. Radiology. 2005 Sep;236(3):1020–5.

10. Wang Z, Sutton LN, Cnaan A, Haselgrove JC, Rorke LB, Zhao H, et al. Proton MR spectroscopy of pediatric cerebellar tumors. AJNR Am J Neuroradiol. 1995 Oct;16(9):1821–33.

11. Vicente J, Fuster-Garcia E, Tortajada S, Garcia-Gomez JM, Davies N, Natarajan K, et al. Accurate classification of childhood brain tumours by in vivo (1)H MRS - a multi-centre study. Eur J Cancer. 2013 Feb;49(3):658–67.

12. Orphanidou-Vlachou E, Auer D, Brundler MA, Davies NP, Jaspan T, MacPherson L, et al. 1H magnetic resonance spectroscopy in the diagnosis of paediatric low grade brain tumours. European Journal of Radiology. 2013 Jun;82(6):e295–e301.

13. Murphy M, Loosemore A, Clifton AG, Howe FA, Tate AR, Cudlip SA, et al. The contribution of proton magnetic resonance spectroscopy (1HMRS) to clinical brain tumour diagnosis. Br J Neurosurg. 2002 Aug;16(4):329–34.

14. Moller-Hartmann W, Herminghaus S, Krings T, Marquardt G, Lanfermann H, Pilatus U, et al. Clinical application of proton magnetic resonance spectroscopy in the diagnosis of intracranial mass lesions. Neuroradiology. 2002 May;44(5):371–81.

15. Galanaud D, Nicoli F, Chinot O, Confort-Gouny S, Figarella-Branger D, Roche P, et al. Noninvasive diagnostic assessment of brain tumors using combined in vivo MR imaging and spectroscopy. Magn Reson Med. 2006 Jun;55(6):1236–45.

16. Shiroishi MS, Panigrahy A, Moore KR, Nelson MDJ, Gilles FH, Gonzalez-Gomez I, et al. Combined MRI and MRS improves pre-therapeutic diagnoses of pediatric brain tumors over MRI alone. Neuroradiology. 2015 Sep;57(9):951–6.

For any queries with the interpretation of MRS spectra, please contact :-

Dr Karen Manias
Clinical Research Fellow Paediatric Oncology
Brain Tumour Research Group
karen.manias@bch.nhs.uk

APPENDIX 4

CONFERENCE ABSTRACTS

Abstracts submitted to conferences and accepted as either first author oral presentations or first author poster presentations are included in the pages below.

International Society of Paediatric Neuro-Oncology (ISPNO) Meeting, Denver, June 2018 (poster)

Diagnostic accuracy and added value of qualitative radiological review of ^{1}H-MRS in evaluation of childhood brain tumors

Manias KA[1,2], Gill SK[1,2], MacPherson L[2], Oates A[2], Pinkey B[2], Davies P[2], Zarinabad N[1,2], Davies NP[1,2,3], Zarinabad N[1,2], Babourina-Brooks B[1,2], Wilson M[1,3], Peet AC[1,2]
[1]Institute of Cancer and Genomic Sciences, University of Birmingham, Birmingham, UK [2]Birmingham Children's Hospital NHS Foundation Trust, Birmingham, UK
[3]Department of Imaging and Medical Physics, University Hospitals Birmingham NHS Foundation Trust, Birmingham, UK

Background: ^{1}H-Magnetic Resonance Spectroscopy (MRS) facilitates non-invasive diagnosis of pediatric brain tumors through providing metabolite profiles. Prospective studies of diagnostic accuracy and comparisons with conventional Magnetic Resonance Imaging (MRI) are lacking.
Aim: To evaluate diagnostic accuracy of qualitative radiological review of MRS for childhood brain tumors, and determine added clinical value compared with conventional MRI.
Methods: Children presenting to a Tertiary Pediatric Centre with brain lesions from December 2015-17 were eligible for inclusion. MRI and single-voxel MRS were acquired on 52 tumors and sequentially interpreted by three radiologists, blind to histopathology. Proportions of correct diagnoses and inter-rater agreement at each stage were compared. Cases were reviewed to determine added value through increased certainty of correct diagnosis, reduced number of differentials, or diagnosis following spectroscopist evaluation. Final diagnosis was agreed by the Tumor Board (TB) at study end.
Results: Radiologists' principal MRI diagnosis was correct in 69%, increasing to 77% with MRS. MRI+MRS resulted in significantly more additional correct diagnoses than MRI alone ($p=0.035$). There was significant increase in inter-rater agreement when correct with MRS ($p=0.046$). Added value following radiologist interpretation of MRS occurred in 73% of cases, increasing to 83% with additional spectroscopist review. First histopathological diagnosis was available a median 9.5 days following imaging, with 25% of all patients managed without conclusive histopathology.
Conclusion: MRS can improve accuracy of non-invasive diagnosis of pediatric brain tumors and add value in the diagnostic pathway. Incorporation into practice has potential to facilitate early diagnosis, guide treatment planning and improve patient care.

SIOPe, Prague, September 2017 (oral)

Functional Imaging in CNS Germ Cell Tumors.

Manias KA[1,2], Rose HEL[1], Withey S[1], Peet AC[1,2]

[1]Institute of Cancer and Genomic Sciences, University of Birmingham, Birmingham, UK [2]Birmingham Children's Hospital NHS Foundation Trust, Birmingham, UK

Background: Functional imaging provides quantitative information to complement more traditional imaging techniques. Accurate non-invasive diagnosis of Intracranial Germ Cell Tumours would be clinically important as treatment differs according to histological subtype. AIM: To describe functional imaging characteristics of different histological subtypes of IGCTS, and to identify imaging characteristics likely to facilitate their differentiation.

Methods: This was a multicentre study using data from the CCLG functional imaging database, evaluating diagnostic scans of patients imaged at 5 recruiting centres between 2005 and 2017. Our cohort included 46 patients comprised of 21 germinomas and 25 NGGCTs (including 12 teraomas, 6 unbiopsied secreting germ cell tumurs, 4 yolk sac tumours and 3 mixed GCTs)

Results: Comparison of ADC histogram parameters of different histological subtypes of IGCTs revealed significant differences in ADC median, 25^{th} and 75^{th} percentiles. Median ADC was significantly lower in germinomas than NGGCTs, reflecting their increased cellularity. The mean ADC histograms of germinomas and NCCGTS were also distinct, with germinomas shifted to the left reflecting. All germ cell tumours had a low FA on DTI, which may be attributed to the highly cellular nature of the tumours leading to isotropic restriction of diffusion. MR spectra of all IGCTs revealed high levels of lipids, with germinomas characterised by the presence of taurine and higher levels of choline and creatine than other histological subtypes. DSC showed Germinomas to have a higher rCBV than NGGCTs.

Conclusion: Functional imaging reflects the histological characteristics of IGCTs. Germinomas are characterised by a low ADC with little heterogeneity on DWI, low FA on DTI, high lipids, tcho, cr and taurine on MRS, and high rCBV on DSC. NGGCTs are characterised by higher ADC and more heterogeneity on DWI, low FA on DTI, high lipids on MRS with less tcho and taurine, and lower rCBV on DSC. In general, secreting GCT lie between germinomas and teratomas. These encouraging preliminary findings require validation with a larger tumour cohort.

SIOPe, Prague, September 2017 (oral)

Added value of ^{1}H-MRS for the diagnosis of paediatric brain tumors.

Manias KA[1,2], English M[2], Gill SK[1,2], MacPherson L[2], Nicklaus-Wollenteit I[2], Rodrigues D[2], Peet AC[1,2]

[1]Institute of Cancer and Genomic Sciences, University of Birmingham, Birmingham, UK [2]Birmingham Children's Hospital NHS Foundation Trust, Birmingham, UK

Background. Magnetic resonance spectroscopy (MRS) aids non-invasive diagnosis of pediatric brain tumors, but use in clinical practice is not well documented. We aimed to review clinical use of MRS, establish added value in non-invasive diagnosis and investigate potential impact on patient care.

Methods. 69 children with lesions imaged using MRS and reviewed by the Tumor Board (TB) from January 2014-2016 met inclusion criteria. Contemporaneous MRI diagnosis, spectroscopy analysis, histopathology and clinical information were reviewed. Final diagnosis was agreed by the TB at study end.

Results. Five cases were excluded for lack of documented MRI diagnosis. The principal MRI diagnosis by general pediatric radiologists was correct in 59%, increasing to 73% with addition of MRS. Of the 73%, 19.1% (95%CI (9.1%, 33.3%)) were incorrectly diagnosed with MRI alone. MRS led to a significant improvement correct diagnosis over all tumor types (p=0.012). Of MRI correct diagnoses, confidence increased in 37% by adding MRS with none incorrectly re-diagnosed. Indolent lesions were diagnosed non-invasively in 85% with MRS a major contributor to 91% of these. Of all patients, 39% were managed without histopathological diagnosis. MRS contributed to diagnosis in 68% of this group, modifying it in 12%. MRS influenced management in 33% of cases, mainly through avoiding and guiding biopsy and aiding tumor characterisation.

Conclusion. MRS can improve accuracy and confidence in non-invasive diagnosis of pediatric brain lesions in clinical practice. There is potential to improve outcomes through avoiding biopsy of indolent lesions, aiding tumor characterisation and facilitating earlier family discussions and treatment planning.

Childhood Cancer and Leukaemia Group (CCLG) Annual Summer Meeting, London, July 2017 (oral and poster)

Differentiating between benign and malignant solid paediatric tumours and identifying tumour type using diffusion-weighted MRI and quantitative Apparent Diffusion Coefficient (ADC)

Karen Manias[1,2], Katharine Foster[3], Niloufar Zarinbad[1,2], Andrew Peet[1,2]

1 Institute of Cancer and Genomic Sciences, University of Birmingham, Birmingham, UK, 2 Department of Paediatric Oncology, Birmingham Children's Hospital, Birmingham, UK, 3 Department of Radiology, Birmingham Children's Hospital, Birmingham, UK

Background: Apparent diffusion coefficient (ADC) reflects tissue cellularity. As solid malignant tumours are highly cellular, ADC could potentially be used to non-invasively discriminate between benign and malignant paediatric tumours or differentiate tumour type.

Aim: The aim of this feasibility study was to determine whether ADC values could be used to differentiate benign from malignant solid tumours in children or distinguish tumour type.

Methods: Thirty-eight children, with 32 malignant and 6 benign tumours, were included in this prospective observational study. Malignancies included neuroblastoma, wilms, rhabdoid, rhobdomyosarcoma, hepatoblastoma and germ cell tumours, and benign lesions consisted of vascular malformations, abscesses, haemangiomas and ganglioneuromas. All children were imaged using multi-b value diffusion-weighted MRI at diagnosis. Analysis was performed by drawing regions-of-interest around the whole tumour from which ADC histograms were constructed. Median, 25th and 75th percentile ADC values and entropy were calculated for all benign and malignant tumours and compared using the Kruskal-Wallace test.

Results: Although ADC values were higher in benign than malignant tumours, this did not reach significance (ADC median $p = 0.496$; 25th centile = 0.066; 75th centile 0.447). Entropy was higher in malignant lesions, but not significantly so ($p = 0.066$). It was not possible to differentiate between individual malignant tumour types in this small cohort using the ADC values evaluated.

Conclusion: Conducing and interpreting diffusion-weighted MRI at diagnosis of childhood solid tumours using quantitative ADC and histogram analysis is feasible. Our study did not identify significant differences between ADC values of different paediatric tumours, although a trend towards higher ADC in benign lesions was observed. This finding deserves further evaluation with a larger cohort of children prior to drawing robust conclusions.

International Society of Magnetic Resonance in Medicine (ISMRM) 17th Annual Meeting, 2017(poster)

The role of ADC histogram analysis in discriminating between benign and malignant tumours in children

Karen Manias[a,b], Niloufar Zarinabad[a], Emma Meeus[a], Katharine Foster[c], Paul Davies[a], Jan Novak[a], Andrew C. Peet [a,b] **a.** Institute of Cancer and Genomic Sciences, University of Birmingham, Edgbaston, Birmingham, UK, B15 2TT **b.** Department of Paediatric Oncology, Birmingham Children's Hospital, Steelhouse Lane, Birmingham, UK, B4 6NH **c.** Department of Radiology, Birmingham Children's Hospital, Steelhouse Lane, Birmingham, UK, B4 6NH

Synopsis.
We evaluated histogram analysis of ADC maps to differentiate benign from malignant solid paediatric tumours in children and distinguish tumour type. Fifty children (38 malignant, 12 benign tumours) were imaged using multi-b value diffusion-weighted MRI at diagnosis. Whole tumour regions-of-interest (ROIs) were drawn, ADC histograms constructed, and median, 2^{nd}-98^{th} percentile ADC values, skewness, kurtosis and entropy calculated. ADC histogram parameters are significantly different between malignant and benign lesions, with skewness and kurtosis predictive of malignancy. These findings deserve further evaluation with a larger cohort of children.

Purpose. Definitive diagnosis of solid tumours in children is not possible using conventional imaging alone. Diffusion-Weighted MR Imaging (DWI) provides information about tissue cellularity through measuring the microscopic rate of water diffusion. Images acquired with high and low-diffusion weighting (b-values) are used to calculate the Apparent Diffusion Coefficient (ADC), a quantitative measure with an inverse relationship with cellularity [1-5]. Constructing ADC histograms may provide information about tumour heterogeneity to non-invasively discriminate benign from malignant tumours or differentiate tumour type.

This study aimed to evaluate the value of histogram analysis of ADC maps in differentiating benign from malignant solid tumours in children or distinguishing tumour type, and identify histogram parameters predictive of malignancy.

Methods. Fifty children (38 malignant, 12 benign tumours) were included. Malignancies included neuroblastoma, wilms, rhabdoid, rhabdomyosarcoma and hepatoblastoma. Benign lesions consisted of vascular malformations, lipomas, mesoblastic nephromas and ganglioneuromas.

All patients underwent 1.5T MR examination (Siemens Avanto, Siemens Healthcare, Erlangen, Germany). The imaging protocol consists of fat-suppressed axial pre- and post-gadolinium T1-W turbo spin echo, axial and coronal T2-W short tau inversion recovery. DW-MRI was acquired using an echo-planar imaging (EPI) sequence in an axial acquisition plane with a field of view (FOV) 187 x 250 mm^2, matrix size 144 x 192, slice thickness 5.0mm, gap 5mm. For each subject 6 b-values (0, 50, 100, 150, 600, 1000 s/mm^2) were acquired in three orthogonal directions with TR/TE = 5700/92 m/s.

ADC maps were automatically generated by scanner software MIROI. An in-house developed medical image analysis toolbox was used for data extraction and regions of interest (ROI) analysis. ROIs were drawn in MIROI around the entire solid tumour on high resolution B0 images by an experienced radiologist prior to overlay on matched ADC maps. Conventional MR guided definition of the outline of the tumour at each consecutive tumour-containing slice, excluding peritumoural oedema. Median,

2^{nd}, 5^{th}, 10^{th}, 15^{th}, 25^{th}, 75^{th}, 85^{th}, 90^{th}, 95^{th} and 98^{th} percentile ADC, skewness, kurtosis and entropy were extracted and their discriminatory potential evaluated. Groups were compared using the Kruskal-Wallice test and p values reported. Multivariate discriminant analysis determined the combination of histogram parameters most predictive of malignancy, and ROC curve analysis the diagnostic value for malignancy of each significant parameter.

Results. ADC values were significantly lower in malignant than benign tumours (median, 2^{nd}, 5^{th}, 10^{th}, 15^{th}, 25^{th}, and 75^{th} percentile ADC; p=0.004 to p=0.035). Higher percentile values (85^{th}, 95^{th} and 98^{th}) did not reach statistical significance. Malignant lesions had more positively skewed histograms (p<0.0001), and significantly higher kurtosis (p<0.0001) and entropy (p=0.031) (Table 1, Figure 1). Discriminant analysis revealed skewness and kurtosis as highly predictive of malignancy (accuracy 90%). In ROC analysis, skewness yielded the best Area Under Curve, AUC (0.84, p=0.001, 95%CI 0.653-1.00, sensitivity 92%, specificity 67%) with cut-off 0.0159. It was not possible to differentiate individual malignant tumour types in this small cohort.

Of clinical relevance, malignant neuroblastoma could be distinguished from benign ganaglioneuroma through the former demonstrating significantly lower median, 2^{nd}, 5^{th}, 10^{th}, 15^{th}, 25^{th}, 75^{th} and 85^{th} centile (p=0.004) ADC values, more positive skewness (p=0.004) and higher kurtosis (p=0.009). These lesions cannot be differentiated on conventional MR imaging.

Discussion. Histogram analysis of ADC maps using a whole-tumour ROI approach could facilitate non-invasive differentiation of malignant from benign body tumours in children with 2^{nd}, 5^{th}, 10^{th}, 15^{th}, 25^{th}, 50^{th} and 75^{th} percentile ADC significantly lower and skewness and kurtosis significantly higher in malignancy. Our finding of low ADC of malignant lesions corresponds to other paediatric studies [1,6,7].

This is the first study of ADC histogram analysis to differentiate between childhood tumours. Previous paediatric studies evaluating mean or median ADC [6-9] do not account for tumour heterogeneity. A histogram-based evaluation provides information about skewness, kurtosis and entropy, reflecting histological characteristics. Skewness and kurtosis were significant predictors of malignancy. Similar findings have been reported in adult studies [10-12]. High skewness could equate to high cellularity reflected by dense population of the left end of the histogram corresponding to low ADC values.

Although histograms of different tumour types appear morphologically different (Figures 3-5), we were unable to identify parameters predictive of individual malignant tumour type. More sophisticated multi-variate analysis may help in this discrimination, but more cases are needed.

Conclusion. Conducting and interpreting diffusion-weighted MRI of childhood solid tumours using quantitative ADC and histogram analysis is feasible. ADC histogram parameters are significantly different between malignant and benign lesions. Skewness and kurtosis are highly predictive of malignancy and potentially useful non-invasive biomarkers. These findings deserve further evaluation with a larger cohort of children.

Figure Captions. (all figures are included in Chapter 4 of the body of the thesis)

Figure 1.

Table 1. Comparison of median ADC histogram parameters between malignant and benign childhood tumours

Figure 2. a-d.

Box plots show comparison of ADC histogram parameters (ADC median (a), skewness (b), kurtosis (c) and entropy (d) for benign and malignant paediatric tumours. Line in box represents the median, height of the box represents the interquartile range, whiskers are the lowest and highest data points within 1.5 interquartile range, and asterixes indicate outliers.

Figure 3. a-c.

A 2 year old girl with a left sided neuroblastoma. Axial T2-weighted image (a) shows a large abdominal mass lying anterior to the left kidney. ADC map was obtained and a whole-tumour ROI selected (b). The corresponding histogram of the neuroblastoma (c) shows ADC median $0.996x10^{-3}$ mm^2/s, kurtosis 2.25150, skewness 0.0216472 and entropy 7.466.

Figure 4. a-c.

A 3 year old boy with a right sided wilms tumour. Axial T2-weighted image (a) shows a large, lobulated, heterogeneous tumour arising from the right kidney. The mass is prediminantly solid, but contains minor haemorrhage and small cystic lesions. Solid components restrict diffusion. ADC map was obtained and a whole-tumour ROI selected (b). The corresponding histogram of the wilms tumour (c) shows ADC median $0.738x10^{-3}$ mm^2/s, kurtosis 2.17527, skewness 0.0238226 and entropy 6.82697.

Figure 5. a-c.

A 6 year old boy with a left-sided ganglioneuroma. Axial T2-weighted image (a) shows a well-defined round mass in the left side of the abdomen. The mass enhances heterogeneously and does not restrict diffusion. ADC map was obtained and a whole-tumour ROI selected (b). The corresponding histogram of the ganglioneuroma (c) shows ADC median $1.576x10^{-3}$ mm^2/s, kurtosis 2.02974, skewness -0.0195563 and entropy 6.50132.

References.

1. Humphries PD, Sebire NJ, Siegel MJ, Olsen OE. Tumors in pediatric patients at diffusion-weighted MR imaging: apparent diffusion coefficient and tumor cellularity. Radiology. 2007 Dec;245(3):848–54.
2. Kralik SF, Taha A, Kamer AP, Cardinal JS, Seltman TA, Ho CY. Diffusion imaging for tumor grading of supratentorial brain tumors in the first year of life. AJNR Am J Neuroradiol. 2014 Apr;35(4):815–23.
3. Yamashita Y, Kumabe T, Higano S, Watanabe M, Tominaga T. Minimum apparent diffusion coefficient is significantly correlated with cellularity in medulloblastomas. Neurol Res. 2009 Nov;31(9):940–6.
4. Gauvain KM, McKinstry RC, Mukherjee P, Perry A, Neil JJ, Kaufman BA, et al. Evaluating pediatric brain tumor cellularity with diffusion-tensor imaging. AJR Am J Roentgenol. 2001 Aug;177(2):449–54.
5. Dominguez-Pinilla N, Martinez de Aragon A, Dieguez Tapias S, Toldos O, Hinojosa Bernal J, Rigal Andres M, et al. Evaluating the apparent diffusion coefficient in MRI studies as a means of determining paediatric brain tumour stages. Neurologia. 2015 Feb.
6. Abdel Razek AAK, Gaballa G, Elhawarey G, Megahed AS, Hafez M, Nada N. Characterization of pediatric head and neck masses with diffusion-weighted MR imaging. Eur Radiol. 2009 Jan;19(1):201–8.
7. Gawande RS, Gonzalez G, Messing S, Khurana A, Daldrup-Link HE. Role of diffusion-weighted imaging in differentiating benign and malignant pediatric abdominal tumors. Pediatr Radiol. 2013 Jul;43(7):836–45.

8. Kocaoglu M, Bulakbasi N, Sanal HT, Kismet E, Caliskan B, Akgun V, et al. Pediatric abdominal masses: diagnostic accuracy of diffusion weighted MRI. Magn Reson Imaging. 2010 Jun;28(5):629–36.
9. Lope LA, Hutcheson KA, Khademian ZP. Magnetic resonance imaging in the analysis of pediatric orbital tumors: utility of diffusion-weighted imaging. J AAPOS. 2010 Jun;14(3):257–62.
10. Suo S-T, Chen X-X, Fan Y, Wu L-M, Yao Q-Y, Cao M-Q, et al. Histogram analysis of apparent diffusion coefficient at 3.0 T in urinary bladder lesions: correlation with pathologic findings. Acad Radiol. 2014 Aug;21(8):1027–34.
11. Pereira JAS, Rosado E, Bali M, Metens T, Chao S-L. Pancreatic neuroendocrine tumors: correlation between histogram analysis of apparent diffusion coefficient maps and tumor grade. Abdom Imaging. 2015 Oct;40(8):3122–8.
12. Xu XQ, Hu H, Su GY, Liu H, Hong XN, Shi HB, et al. Utility of histogram analysis of ADC maps for differentiating orbital tumors. Diagn Interv Radiol. 2016 Mar;22(2):161–7.

Childhood Cancer and Leukaemia Group (CCLG) Annual Summer Meeting, Newcastle, July 2016 (oral and poster)

Evaluating chemotherapeutic response of paediatric solid tumours using diffusion-weighted MRI and quantitative apparent diffusion coefficient (ADC)

Karen Manias[1,2], Katharine Foster[3], Niloufar Zarinbad[1,2], Andrew Peet [1,2]

1 Institute of Cancer and Genomic Sciences, University of Birmingham, Birmingham, UK, **2** Department of Paediatric Oncology, Birmingham Children's Hospital, Birmingham, UK, **3** Department of Radiology, Birmingham Children's Hospital, Birmingham, UK

Background: Assessment of the response of paediatric solid tumours to chemotherapy is predominantly based on size reduction, which may be unreliable in the presence of necrosis. As apparent diffusion coefficient (ADC) reflects tissue cellularity, measuring changes in ADC obtained by diffusion-weighted MRI could potentially reflect early oncological response to treatment.

Aim: The aim of this study was to determine whether measuring changes in ADC values and distribution could be used to assess chemotherapeutic response in childhood solid tumours.

Methods: Thirteen children were included in this prospective observational study. A mixed group of tumours including wilms, neuroblastoma, hepatoblastoma and rhabdomyosarcoma were evaluated. All children were imaged using multi-b value diffusion-weighted MRI at diagnosis and after chemotherapy. Analysis was performed by drawing regions-of-interest around the whole tumour from which ADC histograms were constructed. Pre- and post-chemotherapy median, 25^{th} and 75^{th} percentile ADC and entropy were calculated and compared using the Wilcoxon signed rank test.

Results: Post-chemotherapy ADC values were significantly higher than those obtained at diagnosis. Tumours demonstrated a significant increase in 25^{th} centile ($p = 0.005$) and median ($p = 0.043$) ADC and a significant decrease in entropy ($p = 0.005$). Increase in 75^{th} centile ADC did not reach significance ($p = 0.255$).

Conclusion: Diffusion-weighted imaging and quantitative ADC analysis is a promising non-invasive biomarker of chemotherapeutic response of childhood solid tumours. Further work is needed to validate these preliminary results in a larger cohort of children and determine potential impact on clinical practice.

International Society of Paediatric Neuro-Oncology (ISPNO) Meeting, Liverpool, June 2016 (oral)

The added value of 1H Magnetic Resonance Spectroscopy for the non-invasive diagnosis of paediatric brain lesions in clinical practice

Manias KA[1,2], English M[2], Gill SK[1,2], MacPherson L[2], Nicklaus-Wollenteit I[2], Rodrigues D[2], Peet AC[1,2]

[1]Institute of Cancer and Genomic Sciences, University of Birmingham, Birmingham, UK [2]Birmingham Children's Hospital NHS Foundation Trust, Birmingham, UK

Neuro-Oncology 18(suppl:iii167.1-iii167 · June 2016 DOI: 10.1093/neuonc/now083.109.

Background. Magnetic resonance spectroscopy (MRS) aids non-invasive diagnosis of paediatric brain tumours, but use in clinical practice is not well documented. We aimed to review clinical use of MRS, establish added value in non-invasive diagnosis and investigate potential impact on patient care.

Methods. 69 children with lesions imaged using MRS and reviewed by the Tumour Board (TB) from January 2014-2016 met inclusion criteria. Contemporaneous MRI diagnosis, spectroscopy analysis, histopathology and clinical information were reviewed. Final diagnosis was agreed by the TB at study end.

Results. Five cases were excluded for lack of documented MRI diagnosis. The principal MRI diagnosis by general pediatric radiologists was correct in 59%, increasing to 73% with addition of MRS. Of the 73%, 19.1% (95%CI (9.1%, 33.3%)) were incorrectly diagnosed with MRI alone. MRS led to a significant improvement correct diagnosis over all tumor types (p=0.012). Of MRI correct diagnoses, confidence increased in 37% by adding MRS with none incorrectly re-diagnosed. Indolent lesions were diagnosed non-invasively in 85% with MRS a major contributor to 91% of these. Of all patients, 39% were managed without histopathological diagnosis. MRS contributed to diagnosis in 68% of this group, modifying it in 12%. MRS influenced management in 33% of cases, mainly through avoiding and guiding biopsy and aiding tumor characterisation.

Conclusion. MRS can improve accuracy and confidence in non-invasive diagnosis of pediatric brain lesions in clinical practice. There is potential to improve outcomes through avoiding biopsy of indolent lesions, aiding tumor characterisation and facilitating earlier family discussions and treatment planning.